UNIVERSITÉ DU
LUXEMBOURG

PhD-FSTM-2023-012
The Faculty of Science, Technology and Medicine

DISSERTATION

Defense held on 10/02/2023 in Luxembourg

to obtain the degree of

DOCTEUR DE L'UNIVERSITÉ DU LUXEMBOURG

EN SCIENCES DE L'INGÉNIEUR

by

Matthias BRABAND
Born on 20 July 1988 in Trier, (Germany)

QUANTIFICATION OF INFLUENCING FACTORS OF AN ENERGY-EFFICIENT LONGITUDINAL CONTROL OF BATTERY ELECTRIC VEHICLES

Dissertation defense committee

Dr.-Ing. Holger VOOS, Dissertation Supervisor
Professor, Université du Luxembourg

Dr.-Ing. Jean-Régis HADJI-MINAGLOU, Chairman
Professor, Université du Luxembourg

Dr.-Ing. Raphaël FRANK, Vice Chairman
Professor, Université du Luxembourg

Dr.-Ing. Matthias SCHERER
Professor, University of Applied Sciences Trier

Dr.-Ing. Daniel GÖRGES
Professor, Technical University of Kaiserslautern

UNIVERSITY OF LUXEMBOURG

DOCTORAL THESIS

Quantification of Influencing Factors of an Energy-Efficient Longitudinal Control of Battery Electric Vehicles

Author:

Matthias Braband, M.Sc.

Supervisors:

Prof. Dr.-Ing. Holger VOOS

Prof. Dr.-Ing. Matthias SCHERER

Prof. Dr.-Ing. Jean-Régis HADJI-MINAGLOU

A thesis submitted in fulfillment of the requirements for the degree

Doctor of Philosophy in Electrical Engineering to the

Automation & Robotics Research Group

Interdisciplinary Centre for Security, Reliability and Trust

December 2022

Declaration of Authorship

I, Matthias Braband, declare that this thesis titled, *'Quantification of Influencing Factors of an Energy-Efficient Longitudinal Control of Battery Electric Vehicles'* and the work presented in it are my own. I confirm that:

- This work was done wholly or mainly while in candidature for a research degree at this University.

- Where any part of this thesis has previously been submitted for a degree or any other qualification at this University or any other institution, this has been clearly stated.

- Where I have consulted the published work of others, this is always clearly attributed.

- Where I have quoted from the work of others, the source is always given. With the exception of such quotations, this thesis is entirely my own work.

- I have acknowledged all main sources of help.

- Where the thesis is based on work done by myself jointly with others, I have made clear exactly what was done by others and what I have contributed myself.

Signed:

Date:
December 27, 2022, Bubenreuth

Abstract

Global warming forces the automotive industry to reduce real driving emissions and thus, its CO_2 footprint. Besides maximizing the individual efficiency of powertrain components, there is also energy-saving potential in the choice of the driving strategy. Thus, model predictive control based advanced driver assistance systems to reduce the energy consumption during driving gains a significant interest in the literature. However, this results in a complex control system with many parameter dependencies that could possibly affect the energy efficiency of the vehicle. Most of these parameters are subject to uncertainties. Thus, the important question remains how these parameter uncertainties affect the energy efficiency of the system and how a driver assistance system should be designed to be robust against these uncertainties. To answer this question this thesis applies variance-based sensitivity analyses to design an appropriate driver assistance system and to quantify the influences of the uncertain system and controller parameters.

First, a detailed vehicle and powertrain model of a battery electric vehicle is evolved and verified on component test benches. The parameter uncertainties and their sensitivities were investigated on typical urban and interurban commuter routes using quantitative variance-based sensitivity analysis methods. Based on these findings an economic nonlinear model predictive control eco-cruise control is derived which takes the identified parameter dependencies into account. The developed economic nonlinear model predictive control system is evaluated on artificial drive cycles and compared to a linear model predictive control approach as often outlined in the literature.

Afterwards, the closed loop control system, consisting of the developed economic nonlinear model predictive control and the detailed vehicle model, is analyzed on typical urban and interurban commuter routes using variance-based sensitivity analysis. The findings and parameter dependencies are outlined and discussed. It has been shown, that vehicle parameters as well as controller parameters impact the energy consumption and the driving time of the vehicle. It has been outlined that if the as influential identified parameters are optimized, an average energy-saving potential on the investigated routes of 10.5 % exists by only increasing the driving time of 0.7 %.

Acknowledgements

Contents

List of Figures

List of Tables

Acronyms

ACC Adaptive Cruise Control. 2, 9–12, 142

ADAS Advanced Driver Assistance System. 2

ANOVA Analysis Of Variance. 14, 27

BEV Battery Electric Vehicle. 1–6, 9, 10, 12, 16, 17, 37, 41, 44, 45, 95, 97, 114, 119, 121, 123, 133, 138, 139, 141

CACC Cooperative Adaptive Cruise Control. 2, 10, 12

CC Cruise Control. 2, 9–11, 142

CDF Cumulative Distribution Function. 21

CFD Computational Fluid Dynamics. 44, 46

CVT Continious Variable Transmission. 10

DEM Digital Elevation Model. 75

DoE Design of Experiment. 15

DP Dynamic Programming. 10

DTB1 Drive Testbench 1. 63, 69–72, 145, 146

DTB2 Drive Testbench 2. 47, 146

EIS Electrochemical Impedance Spectroscopy. 52

ENMPC Economic Nonlinear Model Predicitive Control. xvii, 1, 3–5, 13, 37, 40, 41, 97, 99, 103–105, 113–117, 119–121, 123, 127, 130–132, 137–139, 141, 142

EV Electric Vehicle. 13

FAST Fourier Amplitude Sensitivity Test. 15, 17

FEM Finite Element Method. 81

HDMR High-Dimensional Model Representation. 23, 25, 26, 34

HEV Hybrid Electric Vehicle. 10, 12, 13

ICDF Inverse Cumulative Distribution Function. 23, 28

ICE Internal Combustion Engine. 10, 12, 13

IGBT Insulated Gate Bibolar Transistor. xiii, xiv, xvi, xxii–xxv, 57–63, 81, 143, 158

Li-ion Lithium-ion. 16, 48, 49

LMPC Linear Model Predective Control. xvii, 3, 5, 9, 10, 13, 37, 40, 41, 117, 119–121

LQR Linear Quadratic Regulator. 38

MC Monte-Carlo. 4, 15–17, 20, 22, 28–31, 93, 95, 139, 141

MLD Mixed Logical Dynamics. 9

MPC Model Predictive Control. 2, 3, 5, 8–11, 14, 37, 39–41, 43, 74, 79, 97, 112, 117

NEDC New European Driving Cycle. 74

NLP Nonlinear Program. 38

NMPC Nonlinear Model Predictive Control. 3, 5, 9, 10, 13, 37, 40, 41

OAT One-At-a-Time. 14–16, 19, 21

OCP Optimal Control Problem. 9–11, 37–41

PDF Probability Density Function. xvii, 22–24, 79, 80, 93, 95, 123, 132, 139, 141

PLC Programmable Logic Controller. xxii, 149, 151

PMSM Permanent Magnet Synchronous Machine. xiv, 44, 45, 65, 68, 71, 81, 145, 147, 148, 151, 152

PWM Pulse Width Modulation. 57, 69, 70

QP Quadratic Programming. 40

RMSE Root Mean Squared Error. xvii, 55, 56

SEI Solid Electrolyte Interphase. 49

SMPC Stochastic Model Predictive Control. 10, 13

SoC State of Charge. 51–54, 123

SQP Sequential Quadratic Programming. 11, 38, 39

TRMS True Root Mean Squared. 147

VSI Voltage Source Inverter. xiii, 57, 65

WLTP Worldwide Harmonised Light Vehicles Test Procedure. 1, 74

XCP Universal Measurement and Calibration Protocol. 143, 145

Symbols

For the symbol list and the equations throughout this thesis the following conventions were considered:

Constants in normal font, e.g.	π, e
Units in normal font, e.g.	$\mathrm{V}, \mathrm{A}, \mathrm{Hz}$
Scalar variables in normal italics, e.g.	i, I
Vector variables in bold italics, e.g.	$\boldsymbol{i}, \boldsymbol{I}$
Complex variables are underlined, e.g.	$\underline{i}, \underline{I}$
Amplitudes and estimated values with a circumflex, e.g.	$\hat{i}, \hat{I}$
Mean values with a macron, e.g.	$\bar{i}, \bar{I}$
Sets are outlined with uppercase calligraphic letters, e.g.	$\mathcal{U}$

In addition to that the following rules apply:

- Time varying values are depicted with lower case letters.

- Average values (e.g. RMS) and time constant values are outlined with capital letters.

Greek letters

Symbol	Description	Unit
α	Slope angle	rad
α_{cu}	Copper temperature coefficient	-
α_{pm}	Temperature coefficient of the permanent magnet	-
α_D	Diode temperature coefficient	-
α_T	IGBT temperature coefficient	-
$\varepsilon_{CT,c}$	Constant measurement error of the current transducer	%
$\varepsilon_{CT,f}$	Measurement error of the current transducer	%
$\varepsilon_{I,PA,mr}$	Measurement range dependent current measurement error of the power analyzer	%
$\varepsilon_{I,PA,mv}$	Measurement value dependent current measurement error of the power analyzer	%
ε_{max}	Convergence error bound	-
ε_{PLC}	Error of the analog input of the PLC	%
$\varepsilon_{\hat{S}_j}$	Scalar error measure for first order Sobol indices of parameter j	-
$\varepsilon_{\hat{S}_{T_j}}$	Scalar error measure for total order Sobol indices of parameter j	-
$\varepsilon_{\hat{S}_j^G}$	Scalar error measure for first order Sobol indices of parameter j	-
$\varepsilon_{\hat{S}_{T_j}^G}$	Scalar error measure for total order Sobol indices of parameter j	-
$\varepsilon_{TMS,M}$	Torque measurement error of the torque measuring shaft	%
$\varepsilon_{TMS,n}$	Velocity measurement error of the torque measuring shaft	%
$\varepsilon_{U,PA,mr}$	Measurement range dependent voltage measurement error of the power analyzer	%
$\varepsilon_{U,PA,mv}$	Measurement value dependent voltage measurement error of the power analyzer	%
ζ_d	Direct iron loss resistance	Ω
ζ_q	Quadrature iron loss resistance	Ω
η_{ds}	Drive system efficiency	-
η_{gb}	Gearbox efficiency	-
η_{em}	Electrical drive efficiency	-
η_{inv}	Inverter efficiency	-
η_{sys}	System efficiency	-
$\vartheta_{0,cu}$	Reference temperature stator	°C
$\vartheta_{0,pm}$	Reference temperature permanent magnet	°C
ϑ_{air}	Ambient temperature	°C
ϑ_b	Battery temperature	°C
$\vartheta_{j,D}$	Diode junction temperature	°C
$\vartheta_{j,T}$	IGBT junction temperature	°C
$\vartheta_{ref,D}$	Diode reference temperature	°C
$\vartheta_{ref,T}$	IGBT reference temperature	°C
ϑ_{ro}	Rotor temperature of the electrical drive	°C
ϑ_{st}	Stator temperature of the electrical drive	°C
ϑ_{wg}	Inverter coolant temperature	°C
μ_i	Mean of Elementary Effect of parameter i	-
μ_i^*	Mean of the absolute Elementary Effect of parameter i	-

Symbol	Description	Unit
ξ_d	Direct synthetic iron loss parameter	rad^2/As^3
ξ_q	Quadrature synthetic iron loss parameter	rad^2/As^3
ρ_{air}	Air density	kg/m^3
σ_i	Standard deviation of Elementary Effect of parameter i	-
φ	Phase shift between the voltage and current vector	rad
φ_{el}	Electrical angle of the drive	rad
φ_m	Mechanical rotor angle of the electrical drive	rad
Ψ_d	Direct magnetic flux of the electrical drive	Vs
Ψ_{pm}	Magnetic flux of the permanent magnet of the electrical drive	Vs
Ψ_{pm,ϑ_0}	Reference flux of the electric drive	Vs
Ψ_q	Quadrature magnetic flux of the electrical drive	Vs
$\boldsymbol{\Omega}$	Unit hypercube	-
ω_{el}	Electrical angular velocity of the electrical drive	rad/s
ω_m	Angular shaft velocity of the electrical drive	rad/s

Latin letters

Symbol	Description	Unit
$a_{c,D}$	Linear diode conduction loss parameter	V
$a_{c,T}$	Linear IGBT conduction loss parameter	V
a_{ego}	Vehicle acceleration	ms^2
$a_{E_{Err}}$	Linear diode reverse recovery loss coefficient	Vs
$a_{E_{on}}$	Linear IGBT turn on loss coefficient	Vs
$a_{E_{off}}$	Linear IGBT turn off loss coefficient	Vs
A_v	Frontal area	m^2
b_{c_D}	Quadratic diode conduction loss parameter	V/A
b_{c_T}	Quadratic IGBT conduction loss parameter	V/A
$b_{E_{Err}}$	Quadratic diode reverse recovery loss coefficient	Vs/A
$b_{E_{on}}$	Quadratic IGBT turn on loss coefficient	Vs/A
$b_{E_{off}}$	Quadratic IGBT turn off loss coefficient	Vs/A
C_1, C_2	Capacities of the battery equivalent circuit model	F
C_c, C_t	Heat capacities of the equivalent thermal model of one battery cell	Ws/K
$c_{E_{Err}}$	Constant diode reverse recovery loss coefficient	Ws
$c_{E_{on}}$	Constant IGBT turn on loss coefficient	Ws
$c_{E_{off}}$	Constant IGBT turn off loss coefficient	Ws
c_r	Rolling resistance coefficient	-
c_w	Air drag resistance coefficient	-
$D_{1\dots6}$	Diodes of the inverter	-
$E(\cdot)$	Expectation operator	-
$E(\cdot|\cdot)$	Conditional expectation operator	-
E_b	Supplied battery energy	Ws
EE_i	Elementary Effect of parameter i	-

Symbol	Description	Unit
F_a	Acceleration resistance force	N
F_{air}	Air drag resistance force	N
F_L, F_R	Longitudinal force on the left/right wheel	N
F_r	Rolling resistance force	N
F_s	Slope resistance force	N
f_s	Switching frequency	Hz
g	Gravitational constant	m/s^2
h	Road elevation	m
$\hat{I}$	Phase current amplitude	A
I_0	Current offset of the current transducer	A
I_{AC}	AC RMS phase current	A
i_b	Battery current	A
i_d	Direct current	A
i_{D_2}	Current through diode D_2	A
I_{DC}	RMS DC current measurement	A
i_g	Gearbox gear ratio	-
i_q	Quadrature current	A
i_{T_1}	Current through IGBT T_1	A
i_U, i_V, i_W	Phase currents	A
I_U, I_V, I_W	RMS phase current measurements	A
L_d	Direct inductance of the electrical drive	H
L_q	Quadrature inductance of the electrical drive	H
L_s	Stator inductance of the electrical drive	H
M_1	Modulation index of the fundamental wave	-
M_3	Modulation index of the third harmonic	-
M_{air}	Air gap torque of the electrical drive	Nm
m_{eq}	Equivalent vehicle mass	kg
M_D	Sum of all shaft torques	Nm
M_{em}	Shaft torque of the electrical drive	Nm
M_L, M_R	Shaft torques of the left/right wheel	Nm
m_v	Vehicle mass	kg
n_{cell}	Number of battery cells	-
p	Pole pairs of the electrical drive	-
P_{AC}	RMS AC power measurement	W
P_{c,D_2}	Conduction losses on diode D_2	W
P_{c,T_1}	Conduction losses on IGBT T_1	W
P_{DC}	RMS DC power measurement	W
P_{E_{Err},D_2}	Diode D_2 reverse recovery losses	W
P_{E_{on},T_1}	IGBT T_1 on switching losses	W
P_{E_{off},T_1}	IGBT T_1 off switching losses	W
P_{inv}	Summarized inverter losses	W
P_{em}	Supplied mechanical power of the electrical drive	W
P_{pto}	Power demand of the auxiliary consumers	W
$P_{v,b}$	Battery losses	W
P_w	Supplied mechanical power of the gearbox	W

Symbol	Description	Unit
Q_b	Maximum available electrical charge of one cell	As
Q_{SoC}	Stored electrical charge of one cell	As
R_1, R_2	Resistances of the battery equivalent circuit model	Ω
r_c	Curve radius	m
R_s	Series resistance of the battery equivalent circuit model	Ω
R_{s,ϑ_0}	Reference stator resistance of the electrical drive	Ω
$R_{th_{ca}}, R_{th_{ct}}, R_{th_{ta}}$	Thermal reistances of the equivalent thermal model of one battery cell	K/W
$R_{th_{jw},D}$	Thermal resistance between one diode and the coolant	K/W
$R_{th_{jw},T}$	Thermal resistance between one IGBT and the coolant	K/W
r_w	Wheel radius	m
s_{ego}	Traveled distance of the vehicle	m
S_i	First order Sobol indices of parameter i	-
S_{T_i}	Total order Sobol indices of parameter i	-
S_i^G	First order generalized Sobol indices of parameter i	-
$S_{T_i}^G$	Total order generalized Sobol indices of parameter i	-
$\hat{S}_i$	Estimated first order Sobol indices of parameter i	-
$\hat{S}_{T_i}$	Estimated total order Sobol indices of parameter i	-
$\hat{S}_i^G$	Estimated first order generalized Sobol indices of parameter i	-
$\hat{S}_{T_i}^G$	Estimated first order generalized Sobol indices of parameter i	-
SoC	State of charge of the battery system	-
$T_{1...6}$	IGBT devices of the inverter	-
t_d	Driving time	s
$\mathbf{u}(t)$	Control vector	-
U_{AC}	AC RMS phase voltage	V
u_d	Direct voltage	V
u_{DC}	DC-bus voltage	V
U_{DC}	RMS DC voltage measurement	V
u_k	Battery system terminal voltage	V
u_{ocv}	Open circuit voltage of one battery cell	V
u_q	Quadrature voltage	V
u_{RC1}, u_{RC2}	Voltage drop on the series resistances on the RC elements of one battery cell	V
u_{R_s}	Voltage drop on the series resistance of one battery cell	V
$u_{ref,D}$	Diode reference blocking voltage working point	V
$u_{ref,T}$	IGBT reference blocking voltage working point	V
u_U, u_V, u_W	Phase voltages	V
U_{UV}, U_{UW}, U_{VW}	RMS phase-to-phase voltage measurements	V
$V(\cdot)$	Variance operator	-
v_{ego}	Vehicle velocity	m/s
v_{max}	Maximum allowed legal speed	m/s
$\mathbf{x}$	State vector of a dynamic system	-
$\mathbf{x}_0$	Initial system state vector	-

1 Introduction

This thesis presents the quantification of influencing factors on the energy efficiency of a longitudinal controlled Battery Electric Vehicle (BEV) using sensitivity analysis methods. Besides this, the sensitivity analysis is used to develop an Economic Nonlinear Model Predicitive Control (ENMPC) for the longitudinal control of the vehicle, which is robust against parameter changes.

This chapter is structured as follows. Section 1.1 outlines the research context. In Section 1.2, the problem statement and the motivation for conducting this study are given. The aim and scope are presented in Section 1.3 and the scientific contribution of this thesis is outlined in Section 1.4. At least in Section 1.5, the outline of the thesis is presented.

1.1 Context of the Study

Global warming caused by industrialization, the immense use of fossil fuels and the associated greenhouse gas emissions is one of the most severe problems. In the 2015 Paris climate agreement [1], nearly all countries pledged to limit global warming to a maximum of $1.5\,^\circ$C compared to the pre-industrial era. To achieve this goal, current CO_2 emissions must be massively reduced. For example, Germany adopted its intentions in this regard in 2016 in its Climate Protection Plan 2050 [2]. Here, CO_2 emissions must be reduced by up to $95\,\%$ by 2050. Since the transport sector accounts for $21.76\,\%$ [3] of global greenhouse gas emissions, of which $18\,\%$ are caused by road traffic, a significant climate protection potential exists here.

One approach to reducing emissions in the transportation sector is to replace internal combustion engines with battery-electric drives. Due to the improved efficiency of the electric drive, this leads to an improvement in the CO_2 footprint of the vehicle and makes local emission-free operation possible. In Germany, however, it is currently not possible to completely reduce the overall CO_2 emissions of an electric vehicle during operation due to the composition of the electricity supply mix. CO_2 emissions for the production of electricity amounted to $485\,\mathrm{g/kWh}$ on average in 2021 in Germany [4]. The example of a VW up! with a Worldwide Harmonised Light Vehicles Test Procedure (WLTP) consumption of $12.9\,\mathrm{kWh/100km}$ corresponds to emissions of $6.25\,\mathrm{kg/100km}$ compared to $10.1\,\mathrm{kg/100km}$ for the same vehicle with a gasoline engine. Therefore, the emissions caused by the transport sector will only be reduced to a limited extent by replacing internal combustion engines with battery-electric drives.

Nevertheless, there are many other aspects that can reduce the energy consumption of vehicles, including environmental conditions, such as the weather or road surface conditions, the driving style of the driver and the vehicle itself [5]. Especially for BEVs with long recharge times and lower ranges than internal combustion engines saving energy during operation plays a crucial role. Thus, the development of energy-efficient driving strategies to reduce fuel consumption has gained significant industrial interest [6]. Energy-efficient driving, commonly referred to as eco-driving, describes the reduction of fuel consumption by operating the vehicle along its energy-optimal velocity trajectory. It can be processed by a human driver using learned patterns to achieve low energy consumption, for example, through smooth acceleration or deceleration and maintaining a constant speed. Furthermore, eco-driving is capable of reducing traffic fatalities and can reduce the risk of traffic accidents [6]. However, without exact knowledge of the energy-optimal operating points of the vehicle and the upcoming driving situation, a human driver can

only reach a sub-optimal driving strategy.

The digitization of modern vehicles has led to a rapid increase in the real-time information available through Car2X technologies. In addition to the vehicle's inertial sensor system, ultrasound, radar, camera and LiDAR-based environmental sensors provide information about the vehicle's surrounding area. Furthermore, networking with infrastructure and map data providers makes it possible to obtain real-time information about traffic, speed limits, and the current route profile, for example. Likewise, the available computing capacity in modern vehicles has increased tremendously so that even more complex algorithms can be realized without violating real-time capability.

With these sensor and computational capabilities, modern Advanced Driver Assistance System (ADAS) are developed. It exists a wide range of different ADAS functions. Simple, purely informal systems such as traffic sign recognition provide the driver with additional information to perform the driving task more effectively. In addition, numerous ADAS functions take over a part or even the entire driving task from the driver. This can be limited to the longitudinal or lateral control of the vehicle but can also involve both. For this purpose, the system is able to control the brake and engine for longitudinal control and the active steering for lateral control based on the environmental and vehicle information. Well-established longitudinal control systems are Cruise Control (CC), Adaptive Cruise Control (ACC) and Cooperative Adaptive Cruise Control (CACC). All of these systems automate the vehicle's throttle and brake control to affect the vehicle's velocity trajectory. CC systems optimize the speed trajectory without considering the traffic ahead. As an extension, ACC systems include one or more vehicles in front and optimize their own speed and the distance to the vehicles to ensure safe driving. CACC systems combine several vehicles into a group by using vehicle-to-vehicle communication and the group is controlled according to different optimization criteria. However, all of the approaches are capable of including energy-efficient driving as an optimization criterion.

Due to the large amount of available information and the computational capabilities of modern vehicles, especially the development of advanced eco-driving algorithms has gained significant research interest. However, an eco-driving algorithm faces multiple design objectives, where some of them are contradictory. For instance, the trade-off between the driving time and the required energy will lead to contrary optimization goals. Furthermore, the ADAS controller needs to consider constraints, e.g., actuator limits or boundaries for a safe driving scenario. Thus, Model Predictive Control (MPC) is mainly used in the literature since it is able to consider constraints and operate close to them. Furthermore, this algorithm is capable of combining contrary goals in the controller design.

However, several powertrain components such as battery, inverter and drive are involved to operate the vehicle at the desired velocity trajectory. Consequently, designing an energy-efficient top-level controller which considers the powertrain behavior sufficient and is still real-time capable is a difficult task. The resulting closed-loop system consisting of the top-level controller and the vehicle leads to a complex system with plenty of parameters and dependencies.

1.2 Problem Statement and Motivation

The development of modern battery technologies is progressing rapidly. Nevertheless, battery systems currently available on the market and used in series-produced vehicles do not achieve the same usual ranges and charging times as a comparable combustion engine vehicle. Due to the high weight, volume and cost requirements of a battery system, vehicles cannot be equipped with batteries of any size. Thus, an efficient operation of the vehicle plays a major role in addition to the above-mentioned environmental aspects also with regard to an increase in range. Consequently, besides the actual trends in battery research, the research and development focus emphatically on eco-driving strategies to increase the range of BEVs.

The most promising approach for this multi-objective target of eco-driving are MPCs, where the most recent developments of eco-driving algorithms are presented in Chapter 2. The controller approaches range from simplified LMPCs to Nonlinear Model Predictive Controls (NMPCs) and stochastic approaches. Furthermore, these controllers have already been successfully applied to internal combustion engines, hybrid vehicles and electric vehicles.

However, all of the approaches mentioned above are complex closed-loop control systems with a large number of system and controller parameters, which all possibly influence the system behavior. This raises the question which parameters of the vehicle and the powertrain should be considered in the controller and how parameter uncertainties affect the performance of the resulting eco-driving algorithm. This question is still unanswered in the literature and a quantification of these parameter dependencies has not been done.

Quantification of parameter influences is denoted in the literature as sensitivity analysis. Several qualitative and quantitative methods exist to analyze mathematical models regarding their parameter sensitivity. The most popular and promising methods are the qualitative Morris parameter screening [7] and the quantitative variance-based sensitivity analysis, first introduced by Sobol [8]. In particular, in the context of analyzing the energy efficiency of BEVs, several studies exist (e.g., [9, 10]) which highlight the potential of these statistical investigations. However, analyses on vehicle level usually simplify the underlying powertrain components due to reducing the computational effort or because of a lack of detailed knowledge of each powertrain component. In contrast, evaluations on the component level (e.g., [11–13]) do not consider dependencies on system level. Further, as far as the author is aware, currently known analyses of BEVs are limited to pre-recorded speed profiles at vehicle level or predefined operating points at component level. The degree of freedom of an optimized speed trajectory by an eco-driving approach has thus not been considered further in the analyses performed so far.

For the above reasons, the motivation of this thesis is to combine a detailed vehicle and powertrain model with an ENMPC-based eco-driving algorithm which can, compared to other sensitivity analyses, additionally utilize the degree of freedom of the vehicle speed. Furthermore, the sensitivity analysis of this detailed vehicle model enables the possibility of determining the relevant parameters which should be included in the controller design. Thus, there exists high potential to optimize the controller design. Additionally, the closed-loop sensitivity analysis provides insights into the system behavior to quantify the parameter influences that affect the optimization result, which enables precisely improving the controller robustness and performance.

1.3 Aim and Scope

This thesis aims to quantify the influence of system and controller parameters on the energy efficiency and the control behavior of an ENMPC-controlled vehicle.

In order to reach the objectives of this study, the following research questions will be addressed:

1. How should a suitable model for a quantitative sensitivity analysis be designed and validated?

2. How should a sensitivity analysis be designed to obtain reliable and resilient sensitivity results?

3. Which parameters are important and which can be neglected?

4. How can these parameter dependencies be quantified?

5. How can the time dependence of technical processes be treated in a sensitivity analysis?

6. How is the vehicle's energy consumption affected by parameter uncertainties when driving predefined velocity profiles?

7. How should the eco-driving controller be designed using the knowledge about parameter importances?

8. How does the proposed eco-driving controller perform in various driving situations?

9. Which parameter uncertainties influence the closed-loop eco-driving most and should be considered to improve the robustness of the proposed ENMPC?

The first research question is answered by adapting well-known models of all vehicle components, including the longitudinal motion, battery, inverter and electrical drive models, to meet the requirements for accuracy and computation time. All proposed component models are validated on test benches to ensure that the proposed simulation models have sufficient accuracy for the sensitivity analysis.

To answer research questions 2-5, a literature review on sensitivity analysis has been done to choose appropriate sensitivity analysis methods. In particular, the consideration of time-dependent processes poses a special challenge that is considered in this application. Since the sensitivity results are estimates based on Monte-Carlo (MC) simulations, methods for ensuring convergence of the estimators are also outlined and discussed in this thesis. The question of which parameters are important and which can be neglected is answered using a qualitative screening technique to reduce the computational effort. In contrast, the quantification of parameter influences is ensured by using generalized Sobol indices.

Question 6 is addressed by an open-loop sensitivity analysis of the proposed vehicle using predefined velocity profiles on representative routes for the use case of commuting in an urban and interurban environment.

The results of this open-loop sensitivity analysis are used to answer research question 7. They are used to identify relevant parameters which should be considered in the controller design. The resulting controller is an ENMPC which optimizes the speed trajectory to improve the energy efficiency of the vehicle. To avoid disturbing traffic influences in the results, no preceding vehicles are considered in this controller approach. However, an integration of preceding vehicles is possible in the presented control concept. The proposed ENMPC optimizes the vehicle speed considering the vehicle dynamics, the powertrain condition, road geometries and traffic sign information. Its performance is evaluated in various driving situations to answer research question 8.

The most interesting question, which closed-loop parameters have the most significant impact on energy efficiency, is answered by a sensitivity analysis of the vehicle with active ENMPC. Here, the relevant parameters are identified and improvements to the controller are discussed to achieve the best possible energy savings potential of this optimized system. Especially, the measurement or estimation errors of vehicle parameters such as the vehicle mass are discussed.

1.4 Significance of the Study

The main contributions of this thesis to the field of ENMPC based longitudinal motion of a BEV as well as the novel approach of sensitivity analysis of a closed-loop eco-driving system are highlighted in the following:

1. *Building detailed models on component and vehicle level which are optimized regarding accuracy and computation time.*
   The vehicle and powertrain models are developed to represent the energy consumption accurately. Furthermore, the computation time is reduced to a minimum without losing accuracy to fit as a basis for the sensitivity analysis.

2. *Development of a sensitivity analysis framework that is capable of performing screenings as well as variance-based sensitivity analyses and which considers temporal dependencies.*
   A suitable sensitivity framework is developed, which consists of the sample generation, a Morris screening and the variance-based sensitivity analysis using generalized Sobol indices which considers temporal dependencies. Furthermore, the framework is expanded with two methods to ensure convergence of the sensitivity estimators, which is crucial for reliable sensitivity analysis results.

3. *Using sensitivity analysis results as a foundation for an eco-driving algorithm.*
   The development of the ENMPC is based on the results of the open-loop sensitivity analysis. This novel approach ensures that all relevant parameters are considered in the controller and that this important decision is based on quantified results.

4. *Real-time capable ENMPC approach.*
   The presented ENMPC and its implementation strategy of using only the relevant parameters inside the optimization problem together with the fast HPIPM solver lead to a real-time capable controller.

5. *Closed-loop sensitivity analysis of an ENMPC based eco-driving algorithm.*
   The novel sensitivity analysis approach applied to a closed-loop eco-driving algorithm and the associated identification of relevant parameters opens up new potential for optimization.

6. *Quantification of parameter influences.*
   The novel approach of a variance-based sensitivity analysis enables quantifying parameter influences in such a complex system and connecting the effects on the energy efficiency with their cause.

7. *Focusing on the most relevant parameters for controller improvements.*
   The proposed sensitivity analysis opens the possibility of identifying the most relevant parameters even in complex systems. Consequently, researchers or developers are able to focus on the most relevant parameters to improve the controller performance efficiently.

1.5 Outline of the Thesis

In Chapter 2, the actual state of the art and state of the research related to eco-driving and sensitivity analysis and their applications is presented.

Chapter 3 presents the theory of sensitivity analysis. It includes an overview of modern sensitivity analysis methods and outlines a summary of the used methods of Morris and Sobol. Furthermore, the sensitivity analysis process consists of the sample generation, estimation of the sensitivity indices and ensuring convergence.

In Chapter 4, the theory of MPC-based control approaches is presented. Especially the differences between LMPC, NMPC and ENMPC are outlined.

Chapter 5 presents the detailed and computation time optimized models of the BEV, consisting of a battery, inverter, electric drive, gearbox, vehicle and environmental model. Furthermore, the drive cycles which are used for the evaluation of the energy consumption of the BEV are outlined.

In Chapter 6, the open-loop sensitivity analysis of the BEV is outlined. The complete process, including the definition of the parameter distribution, performing a Morris screening and a variance-based sensitivity analysis as well as ensuring convergence of the estimates, is presented and discussed.

Chapter 7 focuses on the development of the proposed ENMPC using the results of the open-loop sensitivity analysis. Furthermore, the performance of this controller at artificial and real drive cycles is

outlined.

In Chapter 8, the closed-loop sensitivity analysis of the BEV is outlined. Based on the results, also possible controller improvements are discussed.

The thesis concludes in Chapter 9 with the findings, a discussion of the contributions and an outlook for future research in this area.

2 State of the Art

The following chapter presents the literature review on the current state of the art. For this purpose, current approaches to energy-efficient driving are discussed and their field of application and limitations are shown. Furthermore, an overview of sensitivity analysis methods is given and existing applications of sensitivity analyses on technical systems are presented.

2.1 Energy-Efficient Driving

Energy-efficient driving describes the process of maneuvering a vehicle over a certain distance with the lowest possible energy consumption by adjusting the speed trajectory. In order to achieve this goal, the vehicle driver or a corresponding assistance system must recognize and observe a wide range of boundary conditions. This chapter explains the boundary conditions to which energy-efficient driving is subject. Furthermore, a current overview of the existing literature in the field of assistance systems is given, which adapts the speed trajectory of the vehicle under consideration of boundary conditions in order to move the vehicle as energy-optimal as possible.

2.1.1 Influences on the Energy Consumption

The influences on the energy efficiency can be divided into four categories: Construction-related vehicle characteristics, selected route and environmental influences, traffic-related boundaries and driving behavior.

The construction-related vehicle characteristics are defined during the construction of the vehicle. This includes vehicle mass, vehicle aerodynamics, and tire selection. All these factors influence the vehicle's driving resistance and thus determine the required wheel-side drive energy that must be provided by the powertrain. This required energy is provided by one or more energy storage units within the vehicle. Depending on the type of drive, the energy, which is usually provided chemically, must be converted and transformed into a mechanical propulsion power at the wheel. The efficiency of this conversion with all the components involved plays a decisive role in the energy consumption of the vehicle. Furthermore, auxiliary consumers, such as air conditioning or lights, must also be supplied from these energy storage units and contribute to the overall consumption of the vehicle.

In addition to the construction-related vehicle characteristics, the environment, as well as the selected driving route, also influence the energy consumption of the vehicle. Different weather conditions, e.g., fog or rain, influence the driven velocity and the road surface characteristics. Furthermore, the use of auxiliary consumers, like using the lights or air conditioning, is affected by the environmental conditions. Additionally, they influence the thermal conditions and efficiency of powertrain components. The stationary boundary conditions such as speed limits, curve radii, intersections or traffic lights affect the choice of the optimal vehicle speed. Furthermore, road slopes and the road surface condition influence the driving resistances.

The traffic environment of the vehicle sets dynamic boundary conditions. In such a situation, the vehicle speed must be individually adapted to this environment.

The above-mentioned boundary conditions provide the framework for the driver to adjust the vehicle speed to influence energy consumption positively. However, energy-optimal driving depends on three different factors: Will, knowledge and skills. Specifically, this means that in addition to the will to reduce energy consumption through his driving style, the vehicle driver must also have the appropriate knowledge about energy-efficient driving and be able to apply it. Due to the multitude of influencing factors mentioned above, this task can therefore often only be performed suboptimally by an individual and leads to wasted saving potential. Consequently, numerous energy-efficient driver assistance systems have been developed in the past for different drive concepts and boundary conditions to either support the driver in this task or to relieve him of this task altogether. A comprehensive literature review of these eco-driving systems will be given in the next section.

2.1.2 Assistant Systems for Energy-Efficient Driving

In this section, the literature review on energy-efficient or eco-driving systems is presented. Since the focus is on the energy-efficient longitudinal control of vehicles, only systems that can perform the longitudinal control task partially or fully automatically are listed here. The evaluation is done concerning its methodological as well as application-related properties and limitations and is evaluated accordingly. Therefore, a distinction is made between the following properties or evaluation criteria:

- **Control approach:**
  The literature review focus on MPC-based control approaches as it seems to be the most promising approach in the recently published literature. All MPC-based approaches have in common that an optimization problem, including constraints and a cost objective, is solved. However, the choice of the optimization problem class influences the control approach's complexity and the real-time capability. Therefore, a distinction is made here between linear, nonlinear, economic and stochastic methods. Furthermore, this subitem evaluates whether the presented algorithms have real-time capability since this is a major concern for a practical application.

- **Control objective:**
  The origin of assistance systems is not to optimize energy efficiency but to increase the comfort and safety of the driver or passengers. Nevertheless, promising approaches in the field of eco-driving exist there as well. Therefore, this evaluation discusses which optimization goal is being pursued.

- **Driving use case:**
  The use case for which the investigated systems are designed determines the complexity of the longitudinal control task. While the complexity on highways and rural roads is rather low, it increases significantly in urban areas. Due to the high traffic density and the variety of traffic control systems, high demands are placed on the optimization.

- **Driving constraints:**
  Here, the constraints considered for optimized longitudinal vehicle guidance are discussed. This includes, for example, the consideration of a legally prescribed maximum speed, curve radii, traffic lights or intersections, or a slower moving vehicle in front.

- **Environmental information:**
  Ambient information is typically required to realize predictive energy-optimal longitudinal control. This can be, for example, information about road gradients and curve radii in the form of map data. This is often additionally supplemented by the measurement of the vehicle in front with different sensor systems. Modern approaches also use Car2X interfaces to communicate with other vehicles or the infrastructure.

- **Powertrain type:**
  The used drive technology significantly impacts the design of the optimization problem. The distinction between trucks and cars is mainly reflected in the different weights as well as in the

purpose of use. For conventional drives and hybrid vehicles, there is also an additional degree of freedom of gear selection. Likewise, some approaches for hybrid vehicles also involve power management for efficient energy distribution. In the case of electrically driven vehicles, the gear selection and active power management are usually omitted. However, a significant advantage of hybrid and electric vehicles is the considerable recuperation potential.

- **System realization:**
  In addition to the formulation of the optimization system, the corresponding implementation is also part of it. At this point, it is evaluated whether it is a simulation study or whether the presented assistance system has been implemented in a vehicle on real hardware capable of real-time computation.

- **System evaluation:**
  Evaluation of systems, whether simulative or under real traffic conditions, represents an integral part of a system assessment. Basic functionality is often demonstrated on artificial driving cycles or driving profiles, whereas some studies have tested the systems on representative routes or in real road traffic.

The above points are discussed in more detail below and the literature is separated into these categories. Furthermore, a summary of the considered topics can be found in Table 2.1.

Control approaches

The first approaches on energy-efficient longitudinal control of vehicles date back to the work of Gilbert [14] and Schwarzkopf [15]. In [14], the first fuel economic CC system and in [15], an optimal control based on Pontryagin's maximum principle considering varying terrain was introduced. The first ACC approach using MPC was introduced in [16] with the focus on collision avoidance to prevent accidents with the preceding traffic. In [17], a predictive eco-CC system using slope information for a heavy-duty truck used in North America was presented. The first ACC systems using LMPC were outlined in [18,19]. [18] developed an ACC for a gasoline smart vehicle including the gear shift logic directly into the optimization problem by using an Mixed Logical Dynamics (MLD) prediction model description where the nonlinearities are approximated using a piecewise affine model. In contrast, [19] compensates the nonlinearities of the vehicle model by an inverse model. To reduce the required computation time, an explicit LMPC-based ACC algorithm was presented in [20,21], which calculatess the computationally intensive solution of the Optimal Control Problem (OCP) offline beforehand and stores it as a lookup table in the controller. Furthermore, the presented ACC system is Stop&Go capable and can be parameterized for different vehicles. However, [20,21] do not focus on energy efficiency.

In addition to these initial approaches, various eco-driving solutions have been published in the past decade. Due to the steadily increasing computing power in vehicles, besides linear optimization problems also nonlinear, economic and stochastic ones gained more and more interest.

Recent LMPC publications are [22–26]. In [22], an LMPC-based eco-ACC system for a commercial vehicle is presented where the ride comfort, driver permissible tracking range of preceding vehicles and rear-end safety are formulated as linear constraints. The approach of [23] outlines an eco-CC system for a commercial vehicle but is not acting closed-loop on the vehicle. It only provides an optimized vehicle trajectory for energy-efficient driving to the driver. In [24,25], a novel LMPC approach is presented where the powertrain characteristics of a Smart ED BEV are modeled as a lookup table and integrated into a convex OCP using separable programming and linear constraints. Furthermore, the prediction model of [24,25] is formulated and discretized in the space domain instead of the time domain, resulting in a speed-independent prediction horizon length. In addition, the longitudinal vehicle motion is modeled using a kinetic energy representation, which omits the need of a nonlinear prediction model. In [26], the advantages of state and space domain modeling are combined, resulting in a nonlinear model description. However, the presented models are linearized to obtain an NMPC approach.

Due to the nonlinear vehicle characteristics, many NMPC-based approaches have been presented to overcome the limitations of LMPCs. In [27], an NMPC-based ACC system is presented, which utilizes real-time traffic information of traffic speed and density using Car2X technologies. Another NMPC approach is outlined in [28] using the information of up and down slopes in an eco-ACC to improve the fuel consumption of an Internal Combustion Engine (ICE) vehicle. The concept is extended in [29], where the NMPC prediction model is formulated based on experimentally obtained driving data to estimate the acceleration or deceleration profile of preceding vehicles. In addition, it was extended to include traffic lights for the urban use case. In [30], the presented NMPC of [29] is evaluated simulative for 100 different vehicles using the AIMSUM microscopic traffic simulator and real-time capability is shown. An NMPC full range ACC including Stop&Go capability is postulated in [31] and in [32], a novel algorithm for switching between the ACC and CC is outlined. Other approaches of NMPC-based ACC systems are found in [33, 34], where in [33], the preceding vehicle is predicted assuming a constant velocity without acceleration. [34] proposed a real-time capable dynamic programming approach for solving the OCP. A novel combination of two independent NMPCs with individual optimization targets is described in [35]. The first NMPC ensures energy-efficient driving, whereas the second defines an optimal velocity for passing through the traffic lights in a green wave. Another example of a Car2X application is given in [36], where an NMPC-based CACC system is proposed. The communication between two consecutive driving vehicles is used to estimate the preceding vehicle motion more precisely to improve the energy efficiency of the following vehicle. A further approach using Car2X technology can be found in [37], where the NMPC for calculating the optimal vehicle velocity is solved online in the cloud. In the vehicle itself, an NMPC is used to control the velocity. A novel NMPC prediction model for a BEV was introduced in [38] using hyperfunctions to model traffic and road geometry data. The most recent NMPC-based formulations can be found in [39–42]. In [39], a novel real-time capable NMPC combining eco-ACC and safety requirements for congested traffic situations is introduced. In [40], an NMPC-based CC for an Hybrid Electric Vehicle (HEV) is introduced, where the focus is on comparing the C/GMRES and Newton/GM-RES solvers regarding real-time capability. Since the parameterization of an optimization problem could be a difficult task, [41] presents a novel auto-tune approach for an NMPC-based eco-driving algorithm. The optimization of HEVs is still a current area of research. In [42], an approach combining the different degrees of freedom of an HEV into one optimization problem is presented. It consists of optimizing the speed in relation to the preceding vehicle, the energy management between the ICE and the electrical drive system by also optimizing the gear ratio of the Continious Variable Transmission (CVT) gearbox.

Since the traffic behavior in front of the vehicle is non deterministic, several Stochastic Model Predictive Control (SMPC) approaches exist. In [43], the SMPC is used to control the complex system of driver and vehicle in an ACC system. The driver behavior is modeled as a stochastic system using Markov chains which is updated online by applying a simple learning algorithm to it. However, the vehicle dynamics are modeled deterministically. A CACC system based on a linear SMPC is presented in [44], where the optimization goal is to minimize the piecewise linear approximation of the vehicle's fuel consumption map. The preceding vehicle is modeled using a conditional Gaussian model based on the current measurement and upcoming traffic light signals. A novel SMPC ACC approach to control a BEV is presented in [45, 46]. The preceding vehicle is modeled by a stochastic representation and chance constraints are used to regulate the relative distance between the vehicles. To achieve real-time capability, the algorithm is formulated using Pontryagin's Minimum Principle. Additionally, a novel risk-sensitive formulation of uncertainties is included in this eco-ACC control concept.

For the approaches mentioned above, several algorithms to solve the proposed OCPs are used. The solving strategies could be divided into three different categories: Dynamic Programming (DP), offline solutions and online solutions using iterative solving strategies for OCPs. DP is a technique based on Bellman's principle of optimality [47]. The main advantage of this strategy is that each OCP whether linear or nonlinear, can be solved. However, the calculation demand rises extensively for growing problem sizes. Nevertheless, several approaches of the above-discussed literature use DP as a solution and are outlined in [34, 37]. One promising approach of offline solutions is the explicit MPC. However, this solution is limited to linear or convex OCPs, where the state space can be divided into polyhedral sets

where each set of the state space consists of an affine projection of the actual state vector to the control sequence. The affine projections and the boundaries of these polyhedral sets can be calculated offline and stored in a lookup table for the use in an online algorithm. The approaches [20, 21] uses such an explicit formulation. Most of the approaches presented above use different types of online solution algorithms based on interior-point or active-set methods. The well-known C/GMRES algorithm is used in [28–30, 35, 38, 41, 45, 46]. However, several other algorithms are used to solve the optimization problem. In [24, 25], the quadprog algorithm is used. Ipsolve was used by [44] and NPSOL was used by [27]. CVX-GEN and Cplex were used by [27] and [23]. Further, a Dantzig-Wolfe active set algorithm was applied in [22]. Another promising class of algorithm for real-time capability for nonlinear OCP are Sequential Quadratic Programmings (SQPs) which are used by [36, 42]. However, several authors have not outlined which solvers are used to compute the OCP [17, 19, 26, 31–33, 39, 43].

Control objective

In the following, the control objective of the different approaches is discussed. The main distinction here is between energy efficiency and other optimization goals. In the presented literature, only a few sources are outlined where the optimization goal has not an energy-efficient motivation. The approaches [20, 21, 31, 32] outline ACC following solutions where the optimization goal is mainly a smooth and safe following behavior optimally targeting the desired headway.

The other discussed literature focus on eco-CC or eco-ACC driving. They mainly differ in the driving use cases, the considered constraints, the vehicle type and which environmental information are used.

Driving use case

Highways and rural roads represent less complex driving situations, whereas the complexity in urban areas increases significantly and many boundary conditions have to be considered. Thus, the presented literature is divided into separate driving use cases. MPC algorithms for highway use are presented in [17, 20–27, 31, 32, 37, 40] and for rural use in [17, 18, 20, 21, 23–25, 31–33, 37–40, 45, 46]. The more complex task of optimizing driving in the city use case is outlined in [19–22, 26, 28–32, 34–37, 39, 41, 42, 44], whereas only [20, 21, 26] consider Stop&Go scenarios.

Driving constraints

The driving constraints determine the limits within which the velocity trajectory can be optimized and which information is used for this purpose. Especially for urban areas, considering intersections and traffic lights is of interest. Since most of the presented papers are eco-ACC approaches considering the traffic around the vehicle plays an important role and is considered in [18, 20–22, 24–33, 36, 37, 39, 42–46]. Besides the traffic around the vehicle, also the legal speed limits are considered as a boundary to achieve a legal driving by [18, 24–30, 34–46]. Furthermore, to improve a safe driving, the maximum curvature speed is considered by [23–25, 38, 41, 45, 46]. Especially for the urban environment, the approaches of [23, 28–30, 35, 44] also consider intersections or traffic lights in their optimization problem.

Environmental information

To enable predictive behavior of the controller, information about the further course of the route and the surrounding traffic of the vehicle must be provided, depending on the scope of the MPC. Digital map data for the supply of elevation and slope data, as well as curve radii and traffic sign information are used in [17–19, 23–26, 28–32, 34, 35, 37–41, 44–46]. Information about the preceding vehicle, which is usually measured by sensors, is used in [18–22, 24, 26–33, 36, 37, 39, 42–46, 48]. More advanced assistance

systems also use Car2X communication, for example, to communicate with the traffic light control system of a city or with another vehicle in the course of a CACC algorithm. Car2X communication is used by [23, 27, 30, 35, 37, 44].

Powertrain and vehicle type

Depending on the powertrain or vehicle type, different degrees of freedom for the optimization exists. Therefore, the powertrain type of the studied literature is divided into commercial vehicles and passenger cars with ICE, HEVs and BEVs. Since the application of eco-driving algorithms on commercial vehicles has significant economic potential, the work of [17, 23, 49] focus on energy-optimal driving of commercial vehicles. However, most of the work is related to passenger cars. In [18, 19, 27–32, 36, 41, 44] approaches for vehicles with ICEs are presented. Mostly, the exact vehicle type is not specified in the corresponding literature. Regarding the ICE vehicles, only [18, 27] outlined which vehicle was used. In [27], an Audi A8L and in [18], a Smart is used. The publications [33, 35, 39, 40, 42, 43] focus on optimizing an HEV powertrain. Not all types of vehicles are outlined. However, in [39] and [40] the usage of a Toyota Prius is stated. The most recent sources focus more on optimizing BEVs. [24, 25, 45, 46] used a Smart ED and [37] utilized a Nissan Leaf. In [26, 34], no further details about the test vehicle are given. [20, 21] presented a generic approach for passenger cars that should work on all powertrain types. However, it was tested on an Audi S8 with ICE. In [33], whether the powertrain type nor the vehicle was given.

System realization

The system realization shows how far the eco-driving concept has been transferred into practice or whether it has currently only been validated simulatively. Most of the approaches presented in the literature are validated simulatively. These are [17–19, 22, 26–35, 37–46]. However, a few approaches are also validated within a test vehicle [20, 21, 23–25] or on a test bench setup [36].

System evaluation

To obtain a reliable conclusion about the control behavior and the saving potential of the eco-driving algorithms, suitable drive cycles must be defined and used. To evaluate the general performance of the proposed concepts, in [18, 19, 22, 24–26, 29–33, 36, 38–40, 42–44] artificial drive cycles are used. However, to obtain realistic energy-saving potentials in [23, 27, 28, 34, 35, 37, 41, 45, 46] real driving scenarios are used. In [41], an urban route through São Carlos and in [34], a city scenario in Columbus, Ohio is presented. A rural route from Landshut to Kaiserslautern is outlined in [37]. The eco-ACC algorithms proposed in [45, 46] are tested on a test track of a tire manufacturer. In [27], a rural and highway route from Palo Alto to San Jose is outlined as realistic driving scenario and [23] used an interurban 12.9 km long test route.

The literature discussed above regarding the various requirements for an eco-driving algorithm and its evaluation is summarized in Table 2.1. In summary, the literature review shows that there is already a wide variety of different approaches to eco-driving. Nevertheless, these approaches differ significantly in their respective fields of application and the methodology used. In particular, the choice of the optimization problem, the scope and the accuracy of the prediction model, as well as the considered constraints are often determined from empirical values or assumptions to solve the task. Furthermore, only artificial driving cycles are often used in the evaluation of fuel economy, which usually does not reflect the real use of the vehicle.

For these reasons, there is a need for further research at this point, which will be answered in this thesis. Thus, the related research questions, as already outlined in Section 1.3, need to be answered.

Table 2.1: Literature Review on energy-efficient longitudinal control approaches. Legend: ●=yes, ○=No, ◐=partially, ?=information not given

Source	Control approach					Control objective		Driving Use-Case			Driving constraints				Environmental information			Powertrain type				System realization		System evaluation	
	LMPC	NMPC	ENMPC	SMPC	Real-time capable	Eco-driving	Other	Highway	Rural	Urban	Speed limit	Curvatures	Intersections and traffic lights	Traffic	Digital map data	Preceding vehicle measurement	Car2X interface	Commercial vehicle	Passenger car, ICE	Passenger car, HEV	Passenger car, EV	Simulative	Test vehicle	Test track/Test scenarios	Real driving scenarios
[17]	○	●	○	○	?	●	○	●	●	◐	●	○	○	○	●	○	○	●	○	○	○	●	○	○	●
[18]	●	○	○	○	●	●	○	●	○	●	○	○	○	●	●	●	○	○	●	○	○	●	○	●	○
[19]	●	○	○	○	●	●	○	●	○	●	○	○	○	●	●	●	○	○	●	○	○	●	○	●	○
[20, 21]	●	○	○	○	●	○	●	●	●	●	○	○	○	●	○	●	○	○	●	○	○	●	●	●	◐
[22]	●	○	○	○	?	●	○	●	○	●	○	○	○	●	○	○	○	●	○	○	○	●	○	●	○
[23]	●	○	○	○	●	●	○	●	●	●	●	●	●	○	●	○	●	●	○	○	○	○	●	○	●
[24, 25]	●	○	○	○	●	●	○	●	●	◐	●	●	○	●	●	●	○	○	○	○	●	●	●	●	○
[26]	◐	◐	○	○	◐	●	○	●	●	●	●	○	○	●	◐	◐	○	○	○	○	●	●	○	◐	○
[27]	○	●	○	○	○	●	○	●	○	○	●	○	○	●	○	●	●	○	●	○	○	●	○	○	◐
[28]	○	●	○	○	●	●	○	○	○	●	○	○	○	○	●	○	○	○	●	○	○	●	○	●	○
[29]	○	●	○	○	●	●	○	○	○	●	●	○	●	●	●	○	●	○	●	○	○	●	○	●	◐
[30]	○	●	○	○	●	●	○	○	○	●	◐	○	●	●	◐	●	●	○	●	●	●	●	○	●	○
[31]	○	●	○	○	?	○	●	●	●	●	○	○	○	●	●	●	○	○	●	○	○	●	○	●	○
[32]	○	●	○	○	●	○	●	●	●	●	○	○	○	●	●	●	○	○	●	○	○	●	○	●	○
[33]	○	●	○	○	?	●	○	○	●	○	○	○	○	●	○	●	○	?	?	?	?	●	○	●	○
[34]	○	●	○	○	◐	●	○	○	○	○	●	○	○	○	●	○	○	○	○	○	●	●	○	○	◐
[35]	○	●	○	○	●	●	○	○	○	●	●	○	●	○	●	○	●	○	○	●	○	●	●	○	◐
[36]	○	●	○	○	●	●	○	○	○	●	●	○	○	●	○	●	●	○	●	○	○	●	◐	●	○
[37]	○	●	○	○	◐	●	○	●	○	●	●	○	●	●	●	●	●	○	○	○	●	●	○	○	◐
[38, 50]	○	●	●	○	●	●	○	◐	●	○	●	●	○	○	●	○	○	○	○	○	●	●	○	●	○
[39]	○	●	○	○	○	●	○	◐	●	●	●	○	○	●	●	○	○	○	○	●	○	●	○	●	○
[40]	○	●	○	○	●	●	○	●	●	○	●	○	○	○	●	○	○	○	○	●	○	●	○	●	○
[41]	○	●	○	○	●	●	○	○	○	●	●	●	○	○	●	○	○	○	●	○	○	●	○	●	◐
[42]	○	●	○	○	◐	●	○	○	○	●	●	○	○	●	●	○	○	○	○	●	○	●	○	●	○
[43]	●	○	○	●	?	●	○	◐	●	○	●	○	○	●	○	○	○	○	○	●	○	●	○	●	○
[44]	○	○	○	●	?	●	○	○	○	●	●	○	●	●	●	○	●	○	●	○	○	●	○	●	○
[45, 46]	○	○	●	●	●	●	○	◐	●	◐	●	●	○	●	●	●	○	○	○	○	●	●	○	●	○

2.2 Sensitivity Analysis

Sensitivity analysis studies systems in terms of their response to parameter variations. The variation of parameters here can cause differently intense reactions of the output. Likewise, there may be interactions between individual parameters in the investigated system so that the examined model output reacts nonlinearly to the parameter variations when they are excited together. Sensitivity analysis plays an important role in evaluating systems in terms of their robustness to parameter variations. Furthermore, sensitivity analysis methods can identify influential parameters and distinguish them from non-influential ones. The MPC-based eco-driving approaches are complex closed-loop control systems with a large number of system and controller parameters which all possibly influence the system behavior. Therefore, quantifying these influences on the energy consumption and the driving behavior is an important task and can be answered using sensitivity analysis.

Some promising approaches for systematic sensitivity analysis of technical systems exist in the literature. A basic overview of the history and classification of these methods is given in Section 2.2.1. Furthermore, Section 2.2.2 presents technical applications and the associated benefits of sensitivity analysis but also discusses further research needs in relation to energy-efficient driving.

2.2.1 Local and Global Methods of Sensitivity Analysis

Sensitivity analysis methods can be divided into two approaches: Local and global. Local methods are characterized by their limited exiting area around a specific working point. Usually, they are designed as an One-At-a-Time (OAT) experiment where only one factor at one time is varied. Typical evaluation measures for local sensitivity methods are difference and differential quotient. The limited area around the actual working point of local methods forces the results to get falsified when the models are nonlinear and the operating point of the analysis is too far away from the operating point of the system. Furthermore, local methods that belong to an OAT design are not able to identify interactions between parameters since only one parameter at one time is varied. To overcome this constraint global sensitivity analysis methods has been developed.

The mathematical foundation of local sensitivity analysis methods was laid in the 80s [51, 52]. A good overview of the earliest publication can be found in [53]. However, due to the ease of implementation and interpretation of the results, 34 % of current publications on sensitivity analysis and its application still use local OAT methods [54].

One common global sensitivity analysis approach is to graphically analyze the parameter dependencies using scatterplots. However, such graphical methods are limited. The influence of parameters is only determined qualitatively and interactions between parameters usually cannot be detected. Furthermore, the clarity decreases significantly for an increasing number of assessed parameters. Popular nongraphical methods for global sensitivity analysis are regression and correlation analyses, where the coefficients serve as an evaluation measure. However, they are limited to some model restrictions and produce only accurate results on linear or monotonic models. A good overview of these conventional methods is given in [55].

To compensate for the disadvantages of local methods and graphical evaluation, new methods were published in the early 1990s that allow global sensitivity analysis even for nonlinear models. The most common global sensitivity analysis methods are analyzing the variance of the corresponding model outputs. Here, the variance of the individual parameter influences is set in relation to the total variance of the output. Thus, the proportion caused by a parameter can be quantified. With this kind of description, it becomes possible to make a quantitative statement about the direct influence of a parameter and additionally its interactions with other parameters on the output. The foundation for these variance-based sensitivity analysis methods was laid by Sobol [8], where a unique solution scheme for the Analysis Of Variance (ANOVA)-based model description was given. Here, the direct influence of one parameter is

called first order or main effect. Interaction effects between parameters can be quantified using the total order effect. For very few or only very simple models, the integrals from [8] can be determined analytically. Consequently, the integrals must be approximated by a Monte Carlo simulation for more complex models. In the literature, two different MC strategies are developed.

The first approach is based on a spectral analysis scheme where the input parameters are exited with a specific fundamental frequency. The parameter input space is covered using this fundamental frequency and a specific sampling rate. The calculation of the sensitivity indices is based on a Fourier analysis which is done after the simulation. The first publication of this Fourier Amplitude Sensitivity Test (FAST) method can be found in [56] for calculating the total effect, whereas in [57], an extended FAST method is presented to analyze also the interaction effects. In [58, 59], strategies for a more efficient covering of the input parameter space by the FAST methods are proposed.

The second approach directly estimates the sensitivity indices using MC simulations. A comprehensive review on current estimation techniques for first order and total effects is given in [60]. The sampling scheme significantly influences the convergence rate of the estimators. Consequently, several strategies for an efficient sample generation are outlined in the literature [61–65]. Since the MC simulations are computationally extensive, often a qualitative screening method is used in advance to separate important from unimportant parameters. The most promising approach for such a preselection is given by Morris [7]. Morris proposed a modified OAT design to calculate difference quotients locally but repeated the procedure with different starting points to cover the analyzed parameter space more completely. Thus, a semi-global qualitative screening method is available for analyzing complex models.

The methods discussed above do not consider temporal or functional model outputs. However, technical applications usually include time dependencies in their model description. First approaches which apply variance-based sensitivity analysis to functional outputs are given in [66–68]. A general framework for treating temporal dependencies was first presented by Alexanderian [69] using generalized Sobol indices.

2.2.2 Technical Applications of Sensitivity Analysis Methods

The methodological work is mainly limited to the evaluation of academic test models. However, several applications of variance-based sensitivity analysis on technical systems have been presented in the past.

In [70], a variance-based sensitivity analysis is performed using FAST to investigate two different Kalman filters for the kinematic and position estimation of a moving object. Another early investigation is presented in [71], where the dynamic response of a nuclear turboset is analyzed using Morris screening and the Sobol indices are calculated using the FAST algorithm. The first experimentally assessment of a controlled system based on Design of Experiment (DoE) using a Latin-Hypercube sampling was presented in [72]. Especially for such large and complex models, sensitivity analysis is used both for model analysis and as parameterization support. In [73], it is evaluated if a Morris screening-based method can replace the variance-based sensitivity analysis to reduce the computational effort in computing the sensitivity indices of complex distributed watershed models. A similar investigation was made in [74], where three different global sensitivity analysis methods are compared to access the most relevant processes in wastewater treatment systems. The assessed methods are standardized regression coefficients, Morris screening and extended-FAST variance-based sensitivity analysis with the goal of factor fixing and factor prioritization in a model with 21 model outputs and 79 inputs. Another publication related to civil engineering was given in [75], where a derivative-based sensitivity measure is applied to a complex reservoir simulator model. Furthermore, the comparison of linear regression, Morris screening and variance-based sensitivity analysis to assess building energy models was presented in [76]. The analysis of charge transport models is given in [77]. They typically consist of at least 10 undefined or ill-defined parameters. In this publication, Sobol indices are used to evaluate the impact of ill-defined parameters

to fix the non-influential parameters to a specific value and to prioritize the estimation of the most influential parameters. The first direct application of Morris screening and the calculation of Sobol indices for systems with functional outputs was presented in [78]. Here, the methods were applied to an IR photo-diode front-end model.

The above-outlined publications do not directly belong to the assessment of vehicles or vehicle components but outline the potential of sensitivity analyses in technical applications. However, there exists a small number of recent publications where components or vehicles are investigated using sensitivity analysis. In [79], a Morris screening for analyzing parameter dependencies in a battery equivalent circuit of a Lithium-ion (Li-ion) battery is presented. A single particle Li-ion battery model with electrolyte was analyzed in [12]. The focus was to identify the nonimportant parameters to simplify the model and to identify the most relevant parameters to focus on them for parameter estimation research and thus to improve the model quality. In [13, 80, 81] electrical drive systems of propulsion systems for vehicles are investigated. An only qualitative OAT screening was done in [80] by varying the assessed parameters 50 % around their nominal values with the goal of reducing the complexity of thermal models for electric machines in integrated starter-generators. In [13, 81], a Morris screening and a variance-based sensitivity analysis were performed to quantify the influence of measurement and manufacturing uncertainties on the torque accuracy of electric drive systems for BEVs.

The influence of environmental factors, e.g., wind, rolling resistance and temperature, on the energy consumption of a BEV at vehicle level was investigated in [82] using a simple OAT design. This work was expanded by a statistical assessment of the same environmental factors in [83]. However, the used statistical methods are not directly mentioned in the publication. Another recent sensitivity analysis of energy demand estimation of a BEV was outlined in [10], where no detailed considerations of the powertrain are included. The powertrain components are simplified using static power maps where further dependencies were neglected. A plug-in hybrid heavy vehicle analysis for optimal energy management was outlined in [84] using a simple OAT design. A similar study was done in [85] to improve an efficient loss model of a commercial electric vehicle. Likewise, the sensitivity analysis uses a simple OAT design where the most important parameters are varied by 5 % from their nominal parameters and the increase in range is evaluated. The most complete and systematic analyses at the vehicle level are given in [9, 86]. In [86], real driving data from buses were collected during operation in Finland and a sensitivity analysis of the energy uncertainty regarding the ambient temperature, the applied DC-power, the aggressivity of the drive and the stops per kilometer were investigated using Scatterplots and Sobol indices. Based on this work, in [9], a surrogate model is presented to predict the energy demand of electric city buses in varying driving conditions in real time. The proposed surrogate model is analyzed regarding the robustness of parameter changes using a variance-based sensitivity analysis where the ambient temperature, the rolling resistance and the payload are determined as the most influential parameters for the energy demand estimation.

The aforementioned application examples outline the great potential of sensitivity analyses. However, the publications of sensitivity analyses at vehicle level did not include detailed powertrain models, whereas the component-level evaluations did not consider dependencies at the system level. The outlined investigations were carried out using pre-recorded velocity profiles at vehicle level and specific working points or load profiles at component level. In particular, combining an eco-driving sensitivity analysis evaluation at vehicle level using detailed component models is still an open research topic. Furthermore, temporal dependencies are often not considered precisely in the discussed literature. In addition, most of the applications of variance-based sensitivity analysis using an MC-based estimation of the sensitivity indices did not outline an assessment of the approximation error for the used estimators. However, analyzing the convergence of the estimators is crucial for providing reliable sensitivity analysis results.

Therefore, there is a need for further research in the sensitivity analysis of eco-driving systems, primarily for the application in BEVs. At first, a detailed simulation model must be created, which includes

the components of the powertrain and the vehicle. This model must meet the requirements of a sensitivity analysis. This includes, on the one hand, that the examined output variables of the model must be represented as accurately as possible. On the other hand, the model must be optimized in terms of computing time to be able to calculate the required model runs of the MC simulation in a reasonable amount of time. Furthermore, the extension of the classical Sobol indices concerning temporal dependencies has to be considered. Moreover, methods have to be integrated to assess the approximation errors of the used estimators of the Sobol indices.

2.3 Conclusions

In this chapter, a comprehensive review of the actual state of the art of eco-driving and sensitivity analysis was given. At first, the influences on the energy consumption of vehicles were discussed. In addition, a literature review of eco-driving algorithms was presented. It has been shown that numerous of already published eco-driving approaches exist but with different use cases and for different types of vehicles. Also, the considered constraints vary for most approaches. In addition, it has been outlined that the evaluation of the system has mostly been done on artificial test tracks, which do not always allow an expressive statement about the energy efficiency of the proposed algorithms.

The second part of this chapter consists of a review of sensitivity analysis methods and their application to technical systems. A review of local and global sensitivity analysis methods was presented and their advantages and disadvantages were discussed. It was outlined that the most recent publications for quantitative sensitivity analysis focus on variance-based methods like the Sobol indices and FAST. Furthermore, recent publications for considering systems with temporal or functional outputs were outlined and discussed. At least a review on the application of several sensitivity analysis methods to technical applications was done. It was outlined that several publications exist outside of the automotive application using sensitivity analysis for model reduction and model analysis, which highlights the method's potential. However, it was shown that, in particular, in the examination of automotive systems and closed-loop control systems, only a few publications exist. Furthermore, it can be stated that most of the publications do not entirely cover the analysis of a BEV and did not provide sufficient approximation quality measures for the MC-based sensitivity measures. Consequently, actual research needs were derived and outlined at the end of this chapter.

3 Sensitivity Analysis

Sensitivity analysis, in general, deals with the question of how an output of interest of a model reacts to changes or uncertainties in the input parameters of this model. The main questions that arise are:

1. Which parameter has which amount of influence on the output, and how are they ranked to each other?

2. Which parameters have negligible influence on the output and can be neglected?

3. Are there interactions between input parameters, and thus the model behaves nonlinearly?

Especially in complex models with plenty of input parameters the answer to this questions becomes very important and not easy to answer.

The easiest and first used approach to Sensitivity Analysis is known as the local approach. Usually, only minor changes around a nominal working point are evaluated by varying only one input parameter at each evaluation. These attempts are called OAT approaches and their mathematical foundation was laid in the 1980s [51, 52], mainly based on difference and differential derivatives. However, the local method provides only suitable results in small areas around the nominal values for nonlinear models. Also, the analysis of nonlinearities or interactions among different input factors is impossible. To overcome these limitations, a new class of Global Sensitivity Analysis [7, 8] methods have been developed that cover the entire parameter space and are also capable of analyzing nonlinearities and interaction effects. Also, they are not limited to some kind of model, nor a priory knowledge of the models is needed.
Besides their local or global validity, the methods can also be divided into screening and variance-based methods. The main difference between these approaches is the possibility of quantifying sensitivities. Screening methods are used to qualitatively evaluate the sensitivities of input parameters, whereas variance-based techniques are able to quantify the contribution of each parameter to the output variance. Practice has often shown that only a few inputs are influential [87]. Thus, screening methods are mainly used to answer the question of which parameters are noninfluential and can be neglected in a variance-based quantitative setting. This two-step approach is caused by the computational costs of variance-based sensitivity setups. Using screening methods to identify noninfluential parameters to exclude them from the variance-based sensitivity analysis causes a significant improvement in the computational effort.

Figure 3.1 outlines an overview of sensitivity analysis methods used in the literature. Screening can be done using supersaturated design [88] and sequential bifurcations [89]. If the number of experiments is in the same order as the number of inputs, fractional factoring RIII or RIV design [90] can be used. However, all of these proposed screening methods make assumptions about the underlying model behavior and only outline the first order effects. Morris screening [7], on the other hand, is model-independent with acceptable computational cost and outlines, in addition, the estimates of the main and total order effects.

Also, several methods are outlined in the literature for the quantitative variance-based sensitivity analyses. For linear and monotonic models, linear or rank regression models can be considered. Nevertheless, as shown in Figure 3.1, most of the proposed methods are also applicable to more complex models. The techniques of metamodeling [91, 92] and smoothing [93] are used to reduce the complexity and thus the computation time of the investigated model by substituting the original model with easier representations with nearly similar behavior. To work directly with the developed models without using substitutes or
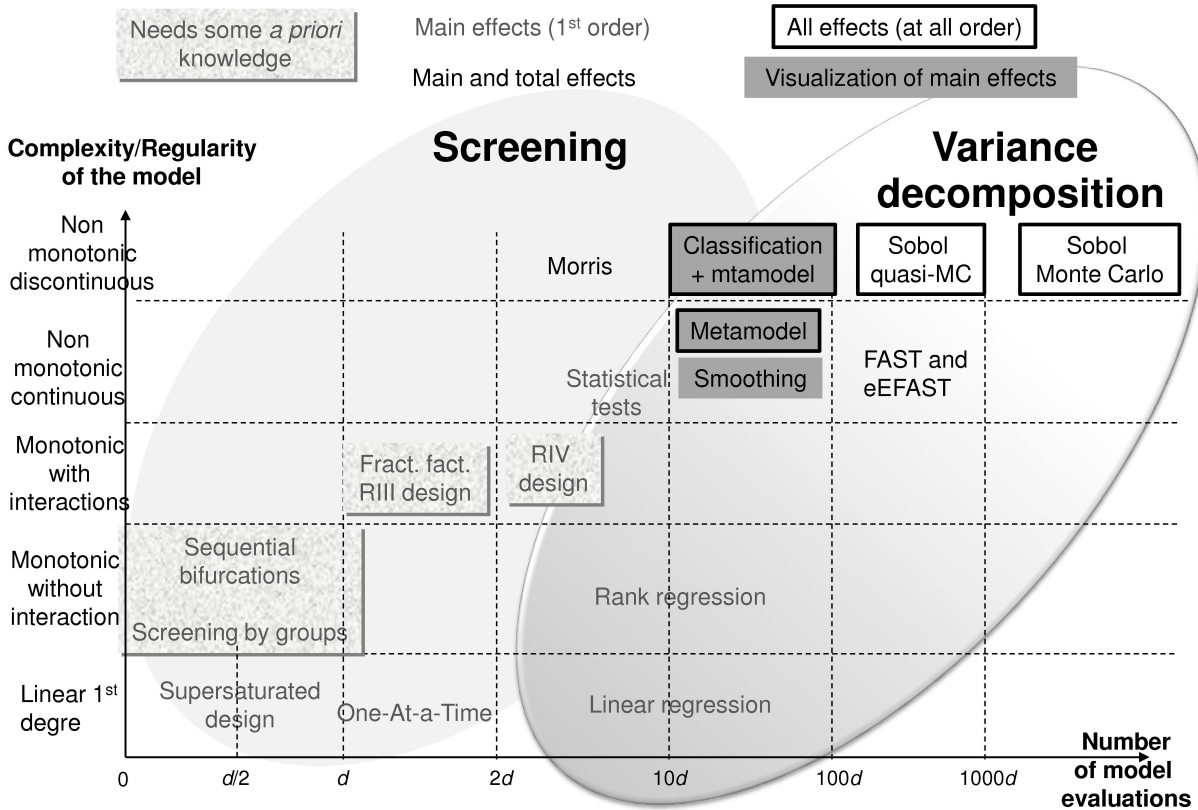
Figure 3.1: Overview of Sensitivity Methods [87]. d denotes the number of input parameters

surrogates only FAST [56], eFAST [57] and Sobol-MC [8] are suitable but with higher computational costs. However, if the models are well designed for fast computing, the Sobol quasi-MC algorithms' direct usage is realizable. The difference between Sobol quasi-MC and the Sobol-MC method is the type of sampling strategy. Sobol quasi-MC uses low discrepancy sequences for improving the convergence of the estimators, whereas Sobol-MC methods use pseudorandom numbers.

To conclude the above depicted summary, it can be outlined that the used sensitivity methods should be Sobol quasi-MC for the quantitative analysis and the Morris screening for the qualitative analysis. The choice has the following reasons:

- Model independence

- Capacity to capture the full range of influence of each input factor

- Appreciation of interaction effects among input factors

- Suitable computational effort in combination with a screening method and a properly designed system model

In addition to the classical variance-based sensitivity analysis, the functional or temporal dependency of technical processes needs to be considered when analyzing physical systems. Thus, the Generalized Sobol indices [69], as an extension to the work of [8], are used throughout this thesis. Furthermore, the sensitivity indices are computed using conditional expectation values and the integrals for calculating them need to be estimated in a MC simulation. Also, the convergence of the estimators needs to be ensured.

3.1 Morris Screening

Morris screening [7] offers an efficient method for qualitatively estimating the influences of parameters on a model output. The main idea is based on the elementary effect

$$EE_i = \frac{f(x_1, x_2, \ldots, x_{i-1}, x_i + \Delta, x_{i+1}, \ldots, x_k) - f(\mathbf{x})}{\Delta} \tag{3.1}$$

for a given model $y = f(\mathbf{x})$ with y as the model output and $\mathbf{x} = [x_1, x_2, \ldots, x_k]$ as the parameter input vector, where $\mathbf{x}$ denotes a randomly drawn sample out of the random variable vector $\mathbf{X}$ in the k-dimensional unit hypercube

$$\mathbf{\Omega}^k = \{\mathbf{x} \mid 0 \le x_i \le 1; i = 1, \ldots, k\}. \tag{3.2}$$

This is no loss of generality as the transformation from the unit hypercube to another probability distribution and input space can be easily achieved using the corresponding inverse Cumulative Distribution Function (CDF). Due to the addition of the variation Δ to the i-th parameter in the numerator and the use in the denominator, the elementary effect can be understood as a partial difference quotient. Δ is defined as the step size over a p-level grid in the input parameter space $\mathbf{\Omega}$. The step size $\Delta \in \{\frac{1}{p-1}, \frac{2}{p-1}, \ldots, 1 - \frac{1}{p-1}\}$ needs to be specified for the analysis. It has been shown that if p is even, a good choice is $\Delta = \frac{p}{2(p-1)}$ [7, 94] as it guarantees an equal-probability sampling.

In [7] also a novel scheme for defining the trajectory through the input parameter space is proposed while reducing the effort of model runs. For a given randomly sampled starting vector $\mathbf{x}^*$ from the vector $\mathbf{X}$ in the p-level grid, the first trajectory point $\mathbf{x}^{(1)}$ is obtained by increasing one or more components by Δ. The second trajectory point is generated by only increasing or decreasing the i-th component of $\mathbf{x}^{(1)}$, resulting in $\mathbf{x}^{(2)} = \mathbf{x}^{(1)} + e_i\Delta$ or $\mathbf{x}^{(2)} = \mathbf{x}^{(1)} - e_i\Delta$ where i is randomly chosen from the set $\{1, 2, \ldots, k\}$ and e_i denotes the unit vector. The next trajectory point is then calculated with $\mathbf{x}^{(3)} = \mathbf{x}^{(2)} + e_j\Delta$ or $\mathbf{x}^{(3)} = \mathbf{x}^{(2)} - e_j\Delta$ and the constraint $i \ne j$. This ensures that each new trajectory point will point in another direction in the input parameter space. This scheme will be continued up to $\mathbf{x}^{(k+1)}$. The proposed trajectory produces one elementary effect for each parameter. But, using only one elementary effect for each parameter does not provide a satisfactory covering of the input parameter space. Thus, the calculation of elementary effects is done for r different input trajectories with varying starting points $\mathbf{x}^*$ resulting in $N_m = r(k+1)$ needed simulation runs. In practice, it has been shown that $p = 4$ and $r = 10$ are typical values for producing valuable results [95–97]. A typical sampling scheme of this OAT-design for $p = 4$ and $r = 2$ in the two-dimensional input parameter space is outlined in Figure 3.2. It can be seen that $r = 1$ will not sufficiently cover the input parameter space, but with an increasing number of r, a better state-space exploration is achieved. Furthermore, the expansion to r trajectories will qualitatively determine nonlinear model dependencies.

As sensitivity measures the mean μ_i, the mean of the absolute values μ_i^* and the standard deviation σ_i of the elementary effects are considered. The measures

$$\mu_i = \frac{1}{r} \sum_{j=1}^{r} EE_i^j \tag{3.3}$$

and

$$\sigma_i = \sqrt{\frac{1}{r-1} \sum_{j=1}^{r} (EE_i^j - \mu_i)^2} \tag{3.4}$$

were first presented in [7]. μ_i assesses the overall influence of the i-th parameter on the output, whereas σ_i is an effective measure to estimate nonlinear or interaction effects in the model. However, using the proposed measure μ_i has the disadvantage that type II errors can occur, which can result in failing to
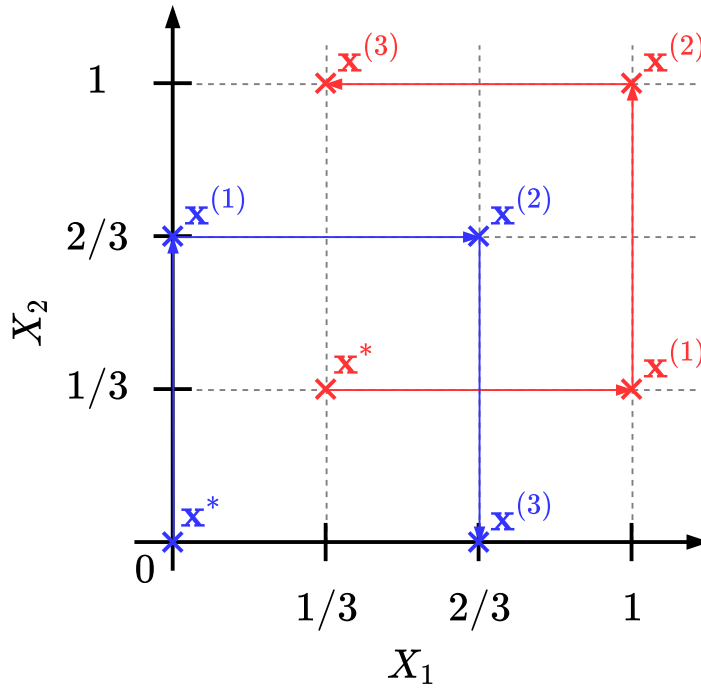
Figure 3.2: Example trajectories for a Morris screening for $k = 2$, $p = 4$, $\Delta = \frac{2}{3}$ and $r = 2$. The blue points outlining the trajectory for $r = 1$ and the red points for $r = 2$.

identify factors with considerable influence on the output. The measure

$$\mu_i^* = \frac{1}{r} \sum_{j=1}^{r} |EE_i^j|, \tag{3.5}$$

first introduced by [98], avoids type II errors by using the absolute values of the elementary effects.

The measures presented above are used to rank the importance of the parameters. Small values of μ_i^* in relation to other parameters indicate a minor influence on the output and the related parameters can be neglected in the quantitative sensitivity setup. In contrast, large values, in comparison to the other parameters, express a significant influence and the related parameters need to be considered in the quantitative setup. Furthermore, σ_i outlines the presence of nonlinearities in the model and thus provides a qualitative insight into the model structure.

3.2 Variance-Based Sensitivity Analysis

In a variance-based sensitivity analysis the variance of one or more model outputs is considered as a measurement for the analysis. The basis for this kind of analysis is a classical uncertainty analysis. The uncertainties of model inputs or parameters are treated as random variables and represented with their corresponding Probability Density Function (PDF). The variance and the distribution of the model output is then computed using a MC-simulation considering the uncertainties of the input parameters as outlined in Figure 3.3. However, a classical uncertainty analysis only outlines the variance of the outputs but no conclusion of the cause of this uncertainty can be drawn. This gap is closed by the variance-based sensitivity analysis. It allows the quantification of the influences of each parameter uncertainty on the output variance. In addition, it enables the detection of interactions between input parameters
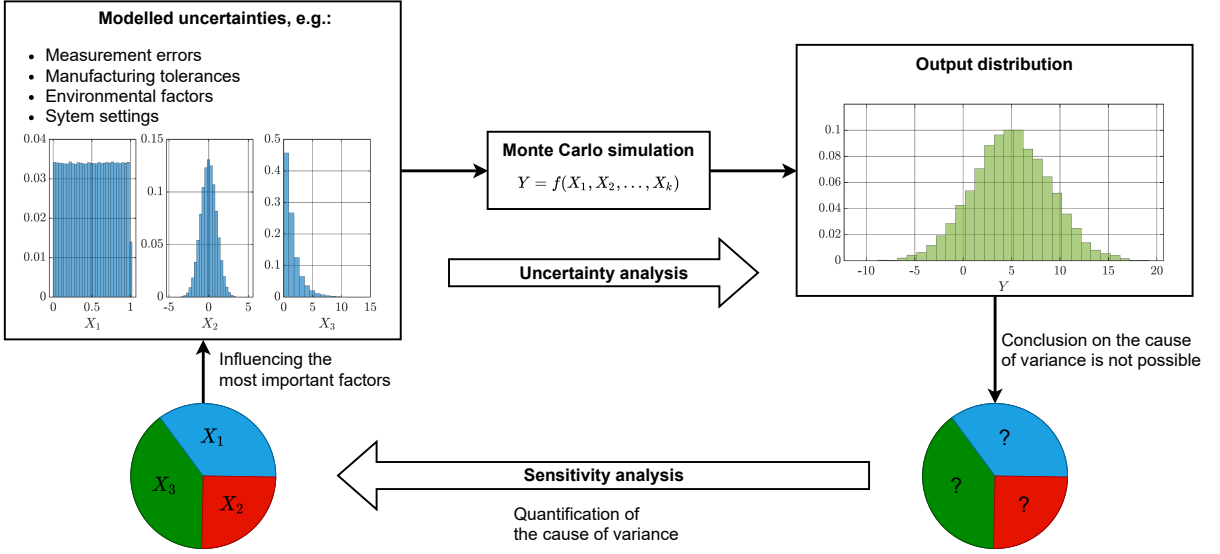
Figure 3.3: Variance-based sensitivity analysis overview

and outlines possible nonlinearities in the model. These quantitative model insights could then be used to focus on the most important parameters in the research or development process to influence the uncertainty of the investigated model outputs at most. The theoretical background of this methodology is explained in the next sections.

3.2.1 Sobol Indices

The generalized description and proof of the model-independent variance-based global sensitivity measures was first published by Sobol in [8].For a better understanding of variance-based sensitivity measures, it is described in summary below.

Considering a square-integrable model $y = f(\mathbf{x})$ in the unit hypercube $\mathbf{\Omega}^k$ where y denotes the system variable to be analyzed with $\mathbf{x} = [x_1, x_2, \ldots, x_k]$ as the input vector with x_i describing the realization of the i-th input parameter. The random variable vector $\mathbf{X}$ contains the independent input parameters, which are uniformly distributed with $X_i \sim \mathcal{U}(0, 1)$. This is not a loss of generality, but it simplifies the calculations since the PDFs in the integrands can be neglected when calculating the expectation values. The unit hypercube Ω^k can be transformed to each desired PDF using the corresponding Inverse Cumulative Distribution Function (ICDF) so that these calculations are identical to the results in the transformed space.

The basic idea behind a variance-based sensitivity analysis is to decompose a function $f(\mathbf{x})$ into a sum of 2^k terms using a High-Dimensional Model Representation (HDMR) to

$$y = f(\mathbf{x}) \quad = f_0 + \sum_{i=1}^{k} f_i(x_i) + \sum_{i=1}^{k} \sum_{i<j}^{k} f_{ij}(x_i, x_j) + \ldots + f_{12\ldots k}(x_1, x_2, \ldots, x_k). \tag{3.6}$$

Here, f_0 describes a constant term without any dependencies on the input vector. Furthermore, the k terms $f_i(x_i)$ express first-order functions with dependencies on only one input parameter x_i. This scheme can be continued up to $\binom{n}{k} = \frac{n!}{k!(n-k)!}$ terms representing n-th order functions with dependencies on n input parameters. In general, the decomposition in (3.6) is not unique, but in [8], it is shown that if the

integrals of each term

$$\int\limits_0^1 f_{i_1,i_2,\ldots,i_s}(x_{i_1}, x_{i_2}, \ldots, x_{i_s})\mathrm{d}x_{i_w} = 0 \quad \text{with} \quad 1 \le i_1 < i_2 < \cdots < i_s \le k, i_w \in \{i_1, i_2, \ldots, i_s\} \quad (3.7)$$

with respect to any of their depending variables are zero, then all terms of the decomposition are orthogonal in pairs, i.e.,

$$\int\limits_0^1 f_i(x_i)f_j(x_j)\mathrm{d}x_i\mathrm{d}x_j = 0 \quad \forall i \ne j. \tag{3.8}$$

As a consequence, the functional decomposition scheme (3.6) is unique.

The remaining question of how to calculate the functions $f_{i_1,i_2,\ldots,i_s}$ can be answered by using the calculation of conditional expectation values. Given the definition of the conditional expectation value

$$E(Y \mid X_i) = \int \cdots \int\limits_{\boldsymbol{\Omega}^k} f(\mathbf{x})\mathrm{d}\{\mathbf{x}\backslash x_i\} = f_0 + f_i(x_i) \tag{3.9}$$

for Y with X_i fixed to some known value leads to

$$f_i(x_i) = E(Y \mid X_i) - f_0 = E(Y \mid X_i) - E(Y) \tag{3.10}$$

for the first-order function terms. Using the conditional expectation values for Y with X_i and X_j fixed defined by

$$E(Y \mid X_i, X_j) = \int \cdots \int\limits_{\boldsymbol{\Omega}^k} f(\mathbf{x})\mathrm{d}\{\mathbf{x}\backslash x_i, x_j\} = f_0 + f_i(x_i) + f_j(x_j) + f_{ij}(x_i, x_j), \tag{3.11}$$

the second-order function terms

$$\begin{aligned} f_{ij}(x_i, x_j) &= E(Y \mid X_i, X_j) - f_i(x_i) - f_j(x_j) - f_0 \\ &= E(Y \mid X_i, X_j) - E(Y \mid X_i) - E(Y \mid X_j) - E(Y) \end{aligned} \tag{3.12}$$

can be obtained similarly. Assuming independence of the input parameters, the calculation of the conditional expectation values can be generalized to the Euclidean space

$$\mathbb{R}^k = \{\mathbf{x} \mid -\infty \le x_i \le \infty; i = 1, \ldots, k\} \tag{3.13}$$

with

$$E(Y \mid X_i) = \int \cdots \int\limits_{\mathbb{R}^k} f(\mathbf{x}) \prod_{\substack{m=1 \\ m\ne i}}^k p_m(X_m)\mathrm{d}\{\mathbf{x}\backslash x_i\} \tag{3.14}$$

$$E(Y \mid X_i, X_j) = \int \cdots \int\limits_{\mathbb{R}^k} f(\mathbf{x}) \prod_{\substack{m=1 \\ m\ne i, m\ne j}}^k p_m(X_m)\mathrm{d}\{\mathbf{x}\backslash x_i, x_j\}, \tag{3.15}$$

where $p_m(X_m)$ denotes the PDF of the m-th parameter. Likewise, this scheme can be continued up to the k-th order term $f_{12\ldots k}(x_1, x_2, \ldots, x_k)$. With the proposed uniqueness and independence of each

functional term in (3.6), the variance of the model output is calculated by

$$V(Y) = \int \cdots \int_{\mathbb{R}^k} (f(\mathbf{x}) - f_0)^2 \prod_{m=1}^{k} p_m(X_m) \mathrm{d}\mathbf{x}$$

$$= \sum_{i=1}^{k} V_i + \sum_{i=1}^{k} \sum_{i<j}^{k} V_{ij} + \ldots + V_{12\ldots k}, \tag{3.16}$$

where the variances are defined by

$$V_i = V(f_i(x_i)) = \int_{-\infty}^{\infty} f_i^2(x_i) p_i(X_i) \mathrm{d}x_i \tag{3.17}$$

$$V_{ij} = V(f_{ij}(x_i, x_j)) = \int_{-\infty}^{\infty} \int_{-\infty}^{\infty} f_{ij}^2(x_i, x_j) p_i(X_i) p_j(X_j) \mathrm{d}x_i \mathrm{d}x_j \tag{3.18}$$

$$\vdots$$

$$V_{12\ldots k} = V(f_{12\ldots k}(x_1, x_2, \ldots, x_k)) = \int \cdots \int_{\mathbb{R}^k} f_{12\ldots k}^2(x_1, x_2, \ldots, x_k) \prod_{m=1}^{k} p_m(X_m) \mathrm{d}\mathbf{x}. \tag{3.19}$$

Normalizing (3.16) by $V(Y)$ leads to

$$1 = \sum_{i=1}^{k} \frac{V_i}{V} + \sum_{i=1}^{k} \sum_{i<j}^{k} \frac{V_{ij}}{V} + \ldots + \frac{S_{12\ldots k}}{V} = \sum_{i=1}^{k} S_i + \sum_{i=1}^{k} \sum_{i<j}^{k} S_{ij} + \ldots + S_{12\ldots k}, \tag{3.20}$$

which represents a normalized decomposition of the sources of variance. S_i denotes the first-order Sobol indices and quantifies the influence of a single parameter X_i on the output of interest. S_{ij} are called second-order effects and indicate the interaction between two parameters X_i and X_j. This scheme can be continued up to the effects of k-th order.

To describe the overall effect of one parameter X_i on the output, including all interactions and non-linear effects, another useful measure exists. The total effect

$$S_{T_i} = S_i + \sum_{\substack{j=1 \\ j \neq i}}^{k} S_{ij} + \ldots + S_{12\ldots k} \tag{3.21}$$

sums up all sensitivity measures of one parameter X_i, including all high order interactions on the output of interest and thus serves as a comprehensive measure for the overall influence of this parameter.

Using the variance decomposition presented in (3.16) and the relations in (3.10), (3.17), (3.12) and (3.18), V_i and V_{ij} can be calculated with

$$V_i = V(E(Y \mid X_i)) - \underbrace{V(E(Y))}_{=0} \tag{3.22}$$

$$V_{ij} = V(E(Y \mid X_i)) - V(E(Y \mid X_i)) - V(E(Y \mid X_J)) - \underbrace{V(E(Y))}_{=0}, \tag{3.23}$$

where the higher-order terms of the HDMR can be determined similarly. However, as shown in Section 3.2.3, the integrals for calculating the statistical moments need to be estimated. Due to the computationally expensive task of this estimation, it is only suitable to consider the first order and total order

effects. Therefore, only the first-order and total effects are further discussed in the following.

As derived above and shown in [8, 60], the first-order indices can be calculated by the relation of the conditional expectation value $V_{X_i}(E_{\mathbf{X}_{\sim i}}(Y \mid X_i))$ and the overall variance $V(Y)$ described by

$$S_i = \frac{V_{X_i}(E_{\mathbf{X}_{\sim i}}(Y \mid X_i))}{V(Y)}. \tag{3.24}$$

For better readability and emphasis of the calculation scheme of the conditional expectation values, an extended syntax is used furthermore. $\mathbf{X}_{\sim i}$ denotes the vector of all parameters except X_i. The inner expectation operator outlines the averaging over all possible values of $\mathbf{X}_{\sim i}$ while keeping X_i fixed and the outer variance is taken over all X_i. As (3.24) outlines, S_i is a normalized index as $V_{X_i}(E_{\mathbf{X}_{\sim i}}(Y \mid X_i))$ varies between zero and $V(Y)$.

The total effect is calculated using [60, 99]

$$S_{Ti} = \frac{E_{\mathbf{X}_{\sim i}}(V_{X_i}(Y \mid \mathbf{X}_{\sim i}))}{V(Y)} = 1 - \frac{V_{\mathbf{X}_{\sim i}}(E_{X_i}(Y \mid \mathbf{X}_{\sim i}))}{V(Y)}. \tag{3.25}$$

An obvious explanation is to consider that $V_{\mathbf{X}_{\sim i}}(E_{X_i}(Y \mid \mathbf{X}_{\sim i}))$ is the first-order effect of $\mathbf{X}_{\sim i}$. Consequently, $V(Y) - V_{\mathbf{X}_{\sim i}}(E_{X_i}(Y \mid \mathbf{X}_{\sim i}))$ must contain all terms in the variance decomposition of (3.16), which include X_i.

The indices can be interpreted as the expected reduction of variance. The numerator of the first-order effects $V_{X_i}(E_{\mathbf{X}_{\sim i}}(Y \mid X_i))$ describes the partial reduction of variance in the output Y if X_i would be fixed to some defined value. Furthermore, the numerator of the total effect $E_{\mathbf{X}_{\sim i}}(V_{X_i}(Y \mid \mathbf{X}_{\sim i}))$ is the amount of variance that would be left if all factors but X_i are fixed. The ordering of the sensitivity measures quantifies their contribution to the overall variance. In other words, small sensitivity measures have only a small influence on the variance of the output, whereas big measures have a significant influence on the output. Moreover, the sensitivity measures have some general properties which are useful for analyzing the structure of the model:

- Due to (3.20) the condition $\sum_{i=1}^{k} S_i \leq 1$ holds.

- Due to (3.21) the condition $\sum_{i=1}^{k} S_{T_i} \geq 1$ holds.

- If $\sum_{i=1}^{k} S_i = 1$ the model is additive.

- If $1 - \sum_{i=1}^{k} S_i \gg 0$ the model has nonlinear behavior or interacting parameters.

- If $S_{T_i} \approx S_i$ no interactions exists. This implies also additivity of the model.

- If $S_{T_i} \approx 0$ the parameter has no influence on the output.

3.2.2 Generalized Sobol Indices

The major drawback of the HDMR described in (3.6) is the neglection of state and time dependencies regarding physical systems. These dependencies will expand the underlying model to

$$y(t) = f(\mathbf{x}, \mathbf{x}_0, t, \mathbf{u}(t)), \tag{3.26}$$

where $\mathbf{x}_0$ denotes the initial system state. Furthermore, the system consists of a control vector $\mathbf{u} = [u_1, u_2, \ldots, u_c]$ with c as the number of control inputs. The proposed extension by $\mathbf{x}_0, t$ and $\mathbf{u}(t)$ leads to state and time-dependent sensitivity indices. As already outlined in [13], the dependency of $\mathbf{x}_0$ and $\mathbf{u}(t)$ can be ensured by covering all of the relevant operating points of the physical system. In this thesis,

this is ensured by defining representative drive cycles concerning the use case of the vehicle as outlined in Section 5.2. Thus, (3.26) simplifies to

$$y(t) = f(\mathbf{x}, t). \tag{3.27}$$

and can also be written as a second-order ANOVA-like decomposition

$$f(\mathbf{x}, t) = f_{\mathcal{U}}(\mathbf{x}_{\mathcal{U}}, t) + f_{\mathcal{U}_\sim}(\mathbf{x}_{\mathcal{U}_\sim}, t) + f_{\mathcal{U},\mathcal{U}_\sim}(\mathbf{x}, t) \tag{3.28}$$

with the complete index set $\mathcal{X} = \{1, \ldots, k\}$, the subset $\mathcal{U} = \{i_1, i_2, \ldots, i_s\} \subset \mathcal{X}$ and the complementary subset $\mathcal{U}_\sim = \{j_1, j_2, \ldots, j_s\} = \mathcal{X} \backslash \mathcal{U}$. The corresponding parameter vectors are $\mathbf{x}_{\mathcal{U}} = [x_{i_1}, x_{i_2}, \ldots, x_{i_s}]$ and $\mathbf{x}_{\mathcal{U}_\sim} = [x_{j_1}, x_{j_2}, \ldots, x_{j_s}]$. The variance of this decomposition is defined by

$$V(f, t) = V_{\mathcal{U}}(f, t) + V_{\mathcal{U}_\sim}(f, t) + V_{\mathcal{U},\mathcal{U}_\sim}(f, t), \tag{3.29}$$

where $V_{\mathcal{U}} = V_i$ holds if the subset $\mathcal{U}$ contains only one element. In this case, (3.29) is equal to (3.16). The subset containing only the i-th parameter will be denoted as $\mathcal{U}_i$.

As outlined in (3.24) and (3.25), the Sobol indices are usually calculated as point-in-time indices. For the scalar case with $V_{\mathcal{U}_i} = V_i$, the sensitivity indices can be expressed with

$$S_i(f, t) = \frac{V_{\mathcal{U}_i}(f, t)}{V(f, t)} \tag{3.30}$$

$$S_{T_i}(f, t) = \frac{V_{\mathcal{U}_i}(f, t) + V_{\mathcal{U}_i,\mathcal{U}_\sim}(f, t)}{V(f, t)} \tag{3.31}$$

for each $t \in [0, T]$. There are several problems using only these point-in-time estimations [69]:

- Pointwise in time indices ignore all time correlations of the process.

- The variance of the process varies in time which skews the relative importance across time.

The first results of sensitivity analyses on functional or vector outputs have been produced in [66–68]. However, a general framework for solving the above-mentioned issues for processes with temporal dependencies was first introduced by [69]. The proposed generalized Sobol indices use covariance operators to take the process evolution over time into account. Also, the second issue regarding the skewing is solved by this approach. The generalized indices are defined by

$$S_i^G(f, T) = \frac{\int_0^T V_{\mathcal{U}_i}(f, t)\mathrm{d}t}{\int_0^T V(f, t)\mathrm{d}t} \tag{3.32}$$

$$S_{T_i}^G(f, T) = \frac{\int_0^T (V_{\mathcal{U}_i}(f, t) + V_{\mathcal{U}_i,\mathcal{U}_\sim}(f, t))\mathrm{d}t}{\int_0^T V(f, t)\mathrm{d}t}, \tag{3.33}$$

which can be simply computed with the approximation

$$S_i^G(f, T) \approx \frac{\sum_{m=1}^N w_m V_{\mathcal{U}_i}(f, t_m)}{\sum_{m=1}^N w_m V(f, t_m)} \tag{3.34}$$

$$S_{T_i}^G(f, T) \approx \frac{\sum_{m=1}^N w_m (V_{\mathcal{U}_i}(f, t_m) + V_{\mathcal{U}_i,\mathcal{U}_\sim}(f, t_m))}{\sum_{m=1}^N w_m V(f, t_m)} \tag{3.35}$$

in a numerical setup with weights $\{w_m\}_{m=1}^N$ for each node $\{t_m\}_{m=1}^N$. The special case of equal weights and uniform time steps is suggested in [100] for time-dependent processes and is used throughout this thesis. It is worth mentioning that $V_{\mathcal{U}_i}(f, t)$ is equal to $V_{X_i}(E_{\mathbf{X}_{\sim i}}(Y \mid X_i))$ for a specific time step t in the process. Similarly, $V_{\mathcal{U}_i}(f, t) + V_{\mathcal{U}_i,\mathcal{U}_\sim}(f, t)$ is equal to $E_{\mathbf{X}_{\sim i}}(V_{X_i}(Y \mid \mathbf{X}_{\sim i}))$ for a specific time step. Thus, the integrals of (3.32) and (3.33) can be easily solved by using the results of the numerators of the

first order (3.24) and the total order (3.25) effect for each discrete time step t_m. The same applies for the denominator using the overall variance $V(Y)$ for a specific time step.

3.2.3 Estimation of the Sensitivity Indices

As the conditional expectation values in (3.24) and (3.25) cannot be directly calculated in an MC simulation, they must be numerically estimated. It was already outlined in Section 3.2.1 that estimating the integrals is a computationally expensive task. However, especially for the first-order and the total-order effects, there exist several estimation strategies that are capable of estimating both effects in one simulation setup [60]. As a consequence, only the first-order and total-order effects are considered in the estimation to keep the computation time within acceptable limits.

In the following an overview is given how the sample data for the MC is generated and how the samples are used to calculate the estimates of the conditional expectation values $\hat{V}_{X_i}(E_{\mathbf{X}_{\sim i}}(Y \mid X_i))$ for the first order and $\hat{E}_{\mathbf{X}_{\sim i}}(V_{X_i}(Y \mid \mathbf{X}_{\sim i}))$ for the total order effects.

The starting points are two independent and uniform sampling matrices in the unit hypercube

$$\mathbf{A} = \begin{bmatrix} a_{11} & a_{12} & \cdots & a_{1k} \\ a_{21} & \ddots & & \vdots \\ \vdots & & \ddots & \vdots \\ a_{N1} & \cdots & \cdots & a_{Nk} \end{bmatrix} \quad \text{with} \quad a_{jg} \in \mathbb{R}^{N \times k} \tag{3.36}$$

$$\mathbf{B} = \begin{bmatrix} b_{11} & b_{12} & \cdots & b_{1k} \\ b_{21} & \ddots & & \vdots \\ \vdots & & \ddots & \vdots \\ b_{N1} & \cdots & \cdots & b_{Nk} \end{bmatrix} \quad \text{with} \quad b_{jg} \in \mathbb{R}^{N \times k} \tag{3.37}$$

as proposed in [60], where the index $g \in \{1, 2, ..., k\}$ denotes the parameter of interest and the index $j \in \{1, 2, ..., N\}$ denotes the number of simulations. The distribution of each parameter can be transformed from the uniform distribution in the unit hypercube to any other probability distribution using its ICDF.

Furthermore, a third dataset

$$\mathbf{A}_{\mathbf{B}}^{(i)} = \begin{bmatrix} a_{11} & \cdots & b_{1i} & \cdots & a_{1k} \\ a_{21} & & b_{2i} & & \vdots \\ \vdots & & \vdots & & \vdots \\ a_{N1} & \cdots & b_{Ni} & \cdots & a_{Nk} \end{bmatrix} \tag{3.38}$$

is obtained from matrix $\mathbf{A}$ where the i-th column is replaced by the i-th column from matrix $\mathbf{B}$. Also, the possibility exists to build the third dataset with

$$\mathbf{B}_{\mathbf{A}}^{(i)} = \begin{bmatrix} b_{11} & \cdots & a_{1i} & \cdots & b_{1k} \\ b_{21} & & a_{2i} & & \vdots \\ \vdots & & \vdots & & \vdots \\ b_{N1} & \cdots & a_{Ni} & \cdots & b_{Nk} \end{bmatrix} \tag{3.39}$$

by replacing the i-th column of matrix $\mathbf{B}$ with the i-th column of matrix $\mathbf{A}$. However, [60] has shown that the points of $\mathbf{A}$ and hence of $\mathbf{A}_{\mathbf{B}}^{(i)}$ are better distributed than the points of $\mathbf{B}$ and $\mathbf{B}_{\mathbf{A}}^{(i)}$ when using quasi-random sequences. Thus, only the matrix triplets $\mathbf{A}$, $\mathbf{B}$ and $\mathbf{A}_{\mathbf{B}}^{(i)}$ are considered throughout the thesis. Since the matrices $\mathbf{A}$ and $\mathbf{A}_{\mathbf{B}}^{(i)}$ have the coordinates $\mathbf{X}_{\sim i}$ in common, the change from $\mathbf{A}$ to $\mathbf{A}_{\mathbf{B}}^{(i)}$ can be seen as a step in the X_i direction. The same explanation can be given by moving from $\mathbf{B}$ to $\mathbf{A}_{\mathbf{B}}^{(i)}$ as a step along the $\mathbf{X}_{\sim i}$ direction. Thus, the information provided by these data triplets consist of all the needed information to estimate the first order and total order sensitivity indices.

The estimation itself, especially for computational improvements, is still a current research subject and multiple estimators for the first-order and total-order sensitivity indices exist. As the estimators mainly differ in their convergence behavior based on the used MC sample size and thus in the needed computation time, a set of different estimators is used and compared throughout the thesis. They are outlined in Table 3.1 for the estimates of the conditional expectation values $\hat{V}_{X_i}(E_{\mathbf{X}_{\sim i}}(Y \mid X_i))$ and $\hat{E}_{\mathbf{X}_{\sim i}}(V_{X_i}(Y \mid \mathbf{X}_{\sim i}))$. The denominators of (3.24) and (3.25) are estimated using the sample vari-

Table 3.1: First order and total order estimators

$\hat{V}_{X_i}(E_{\mathbf{X}_{\sim i}}(Y \mid X_i))$	Author
$\frac{1}{N}\sum_{j=1}^{N} f(\mathbf{A})_j f(\mathbf{B}_{\mathbf{A}}^{(i)})_j - f_0^2$	Sobol [8]
$V(Y) - \frac{1}{2N}\sum_{j=1}^{N}\left(f(\mathbf{B})_j - f(\mathbf{A}_{\mathbf{B}}^{(i)})_j\right)^2$	Jansen [101]
$\frac{1}{N}\sum_{j=1}^{N} f(\mathbf{B})_j\left(f(\mathbf{A}_{\mathbf{B}}^{(i)})_j - f(\mathbf{A})_j\right)$	Saltelli et. al. [60]
$\hat{E}_{\mathbf{X}_{\sim i}}(V_{X_i}(Y \mid \mathbf{X}_{\sim i}))$	
$\frac{1}{2N}\sum_{j=1}^{N}\left(f(\mathbf{A})_j - f(\mathbf{A}_{\mathbf{B}}^{(i)})_j\right)^2$	Jansen [101]
$\frac{1}{N}\sum_{j=1}^{N} f(\mathbf{A})_j\left(f(\mathbf{A})_j - f(\mathbf{A}_{\mathbf{B}}^{(i)})_j\right)$	Sobol [102]

ance [94]

$$\hat{V}(Y) = \frac{1}{N-1}\sum_{i=1}^{N}(Y - \overline{Y})^2. \tag{3.40}$$

Since the estimators outlined in Table 3.1 use the matrices $\mathbf{A}, \mathbf{B}$ and $\mathbf{A}_{\mathbf{B}}^{(i)}$ as inputs, it can be seen from (3.36), (3.37) and (3.38) that the needed simulation runs for the proposed MC setup are $N_s = N(k+2)$.

Using the above outlined estimators, the Sobol indices can be calculated by

$$\hat{S}_i(t) = \frac{\hat{V}_{X_i}(E_{\mathbf{X}_{\sim i}}(Y(t) \mid X_i))}{\hat{V}(Y(t))} \tag{3.41}$$

$$\hat{S}_{T_i}(t) = \frac{\hat{E}_{\mathbf{X}_{\sim i}}(V_{X_i}(Y(t) \mid \mathbf{X}_{\sim i}))}{\hat{V}(Y(t))} \tag{3.42}$$

for a specific point in time t. Similarly, the estimates of the generalized Sobol indices are defined by

$$\hat{S}_i^G(T) = \frac{\int_0^T \hat{V}_{X_i}(E_{\mathbf{X}_{\sim i}}(Y(t) \mid X_i))\mathrm{d}t}{\int_0^T \hat{V}(t)\mathrm{d}t} \tag{3.43}$$

$$\hat{S}_{T_i}^G(T) = \frac{\int_0^T \hat{E}_{\mathbf{X}_{\sim i}}(V_{X_i}(Y(t) \mid \mathbf{X}_{\sim i}))\mathrm{d}t}{\int_0^T \hat{V}(t)\mathrm{d}t}. \tag{3.44}$$

The sampling strategy of the matrices $\mathbf{A}$, $\mathbf{B}$ and $\mathbf{A}_{\mathbf{B}}^{(i)}$ highly affects the convergence behavior of the proposed and used estimators. Furthermore, it is essential to ensure the convergence and the confidence of the proposed estimators. Thus, the sampling strategy and how to ensure convergence will be discussed in the following sections.

3.2.4 Sampling Strategies

In general, the problem in an MC simulation is the approximation of the integral of a function with

$$\int_{\mathbf{\Omega}^k} f(\mathbf{x})\mathrm{d}\mathbf{x} \approx \frac{1}{N}\sum_{i=1}^{N} f(\mathbf{x}_i) \tag{3.45}$$

as the average of the function evaluated at a set of points $\mathbf{x}_i$. The choice of these randomly selected points has a significant impact on the convergence of (3.45). Thus, the question needs to be answered how the sampling matrices $\mathbf{A}$ and $\mathbf{B}$ need to be drawn to provide a fast convergence of the corresponding estimators. The process of generating input sequences for MC simulations has been intensively studied. Since samples cannot be generated randomly in computer experiments several methods exist that approximate the statistical randomness using deterministic and repeatable processes. This class of random number generators is called pseudorandom generators. Popular pseudorandom number generators are the Mersenne-Twister [103], the Advanced Randomization System [104] and the SplitMix [105] generator, to mention just a few. However, the distribution of the points in a pseudorandom generator, especially for small N, is not optimal for a good convergence. As it can be seen from Figure 3.4, in a pseudorandom setup exists clusters and gaps in the input parameter space. Thus, the clustered areas are usually overestimated and the gaps are underestimated in the corresponding statistical analysis. Due to these inhomogeneities, the convergence rate of the estimates calculated with pseudorandom sequences is only $\frac{1}{\sqrt{N}}$ [94].

A good measure of the lumpiness of a drawn sequence is the star discrepancy defined for a given set $\mathcal{P} = \{\mathbf{x}_1, \ldots, \mathbf{x}_N\}$ as [106]

$$D_N^*(\mathcal{P}) = \sup_{\mathbf{x} \in \mathbf{\Omega}^k} \left| \frac{A([\mathbf{0}, \mathbf{x}), N, \mathcal{P})}{N} - \lambda_k([\mathbf{0}, \mathbf{x})) \right|. \tag{3.46}$$

Here, $A([\mathbf{0}, \mathbf{x}), N, \mathcal{P})$ denotes the number of sample points covered by a k-dimensional hypervolume ranging from the origin to $\mathbf{x}$ and λ_k outlines the k-dimensional Lebesque measure. Thus, the star discrepancy can be seen as a maximum deviation between the assumed points of an equally distributed set and the drawn samples using a random number generator.

It can be outlined that if the discrepancy could be minimized, the convergence rate of the estimates for a random number sequence tends towards $\frac{1}{N}$ [107]. Thus, several low-discrepancy sequences have been developed and presented in the literature, like the sequences of Faure [61], Niederreiter [62], Halton [63] and Sobol [64, 65]. A good review of low-discrepancy sequences can be found in [108]. They all have in common that, in contrast to the pseudorandom numbers, they are generated deterministically but with respect to the condition of equal distribution across the input parameter space. A comparison
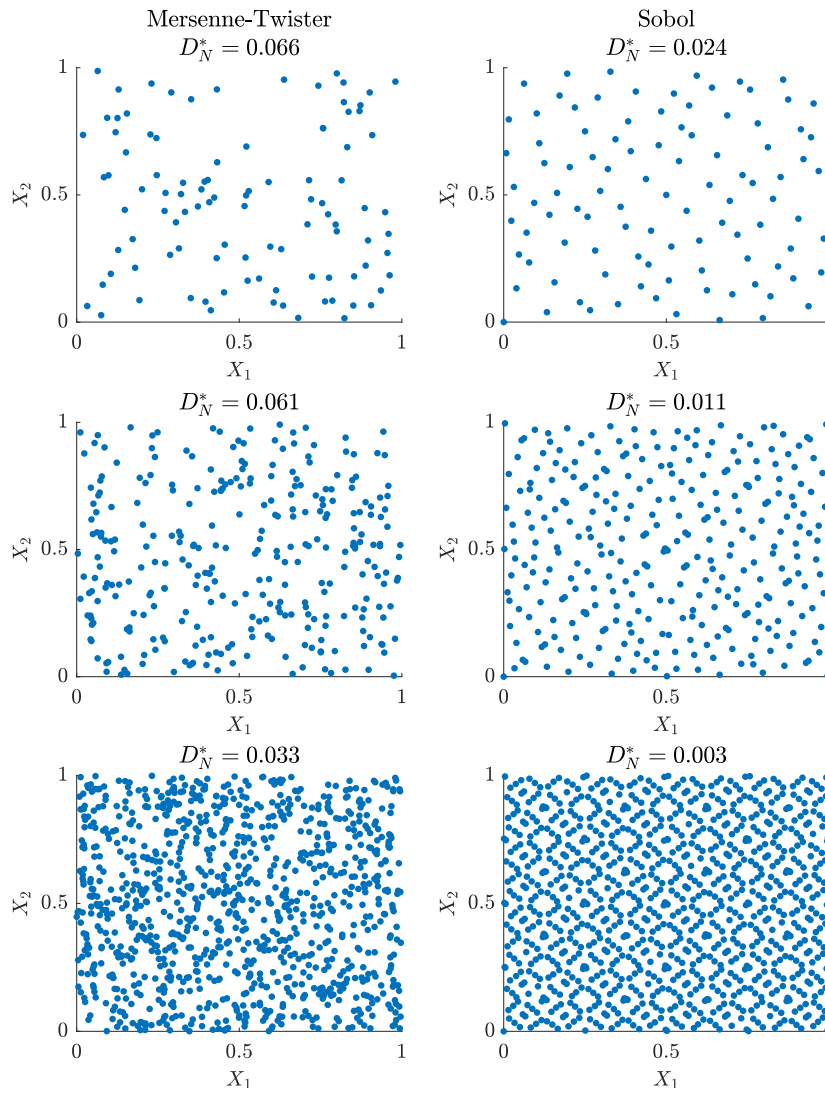
Figure 3.4: Comparison of pseudorandom (Mersenne-Twister) and low-discrepancy (Sobol) sampling of sample size $N = [100, 300, 1000]$ and their corresponding discrepancies D_N^*

of the used Sobol sequences and the Mersenne-Twister-Algorithm, including the corresponding discrepancy values, is outlined in Figure 3.4. It is obvious that the Sobol sequences cover the state space more equal without gaps or clusters than the pseudorandom sequences. Furthermore, it is shown in [109] that Sobol sequences [64, 65] outperform crude MC sampling. Thus, the sample data used throughout this thesis is generated using Sobol sequences. The MC simulations which are performed with low-discrepancy sequences are then called quasi-MC simulations.

3.2.5 Ensuring Convergence of the Estimators

It was already outlined in the previous sections that the sensitivity indices need to be estimated. However, no rule of thumb exists on how big the MC simulation sample size must be to ensure a satisfactory convergence of the proposed estimators. Since the real values of the sensitivity indices are not available during a complex MC simulation, a reliable convergence indicator based on the sampled simulation data

is needed. Otherwise, it could not be proved that the sensitivity analysis results are correct and by which amount the estimation errors compromise the results. Thus, in the following, two independent methods are presented to ensure convergence and to analyze the remaining error of the estimators. Both methods are based on the fact that the estimators, as outlined in Section 3.2.3, are consistent, which means that

$$\lim_{N \to \infty} \hat{S}_i(t) = S_i(t) \tag{3.47}$$

$$\lim_{N \to \infty} \hat{S}_{T_i}(t) = S_{T_i}(t) \tag{3.48}$$

hold for the Sobol indices and

$$\lim_{N \to \infty} \hat{S}_i^G(T) = S_i^G(T) \tag{3.49}$$

$$\lim_{N \to \infty} \hat{S}_{T_i}^G(T) = S_{T_i}^G(T) \tag{3.50}$$

hold for the generalized Sobol indices. The Sobol indices are computed as point in time indices for a specific point t. In contrast, the generalized Sobol indices include all the former points of the time interval $[0, T]$ in one scalar sensitivity measure. Thus, the proposed convergence algorithms need to be considered separately for the Sobol indices and the generalized Sobol indices.

The former method is based on the law of big numbers to calculate a scalar convergence measure, whereas the second method uses bootstrap resampling to calculate the confidence intervals of the sensitivity indices.

Law of Big Numbers

As already outlined in (3.47) to (3.50), the estimated values tend towards their real values for large sample sizes N. However, for the classical Sobol indices, there still exists a time dependency in the measurements. As the proposed convergence measure should provide a scalar indicator, the time dependency of this point in time indices needs to be removed. This is done by computing the mean over the interesting time interval $[t_1, t_n]$ with

$$\overline{\hat{S}_i} = \frac{1}{n} \sum_{m=1}^{n} \hat{S}_i(t_m) \tag{3.51}$$

$$\overline{\hat{S}_{T_i}} = \frac{1}{n} \sum_{m=1}^{n} \hat{S}_{T_i}(t_m). \tag{3.52}$$

Accordingly, (3.51) and (3.52) represent a scalar measure for each computed sensitivity index.

In contrast, the generalized Sobol indices from (3.43) and (3.44) already take the time dependency into account and thus the scalar measures for a specific point in time T are defined by

$$\overline{\hat{S}_i^G} = \hat{S}_i^G(T) \tag{3.53}$$

$$\overline{\hat{S}_{T_i}^G} = \hat{S}_{T_i}^G(T). \tag{3.54}$$

The corresponding convergence errors can now be computed using the consistency property of the estimators. Thus, the proposed measures $\overline{\hat{S}_i}$, $\overline{\hat{S}_{T_i}}$, $\overline{\hat{S}_i^G}$ and $\overline{\hat{S}_{T_i}^G}$ are estimated for different sample sizes $N_1 < N_2 < ... < N_m = N$. The error measures are then obtained from

$$\varepsilon_{\overline{\hat{S}_{i,j}}} = \max_l \left| \overline{\hat{S}_{i,j}} - \overline{\hat{S}_{i,l}} \right| \tag{3.55}$$

$$\varepsilon_{\overline{\hat{S}_{T_{i,j}}}} = \max_l \left| \overline{\hat{S}_{T_{i,j}}} - \overline{\hat{S}_{T_{i,l}}} \right| \tag{3.56}$$

$$\varepsilon_{\overline{\hat{S}_{i,j}^G}} = \max_l \left| \overline{\hat{S}_{i,j}^G} - \overline{\hat{S}_{i,l}^G} \right| \tag{3.57}$$

$$\varepsilon_{\overline{\hat{S}_{T_{i,j}}^G}} = \max_l \left| \overline{\hat{S}_{T_{i,j}}^G} - \overline{\hat{S}_{T_{i,l}}^G} \right| \tag{3.58}$$

with $j \in \{1, 2, ..., m\}$ and $l \in \{j-5, j-4, ..., j, j+1, ..., m\}$. It means that for every sensitivity index $\overline{\hat{S}_{i,j}}$, $\overline{\hat{S}_{T_{i,j}}}$, $\overline{\hat{S}_{i,j}^G}$ and $\overline{\hat{S}_{T_{i,j}}^G}$ with the corresponding sample size N_j, the maximum deviation to the five smaller and all larger sample sizes is calculated. For a better understanding, Figure 3.5 underlines the relations between the sample sizes and the different indices. Finally, to get a single scalar measure for each class
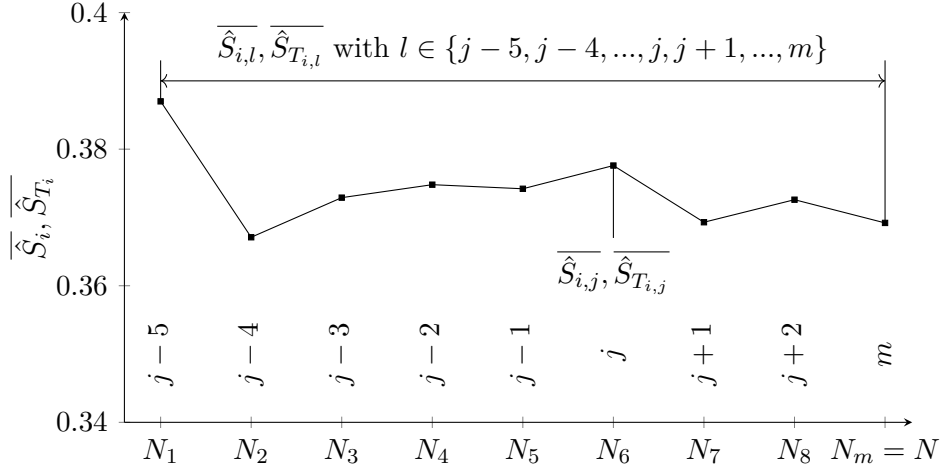
Figure 3.5: Exemplary estimation result for $\overline{\hat{S}_{i,j}}, \overline{\hat{S}_{T_{i,j}}}$ with different sample sizes $[N_1, N_m]$ for parameter i. The process is the same for $\overline{\hat{S}_{i,j}^G}$ and $\overline{\hat{S}_{T_{i,j}}^G}$.

of sensitivity indices, the mean over all parameters

$$\varepsilon_{\hat{S}_j} = \frac{1}{k} \sum_{i=1}^k \varepsilon_{\overline{\hat{S}_{i,j}}} \tag{3.59}$$

$$\varepsilon_{\hat{S}_{T_j}} = \frac{1}{k} \sum_{i=1}^k \varepsilon_{\overline{\hat{S}_{T_{i,j}}}} \tag{3.60}$$

$$\varepsilon_{\hat{S}_j^G} = \frac{1}{k} \sum_{i=1}^k \varepsilon_{\overline{\hat{S}_{i,j}^G}} \tag{3.61}$$

$$\tag{3.62}$$

$$\varepsilon_{\hat{S}_{T_j}^G} = \frac{1}{k} \sum_{i=1}^k \varepsilon_{\overline{\hat{S}_{T_{i,j}}^G}} \tag{3.63}$$

is computed with k as the number of parameters.

Because of (3.47) to (3.50), it is evident that the proposed measures $\overline{\hat{S}_{i,j}}$, $\overline{\hat{S}_{T_{i,j}}}$, $\overline{\hat{S}_{i,j}^G}$ and $\overline{\hat{S}_{T_{i,j}}^G}$ tend to zero for increasing sample sizes. Accordingly, the convergence of the estimators is ensured if

$$\varepsilon_{\hat{S}_j} \leq \varepsilon_{max}, \quad \varepsilon_{\hat{S}_{T_j}} \leq \varepsilon_{max} \tag{3.64}$$

and

$$\varepsilon_{\hat{S}_j^G} \leq \varepsilon_{max}, \quad \varepsilon_{\hat{S}_{T_j}^G} \leq \varepsilon_{max} \tag{3.65}$$

holds, where ε_{max} is a specific error bound. If no sample exists where the error measures undercut the defined error bound, the used sample size was chosen too small and needs to be enlarged. If the measures are below the given error bound, the sample size is suitable for the objective of the sensitivity analysis.

Bootstrap Resampling

Bootstrap resampling, first introduced by [110], is a well-known technique to compute confidence intervals for point estimations. A good overview of actual bootstrap methods is given in [111] and [112]. Furthermore, several approaches exist in the literature to compute bootstrap resamples, especially for sensitivity analysis [111, 113]. Throughout this thesis, bootstrap resampling is used to calculate the confidence intervals for the estimated sensitivity indices $\hat{S}_i(t)$, $\hat{S}_{T_i}(t)$, $\hat{S}_i^G(t)$ and $\hat{S}_{T_i}^G(t)$ and is outlined in the following.

In bootstrap resampling, the simulation results of sample size N are assumed to be the basic population. From this basic population, a random sample of size $N_b \leq N$ is drawn randomly with repetition. This resampling is repeated B times. For each bootstrap sample, the sensitivity measures $\hat{S}_i^b(t)$, $\hat{S}_{T_i}^b(t)$, $\hat{S}_i^{G,b}(t)$ and $\hat{S}_{T_i}^{G,b}(t)$ are calculated. Using the estimated mean and standard deviation of these bootstrap samples

$$\mu_{\hat{S}_i^b}(t) = \frac{1}{B} \sum_{b=1}^{B} \hat{S}_i^b(t) \tag{3.66}$$

$$\hat{\sigma}_{S_i^b}(t) = \sqrt{\frac{1}{B-1} \sum_{b=1}^{B} (\hat{S}_i^b(t) - \mu_{\hat{S}_i^b}(t))^2}, \tag{3.67}$$

the confidence intervals can be calculated. Consequently, the estimated mean and standard deviation of $\hat{S}_{T_i}^b(t)$, $\hat{S}_i^{G,b}(t)$ and $\hat{S}_{T_i}^{G,b}(t)$ are calculated analogously to (3.66) and (3.67). In [113], it is proved that the estimated mean and standard deviation using bootstrap resampling is asymptotically normal distributed and consistent, which can be formalized by

$$\lim_{B \to \infty} \mu_{\hat{S}_i^b}(t) = E(\hat{S}_i^b(t)) = S_i^b(t) \tag{3.68}$$

$$\lim_{B \to \infty} \hat{\sigma}_{S_i^b}(t) = \sqrt{E((\hat{S}_i^b(t))^2) - E(\hat{S}_i^b(t))^2} = \sigma_{S_i^b}(t). \tag{3.69}$$

Definitions (3.68) and (3.69) are also valid when calculating the bootstrap samples for $\hat{S}_{T_i}^b$, $\hat{S}_i^{G,b}$ and $\hat{S}_{T_i}^{G,b}$. The properties (3.68) and (3.69) enable the derivation of reliable confidence intervals if the number of bootstrap samples B is large enough.

3.3 Conclusions

In this chapter, the theoretical foundation of sensitivity analysis is presented. As an introduction, state-of-the-art sensitivity methods are presented, and their advantages and disadvantages are discussed. The decision for the Morris screening as a qualitative and for the Sobol indices as a quantitative method is justified. The theory of Morris Screening and the corresponding sampling scheme, as well as the sensitivity measures based on the elementary effects, are outlined. Furthermore, the process of a variance-based sensitivity analysis as an extension to an uncertainty analysis is outlined. The derivation of the Sobol indices based on the HDMR is summarized, and the interpretation of the first order and total order indices

is discussed. Besides the Sobol indices, the generalized Sobol indices are presented and discussed to deal with the time dependency of physical processes. In addition, the estimation process of the sensitivity indices using different estimators is depicted. This includes comparing different sampling strategies and their impacts on the convergence of the estimators and the assurance of convergence using the law of big numbers and bootstrap resampling.

4 Model Predictive Control

In the following chapter, the concept of MPC is explained in more detail. The evaluation of known control methods, such as PID or state space controllers, refers to individual characteristics of the control loop such as overshoot, settling time, poles, bandwidth or resonance overshoot. In many practical applications, the controller performance cannot be described in such characteristics, or other quantities are of interest. This drawback is addressed in MPC by using an optimization criterion

$$\min_{\mathbf{u}} J(\mathbf{x}, \mathbf{u}) \tag{4.1}$$

as the optimization target of the control problem considering the system states $\mathbf{x}$ and the control inputs $\mathbf{u}$.

Furthermore, MPCs are capable of predicting the states of the controlled system and thus are capable of reacting more distinctly to upcoming changes or measured disturbances. Another major advantage of this method is that state and manipulated variable constraints can be considered directly in the optimization problem and the controller is able to operate close to these constraints. Therefore, using an MPC approach for solving the complex task of energy-efficient longitudinal control of a BEV is a promising approach. The large number of publications, as summarized in Chapter 2, reinforces the suitability of MPC-based methods for energy-efficient longitudinal control.

In this chapter, a general introduction to MPC is given. The concept of receding horizon strategy to transfer the OCP to an MPC is presented. Furthermore, different types of MPC are discussed including LMPC, NMPC and ENMPC.

4.1 Optimal Control

MPC is based on designing and solving an OCP. Optimality in this context always refers to an existing cost function that is optimized. The predictive behavior of the OCP is achieved by using a dynamic model of the plant behavior in the form

$$\dot{\mathbf{x}} = \frac{d\mathbf{x}}{dt} = f(\mathbf{x}, \mathbf{u}) \tag{4.2}$$

with $\mathbf{x} \in \mathbb{R}^n$ states and $\mathbf{u} \in \mathbb{R}^m$ inputs.

The optimization objective is described by the cost function of the OCP and can be expressed for continuous time by

$$J(\mathbf{x}, \mathbf{u}) = \int_0^{t_{end}} \underbrace{J_c(\mathbf{x}(\tau), \mathbf{u}(\tau), \tau)}_{\text{Lagrange term}} d\tau + \underbrace{J_f(\mathbf{x}(t_{end}), t_{end})}_{\text{Mayer term}}. \tag{4.3}$$

It consists of the integral Lagrange part defined by the cost function term $J_c(\cdot)$ and the Mayer term $J_f(\cdot)$ at the end of the prediction horizon t_{end}. The Lagrange term is used to describe control objectives that should be achieved during the prediction before the end of the prediction horizon is reached. In contrast, the Mayer term expresses the control objective at the end of the prediction horizon.

Compared to the conventional Linear Quadratic Regulator (LQR), the OCP further considers constraints on inputs and states using equality and inequality constraints expressed by

$$g_j(\mathbf{x}(t), \mathbf{u}(t)) = 0 \qquad \forall j \in \{1, 2, \ldots, n_g\} \tag{4.4}$$

$$h_j(\mathbf{x}(t), \mathbf{u}(t)) \leq 0 \qquad \forall j \in \{1, 2, \ldots, n_h\} \tag{4.5}$$

with n_g equality and n_h inequality constraints.

The complete OCP, including the above-presented properties, is described by

$$J^*(\mathbf{x}_0) = \min_{\mathbf{u}} \quad J(\mathbf{x}_0, \mathbf{u}) \tag{4.6a}$$

$$\text{s.t.} \qquad \dot{\mathbf{x}} = f(\mathbf{x}, \mathbf{u}) \tag{4.6b}$$

$$\mathbf{x}(0) = \mathbf{x}_0 \tag{4.6c}$$

$$g_j(\mathbf{x}(t), \mathbf{u}(t)) = 0 \qquad \forall j \in \{1, 2, \ldots, n_g\}, t \in [0, t_{end}] \tag{4.6d}$$

$$h_j(\mathbf{x}(t), \mathbf{u}(t)) \leq 0 \qquad \forall j \in \{1, 2, \ldots, n_h\}, t \in [0, t_{end}] \tag{4.6e}$$

with $J^*(\mathbf{x}_0)$ as the optimal solution cost. The optimal input trajectory for the prediction horizon of the OCP is then obtained by

$$\mathbf{u}^*(t) = \arg\min_{\mathbf{u}} J(\mathbf{x}_0, \mathbf{u}) \quad t \in [0, t_{end}). \tag{4.7}$$

The strategy or algorithm for solving the OCP of (4.6) depends on the type of the optimization problem, whether it is linear or nonlinear or if it contains constraints. However, generally, the methods to solve an OCP can be assigned to three categories:

- **Dynamic programming** is one commonly used solving strategy of OCPs. It breaks the problem into smaller sub-problems based on Bellman's principle of optimality [47]. This can be done analytically via the derivation of a particular equation whose solution yields the optimal value (see Hamilton-Jacobi-Bellman or Riccati equations for e.g. linear-quadratic problems), or also numerically.

- **Indirect methods** mostly use variants of Pontryagin's maximum principle [114]. Here, an abstract optimality criterion provides the sufficient conditions of the maximum principle in the form of a boundary value problem, which is solved analytically or numerically utilizing a subsequent discretization.

- **Direct methods** first discretize the problem and thereby transform the optimal control problem into a static optimization problem. This problem is then solved with suitable numerical methods, e.g. SQP methods [115]. The advantage of direct discretization is that no prior knowledge of the solution structure and no estimates regarding critical points are necessary.

In the rest of the thesis, direct methods are used to solve the presented optimization problems. Therefore, the optimization problem (4.6) must be discretized. Commonly used discretization schemes for the prediction model are the methods of Euler [116], Heun [117] or Runge-Kutta [118].

Furthermore, the resulting discrete OCP needs to be transformed to an Nonlinear Program (NLP) in the form

$$\min_{\mathbf{w}} \qquad \Phi(\mathbf{w}) \tag{4.8a}$$

$$\text{s.t.} \quad \mathbf{g}_1(\mathbf{w}) \leq 0 \tag{4.8b}$$

$$\mathbf{g}_2(\mathbf{w}) = 0 \tag{4.8c}$$

by collocation, single shooting or multiple shooting methods [119, 120] so that it can be solved using fast optimization solver, e.g., SQP.

4.2 Receding Horizon Control Strategy

The OCP calculates the optimal control sequence $\mathbf{u}^*(t_k)$ for a given start time t_k and a given prediction model. However, in practice, the prediction model underlies uncertainties or simplifications are made to reduce the complexity. Thus, the prediction model is not able to predict the behavior of a real plant exactly. Furthermore, external disturbances can occur that influence the plant. Consequently, the optimal control sequence $\mathbf{u}^*(t_k)$ computed at time t_k would not result in an equal plant behavior compared to the prediction model. To convert the OCP into a closed-loop MPC scheme, the receding horizon strategy is introduced. An overview of this scheme is outlined in Figure 4.1. The optimal control problem is not
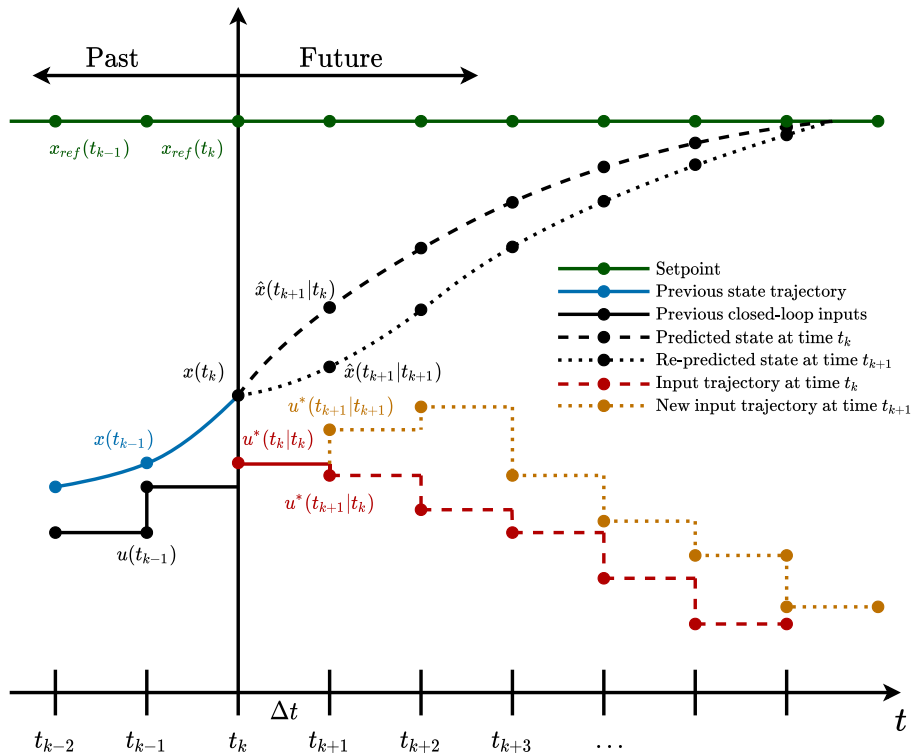
Figure 4.1: Receding horizon principle

solved ones but repetitively with a sampling rate of Δt. At every time step, the initial state $\mathbf{x}_0$ of the OCP is measured and the OCP is solved. Afterward, the first component of the optimal solution vector is fed to the plant as control action. In the next time step t_{k+1}, the optimization problem is solved again with the new measured initial state and the control action is updated again with this new solution.

4.3 Different Types of Model Predictive Control

In the following, the most common types of MPCs are introduced and the differences are outlined. Since the implementation of an MPC must be discrete, the discrete formulations are presented below.

4.3.1 Convex Model Predictive Control

A common MPC formulation is a linear or convex MPC that uses Quadratic Programming (QP)-based OCP to solve the optimization problem. The convexity of this approach is characterized by a quadratic cost function, a linear model and a polyhedral constraint set. The main motivation for this linear approximation is the ease of solving the OCP and low computation times, which supports real-time capability. A typical convex MPC can be defined by

$$\min_{\mathbf{u}} \quad \sum_{k=0}^{N-1} [\mathbf{u}_k' \mathbf{R} \mathbf{u}_k + \mathbf{x}_k' \mathbf{Q} \mathbf{x}_k] + \mathbf{x}_N' \mathbf{Q}_N \mathbf{x}_N \tag{4.9a}$$

$$\text{s.t.} \quad \mathbf{x}_{k+1} = \mathbf{A}\mathbf{x}_k + \mathbf{B}\mathbf{u}_k, \qquad \forall k \in \{0, 1, \dots, N-1\} \tag{4.9b}$$

$$\mathbf{x}_k \in \mathcal{X} \qquad \forall k \in \{0, 1, \dots, N-1\} \tag{4.9c}$$

$$\mathbf{u}_k \in \mathcal{U} \qquad \forall k \in \{0, 1, \dots, N-1\} \tag{4.9d}$$

$$\mathbf{x}_N \in \mathcal{X}_f \tag{4.9e}$$

$$\mathbf{x}(0) = \mathbf{x}_0 \tag{4.9f}$$

$$\mathbf{Q} \succeq 0, \mathbf{Q}_N \succeq 0, \mathbf{R} \succ 0 \tag{4.9g}$$

for a given prediction horizon length N. To ensure convexity of the optimization problem, the weighting matrices $\mathbf{Q}$ and $\mathbf{Q}_N$ must be positive semidefinite and $\mathbf{R}$ is positive definite. Furthermore, the sets $\mathcal{X}$ and $\mathcal{X}_f$ are invariant compact sets and the set $\mathcal{U}$ denotes the feasible input sequences.

4.3.2 Nonlinear Model Predictive Control

For processes with nonlinear behavior or where the linear approximation causes too large prediction errors, the class of NMPC is commonly used in literature. Besides the possibility of including nonlinear prediction models, the constraints and the cost function are also able to consider nonlinearities [121]. Due to the steadily increasing computational capabilities of modern computers, as well as the development of efficient and fast algorithms for solving NMPC, the practical applicability of these systems even for fast system dynamics and the calculation on embedded systems has increased significantly.

A general NMPC formulation can be outlined by

$$\min_{\mathbf{u}} \quad \sum_{k=0}^{N-1} J_c(\mathbf{x}_k, \mathbf{u}_k) + J_f(\mathbf{x}_N) \tag{4.10a}$$

$$\text{s.t.} \quad \mathbf{x}_{k+1} = f(\mathbf{x}_k, \mathbf{u}_k) \qquad \forall k \in \{0, 1, \dots, N-1\} \tag{4.10b}$$

$$g_j(\mathbf{x}_k, \mathbf{u}_k) = 0 \qquad \forall j \in \{1, 2, \dots, n_g\}, \forall k \in \{0, 1, \dots, N-1\} \tag{4.10c}$$

$$h_j(\mathbf{x}_k, \mathbf{u}_k) \leq 0 \qquad \forall j \in \{1, 2, \dots, n_h\}, \forall k \in \{0, 1, \dots, N-1\} \tag{4.10d}$$

$$\mathbf{x}(0) = \mathbf{x}_0 \tag{4.10e}$$

for a given prediction horizon length N. In contrast to the LMPC, the cost function terms $J_c(\cdot)$ and $J_f(\cdot)$, the system model $f(\mathbf{x}_k, \mathbf{u}_k)$, as well as the constraints $g_j(\cdot)$ and $h_j(\cdot)$ could contain nonlinear descriptions. This leads to a controller formulation that is highly flexible for solving more complex control problems.

4.3.3 Economic Model Predictive Control

The concept of ENMPC has gained significant attention in the last years. LMPC and NMPC approaches usually use quadratic cost function for tracking a reference or reaching a predefined setpoint. However, tracking a predefined reference trajectory as close as possible is often not the solution that requires the

fewest resources. Thus, the idea of describing an economic objective, such as the energy consumption of the vehicle, directly in an MPC gets attractive [122].

The main difference between the above presented NMPC and the ENMPC is that the ENMPC uses a terminal stage cost describing the economics of the process that must not be quadratic or achieve some reference tracking [123]. Moreover, the terminal cost of the cost function represents a direct or indirect reflection of the economics of the optimized process. Thus, the ENMPC is not operating the plant at some predefined steady state but rather optimizing the economics by choosing the optimal system state. In practice, the economic terminal cost is often combined with a reference tracking MPC. For instance, this combination can be formulated to a cost function of the form

$$J_c(\mathbf{x}_k, \mathbf{u}_k) = \mathbf{u}_k' \mathbf{R} \mathbf{u}_k + \mathbf{x}_k' \mathbf{Q} \mathbf{x}_k \tag{4.11}$$

$$J_f(\mathbf{x}_N) = l_e(\mathbf{x}_N) \tag{4.12}$$

where $l_e(\cdot)$ describes the economic cost component objective [124] and $J(\cdot)$ outlines the trajectory error. This economic cost function substitutes the NMPC cost function of (4.10).

4.4 Conclusions

MPC is a promising approach for developing predictive, energy-efficient longitudinal controllers for BEV. In this chapter, the concept of MPC based on the solution of an OCP has been presented. Furthermore, the receding horizon control strategy has been introduced to transfer the OCP to an MPC to obtain a closed-loop control. Furthermore, the most commonly used and real-time capable MPCs for longitudinal control are discussed. These concepts include the LMPC, which is described by a convex optimization problem leading to a good solvability but with the drawback of approximations in the prediction model. Instead, NMPC approaches include nonlinearities in the controller design and are capable of predicting and reacting more precisely to nonlinear plants. At least the concept of ENMPC has been presented where the stage cost of the LMPC or NMPC controller consists of an economic penalization of the process in contrast to a standard reference tracking.

5 Detailed Modeling of the BEV and the Environment

Appropriate models of the vehicle and its powertrain components are required as a basis for sensitivity analysis and controller development. For the sensitivity analysis, accurate models are needed that represent the variables of interest as precisely as possible. Uncertainty in the models could otherwise lead to falsified sensitivity analysis results. Thus, special attention must be paid to the simulation models in terms of accuracy and appropriate parameterization and validation. Since the presented sensitivity analysis methods require a large number of model runs, another focus of the modeling is on optimizing the computation time.

The presented models represent the detailed physical description of the vehicle and enable realistic simulations of longitudinal dynamic behavior and fuel consumption. Furthermore, they serve as a basis for the development of the MPC. However, in practice, the models used in the MPC must be kept as simple as possible to achieve real-time capability of the proposed algorithms.

In this work, the early-stage prototype of the proTRon Evolution battery-electric research vehicle of the University of Applied Sciences Trier serves as the basis for the models and their evaluation. A sketch of the vehicle is outlined in Figure 5.1. The project focuses on sustainable mobility, considering the com-
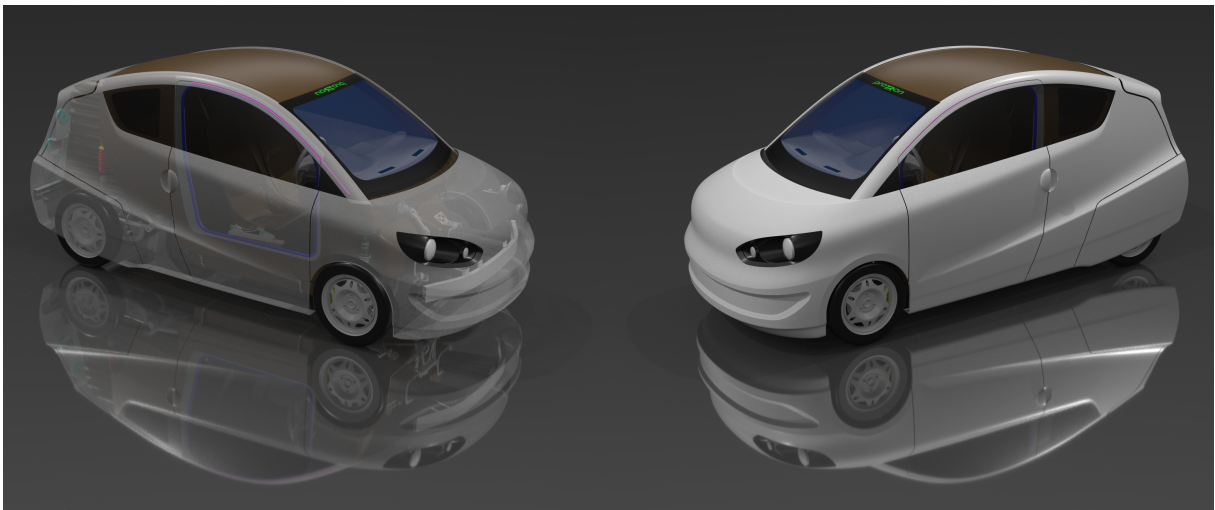
Figure 5.1: Sketch of the proTRon Evolution research vehicle

plete product life cycle. Due to this fact, the vehicle body is primarily made of natural fiber-reinforced plastics to reduce emissions in the manufacturing process. To keep the energy consumption in driving operations as low as possible, a target weight of 550 kg is planned while, at the same time, complying with the crash safety requirements relevant for approval. Furthermore, all mechanical driving resistances are forced to be as small as possible. This is achieved using tires with low rolling resistance properties with dimensions 115/80R15 to reduce the rolling resistance coefficient. Additionally, the aerodynamic

drag coefficient and the vehicle's frontal area are minimized during the development process using Computational Fluid Dynamics (CFD) simulations, resulting in low aerodynamic resistance. The powertrain of the vehicle includes a single-wheel drive on each wheel of the rear axle with EMRAX 188 Permanent Magnet Synchronous Machines (PMSMs). They are powered by a series of 76 40 Ah Winston WB-LYP40AHA lithium iron phosphate accumulators with a nominal voltage of 251 V. A novel transmission concept is used in the vehicle, consisting of a belt drive and a planetary gear with optimized losses within a small installation space close to the wheel. The main specification of the vehicle is outlined in Table 5.1.

The powertrain architecture and the used simulation setup are outlined in Figure 5.2 and represent

Table 5.1: Main specification of the proTRon Evolution test vehicle

Description	Value
Maximum continuous power	30 kW
Maximum motor torque	60 Nm
Maximum driving speed	100 km/h
Planned minimum cruising range	100 km
Battery capacity	10 kWh / 40 Ah
Battery technology	LiFeYPO$_4$
Kerb weight	550 kg
Admissible total weight	970 kg
Transmission ratio	5.85
Tire dimensions	115/80R15
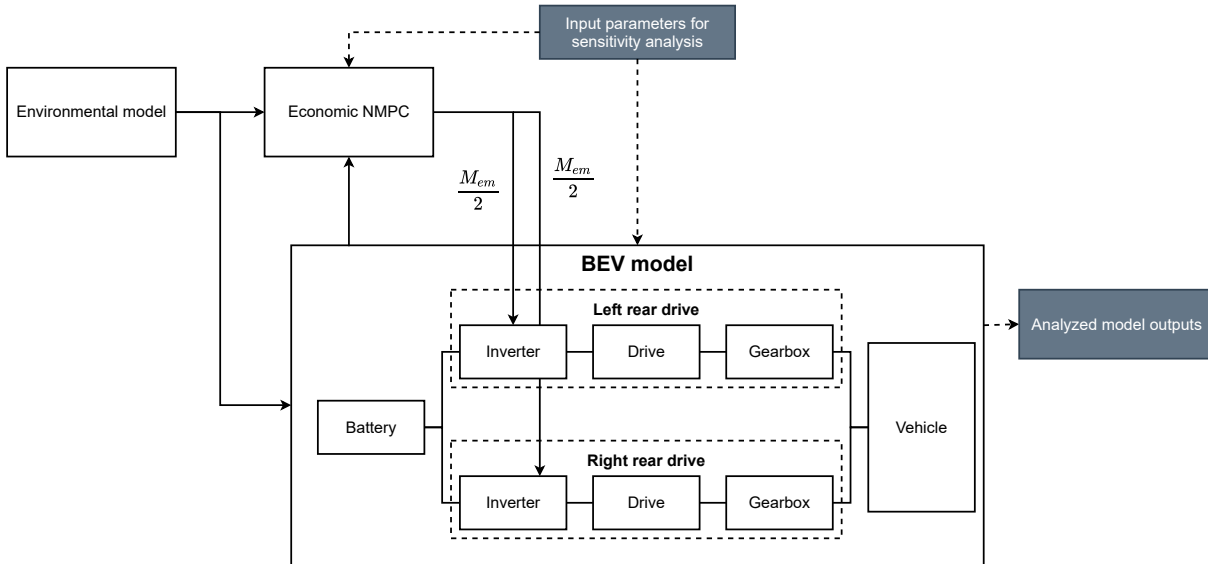
Figure 5.2: Simulation setup of the proTRon Evolution

the basis for the simulative analyses in this thesis. The model consists of the BEV model, including detailed powertrain component models of the battery, inverter, drive and gearbox. Furthermore, an environmental model is included to represent the changeable environment of the vehicle while driving and interaction points for the sensitivity analysis are provided. The modeling of the vehicle, as well as its components and the environmental model, are described in this chapter.

5.1 Modeling and Parameter Determination of the Electric Vehicle

As depicted in Figure 5.2, the BEV model consists of a longitudinal motion model and a detailed power-train model. The powertrain is divided into the battery and two drive units for driving each rear wheel separately. An inverter, a PMSM and a gearbox constitute one drive unit. A detailed explanation of the different model parts is outlined in this section.

5.1.1 Longitudinal Motion and Gearbox Model

The longitudinal motion model considers the mechanical forces acting on the vehicle's center of gravity and a gearbox model transferring the electric drives' mechanical energy to the wheels. The force equilibrium acting on the vehicle, as outlined in Figure 5.3, is described by
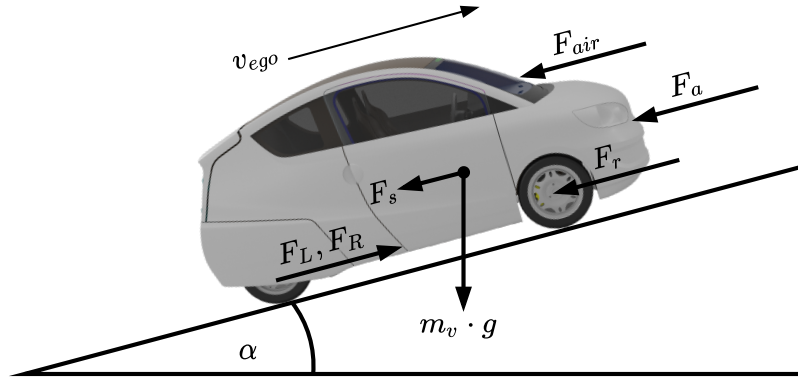
Figure 5.3: Driving resistances

$$F_L + F_R = F_a + F_r + F_s + F_{air}, \tag{5.1}$$

where F_L and F_R are the forces of the left and right rear driving wheel and are powered via the two drive units. The driving resistance forces are composed of the acceleration resistance force F_a, the rolling resistance force F_r, the slope resistance force F_s and the air resistance force F_{air}.

The acceleration resistance force is caused by Newton's second law. It is expressed with

$$F_a = m_{eq} \cdot a_{ego}, \tag{5.2}$$

where m_{eq} denotes the equivalent mass, including the inertia of the rotating parts of the powertrain, which belong to their kinetic energy and a_{ego} describes the acceleration of the vehicle.

The dynamic deformation of the tire causes the rolling resistance force and usually depends on numerous variables. The most important are the vehicle speed v_{ego}, the tire pressure p_T, the tire temperature ϑ_T and the road surface conditions [125]. According to this, the rolling resistance force is described by

$$F_r = c_r(v_{ego}, p_T, \vartheta_T) \cdot m_v \cdot g \cdot \cos(\alpha) \quad \text{with} \quad v_{ego} > 0, \tag{5.3}$$

where c_r is the rolling resistance coefficient, g the gravitational acceleration and α the slope angle of the road. The dependency of c_r on the vehicle speed, the tire pressure and the tire temperature is outlined in
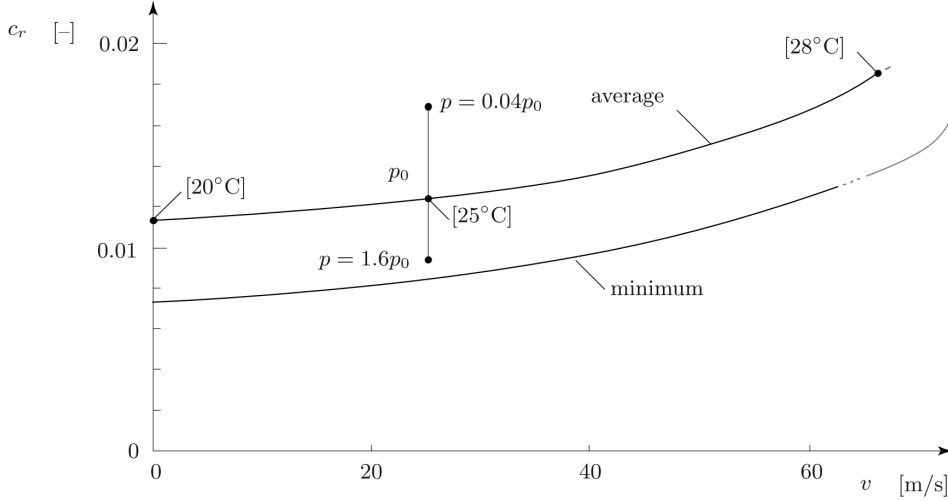
Figure 5.4: Dependencies of the rolling resistance coefficient for v_{ego}, p_T and ϑ_T [125]

Figure 5.4. Nevertheless, based on the assumption that the tire pressure is set correctly and $v_{ego} < 30\,\text{m/s}$ (5.3) can be simplified, which leads to

$$F_r = c_r \cdot m_v \cdot g \cdot \cos(\alpha) \quad \text{with} \quad v_{ego} > 0. \tag{5.4}$$

Similarly, the resistance force caused by the road slope

$$F_s = m_v \cdot g \cdot \sin(\alpha) \tag{5.5}$$

describes the additional force when driving up or downhill.

Furthermore, moving through the surrounding air will cause an aerodynamic resistance force due to the friction of the air on the vehicle's surface. Moreover, the pressure difference between the front and the rear of the vehicle contributes to the aerodynamic resistance force. Also, turbulences caused by the wheel housing, the exterior mirrors, window housings, antennas and other attachments influence the aerodynamic resistance. In general, the aerodynamic behavior of a vehicle is complex and is computed using numerical methods like CFD. However, the approximation of the aerodynamic resistance force by

$$F_{air} = \frac{1}{2}c_w \cdot A_v \cdot \rho_{air} \cdot v_{ego}^2 \tag{5.6}$$

is well known in practice and produces valuable results. In (5.6), c_w denotes the aerodynamic drag coefficient, which is usually identified using CFD simulations or experimental wind tunnel experiments. The flowed surface of the vehicle can be simplified as the projection onto an equivalent rectangular surface with the frontal area A_v, and the density of the surrounding air is represented by ρ_{air}.

Substituting (5.2), (5.4), (5.5) and (5.6) into (5.1) leads to

$$F_L + F_R = m_{eq} \cdot a_{ego} + c_r \cdot m_v \cdot g \cdot \cos(\alpha) + m_v \cdot g \cdot \sin(\alpha) + \frac{1}{2}c_w \cdot A_v \cdot \rho_{air} \cdot v_{ego}^2. \tag{5.7}$$

The traveled distance of the vehicle s_{ego} is obtained by

$$s_{ego}(t) = \int_0^t v_{ego}(\tau)\mathrm{d}\tau \tag{5.8}$$

for a given driving time t.

The conversion from the longitudinal motion model and the associated forces to the rotational model of the drivetrain is achieved by the law of levers. The resulting transformation of the longitudinal driving forces F_L and F_R to the corresponding drive shaft torques M_L and M_R of the wheels is given by

$$M_L = F_L \cdot r_w \tag{5.9}$$

for the left rear wheel and

$$M_R = F_R \cdot r_w \tag{5.10}$$

for the right rear wheel, where r_w describes the radius of the corresponding wheels. Assuming that the same torque is applied on the left and the right wheels, the needed driving force in (5.1) can be described by

$$F_L + F_R = \frac{M_L + M_R}{r_w} = \frac{2M_D}{r_w} \quad \text{with} \quad M_L = M_R. \tag{5.11}$$

The gearbox of one drive unit consists of a belt drive and a planetary gear and is outlined in Figure 5.5. It is modeled using a constant gear ratio i_g and a working point-dependent efficiency map $\eta_{gb}(\omega_m, M_{em})$.
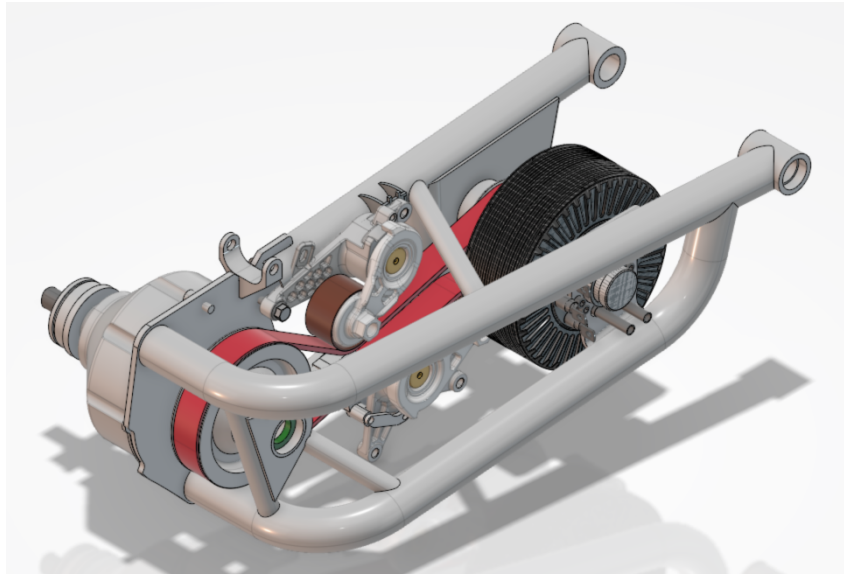
Figure 5.5: Drive unit of the proTRon Evolution

This leads to

$$M_D = M_{em} \cdot i_g \cdot \eta_{gb}(\omega_m, M_{em}), \tag{5.12}$$

describing the transition from the mechanical torque of the electric drives M_{em} to the torques M_D applied to the wheels. The efficiency map was measured on the Drive Testbench 2 (DTB2) for a corresponding drive unit prototype and is outlined in Figure 5.6. For further details regarding the test bench, see Appendix A.2.2.
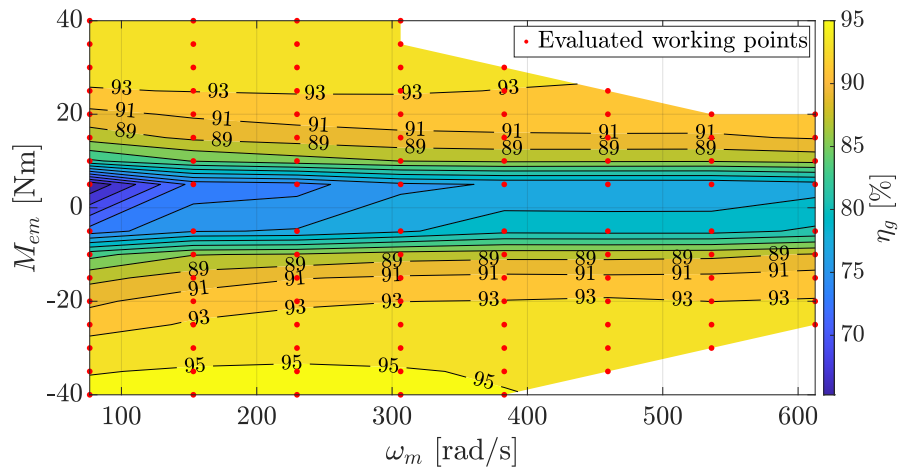
Figure 5.6: Measured efficiency of the gearbox of one drive unit consisting of belt drive and planetary gear.

5.1.2 Battery Model

To better understand how a modern Li-ion accumulator works and how the proposed battery model fits the processes that take place inside a cell, the functional scheme is introduced in advance. In Figure 5.7, the basic functional scheme of one Li-ion cell for the discharge process is given.
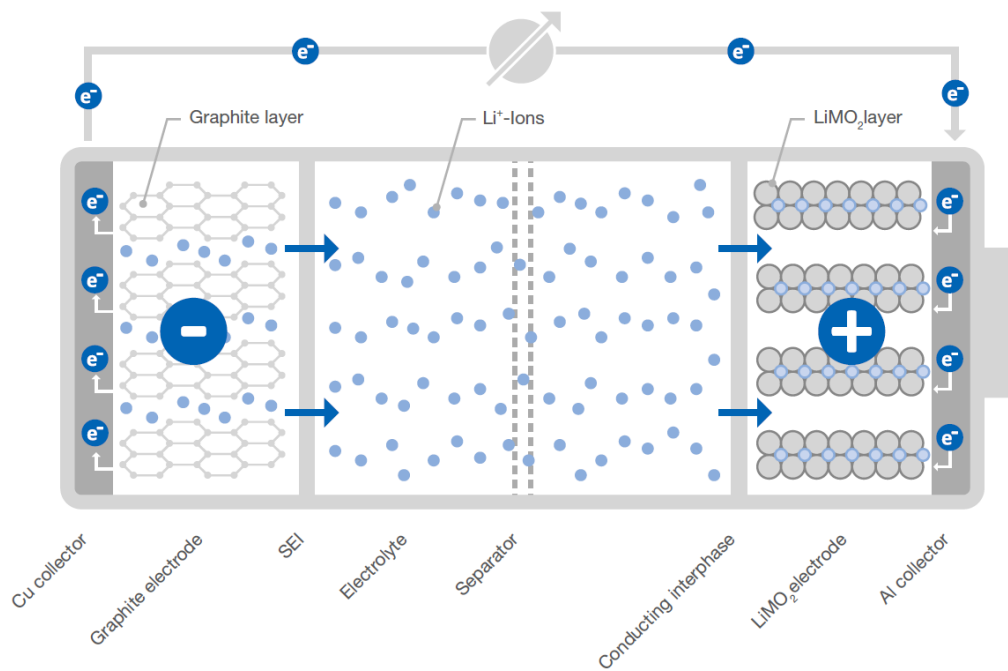
Figure 5.7: Functional scheme of a Lithium ion battery cell during discharging [126].

The cell consists of two different electrodes, which represent a galvanic cell. Since the location of the oxidation and reduction process depends on the direction of electron flow or, in other words, if the cell

is charged or discharged, it is common to define the electrode names for the discharging process. Thus, the negative electrode is defined as the anode and the positive electrode as the cathode. In modern cells, the anode usually consists of a copper foil and a carbon layer on this foil where natural or synthetic graphite is used as it undergoes only a small change of volume during charging and discharging. The positive electrode is typically made out of aluminum and a metal oxide layer applied to it. Commonly used oxides are $LiCoO_2$, $LiMn_2O_4$ and $LiFePO_4$ [127], to mention just a few. Both electrodes are covered in an electrolyte consisting of lithium salt and organic solvents, which are ion conductive. The Solid Electrolyte Interphase (SEI) layer is formed at the interface between the electrolyte and the graphite electrode. It protects the electrode material from the corrosive effect of the electrolyte but at the same time remains conductive to lithium ions. Furthermore, the positive electrode also contains such a barrier which is usually called conducting interphase. To avoid short circuits inside the cell, both electrodes are separated using a semipermeable, lithium-ion conductive membrane as a separator. Lithium is used since it has a high normal potential of $E^0 = -3.045 \, \text{V}$ and is the lightest of all metals. Thus, high gravimetric energy and power densities can be achieved in the galvanic cell [126].

During the discharge process, intercalated lithium is oxidized in the anode. The released electrons are transferred to the cathode via the external circuit. On the other hand, the lithium ions are released from the graphite electrode and diffuse through the SEI layer, the electrolyte, the separator and the conducting interphase to the cathode, where they are finally reduced with the electrons and intercalated in the metal oxide. The aforementioned processes of electron flow and the transition of the lithium ions during discharge results in several electrochemical overvoltages causing the cell voltage on the terminals to drop a certain amount which characterizes the loss behavior of the cell.

If a voltage greater than the open-circuit voltage is applied to the terminals, the processes described above are reversed, and the cell is recharged. The reduced lithium at the anode is stored again in the graphite matrix. Since it is not the focus of this work and modeling, a detailed description of the electrochemical relationships and processes within the individual layers is not provided here. However, a good overview can be found in [127–129].

Modeling the behavior of a modern Li-ion accumulator can be divided into different complexities and different levels of model knowledge. White box models based on reaction kinetics [130, 131] or physically motivated equivalent circuit models [132] provide a detailed basis for understanding the electrochemical processes. However, the complexity of such models also significantly increases the computational cost and parameterization is often only possible with high effort. In contrast, black-box models, such as neural networks [133] and Markov chains [134], are used. They are easy to train or parameterize from existing measurement data. However, the major drawback of this modeling is the missing representation of physical relationships. To reduce the complexity without losing the general physical interpretability of the models, simple equivalent circuit models have been established. These range from a simple representation with a constant voltage source and internal resistance [135] to electrical RC networks [136]. Also, more complex equivalent circuits, including Warburg impedances or nonlinear elements [137, 138], are used in the literature.

The above-outlined modeling techniques are summarized in Table 5.2 and their related properties are listed. As it can be seen, the equivalent circuit models serve as a good compromise between accuracy, physical interpretability, parameterizability and computation time. Thus, an equivalent circuit representation of the battery model is used throughout the thesis and is presented in the following.

In the vehicle, a series connection of 76 $LiFeYPO_4$ prismatic cells with 40 Ah of the type Winston WB-LYP40AHA, as outlined in Figure 5.8, is used. The corresponding equivalent circuit model that is used is outlined in Figure 5.9. It consists of a voltage source u_{ocv}, a series resistor R_s representing the ohmic losses in the battery cell and two RC elements describing the cell dynamics. The series resistance mainly represents the conductive behavior of the electrolyte in the cell and is not frequency-dependent. One RC element models the charge transfer on average frequencies, whereas the other RC element describes the slow diffusion processes at low frequencies. For the proposed equivalent circuit network, the

Table 5.2: Comparison of different modeling techniques

Parameter	Accuracy	Complexity	Physical representation	Good parameterizability
Physical (White Box)	+++	+++ (>50 parameters)	++	-
Equivalent circuits (Grey Box)	++	++ (2-30 parameters)	+	++
Empirical (Black Box)	+	− (2-3 parameters)	—	+++

(a) One cell [139]
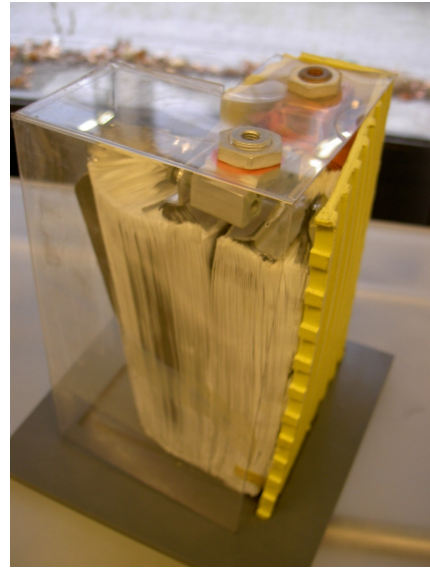
(b) Inside of a cell [140]

Figure 5.8: Winston WB-LYP40AHA cell

terminal voltage is calculated using Kirchhoff's mesh rule with

$$u_k = n_{cell}(u_{ocv} - u_{R_s} - u_{RC1} - u_{RC2}), \tag{5.13}$$

where n_{cell} denotes the number of cells connected in series. Using Kirchhoff's junction rule, the differential equations for the required voltage drops u_{RC1} and u_{RC2} are obtained by

$$\dot{u}_{RC1} = \frac{i_b - \frac{u_{RC1}}{R_1(SoC, i_b, \vartheta_b)}}{C_1(SoC, i_b, \vartheta_b)} \tag{5.14}$$

$$\dot{u}_{RC2} = \frac{i_b - \frac{u_{RC2}}{R_2(SoC, i_b, \vartheta_b)}}{C_2(SoC, i_b, \vartheta_b)}. \tag{5.15}$$

Furthermore, the voltage drop on the series resistance is defined by

$$u_{R_s} = R_s(SoC, i_b, \vartheta_b)i_b. \tag{5.16}$$
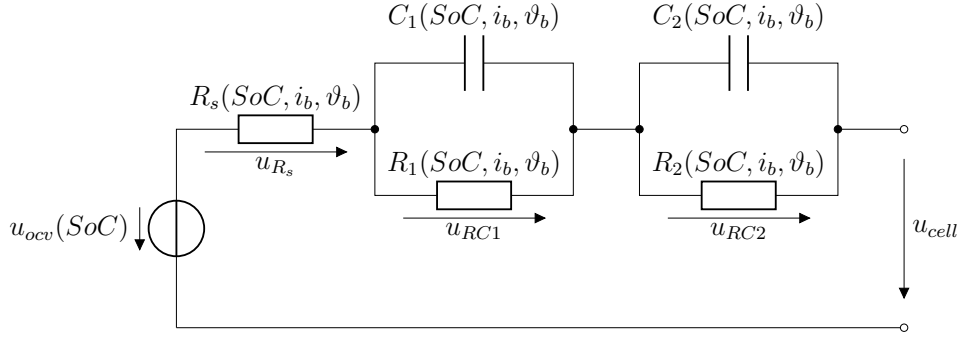
Figure 5.9: Electrical equivalent circuit model of the battery

Since the electrochemical reaction kinetics strongly depends on the actual cell operation point [127, 129], it must be considered in the equivalent circuit model. Thus, as already outlined in (5.14), (5.15) and (5.16), the parameters R_s, R_1, R_2, C_1 and C_2 depend on the actual State of Charge (SoC), defined by

$$SoC = \frac{Q_{SoC}}{Q_b(\vartheta_b)}, \tag{5.17}$$

the battery current i_b and the battery temperature ϑ_b. Here, Q_{SoC} represents the actual stored electrical charge, whereas Q_b is the maximum available electrical charge of one cell. Furthermore, the open-circuit voltage u_{ocv} depends on the actual SoC and Q_b is influenced by ϑ_b. Thus, the identification process of the battery equivalent circuit model needs to be done for each working point.

Furthermore, a thermal model of the used cell is developed and outlined in Figure 5.8. The cell mainly consists of the reactive components inside the cell, a plastic cell housing and the metallic battery terminals, which serve as the contact points of the anode and the cathode. Considering these components, Figure 5.10 outlines the used model for the thermal behavior of a battery cell. In Figure 5.10a, the cross-section of one cell is outlined. The red part in this scheme consists of the battery housing and the reactive part of the cell, including the anode, cathode, separator and electrolyte. In contrast, the yellow part describes the metallic connection of the cell core to the terminals. The corresponding heat capacities

(a) 2D thermal model

(b) Equivalent circuit model
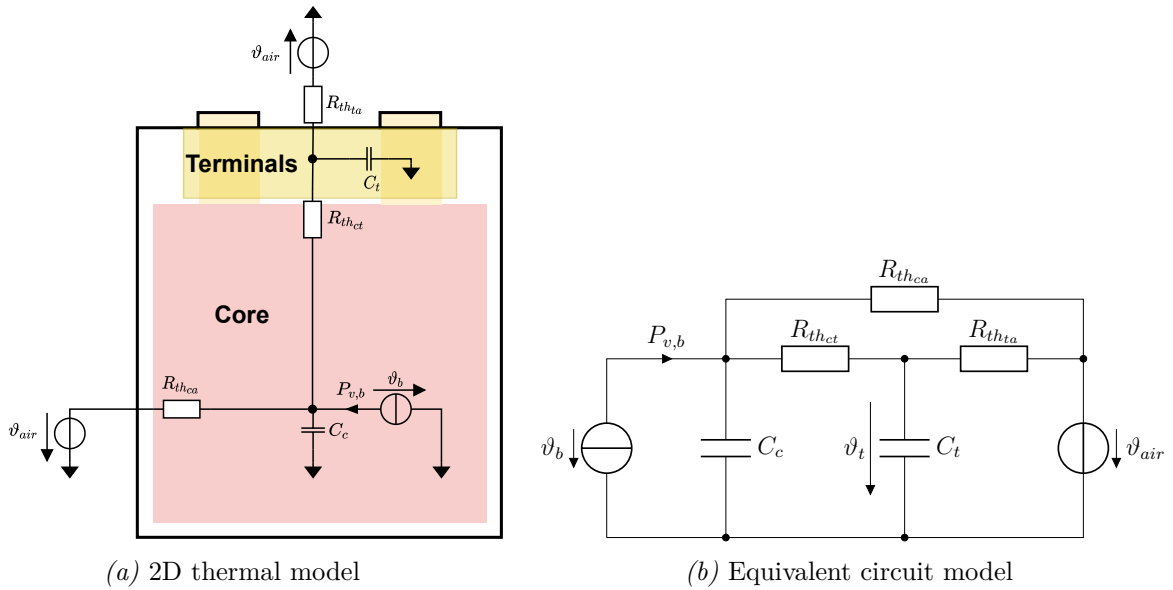
Figure 5.10: Thermal equivalent circuit model of the battery

are assigned to the two areas of the cell. C_c describes the heat capacity of the cell core, whereas the heat capacities of the two terminals are combined in one heat capacity C_t. The dominant heat transfers to the surrounding air take place between the battery core and ambient air through $R_{th_{ca}}$ and between the terminals and ambient air through $R_{th_{ta}}$. Likewise, $R_{th_{ct}}$ represents the remaining heat transfer between the cell core and the terminals. Given the battery loss $P_{v,b}$, caused by the ohmic losses on R_s, R_1 and R_2, the thermal behavior can be described by

$$\dot{\vartheta}_b = \frac{P_{v,b} - \frac{\vartheta_b - \vartheta_{air}}{R_{th_{ca}}} - \frac{\vartheta_b - \vartheta_t}{R_{th_{ct}}}}{C_c} \tag{5.18}$$

and

$$\dot{\vartheta}_t = \frac{\frac{\vartheta_b - \vartheta_t}{R_{th_{ct}}} - \frac{\vartheta_t - \vartheta_{air}}{R_{th_{ta}}}}{C_t} \tag{5.19}$$

using Kirchhoff's junction rule for the equivalent circuit model outlined in Figure 5.10b.

Parameter Identification

The chemical processes of the battery are enclosed inside the housing of a battery cell and spatially distributed over the electrodes and the electrolyte. Thus, internal battery parameters, such as overvoltages of the chemical reactions and inner cell temperatures, cannot be measured directly. Especially for the proposed equivalent circuit modeling approach, the electric circuit's voltages and parameters do not belong directly to physical components. Consequently, the equivalent circuit parameters, the open-circuit voltage and the available battery capacity need to be identified using only the information available from the outside of the battery. These are the battery voltage, battery current and temperatures of the terminals and the housing.

Two different identification techniques are commonly used in the literature to identify the equivalent circuit parameters: The Electrochemical Impedance Spectroscopy (EIS) [137, 141, 142] and current pulse-based identifications [143–147]. The EIS method performs parameter identification in the frequency domain. For this purpose, the battery is excited with a sinusoidal current for different frequencies, and the voltage is measured. Thus, a complex impedance can be calculated for each measured frequency and displayed in a Nyquist diagram. Due to a sinusoidal small-signal excitation, the energy input into the system is low so the operating point, concerning the SoC and the battery temperature, does not shift. However, if the dependence on the actual battery current is also to be investigated, an operating point-dependent DC-current is superimposed on the small signal. The long measurement duration, especially at low frequencies of an EIS, leads to a shift of the operating point concerning SoC and battery temperature.

To overcome the issue of these working point shifts, current pulse-based identifications in the time domain can be used. For this purpose, the battery is excited with a bidirectional pulse of a specific height and duration with a waiting time in between. The height of the pulse corresponds to the actual DC-current working point. Due to the bidirectional character of the identification and the short measurement time, temperature and SoC remains nearly constant during the identification. Furthermore, the rectangular pulses stimulate all frequencies of the battery cell. Thus, an identification without a working point shift is also possible for high currents and low frequencies. The parameters are then identified using a least-square algorithm [148].

Since the battery model, as outlined in Figure 5.9, should cover the working point dependency regarding battery current, SoC and temperature, it is essential to ensure that the operating point is as stable as possible during identification. Thus, the identification procedure for the used battery cell is done using current pulse profiles rather than impedance spectroscopy.

The battery identification is done for a single battery cell using the battery test bench as outlined in Appendix A.1. Figure 5.11 shows the working points of the battery used for the identification process.
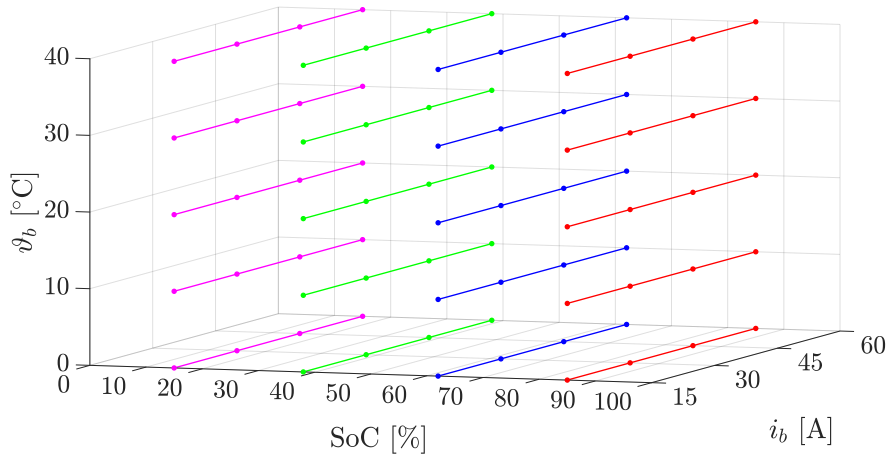
Figure 5.11: Working points used for model identification. Each color represents one measurement cycle. According to [149].

The four colors represent one measurement cycle done at a constant $SoC \in [15, 38, 62, 85]\%$ where each line denotes one current pulse cycle. The used current profile, as outlined in Figure 5.12, consists of a
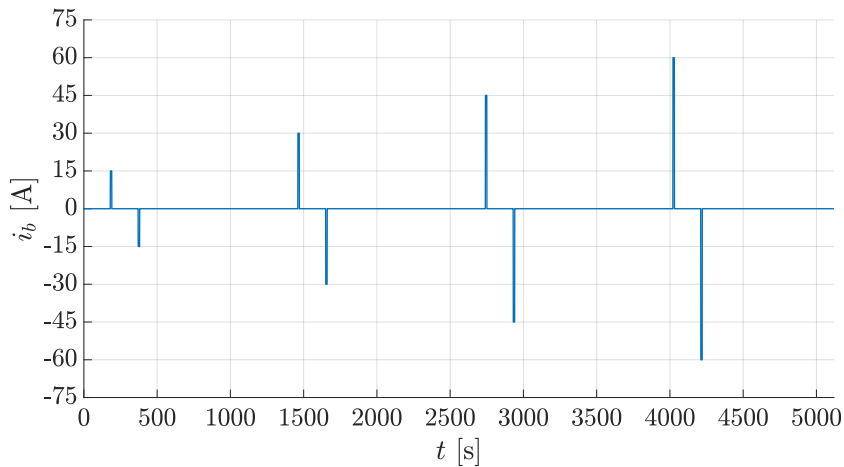
Figure 5.12: Current pulse measurement series. According to [149].

bidirectional current pulse with a pulse length of $10\,\mathrm{s}$ and four different currents $i_b \in [15, 30, 45, 60]\mathrm{A}$. To allow the dynamic processes in the battery to equalize, a wait of 20 minutes is made after each bidirectional pulse. The current height of each pulse represents one load current working point. After one current pulse measurement cycle, the temperature is changed to the next temperature operating point $\vartheta_b \in [0, 10, 20, 30, 40]°\mathrm{C}$ and the terminal voltage response is measured again for the current pulses. This scheme is done for each temperature and SoC working point. The SoC working point change is done by charging the cell up to $100\,\%$ SoC and then discharging it to the target SoC. A waiting time of one hour is kept between the SoC changes to secure the equalization of the dynamic processes. Finally, the identification of the equivalent circuit parameters R_s, R_1, R_2, C_1 and C_2 is done using a least-square algorithm. The identified parameters are outlined in Figure 5.13.

(a) R_s

(b) R_1

(c) R_2

(d) C_1

(e) C_2
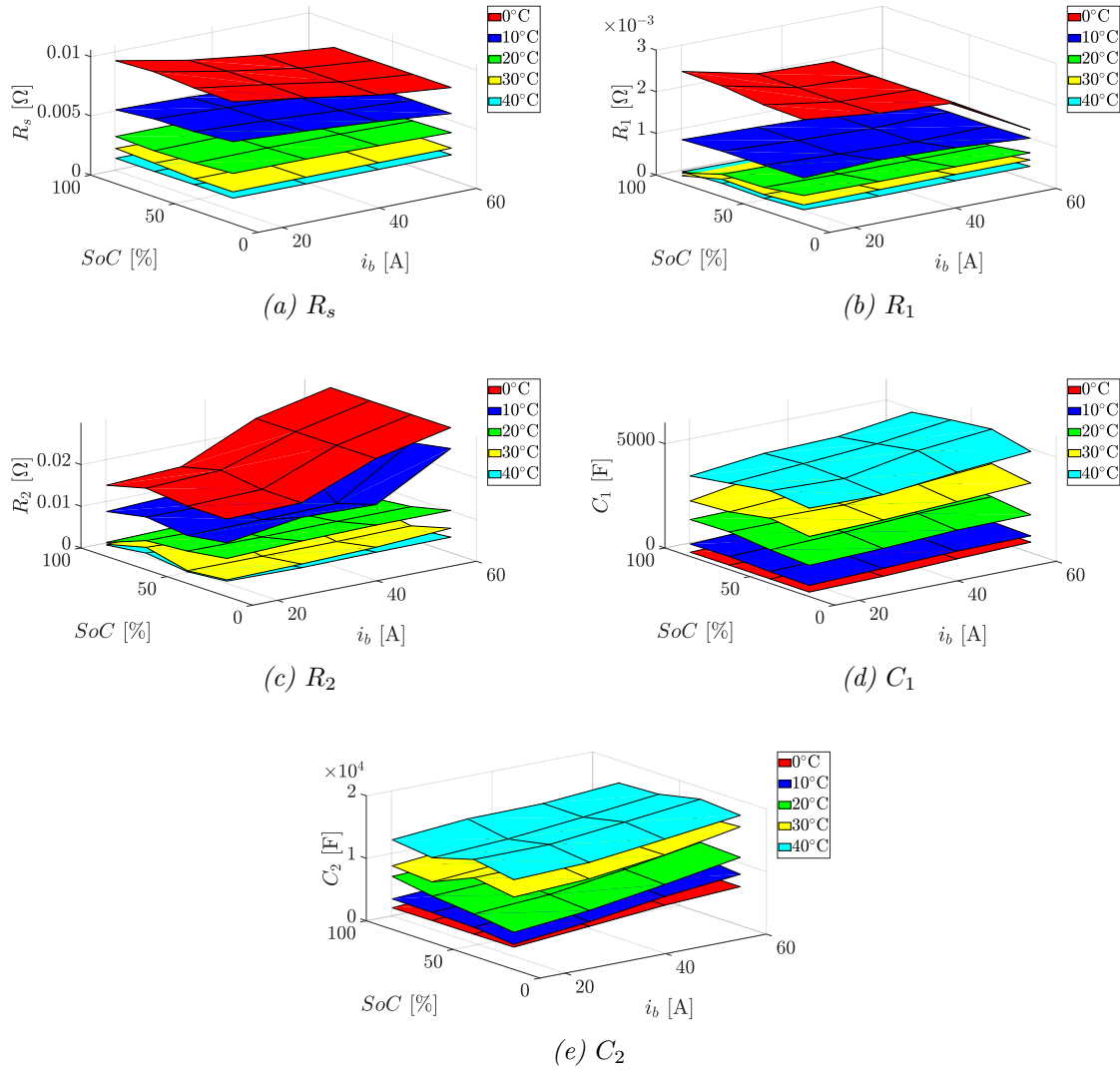
Figure 5.13: Electrical battery parameters, according to [149].

The open-circuit voltage u_{ocv} and its dependency on the SoC also need to be identified. Thus, the terminal voltage of the battery is measured during a charge and discharge of the battery cell from 0 % to 100 % SoC and vice versa. The recorded terminal voltages are averaged and result in the identified open-circuit voltage as outlined in Figure 5.14a. During the identification process of the open-circuit voltage at different temperatures also, the temperature dependency of the maximum available battery capacity Q_b was determined and is outlined in Figure 5.14b.

(a) Open circuit voltage
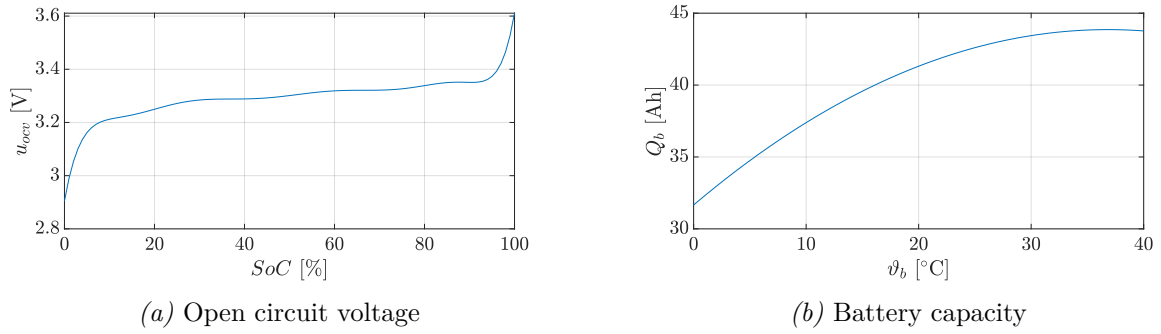
(b) Battery capacity

Figure 5.14: Battery capacity and open circuit voltage, according to [149].

Model Validation

The validation of the parameters is performed on different working points than the identification to ensure that nonlinear dependencies are considered correctly. Figure 5.15 depicts the working points employed for this purpose. The red lines denote the same pulse current profiles used for the identification but at
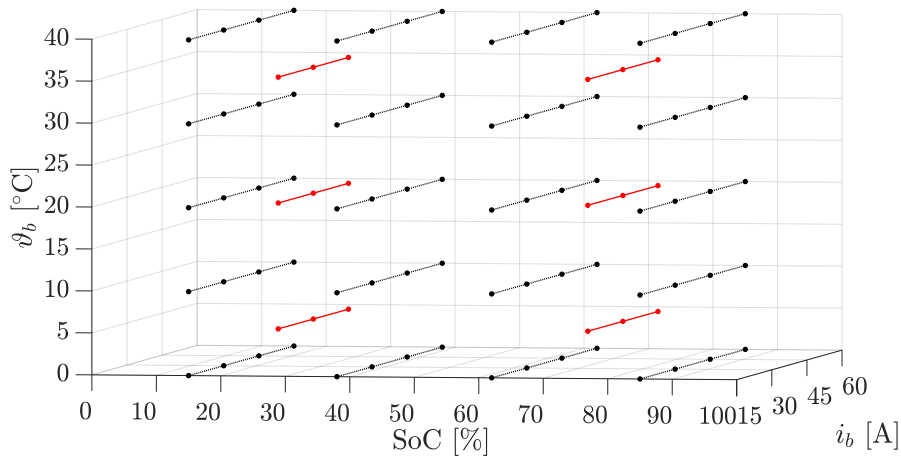
Figure 5.15: Working points used for model validation. Black denotes the working points used for identification and red outlines the points for validation. According to [149].

different working points. The two most distant measurements from each other are exemplarily outlined in Figure 5.16. In general, it can be seen that the simulation model's voltage response shows a good coincidence with the measurements. Especially, the dynamic behavior of the response shows a good correspondence to the measurement. Furthermore, the open-circuit voltage during non-load phases in the current profile coincides with the measurements.

To assess the accuracy of the identified model, Table 5.3 outlines the Root Mean Squared Error (RMSE) of each validation measurement between the simulated and the measured terminal voltage response. It can be summarized that the presented parameterization of the equivalent circuit model satisfactorily reproduces the battery behavior. The thermal parameters of the battery cell were determined in the previous work of [150]. They are investigated by identifying the heat capacities of the used battery materials. Furthermore, the thermal equivalent resistances were experimentally determined. The identified parameters in this work are used throughout this thesis and outlined in Appendix B.
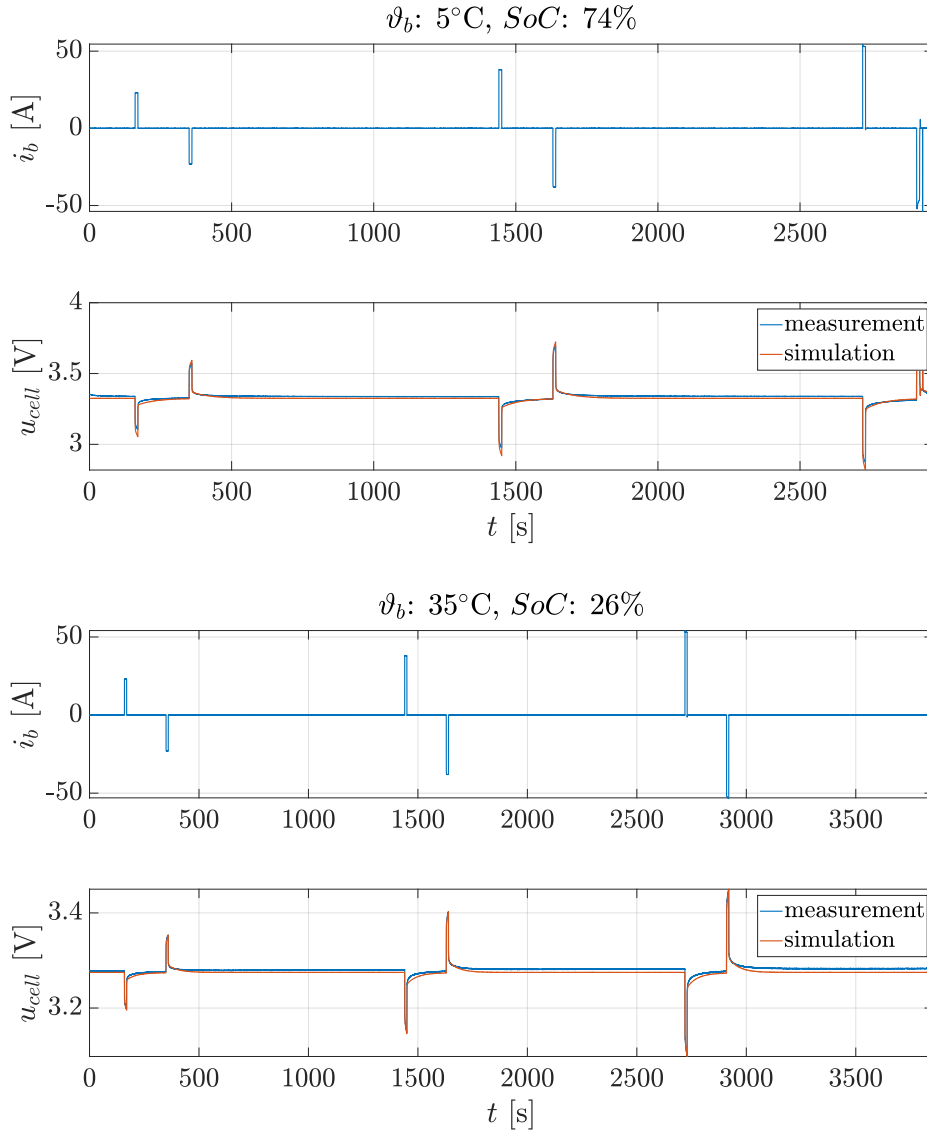
Figure 5.16: Exemplary evaluation measurements for two different working points.

Table 5.3: RMSE of battery model evaluation measurements

Nr	ϑ_b	SoC	RMSE	Relative RMSE
1	5 °C	26 %	13.22 mV	0.4 %
2	20 °C	26 %	8.84 mV	0.27 %
3	35 °C	26 %	3.31 mV	0.1 %
4	5 °C	74 %	14.58 mV	0.44 %
5	20 °C	74 %	11.08 mV	0.34 %
6	35 °C	74 %	6.03 mV	0.18 %
		Mean	9.51 mV	0.29 %

5.1.3 Inverter Model

The following section focuses on modeling the power losses and the thermal behavior of the inverter. In the proposed system, a Voltage Source Inverter (VSI) with an Infineon FS820R08A6P2 power module is used. The circuit diagram of the power electronics is outlined in Figure 5.17. On the left side of the circuit diagram, the connection to the battery is shown with the corresponding DC-link voltage u_{DC} and DC-link current i_{DC}. Also, the virtual ground terminal with the potential $U_{DC}/2$ is depicted. The AC side of the inverter is built up by an Insulated Gate Bibolar Transistor (IGBT) full bridge with an antiparallel free-wheeling diode on each IGBT device. The output terminal voltages u_U, u_V, u_W with their corresponding currents i_U, i_V, i_W represent the interface to the electric drive. To generate a frequency
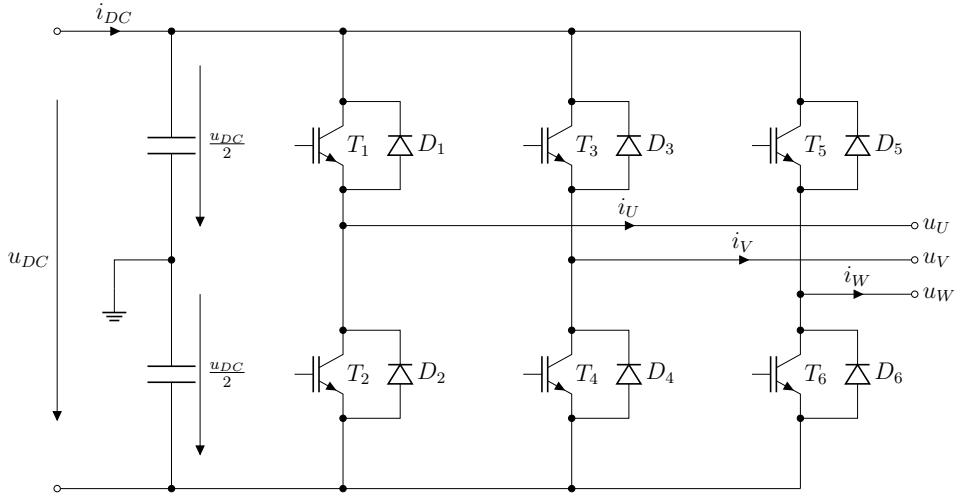
Figure 5.17: VSI equivalent circuit

and amplitude variable AC voltage from the DC-link voltage, the IGBTs must be switched according to a defined pattern using a Pulse Width Modulation (PWM). Due to the PWM, the losses in the inverter consist of conduction and switching losses and depend on the used modulation scheme [151]. In the analyzed inverter, a sine modulation with zero offset is used to improve the voltage utilization [152]. Nevertheless, as the focus is on modeling the loss behavior and not on improving the switching patterns of the inverter, the modulation methods are not discussed in detail in this thesis. However, a good overview is provided in [151] and [152]. Due to the symmetric structure of the inverter and the used modulation scheme, the IGBTs and diodes are loaded identically in one fundamental wave period but with a shift in time. Thus, the power dissipation considerations can be reduced to one IGBT and one diode and are applied to all semiconductors afterwards.

Conduction Losses

The calculation of the conduction losses is carried out for the IGBT and diode pair T_1, D_2 in Figure 5.17. As semiconductors, the IGBTs and the diodes have a current-dependent on-state resistance which causes a corresponding voltage drop and thus produces conduction losses at the devices. The relationship, known as forward characteristics, is shown in Figure 5.18 for the IGBT and the diode of the used power electronics module. Using the forward characteristics, the conduction power losses of the IGBT and the diode

$$p_{c,T_1} = u_{CE}(i_{T_1}, \vartheta_{j,T}) \cdot i_{T_1} \tag{5.20}$$

$$p_{c,D_2} = u_F(i_{D_2}, \vartheta_{j,D}) \cdot i_{D_2} \tag{5.21}$$

(a) IGBT   *(b)* Diode
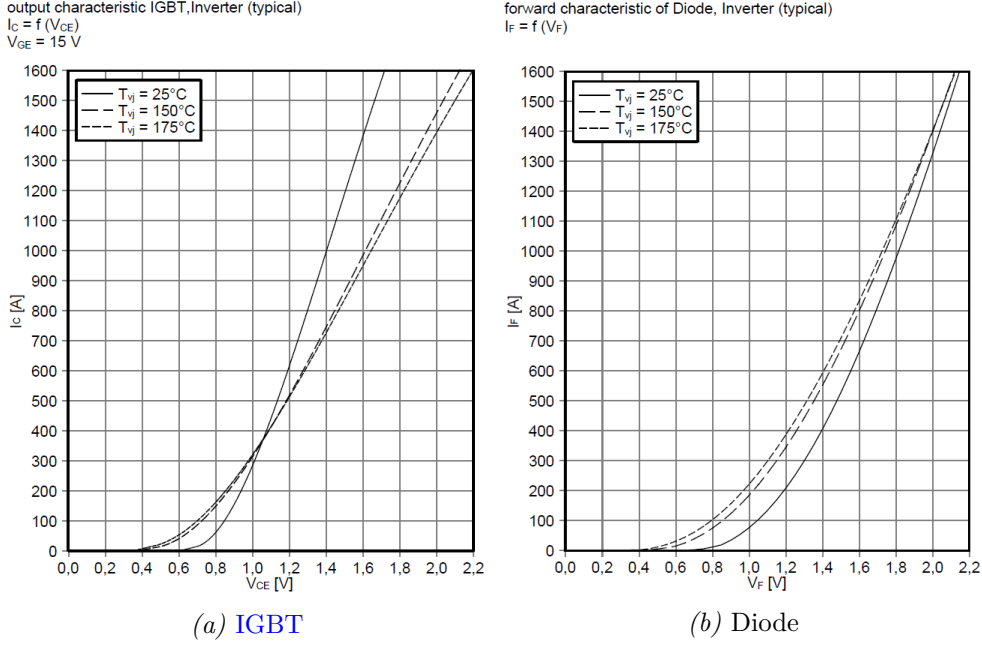
Figure 5.18: Forward characteristics of the used IGBT module [153]

can be calculated for each working point of the semiconductors. Also, the temperature dependencies of the junction temperature of the transistor $\vartheta_{j,T}$ and the diode $\vartheta_{j,D}$ are considered. An analytical formulation of this nonlinear behavior can be achieved by the approximation with a second-order polynomial [154,155]

$$\tilde{p}_{c,T_1} = a_{c,T}(\vartheta_{j,T}) \cdot i_{T_1} + b_{c,T}(\vartheta_{j,T}) \cdot i_{T_1}^2 \tag{5.22}$$

$$\tilde{p}_{c,D_2} = a_{c,D}(\vartheta_{j,D}) \cdot i_{D_2} + b_{c,D}(\vartheta_{j,D}) \cdot i_{D_2}^2 \tag{5.23}$$

using $a_{c,T}(\vartheta_{j,T}), b_{c,T}(\vartheta_{j,T})$ and $a_{c,D}(\vartheta_{j,D}), b_{c,D}(\vartheta_{j,D})$ as junction temperature-dependent fitting coefficients.

The conduction losses of each device are only present during their conduction phases which depend on the used modulation method. These conduction phases can be described by their relative turn-on times [151]

$$\beta_{T_1} = \beta_U(\varphi) \tag{5.24}$$

$$\beta_{D_2} = 1 - \beta_U(\varphi) \tag{5.25}$$

for T_1 and D_2, which are directly related to the applied modulation function. The sine modulation with zero offset can be approximated by adding third-order harmonics to the standard sine modulation [156]. This leads to

$$\beta_{T_1} = \frac{1}{2} + \frac{M_1}{2}\cos(\varphi) + \frac{M_3}{2}\cos(3\varphi) \tag{5.26}$$

$$\beta_{D_2} = \frac{1}{2} - \frac{M_1}{2}\cos(\varphi) - \frac{M_3}{2}\cos(3\varphi) \tag{5.27}$$

with M_1 and M_3 as the corresponding modulation indexes. The modulation index M_1 is defined as

$$M_1 = \frac{\sqrt{u_d^2 + u_q^2}}{u_{DC}/2}, \tag{5.28}$$

with $\sqrt{u_d^2 + u_q^2}$ describing the amplitude of the applied voltage vector. For the proposed sine modulation, $M_1 \in [0, \frac{2}{\sqrt{3}}]$ holds. The ratio between the modulation indexes

$$\xi_M = \frac{M_3}{M_1} = 0.20635 \tag{5.29}$$

is applied according to [156] to obtain good approximation results of the modulation with zero offset. The output current

$$i_U = \hat{I}_N \cos(\varphi_{el} + \varphi) \tag{5.30}$$

at the inverter AC terminal is assumed to be sinusoidal without harmonics. Extending (5.30) with the modulation functions (5.26) and (5.27) leads to

$$i_{T_1} = \beta_{T_1}(\varphi)i_U(\varphi) \tag{5.31}$$
$$i_{D_2} = \beta_{D_2}(\varphi)i_U(\varphi), \tag{5.32}$$

which describe the currents through the semiconductors based on their relative turn-on times. The averaged power dissipation within one fundamental period can be calculated as integral over the instantaneous power

$$P_c = \frac{1}{2\pi} \int\limits_0^{2\pi} p_c(\tau)\mathrm{d}\tau. \tag{5.33}$$

Inserting (5.31) and (5.22) in (5.33) and (5.32) and (5.23) in (5.33) results in

$$P_{c,T_1} = \frac{1}{2\pi} \left(a_{c,T}(\vartheta_{j,T}) \int\limits_{-\frac{\pi}{2}-\varphi}^{\frac{\pi}{2}-\varphi} \beta_{T_1}(\tau)i_U(\tau)\mathrm{d}\tau + b_{c,T}(\vartheta_{j,T}) \int\limits_{-\frac{\pi}{2}-\varphi}^{\frac{\pi}{2}-\varphi} \beta_{T_1}(\tau)i_U(\tau)^2\mathrm{d}\tau \right) \tag{5.34}$$

$$P_{c,D_2} = \frac{1}{2\pi} \left(a_{c,D}(\vartheta_{j,D}) \int\limits_{-\frac{\pi}{2}-\varphi}^{\frac{\pi}{2}-\varphi} \beta_{D_2}(\tau)i_U(\tau)\mathrm{d}\tau + b_{c,D}(\vartheta_{j,D}) \int\limits_{-\frac{\pi}{2}-\varphi}^{\frac{\pi}{2}-\varphi} \beta_{D_2}(\tau)i_U(\tau)^2\mathrm{d}\tau \right). \tag{5.35}$$

Because the semiconductor pair T_1 and D_2 are only conducting during the positive half-wave of the terminal current i_U, the integration limits are defined within the interval $-\frac{\pi}{2} - \varphi \leq \tau \leq \frac{\pi}{2} - \varphi$. Solving the integrals finally leads to the conduction losses for the IGBT

$$P_{c,T_1} = \frac{a_{c,T}(\vartheta_{j,T})\hat{I}_N}{2} \left(\frac{1}{\pi} + \frac{M_1}{4}\cos(\varphi) \right) + b_{c,T}(\vartheta_{j,T})\hat{I}_N^2 \left(\frac{1}{8} + \frac{M_1}{3\pi}\cos(\varphi) + \frac{M_3}{15\pi}\cos(3\varphi) \right) \tag{5.36}$$

and similarly for the diode

$$P_{c,D_2} = \frac{a_{c,D}(\vartheta_{j,D})\hat{I}_N}{2} \left(\frac{1}{\pi} - \frac{M_1}{4}\cos(\varphi) \right) + b_{c,D}(\vartheta_{j,D})\hat{I}_N^2 \left(\frac{1}{8} - \frac{M_1}{3\pi}\cos(\varphi) - \frac{M_3}{15\pi}\cos(3\varphi) \right). \tag{5.37}$$

The phase shift between the voltage and the current vector can be calculated with

$$\cos(\varphi) = \frac{i_d u_d + i_q u_q}{\sqrt{i_d^2 + i_q^2}\sqrt{u_d^2 + u_q^2}} \tag{5.38}$$

using the known *dq* currents and voltages.

Switching Losses

The calculation of the switching losses is carried out similarly to the conduction losses on the IGBT and diode pair T_1, D_2 from Figure 5.17. The switching losses of the IGBT occur during switch-on and switch-off due to the transition from the blocking to the conducting state and vice versa. For the diode, the switching losses are mainly related to the reverse recovery effect during the transition from the on-state to the off-state. The energies for one switching event are given in the corresponding semiconductor
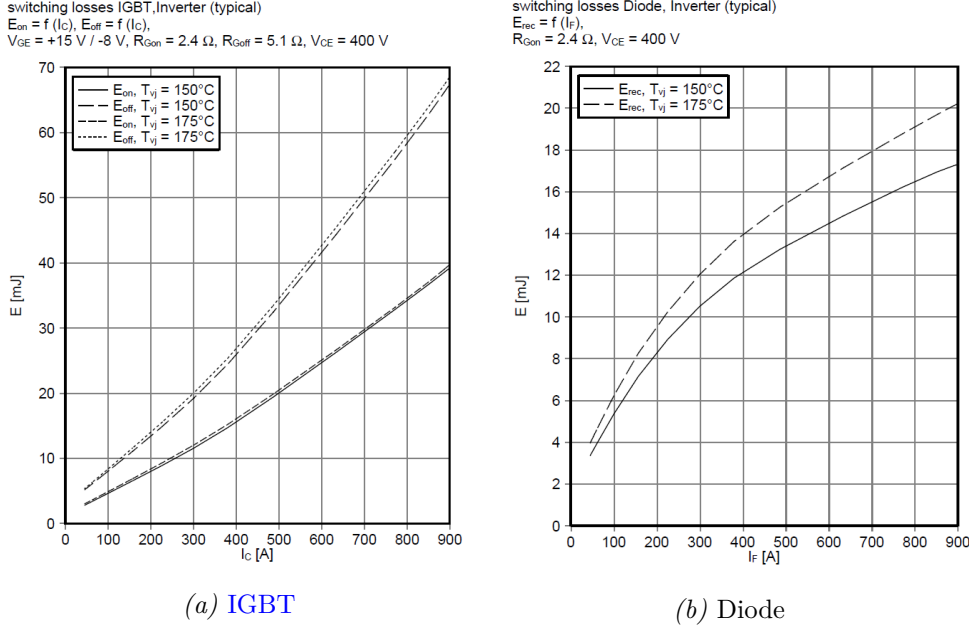
(a) IGBT

(b) Diode

Figure 5.19: Switching energies in dependency of the load current of the used IGBT module [153]

datasheet, as outlined in Figure 5.19, for the used module. In [151, 155–157], a linear dependency of the switching energy on the current in the form

$$w_{sw,lin} = k_{sw,T,D} \cdot i_U(\varphi) \tag{5.39}$$

is assumed. However, as seen in Figure 5.19, the switching losses neither for the IGBT nor the diode behave linearly. Therefore, the switching loss behavior is modeled with a second-order polynomial in the form

$$\tilde{w}_{Eon,T_1} = a_{Eon} \cdot i_U + b_{Eon} \cdot i_U^2 + c_{Eon} \tag{5.40}$$

$$\tilde{w}_{Eoff,T_1} = a_{Eoff} \cdot i_U + b_{Eoff} \cdot i_U^2 + c_{Eoff} \tag{5.41}$$

$$\tilde{w}_{Err,D_2} = a_{Err} \cdot i_U + b_{Err} \cdot i_U^2 + c_{Err} \tag{5.42}$$

for the turn-on and turn-off energy losses $\tilde{w}_{Eon,T_1}(i_U), \tilde{w}_{Eoff,T_1}(i_U)$ of the IGBTs and for the reverse recovery losses $\tilde{w}_{Err,D_2}(i_U)$ of the diodes. For the used sine modulation each semiconductor is switched on and off one time during one fundamental wave period. Thus, a linear dependency of the switching frequency f_s on the switching power losses

$$\tilde{p}_{Eon,T_1} = \tilde{w}_{Eon,T_1}(\varphi) \cdot f_s \tag{5.43}$$

$$\tilde{p}_{Eoff,T_1} = \tilde{w}_{Eoff,T_1}(\varphi) \cdot f_s \tag{5.44}$$

$$\tilde{p}_{Err,D_2} = \tilde{w}_{Err,D_2}(\varphi) \cdot f_s \tag{5.45}$$

exists. Averaging the switching losses over one fundamental wave period with

$$P_{Eon,T_1} = \frac{1}{2\pi} \int_{-\frac{\pi}{2}-\varphi}^{\frac{\pi}{2}-\varphi} \tilde{p}_{Eon,T_1}(\tau) \mathrm{d}\tau \tag{5.46}$$

$$P_{Eoff,T_1} = \frac{1}{2\pi} \int_{-\frac{\pi}{2}-\varphi}^{\frac{\pi}{2}-\varphi} \tilde{p}_{Eoff,T_1}(\tau) \mathrm{d}\tau \tag{5.47}$$

$$P_{Err,D_2} = \frac{1}{2\pi} \int_{-\frac{\pi}{2}-\varphi}^{\frac{\pi}{2}-\varphi} \tilde{p}_{Err,D_2}(\tau) \mathrm{d}\tau \tag{5.48}$$

leads to the global switching losses

$$P_{Eon,T_1} = f_s \left(\frac{c_{Eon}}{2} + \frac{a_{Eon}\hat{I}_N}{\pi} + \frac{b_{Eon}\hat{I}_N^2}{4} \right) \tag{5.49}$$

$$P_{Eoff,T_1} = f_s \left(\frac{c_{Eoff}}{2} + \frac{a_{Eoff}\hat{I}_N}{\pi} + \frac{b_{Eoff}\hat{I}_N^2}{4} \right) \tag{5.50}$$

$$P_{Err,D_2} = f_s \left(\frac{c_{Err}}{2} + \frac{a_{Err}\hat{I}_N}{\pi} + \frac{b_{Err}\hat{I}_N^2}{4} \right). \tag{5.51}$$

In addition to the polynomial fit, also the temperature dependency of the switching losses is considered with the temperature coefficients α_T for the IGBT and α_D for the diode. Furthermore, the switching losses in the datasheet are only given for a specific working point. Particularly, the nonlinear dependency on the blocking voltage [158] needs to be considered. Expanding (5.49) to (5.51) with the aforementioned dependencies leads to

$$P_{Eon,T_1} = f_s \left(\frac{u_{DC}}{u_{ref,T}} \right)^{\kappa_T} \left(1 + \alpha_T(\vartheta_{j,T} - \vartheta_{ref,T}) \right) \left(\frac{c_{Eon}}{2} + \frac{a_{Eon}\hat{I}_N}{\pi} + \frac{b_{Eon}\hat{I}_N^2}{4} \right) \tag{5.52}$$

$$P_{Eoff,T_1} = f_s \left(\frac{u_{DC}}{u_{ref,T}} \right)^{\kappa_T} \left(1 + \alpha_T(\vartheta_{j,T} - \vartheta_{ref,T}) \right) \left(\frac{c_{Eoff}}{2} + \frac{a_{Eoff}\hat{I}_N}{\pi} + \frac{b_{Eoff}\hat{I}_N^2}{4} \right) \tag{5.53}$$

$$P_{Err,D_2} = f_s \left(\frac{u_{DC}}{u_{ref,D}} \right)^{\kappa_D} \left(1 + \alpha_D(\vartheta_{j,D} - \vartheta_{ref,D}) \right) \left(\frac{c_{Err}}{2} + \frac{a_{Err}\hat{I}_N}{\pi} + \frac{b_{Err}\hat{I}_N^2}{4} \right) \tag{5.54}$$

with κ_T and κ_D as nonlinear blocking voltage dependency exponent. $U_{ref,T}$ and $U_{ref,D}$ describe the voltage of the specific blocking voltage working point given in the datasheet on which the switching losses for the IGBT and the diode are measured.

According to the introduced switching and conduction losses, the total losses of the inverter can be calculated with

$$P_{inv} = 6 \left(P_{c,T_1} + P_{c,D_2} + P_{Eon,T_1} + P_{Eoff,T_1} + P_{Err,D_2} \right) \tag{5.55}$$

by adding the individual losses and multiplying them by the number of semiconductors involved.

Thermal Model

The thermal behavior of the used inverter module is mainly defined by the thermal paths between the cooling water and the IGBTs and the diodes. These thermal paths can be divided into one thermal resistance $R_{th_{jw},T}$ between the cooling circuit and one IGBT and one thermal resistance $R_{th_{jw},D}$ between the coolant and one diode. Because the thermal paths of the semiconductors are equal for each IGBT and diode, the model can be simplified. This leads to the equivalent circuit model shown in Figure 5.20. $R_{th_{jw},T}/6$ and $R_{th_{jw},D}/6$ combine all parallel paths of the IGBTs and of the diodes to one thermal
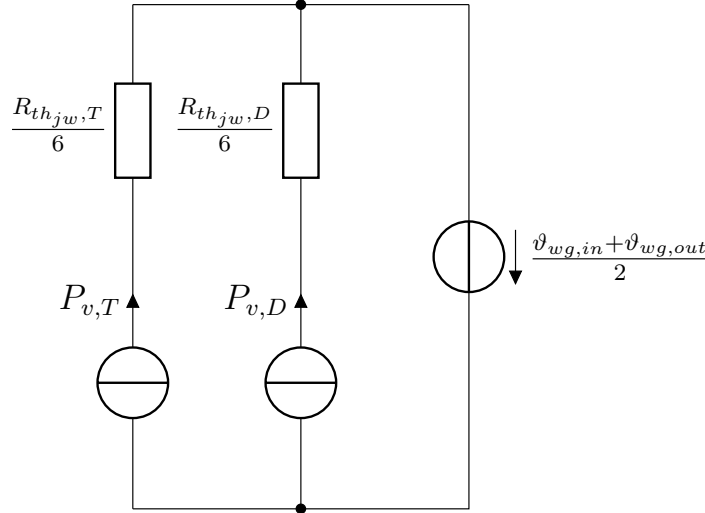
Figure 5.20: IGBT thermal equivalent circuit model

resistance. This is valid because of the symmetric load distribution among each semiconductor device. Therefore, also the thermal losses of each semiconductor are distributed equally. The main advantage of an equivalent circuit diagram model of the thermal behavior is the ease of parameterization of the models [159]. For the module used in the inverter, the thermal resistances are directly given in the datasheet [153]. Using the proposed model, the junction temperatures of the semiconductors $\vartheta_{j,T}$ and $\vartheta_{j,D}$ can be calculated with

$$\vartheta_{j,T} = P_{v,T}\frac{R_{th_{jw},T}}{6} + \vartheta_{wg} \tag{5.56}$$

for the IGBTs and with

$$\vartheta_{j,D} = P_{v,D}\frac{R_{th_{jw},D}}{6} + \vartheta_{wg} \tag{5.57}$$

for the diodes, where ϑ_{wg} denotes the temperature of the coolant.

The relationship between the heat flow $\dot{Q}$ and the corresponding coolant temperature of the inlet ϑ_{in} and the outlet ϑ_{out} can, in general, be calculated with

$$\dot{Q} = \dot{m}c_p(\vartheta_{wg})(\vartheta_{out} - \vartheta_{in}) \tag{5.58}$$

assuming channel flow [160], where $\dot{m}$ denotes the mass flow of the used coolant. Applying (5.58) to the equivalent circuit in Figure 5.20 results in

$$P_{v,T} + P_{v,D} = \rho_{wg}(\vartheta_{wg})\dot{V}_{wg}c_{p,wg}(\vartheta_{wg})(\vartheta_{out} - \vartheta_{in}) \tag{5.59}$$

as the relationship between the power dissipations $P_{v,T}, P_{v,D}$ of the module and the water temperatures $\vartheta_{out}, \vartheta_{in}$ at a given flow rate $\dot{V}_{wg}$ of the coolant. Also, the temperature dependency of the coolant density ρ_{wg} and the specific heat capacity $c_{p,wg}$ from the coolant temperature ϑ_{wg} is considered. Due to the minor temperature increase expected between the inlet and outlet temperature, the coolant temperature is assumed as

$$\vartheta_{wg} = \frac{\vartheta_{wg,in} + \vartheta_{wg,out}}{2}. \tag{5.60}$$

Model Validation

As the proposed models are mean value fundamental wave models, there are some restrictions regarding their validity. They are only accurate with respect to the following conditions [158]:

- Neglection of IGBT and diode switching times

- Assumption of constant junction temperatures over time. This is valid for
  $\omega_{el} \geq 50\,\mathrm{Hz}$

- Neglection of switching frequency ripple in alternating current (sinusoidal current)

- Switching frequency is significantly higher than the fundamental wave frequency

All the above points hold for the use case of a drive system of an electric vehicle. Nevertheless, the assumption of constant junction temperatures is only valid above a certain vehicle speed v_{min} where the condition $\omega_{el} \geq 50\,\mathrm{Hz}$ is satisfied. The minimum vehicle speed can be calculated by

$$v_{min} = \frac{r_w 50\,\mathrm{Hz}}{p i_g}, \tag{5.61}$$

with the wheel radius r_w, the pole pairs p of the electrical drive and the corresponding gearbox ratio i_g. For the vehicle under investigation, this leads to a minimum speed of $5.37\,\mathrm{km/h}$. However, this error is suitable because the major part of the vehicle speed lies above this boundary in a typical application.

The validation of the proposed inverter model is done using Drive Testbench 1 (DTB1). An overview of the test bench can be found in Appendix A.2.1. The model is evaluated regarding its accuracy in terms of efficiency. Accordingly, the efficiency of the inverter is measured and compared to the efficiency of the inverter model for the same static working points. They depend on the torque of the electrical drive M_{em}, the angular velocity of the drive ω_m and the coolant inlet temperature $\vartheta_{wg,in}$ of the inverter.

The measured efficiency of the inverter is outlined in Figure 5.21 and the simulated efficiency is depicted in Figure 5.22. To better evaluate the accuracy of the simulation model, the absolute difference

$$\varepsilon_{\eta_{inv}} = \eta_{inv,m} - \eta_{inv,s} \tag{5.62}$$

with $\eta_{inv,m}$ as the measured and $\eta_{inv,s}$ as the simulated efficiency is shown in Figure 5.23 and serves as an absolute error measurement.

The measured and simulated inverter efficiencies for different coolant inlet temperatures outline a slight dependence on the coolant inlet temperature. Furthermore, it can be seen that the efficiency of the inverter, except for low vehicle speeds, lies above $87\,\%$. The absolute model error highlights that in a wide operational area, the absolute error lies below $3\,\%$. The error grows in the area of small velocities and, in general, for small power conversions of the inverter. However, due to the measurement uncertainties of the power analyzer, which are more considerable in the low power areas of the map, it cannot be distinguished if the growing errors are caused by the measurement uncertainties or due to modeling issues. Further details of the used measurement system and the associated measurement errors can be found in

Appendix A.2.3. Nevertheless, it can be concluded that the proposed inverter model is suitable for the sensitivity analyses due to its low absolute error throughout the entire working space of the inverter.
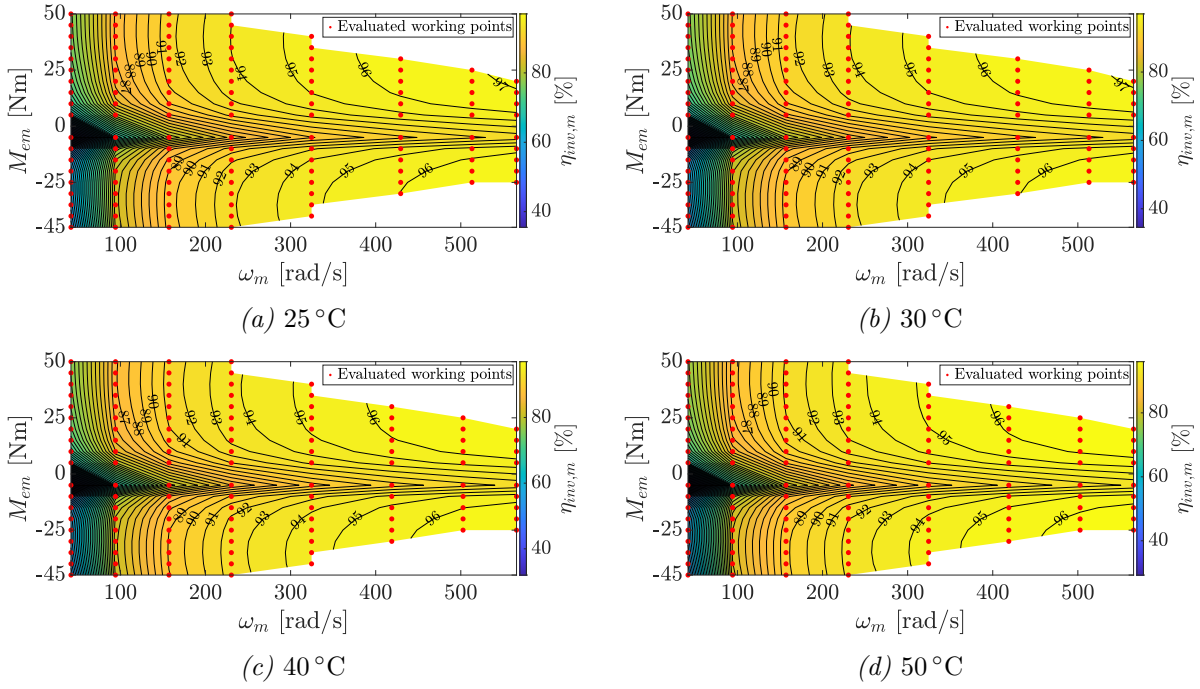
Figure 5.21: Measured inverter efficiency for different coolant inlet temperatures $\vartheta_{wg,in}$.
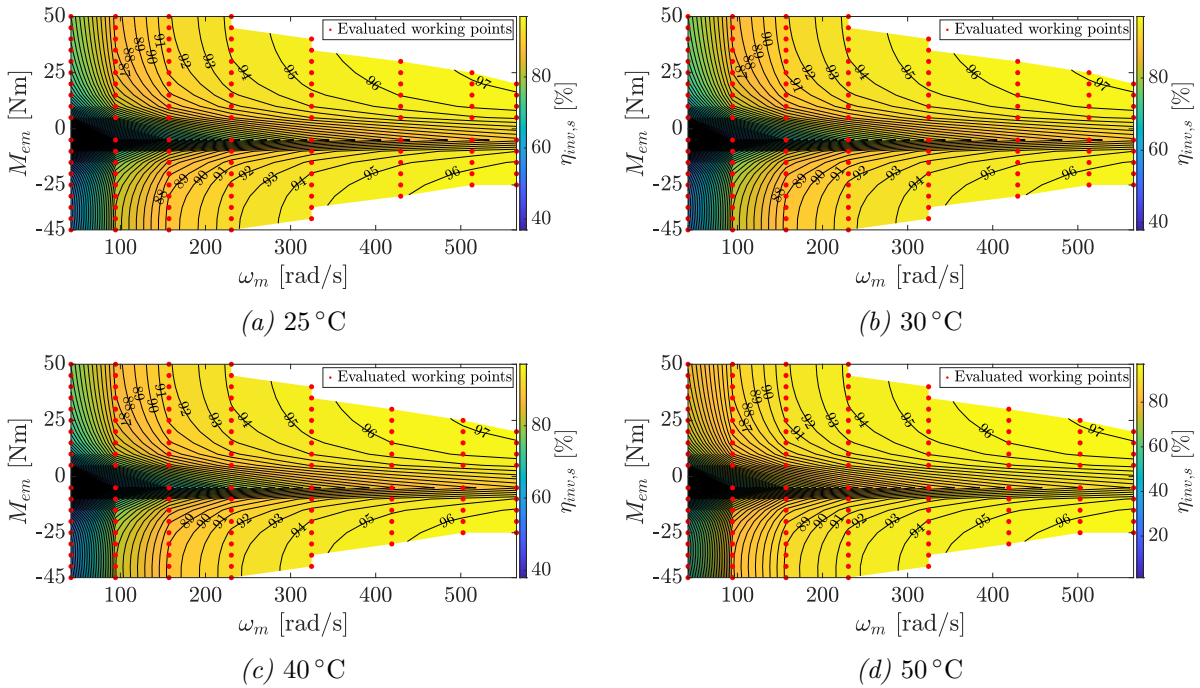
Figure 5.22: Simulated inverter efficiency for different coolant inlet temperatures $\vartheta_{wg,in}$.
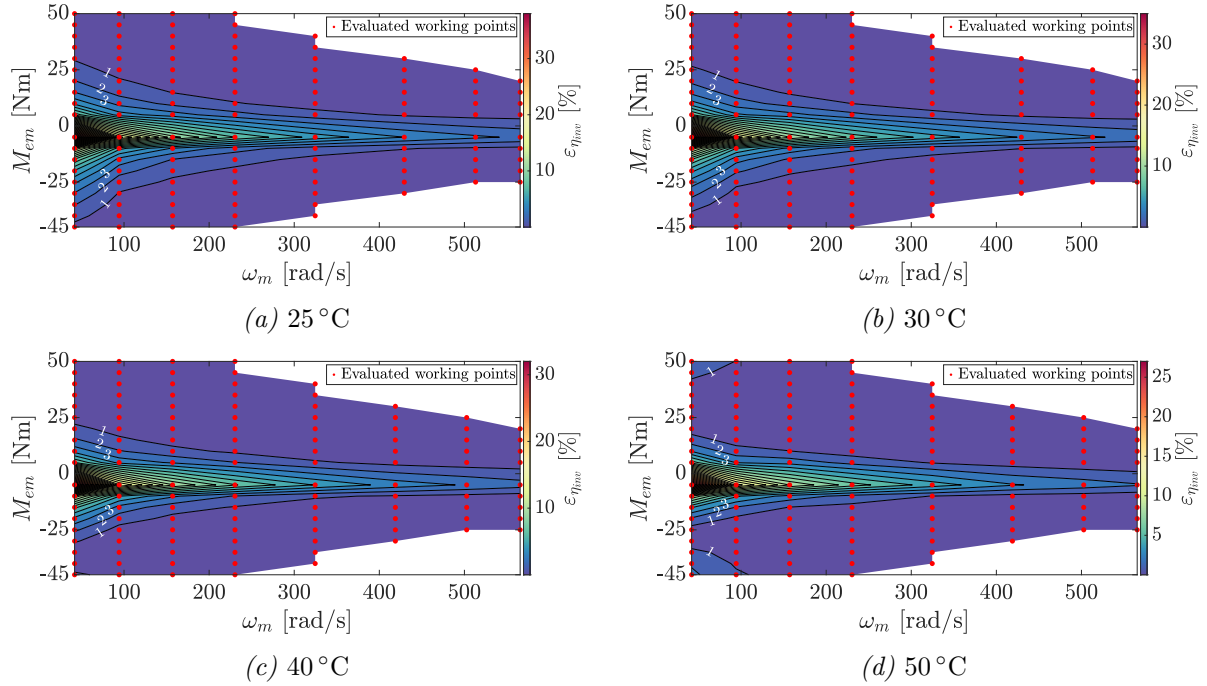
Figure 5.23: Inverter efficiency model deviation for different coolant inlet temperatures $\vartheta_{wg,in}$.

5.1.4 Electrical Drive Model

The following section presents the modeling and validation of the electrical drive. The electric drives used in the vehicle are EMRAX 188 axial flux PMSMs. A common practice of modeling these three-phase machines is the approach of using a fundamental wave model [152, 161, 162]. However, the operation with a VSI causes current harmonics inside the electric drive. Furthermore, the resulting magnetic field in the air gap is, due to constructive reasons, usually not a pure sinusoidal field [163]. Thus, additional nonlinear iron losses will occur and reduce the accuracy of a simple fundamental wave model. Consequently, several approaches were presented in the literature to include nonlinear losses into the fundamental wave model to improve the accuracy [161, 163–165]. Furthermore, the iron saturation in the magnetic paths needs to be considered, resulting in a current or working point dependency of the inductances and the magnetic flux of the drive [161, 162]. The presented models are also optimized regarding computation time for the use in the sensitivity analyses.

For a better understanding of the used model, the evolution from a basic linear fundamental wave model to a calculation time-optimized nonlinear model, including iron losses, is presented and discussed below. Furthermore, the validation of the identified drive parameters is presented in this section.

Reduced to the principal electrical effects, a PMSM can be modeled as a machine consisting of three concentrated stator windings and a permanent magnet located at the rotor. Figure 5.24 shows the equivalent stator circuit.
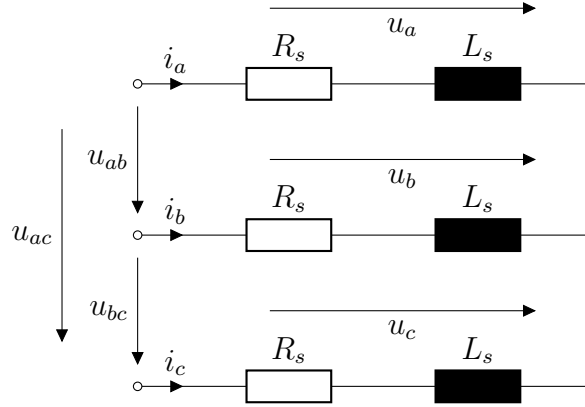
Figure 5.24: Equivalent stator circuit

The law of inductance [166]

$$u_i = -\frac{\mathrm{d}\Psi}{\mathrm{d}t} \tag{5.63}$$

indicates that each change of magnetic flux Ψ in the stator windings results in an induced voltage in the opposite direction. Based on this fundamental law, the stator voltage equation for a three-phase machine can be described by [161, 162, 167]

$$u_a = R_s i_a + \frac{\mathrm{d}\Psi_a}{\mathrm{d}t} \tag{5.64}$$

$$u_b = R_s i_b + \frac{\mathrm{d}\Psi_b}{\mathrm{d}t} \tag{5.65}$$

$$u_c = R_s i_c + \frac{\mathrm{d}\Psi_c}{\mathrm{d}t} \tag{5.66}$$

In addition, due to the star connection of the three stator phases,

$$i_a + i_b + i_c = 0 \tag{5.67}$$

holds. The non-orthogonality of the three stator windings is difficult to model and control. Therefore, it is common in the literature to convert the three-phase system into a rotating stator fixed orthogonal two-phase system with the corresponding coordinates d and q [13, 152, 157, 167, 168]. This amplitude invariant transformation, known as Park transformation and first introduced in [169], given by

$$\begin{bmatrix} x_d \\ x_q \\ x_0 \end{bmatrix} = \frac{2}{3} \begin{bmatrix} \cos(\varphi_{el}) & \cos(\varphi_{el} - \frac{2\pi}{3}) & \cos(\varphi_{el} - \frac{4\pi}{3}) \\ -\sin(\varphi_{el}) & -\sin(\varphi_{el} - \frac{2\pi}{3}) & -\sin(\varphi_{el} - \frac{4\pi}{3}) \\ 1/2 & 1/2 & 1/2 \end{bmatrix} \begin{bmatrix} x_a \\ x_b \\ x_c \end{bmatrix}, \tag{5.68}$$

describes the conversion from the string values x_a, x_b, x_c to the direct and quadrature values x_d, x_q. The transformation depends on the electrical rotor angle

$$\varphi_{el} = p \cdot \varphi_m, \tag{5.69}$$

which is a multiple of the mechanical rotor angle φ_m for drives with more than one pole pair p. The transformation can be simplified if it can be assumed that the three-phase system is symmetric. The

condition for symmetry of the system is outlined in (5.67). Thus, (5.68) simplifies to

$$
\begin{bmatrix} x_d \\ x_q \end{bmatrix} = \frac{2}{3} \begin{bmatrix} \cos(\varphi_{el}) & \cos(\varphi_{el} - \frac{2\pi}{3}) & \cos(\varphi_{el} - \frac{4\pi}{3}) \\ -\sin(\varphi_{el}) & -\sin(\varphi_{el} - \frac{2\pi}{3}) & -\sin(\varphi_{el} - \frac{4\pi}{3}) \end{bmatrix} \begin{bmatrix} x_a \\ x_b \\ x_c \end{bmatrix}, \tag{5.70}
$$

neglecting the x_0 component.

The corresponding inverse transformation from the rotor-based orthogonal system to the stator-based three-phase system is described by

$$
\begin{bmatrix} x_a \\ x_b \\ x_c \end{bmatrix} = \begin{bmatrix} \cos(\varphi_{el}) & -\sin(\varphi_{el}) \\ \cos(\varphi_{el} - \frac{2\pi}{3}) & -\sin(\varphi_{el} - \frac{2\pi}{3}) \\ \cos(\varphi_{el} - \frac{4\pi}{3}) & -\sin(\varphi_{el} - \frac{4\pi}{3}) \end{bmatrix} \begin{bmatrix} x_d \\ x_q \end{bmatrix}. \tag{5.71}
$$

Applying the Park transformation to (5.64), (5.65) and (5.66) results in

$$
u_d = R_s i_d + \frac{\mathrm{d}\Psi_d}{\mathrm{d}t} - \omega_{el}\Psi_q \tag{5.72}
$$

$$
u_q = R_s i_q + \frac{\mathrm{d}\Psi_q}{\mathrm{d}t} + \omega_{el}\Psi_d \tag{5.73}
$$

in *dq*-coordinates with

$$
\Psi_d = \Psi_{pm} + L_d i_d \tag{5.74}
$$

$$
\Psi_q = L_q i_q, \tag{5.75}
$$

where Ψ_{pm} describes the magnetic flux of the permanent magnet and L_d and L_q denote the direct and quadrature inductance. As outlined in the equations above, the induced voltage is based on two physical effects. The first effect is the change of the magnetic flux in the corresponding rotor inductances L_d and L_q. The second effect is caused by the rotation of the rotor

$$
\omega_{el} = \frac{\mathrm{d}\varphi_{el}}{\mathrm{d}t} \tag{5.76}
$$

and, as a result, a change in the magnetic flux in the stator windings during this rotation. Substituting (5.74) and (5.75) into (5.72) and (5.73) leads to the voltage equations

$$
u_d = R_s i_d + L_d \frac{\mathrm{d}i_d}{\mathrm{d}t} - \omega_{el}L_q i_q \tag{5.77}
$$

$$
u_q = R_s i_q + L_q \frac{\mathrm{d}i_q}{\mathrm{d}t} + \omega_{el}(L_d i_d + \Psi_{pm}), \tag{5.78}
$$

which can be expressed as equivalent circuits for each coordinate as outlined in Figure 5.25. The corresponding space vector diagram in Figure 5.26 outlines the relations between the electric and magnetic quantities in the different coordinate systems. Moreover, the angular relationships between the electric quantities in the different coordinate systems are displayed. The magnitude of the induced voltage in the
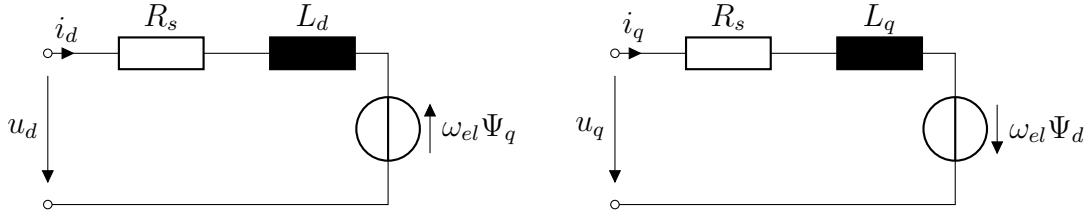
Figure 5.25: Linear PMSM equivalent circuits
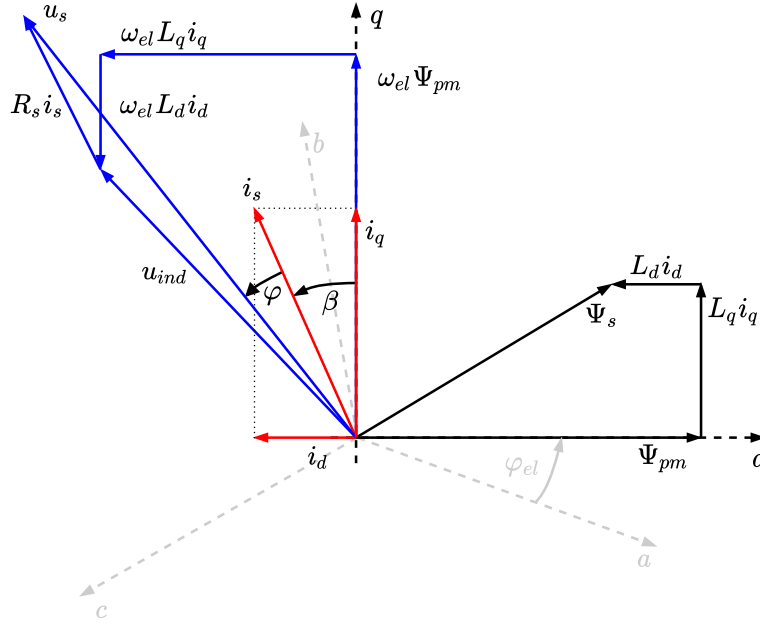
Figure 5.26: Space vector diagram for motor mode in *dq*-coordinates. blue vectors denotes the voltages and red vectors the currents. Black vectors outlined magnetic fluxes.

stator windings u_{ind}, caused by the rotation of the magnetic field, is defined by

$$u_{ind} = |\omega_{el} \sqrt{\Psi_d^2 + \Psi_q^2}|. \tag{5.79}$$

The cosine of the angle φ between the stator current i_s and the stator voltage u_s

$$\cos(\varphi) = \frac{P}{S} = \frac{i_d u_d + i_q u_q}{\sqrt{i_d^2 + i_q^2}\sqrt{u_d^2 + u_q^2}} \tag{5.80}$$

is the effective power factor and describes the percentage amount of electrical energy that is converted in the system.

The generated torque in the air gap of the electrical machine is given by [152, 161, 162]

$$M_{air} = \frac{3}{2}p(\underbrace{\Psi_{pm}i_q}_{\text{Linear part}} + \underbrace{(L_d - L_q)i_d i_q}_{\text{Reluctance part}}). \tag{5.81}$$

It indicates that the torque is composed of a linear part and a reluctance part. With the linear part, the torque can be directly controlled using i_q. For symmetric machine constructions ($L_d = L_q$), the reluctance

part will be zero. However, if the machine is constructed asymmetrically ($L_d < L_q$), a negative current i_d results in an additional torque that achieves higher power densities of the electric drives. Furthermore, the permanent magnet flux could be less compared to symmetrically constructed drives and eddy current losses can be reduced [152]. Consequently, modern drives, particularly for automotive applications, are often constructed asymmetrically.

However, the construction of modern drives for high power densities causes the iron to saturate and behaves nonlinearly [161, 162]. To include these working point-dependent saturation effects, (5.77) and (5.78) are extended to

$$u_d = R_s i_d + \frac{\mathrm{d}L_d(i_d, i_q)i_d}{\mathrm{d}t} - \omega_{el}L_q(i_d, i_q)i_q \tag{5.82}$$

$$u_q = R_s i_q + \frac{\mathrm{d}L_q(i_d, i_q)i_q}{\mathrm{d}t} + \omega_{el}(L_d(i_d, i_q)i_d + \Psi_{pm}(i_q)). \tag{5.83}$$

The working point dependence is characterized by the dependence of L_d, L_q and Ψ_{pm} on the currents i_d and i_q. Figure 5.27 outlines these dependencies for the EMRAX 188, which were identified using the DTB1 as outlined in Appendix A.2.1). Likewise, (5.81) is extended to

(a) Direct inductance L_d *(b)* Quadrature inductance L_q

(c) Magnetic flux Ψ_{pm}
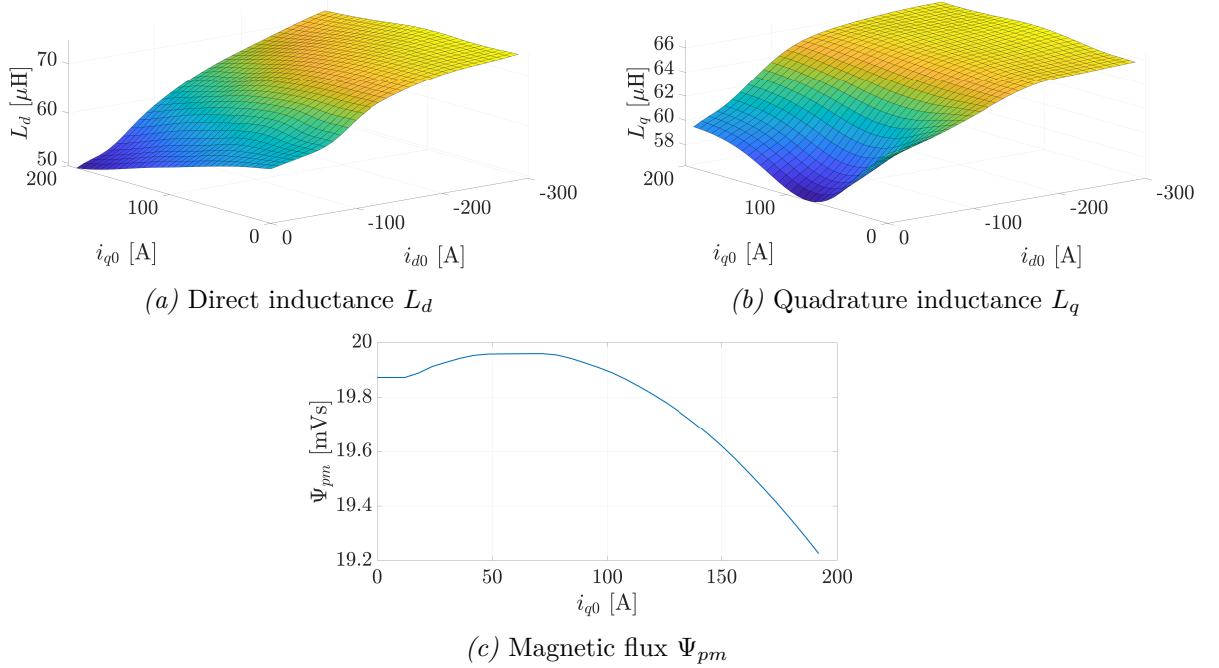
Figure 5.27: Working point-dependent drive parameters.

$$M_{air} = \frac{3}{2}p\left[\Psi_{pm}(i_q)i_q + (L_d(i_d, i_q) - L_q(i_d, i_q))i_d i_q\right] \tag{5.84}$$

to consider the saturation effects.

As the models need to be optimized regarding computation time, the drive model is not exited with a PWM modulated voltage. Instead, the averaged phase voltages are applied to the phases of the system, which result in constant *dq*-currents without harmonics. Furthermore, the time constants of the electrical circuits, consisting of the stator winding resistance R_s and the inductances L_d or L_q, are neglected and constant current working points are assumed. This is reasonable since the electrical time

constants are much smaller than the time constant of the mechanical system. Therefore, $\frac{\mathrm{d}L_d(i_d,i_q)i_d}{\mathrm{d}t} = 0$ and $\frac{\mathrm{d}L_q(i_d,i_q)i_q}{\mathrm{d}t} = 0$ hold for constant current working points and (5.82) and (5.83) simplify to

$$u_d = R_s i_d - \omega_{el} L_q(i_d, i_q) i_q \tag{5.85}$$

$$u_q = R_s i_q - \omega_{el}(L_d(i_d, i_q)i_d + \Psi_{pm}(i_q)). \tag{5.86}$$

Nevertheless, besides the ohmic losses described in the fundamental wave model, additional losses exist, which can be summarized as iron losses. They consist of eddy current losses in the conductive stator and rotor iron parts. Furthermore, hysteresis or re-magnetization losses occur in the sheet packs of the machine. They are mainly caused by the harmonics of the exiting magnetic field of the machine. The loss mechanisms of soft magnetic metals have been studied in detail in [170, 171]. Often, additional parasitic effects, such as the non-sinusoidal supply of the drive by PWM-based inverters [172], are also added to the iron losses. There exist several publications for the analytic calculation of iron losses. One common analytical approach is the Steinmetz-equation [173]

$$P_{i,v} = k f^\alpha \hat{B}^\beta \tag{5.87}$$

with f as the excitation frequency, $\hat{B}$ as the amplitude of the magnetic flux density and k, α and β as magnet material-dependent parameters. The classic Steinmetz equation is only valid for drives with sinusoidal quantities. Especially for PWM-controlled machines, also harmonics exist and the Steinmetz approach becomes less accurate. Due to the nonlinear behavior of the iron, the harmonics cannot be calculated separately using a Fourier analysis [174]. Thus, a modified Steinmetz equation [174]

$$P_{i,v} = f_r(k f^{\alpha-1} \hat{B}^\beta) \tag{5.88}$$

was postulated, using the frequency of the excitation described by f_r. Nevertheless, the excitation needs to be known. To overcome this issue, the generalized Steinmetz equation [175]

$$P_{i,v} = \frac{1}{T} \int_0^T k_1 \left| \frac{\mathrm{d}B}{\mathrm{d}t} \right|^\alpha |B(t)|^{\beta-\alpha} \mathrm{d}t \tag{5.89}$$

was presented in the literature. However, [176] claimed about the accuracy of the generalized Steinmetz equation and introduced an enhanced generalized Steinmetz equation.

Consequently, it can be noted that describing the iron losses of an electric drive analytically is still a research topic and has not finally been solved. Furthermore, the magnet material of the used EMRAX 188 machine and the internal machine geometry are unknown. Thus, the exact course of the magnetic flux density inside the machine is not known for calculating the iron losses using a Steinmetz equation approach. Therefore, in this thesis, the iron losses are not calculated analytically. Instead, two equivalent iron loss resistances are used, which will be added to the fundamental wave model and identified at the DTB1.

Estimating the iron losses with two additional resistances instead of analytically calculating them is a well-known technique in the literature [161, 163, 164, 177, 177, 178]. However, often they are modeled using the same iron-loss resistance for the d and q axis [164, 177, 178] or only for static working points [177–179]. In [163], these issues are addressed and an approach using two separate iron resistances for each axis for the static and dynamic use case is outlined. This approach is used in this thesis to model and identify the iron losses of the EMRAX 188 and is presented in advance.

Figure 5.28 outlines the equivalent circuits in *dq*-coordinates for the static use case according to [163]. ζ_d and ζ_q represent the iron losses which depend on the actual machine working point in M_{em} and ω_{el}. For
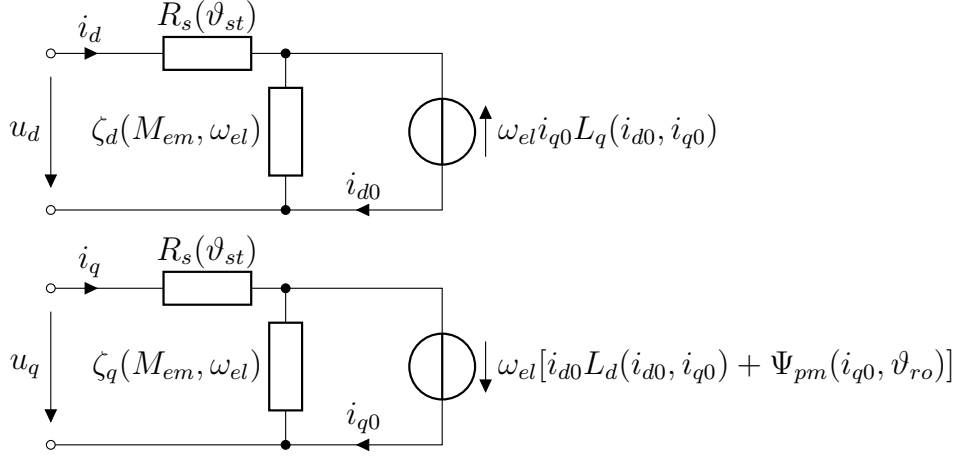
Figure 5.28: Saturation- and iron loss-dependent PMSM equivalent circuits.

a better identification procedure of the iron loss resistances, in [163] synthetic iron loss parameters

$$\xi_d = \frac{\omega_{el}^2 L_d}{\zeta_d} \tag{5.90}$$

$$\xi_q = \frac{\omega_{el}^2 L_q}{\zeta_q} \tag{5.91}$$

are introduced to neglect the dependence of ω_{el}^2 in the identification process. The voltage equations of the iron loss equivalent circuits are described by

$$u_d = (R_s + \xi_q L_d)i_d - \omega_{el}L_q i_q + \xi_q \Psi_{pm} \tag{5.92}$$
$$u_q = (R_s + \xi_d L_q)i_q + \omega_{el}L_d i_d + \omega_{el}\Psi_{pm} \tag{5.93}$$

using the synthetic iron loss parameters instead of the real iron loss resistances. For better readability the working point dependent saturation effects of L_d, L_q and Ψ_{pm} are not outlined in the equations. However, they still exist and shown in Figure 5.28. The corresponding iron loss parameters ξ_d and ξ_q are identified with

$$\xi_d = \frac{\omega_{el}^2 L_d}{\zeta_d} = \frac{u_q - \omega_{el}L_d i_d - R_s i_q - \omega_{el}\Psi_{pm}}{L_q i_q} \tag{5.94}$$

$$\xi_q = \frac{\omega_{el}^2 L_q}{\zeta_q} = \frac{u_d - R_s i_d + \omega_{el}L_q i_q}{L_d i_d + \Psi_{pm}} \tag{5.95}$$

on the DTB1. The identified iron losses for both axis are outlined in Figure 5.29. The corresponding air gap torque of the machine is also influenced by the iron losses and is extended to

$$M_{air} = \frac{3}{2}p\left[\Psi_{pm}\left(i_q - u_q\frac{\xi_q}{\omega_{el}^2 L_q}\right) + (L_d - L_q)\left(i_d - u_d\frac{\xi_d}{\omega_{el}^2 L_d}\right)\left(i_q - u_q\frac{\xi_q}{\omega_{el}^2 L_q}\right)\right]. \tag{5.96}$$

Besides the electrical properties of the drive, also the temperature dependency of the electrical drive needs to be considered. Thus, the temperature dependency of the stator resistance is modeled using

$$R_s = R_{s,\vartheta_0}[1 + \alpha_{cu}(\vartheta_{st} - \vartheta_{0,cu})] \tag{5.97}$$

with R_{s,ϑ_0} as the stator resistance at the reference temperature $\vartheta_{0,cu}$. α_{cu} denotes the temperature coefficient of copper and ϑ_{st} the actual stator temperature. The temperature dependency of the magnet

(a) Direct axis iron loss parameter ξ_d *(b)* Quadrature axis iron loss parameter ξ_q
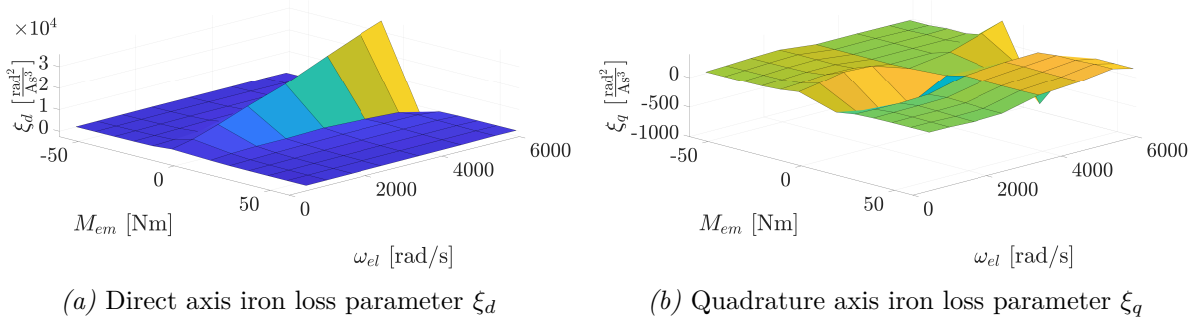
Figure 5.29: Working point-dependent iron losses.

material of the rotor is modeled similarly by

$$\Psi_{pm} = \Psi_{pm,\vartheta_0}[1 + \alpha_{pm}(\vartheta_{ro} - \vartheta_{0,pm})], \tag{5.98}$$

with Ψ_{pm,ϑ_0} as the reference magnetic flux at the reference temperature $\vartheta_{0,pm}$. The temperature coefficient of the used magnet material is denoted by α_{pm}. The power losses in the electric drive system can then be determined as ohmic losses at the winding resistances R_s and the iron loss resistances ζ_d and ζ_q.

Model Validation

The proposed drive model is validated using the DTB1 testbench (see Appendix A.2.1). The model is evaluated regarding its accuracy in terms of efficiency. Accordingly, the efficiency of the drive is measured and compared to the efficiency of the drive model for the same static working points. They depend on the torque of the electrical drive M_{em}, the angular velocity of the drive ω_m and the coolant inlet temperature $\vartheta_{wg,d}$ of the drive.

The measured efficiency of the EMRAX 188 drive is outlined in Figure 5.30 and the simulated efficiency is depicted in Figure 5.31.

To better evaluate the accuracy of the simulation model, the absolute difference

$$\varepsilon_{\eta_{em}} = \eta_{em,m} - \eta_{em,s} \tag{5.99}$$

with $\eta_{em,m}$ as the measured and $\eta_{em,s}$ as the simulated efficiency is shown in Figure 5.32 and serves as an absolute error measurement.

The measured and simulated drive efficiencies for different coolant inlet temperatures outline a slight dependence on the coolant inlet temperature. The reduced efficiency with increasing temperature is caused by the temperature dependency of the copper winding and the permanent magnet of the drive. Copper has a positive temperature coefficient which results in an increased resistance of the stator windings and thus more losses. On the other hand, the magnet material has a negative temperature coefficient which results in less magnetic excitation with increasing temperatures and thus, more current is needed for applying the same torque. But, in general, it can be noted that the drive efficiency, except for low torques, lies above 86 %. The absolute model error highlights that in a wide operational area, the absolute error lies below 3 % for all temperatures. The error grows in the area of small torques and, in general, for small power conversions of the drive. However, due to the measurement uncertainties of the power analyzer, which have more considerable influences in the low power areas of the map, it cannot be distinguished if the growing errors are caused by the measurement uncertainties or due to modeling

issues. Further details of the used measurement system and the associated measurement errors can be found in Appendix A.2.3. However, it can be concluded that the proposed models, concerning their low absolute error throughout the entire working space of the drive, are suitable for sensitivity analysis.
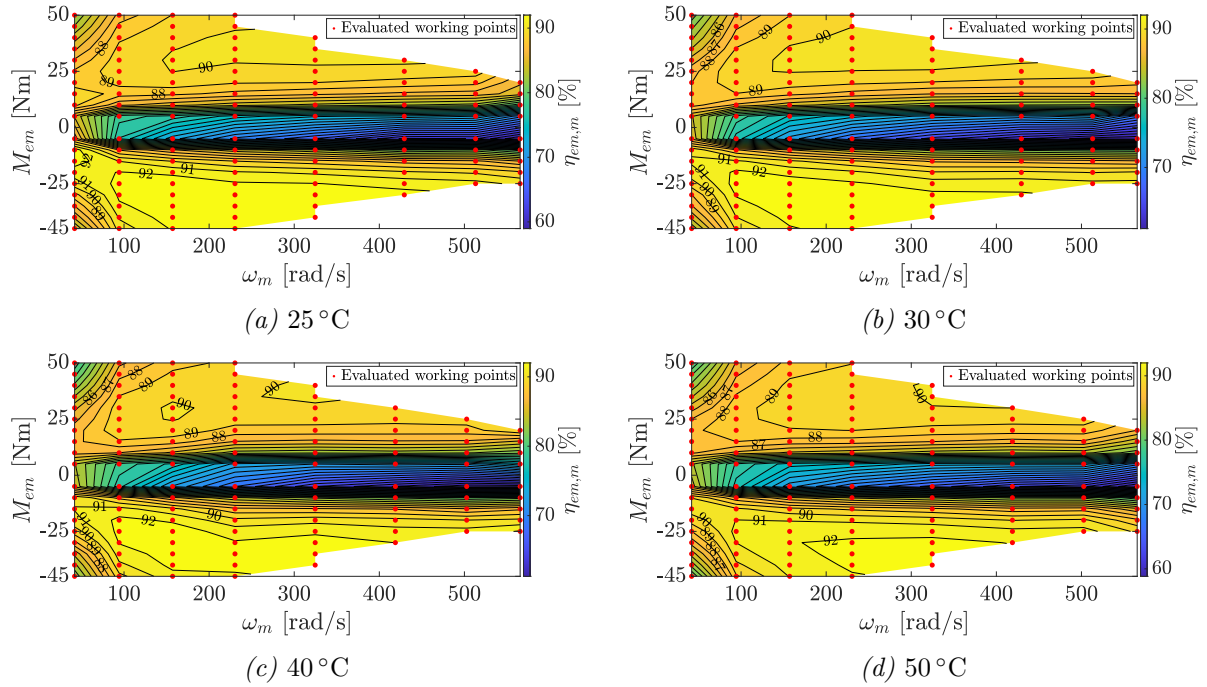
Figure 5.30: Measured drive efficiency for different coolant inlet temperatures $\vartheta_{wg,d}$.
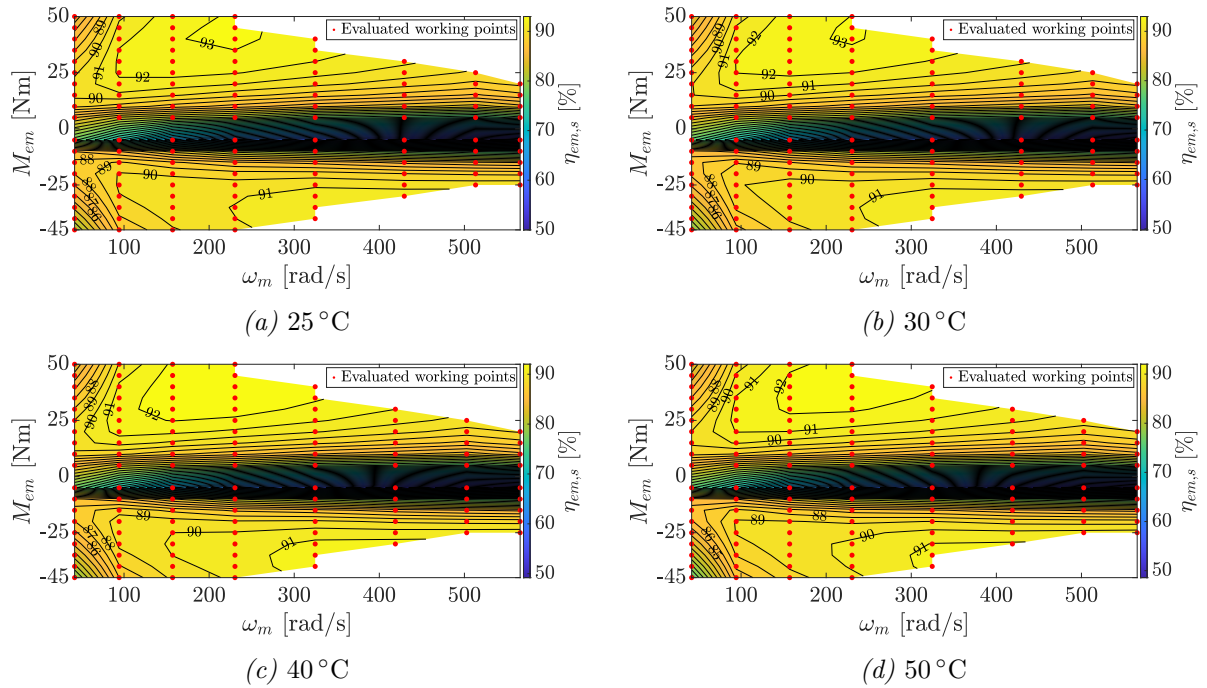
Figure 5.31: Simulated drive efficiency for different coolant inlet temperatures $\vartheta_{wg,d}$.
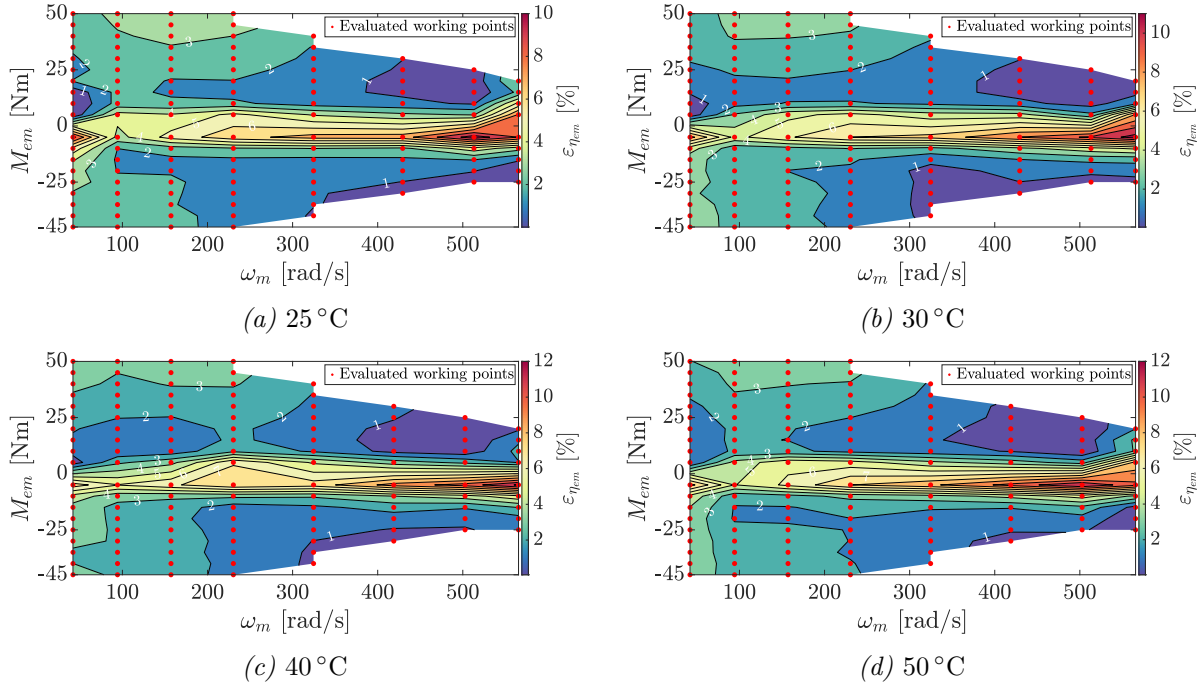
Figure 5.32: Drive efficiency model deviation for different coolant inlet temperatures $\vartheta_{wg,d}$.

5.2 Modeling of the Environment

The energy consumption of the vehicle is no fixed value and is influenced by several environmental conditions, such as the road profile, weather and traffic situation. Consequently, these environmental conditions need to be considered in the simulation model. In the literature, several environmental modeling approaches exist and will be discussed in the following. Furthermore, the used drive cycles for the use-case of the proTRon Evolution are presented. Since the investigation of this thesis does not include the surrounding traffic, it will neither be included in the environmental model nor discussed here.

To quantify the energy consumption of vehicles in the certification process and to be able to determine the corresponding taxation, standardized test cycles such as the New European Driving Cycle (NEDC) [180] were therefore introduced in the European area and the WLTP [181] as its global successor. However, for better comparability, the influencing factors of environment, driving distance and different drivers are systematically excluded in these test procedures by specifying the speed and operating conditions. To improve the validity of these driving cycles, non-binding test cycles exist based on real measured driving collectives. The most well-known European test cycles are the ARTEMIS-cycles [182, 183] and the modem-Hyzem-cycles [184]. Nevertheless, these cycles also use a fixed velocity profile and cannot consider the degree of freedom in the driving speed to optimize energy efficiency. Consequently, modeling the environment using only a drive cycle representation is unsuitable for evaluating a longitudinal model predictive control.

To avoid the drawbacks mentioned above, the proposed environmental model includes additional information about the road slope, the curvature and the legal speed limit of the driven road. A speed profile is not given in the environmental model as it will be optimized by the longitudinal control algorithm. Nevertheless, a manually driven profile is also recorded to compare the driven routes optimized by the MPC with the profile driven by a human driver.

The proposed drive cycles are intended to cover the urban and interurban use case of a typical daily commute to work around the German city Trier where the proTRon Evolution is designed for. Figures 5.33 and 5.34 outline the drive cycles on a map and depict the corresponding legal speed limits v_{max}, curve radii r_c, road slope α and the elevation h for the driven routes.

The resolution of the data, especially the elevation data, can highly affect the accuracy of the energy prediction model. Furthermore, classical Digital Elevation Model (DEM) data is roughly gridded with 30 m resolution and needs to be interpolated [10]. To avoid this inaccuracy, the road information is extracted from the HERE autonomous driving map database [185]. It provides accurate measurements of the required road information in a satisfactory resolution.

The four drive cycles are intended to cover several influences on typical commuting routes. To account for the impact of commuting distances, all selected routes are of different lengths. Furthermore, the elevation profile varies for the chosen routes. It can be seen that the elevation profile is more distinct for drive cycles 1 and 2 than for drive cycles 3 and 4 since the regions outside the river valley are low mountain ranges. Accordingly, drive cycles 1 and 2 are also curvier than drive cycles 3 and 4. The expected driving speed is also different. Drive cycles 1-3 consist only of urban and rural roads and thus, the average legal speed limits are lower than the average legal speed limit of drive cycle 4, which contains highway sections. It is important to mention that the start and endpoints of the route are at the same altitude, which avoids the insertion or extraction of potential energy on the system and thus, falsifying the results of the proposed sensitivity analysis.
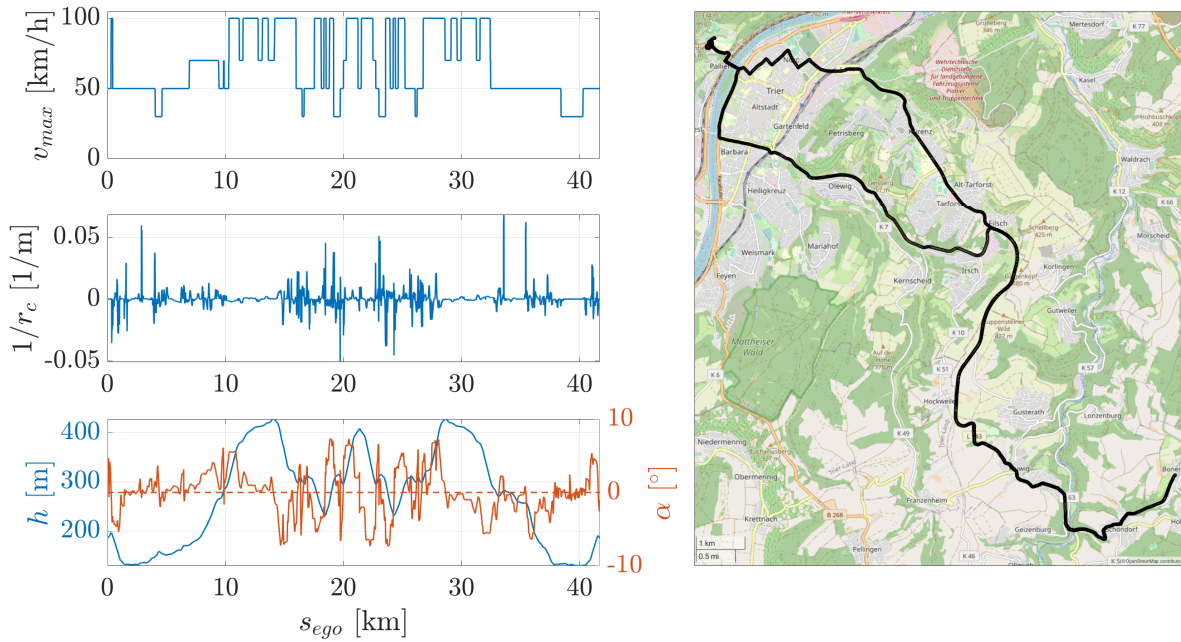
(a) Drive cycle 1
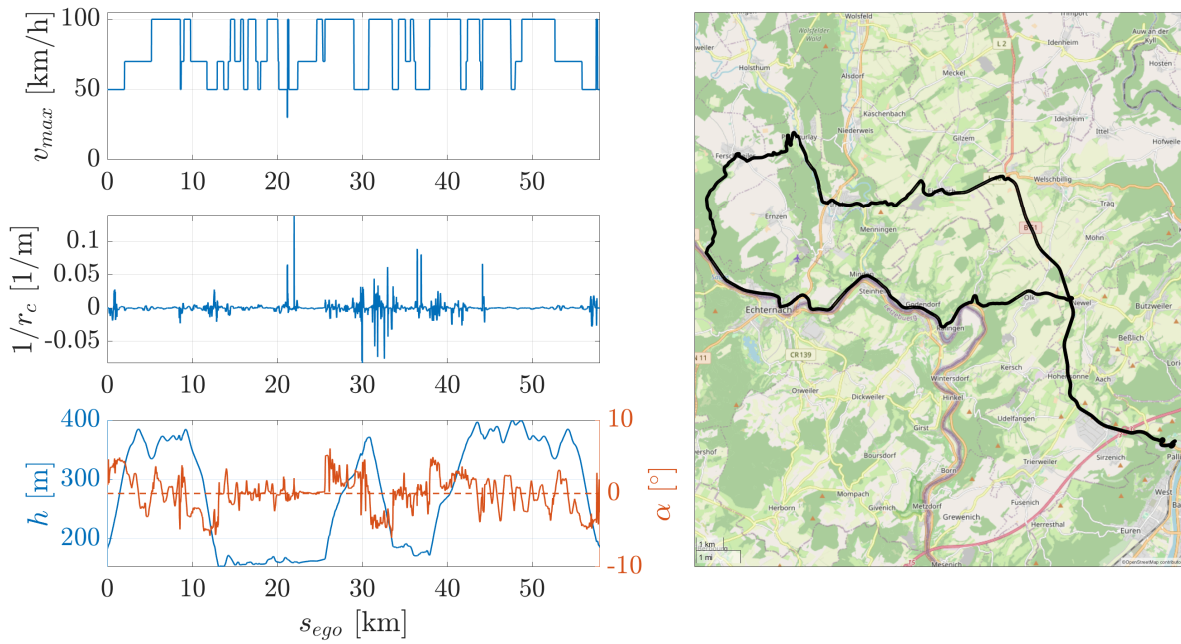
(b) Drive cycle 2

Figure 5.33: Drive cycle overview of drive cycle 1 and 2.
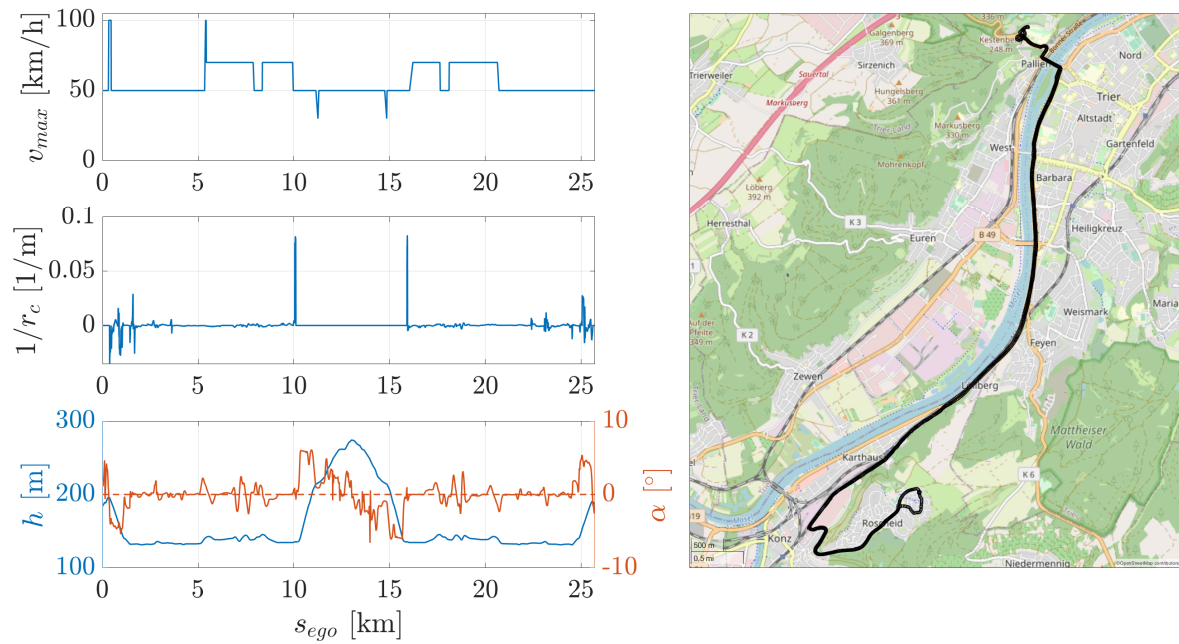
(a) Drive cycle 3
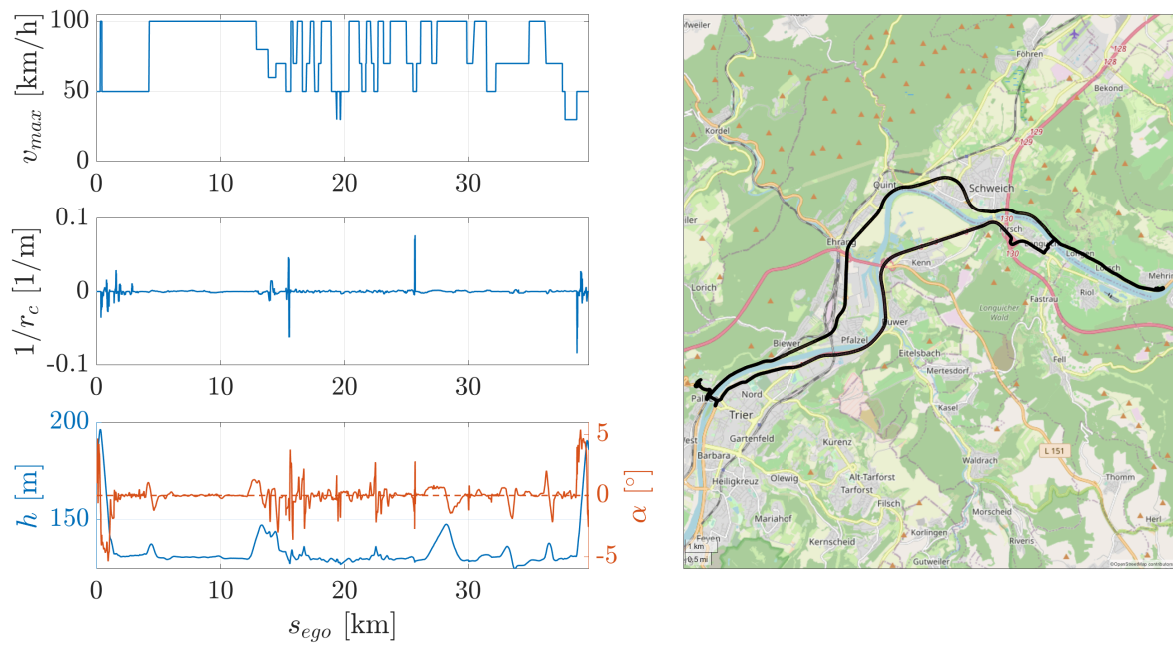
(b) Drive cycle 4

Figure 5.34: Drive cycle overview of drive cycle 3 and 4.

5.3 Conclusions

In this chapter, the modeling of the vehicle and the environment has been presented. The presented models consist of the longitudinal motion model of the vehicle and detailed models of the underlying powertrain components including gearbox, battery, inverter and electrical drive. Each model has been optimized in terms of computation time and accuracy to met the requirements of the sensitivity analyses, especially concerning power dissipation and energy efficiency. To provide accurate models, the parameter of the components has been determined on the battery and drive test benches and the accuracy of the models have been proven for each powertrain component.

To generate realistic driving scenarios also an environmental model has been presented in this chapter. It consists of the route profile, the legal speed limit and curve radii provided by the HERE database and is able to map realistic route scenarios into the simulation. To met the use-case of the proTRon Evolution, four different routes has been presented, denoted as drive cycle 1 to drive cycle 4, describing typical interurban commuter routes. Due to the high model accuracy, the proposed model is suitable for generating reliable sensitivity analysis results regarding the energy consumption and efficiency of the vehicle. Furthermore, the optimization regarding computation time will reduce the computation effort of the sensitivity analysis, as presented in Chapters 6 and 8, to a reasonable level.

6 Sensitivity Analysis of the Open-Loop Longitudinal Control

The models presented in the previous chapter consist of many parameter dependencies which could possibly influence the energy consumption of the vehicle. Developing an MPC which considers all the nonlinear and complex model dependencies will result in a complex controller design that would be difficult to solve and possibly not real-time capable. Consequently, the parameters which affecting the energy efficiency and the energy consumption of the vehicle should be known and integrated into the controller design. Thus, an open-loop sensitivity analysis is presented in this chapter to analyze the proposed vehicle model systematically and to extract the information on which parameters should be integrated into the controller design. In this open-loop setup, the vehicle model is simulated using the fixed velocity profiles on each of the four drive cycles which represents the driving behavior of a human driver as already outlined in Section 5.2.

For the sensitivity analysis at first, the PDFs for the investigated parameters need to be defined. Afterwards, a Morris screening is performed to separate influential from non-influential parameters and to determine the parameter set for the subsequent variance-based sensitivity analysis. The generalized Sobol indices are estimated and the convergence is proven and outlined using the law of big numbers and bootstrap resampling. Correspondingly, the results of the open-loop analysis are presented and the most influential parameters are discussed. At least, the influences of uncertain PDF definitions on the outputs of interest are investigated.

6.1 Definition of the Input Parameter Distributions

To analyze the parameter dependencies using a sensitivity analysis, the distributions of the input parameters, using their corresponding PDFs, need to be defined. The analyzed parameters can be divided into four categories for the open-loop sensitivity analysis: Battery, inverter, drive, and vehicle. The type of parameter uncertainty is divided into two classes: Absolute and relative errors. Absolute errors inject the new parameter value of their corresponding PDF sample directly to the parameter itself, e.g.,

$$P_{pto} \sim \mathcal{U}(a, b), \tag{6.1}$$

for the change in the power demand of the auxiliary consumers. In contrast, relative errors inject only a relative deviation of the corresponding parameters, which are denoted in the following with $e_{(.)}$ where the dot indicates the parameter that is affected relatively. The relative deviation of the battery series resistance $R_{s,b}$, for example, can be expressed by

$$e_{R_{s,b}} = (1 + \varepsilon_r)R_{s,b} \quad \text{with} \quad \varepsilon_r \sim \mathcal{N}(\mu, \sigma^2) \tag{6.2}$$

with $e_{R_{s,b}}$ describing the relative variation caused by the drawn sample value ε_r of its corresponding PDF.

The investigated parameters of the open-loop analysis are outlined in Table 6.1 and will be discussed in the following.

Table 6.1: Distributions of parameters for the open-loop sensitivity analysis.

	Name	Description	Type of error	Distribution	Parameter	Values	Units
Battery	$e_{R_s,b}$	Deviation of series resistance R_s	relative	Normal	μ, σ	0, 0.05/3	−
	e_{C_1}	Deviation of capacitance C_1	relative	Normal	μ, σ	0, 0.05/3	−
	e_{R_1}	Deviation of resistance R_1	relative	Normal	μ, σ	0, 0.05/3	−
	e_{C_2}	Deviation of capacitance C_2	relative	Normal	μ, σ	0, 0.05/3	−
	e_{R_2}	Deviation of resistance R_2	relative	Normal	μ, σ	0, 0.05/3	−
	$e_{u_{ocv}}$	Deviation of open circuit voltage	relative	Normal	μ, σ	0, 0.05/3	−
	ϑ_b	Variation of start temperature	absolute	Uniform	a, b	20, 40	°C
	$R_{th_{ca}}$	Variation of thermal resistance $R_{th_{ca}}$	absolute	Normal	μ, σ	2.6, 0.13/3	Ω
	$R_{th_{ct}}$	Variation of thermal resistance $R_{th_{ct}}$	absolute	Normal	μ, σ	0.37, 0.02/3	Ω
	$R_{th_{ta}}$	Variation of thermal resistance $R_{th_{ta}}$	absolute	Normal	μ, σ	1.05, 0.05/3	Ω
	C_c	Variation of thermal capacitance C_c	absolute	Normal	μ, σ	2544.2, 127.21/3	F
	C_t	Variation of thermal capacitance C_t	absolute	Normal	μ, σ	8.072, 3.4/3	F
Inverter	e_{a_t}	Deviation of forward characteristics IGBT	relative	Normal	μ, σ	0, 0.05/3	−
	e_{b_t}		relative	Normal	μ, σ	0, 0.05/3	−
	e_{a_d}	Deviation of forward characteristics diode	relative	Normal	μ, σ	0, 0.05/3	−
	e_{b_d}		relative	Normal	μ, σ	0, 0.05/3	−
	$e_{a_{Err}}$	Deviation of reverse recovery characteristics diode	relative	Normal	μ, σ	0, 0.05/3	−
	$e_{b_{Err}}$		relative	Normal	μ, σ	0, 0.05/3	−
	$e_{c_{Err}}$		relative	Normal	μ, σ	0, 0.05/3	−
	$e_{a_{Eon}}$	Deviation of turn on losses IGBT	relative	Normal	μ, σ	0, 0.05/3	−
	$e_{b_{Eon}}$		relative	Normal	μ, σ	0, 0.05/3	−
	$e_{c_{Eon}}$		relative	Normal	μ, σ	0, 0.05/3	−
	$e_{a_{Eoff}}$	Deviation of turn off losses IGBT	relative	Normal	μ, σ	0, 0.05/3	−
	$e_{b_{Eoff}}$		relative	Normal	μ, σ	0, 0.05/3	−
	$e_{c_{Eoff}}$		relative	Normal	μ, σ	0, 0.05/3	−
	$\vartheta_{w,in}$	Variation of water inlet temperature	absolute	Uniform	a, b	0, 60	°C
Drive	$e_{R_s,EM}$	Deviation of winding resistance R_s	relative	Normal	μ, σ	0, 0.03/3	−
	e_{L_d}	Deviation of direct inductance L_d	relative	Normal	μ, σ	0, 0.0133/3	−
	e_{L_q}	Deviation of quadrature inductance L_q	relative	Normal	μ, σ	0, 0.015/3	−
	$e_{\Psi_{pm}}$	Deviation of magnetic flux Ψ_{pm}	relative	Normal	μ, σ	0, 0.025/3	−
	e_{ξ_q}	Deviation of quadrature iron losses ξ_q	relative	Normal	μ, σ	0, 0.05/3	−
	e_{ξ_d}	Deviation of direct iron losses ξ_d	relative	Normal	μ, σ	0, 0.05/3	−
	ϑ_{ro}	Variation of rotor temperature ϑ_{ro}	absolute	Uniform	a, b	40, 80	°C
	ϑ_{st}	Variation of stator temperature ϑ_{st}	absolute	Uniform	a, b	40, 80	°C
Vehicle	m_v	Variation of the vehicle mass	absolute	Birnbaum–Saunders	β, γ	652.11, 0.074	kg
	P_{pto}	Variation of auxiliary consumers	absolute	Uniform	a, b	250, 750	W
	ϑ_a	Variation of ambient temperature	absolute	Normal	μ, σ	12.26, 8.53	°C
	p_{air}	Variation of ambient pressure	absolute	Normal	μ, σ	98427.7, 843.09	Pa
	c_r	Variation of rolling resistance	absolute	Uniform	a, b	0.01, 0.015	−

In general, all parameters which are available in the vehicle model of Chapter 5 and are influenceable due to fluctuations in the production or during operation of the vehicle are investigated in the open-loop analysis. Parameter deviations caused by physical effects such as measurement errors or production variations are assumed to be Gaussian distributed which is a legitimate assumption since physical processes whose real PDFs are unknown usually converge to a normal distribution due to the central limit theorem [186,187]. Because manufacturers of components mainly specify only the maximum errors of their products in the datasheets, these errors are treated in the PDFs as 3σ values, ensuring that 99.7 % of the samples lie inside the defined maximum error. Since the cooling circuit of the vehicle was not finally defined during this thesis, all component temperatures are treated independently. However, this opens the possibility of considering the influences of the component temperatures separately.

The battery model is examined regarding the parameters of the equivalent electric circuit model, the thermal model parameters and the battery temperature at the start of the corresponding drive cycle.

As shown in Table 6.1, all battery parameters, except the battery start temperature, are assumed to be Gaussian distributed. The 3σ values of these parameters are set to 5 % according to assumed production fluctuations of the battery. The battery start temperature depends highly on the ambient and operating conditions of the vehicle. It can be influenced, for example, by parking the vehicle outside or in a garage or by the produced waste heat while charging the battery and is assumed to be uniformly distributed.

The inverter parameters consist of the conduction and switching loss parameters of the IGBTs and the diodes, as well as the water inlet temperature of the component. Similarly, as for the battery parameters, the inverter parameters are modeled with Gaussian distributions and $3\sigma = 5$ % due to production fluctuations. The water inlet temperature depends on the cooling cycle layout and the available cooling power. However, as mentioned above, the cooling cycle was not finally defined during this thesis. Thus, the water inlet temperature distribution is assumed to be uniformly distributed, where the upper limit is defined by the maximum allowed water inlet temperature of the inverter manufacturer.

The drive parameters of the EMRAX 188 consist of the electrical equivalent circuit parameters, including iron losses and the temperatures of the stator and the rotor of the drive. A similar examination of a drive system but focusing on the torque accuracy of a PMSM has already been done in previous works [13, 81] where the distributions of the drive parameters are examined using Finite Element Method (FEM) simulations. However, as the EMRAX 188 drive used in the proTRon Evolution is a purchased part, no details regarding the used magnet material or the internal geometry of the magnetic paths are available. Thus, a detailed examination of the machine parameter dependencies as done in [13, 81] is impossible. Therefore, the proposed parameter distributions of these works are also used in this thesis to describe the electrical parameter distributions of the drive. As for the inverter, the rotor and the stator temperatures are assumed to be uniformly distributed.

Parameters that influence the longitudinal motion at the vehicle level are summarized in Table 6.1 in the vehicle section. They consist of the variation in the mass of the vehicle, the power demand of the auxiliary consumers, the ambient temperature, the ambient pressure and the rolling resistance. The vehicle mass is composed of the vehicle tare weight and the occupants in the vehicle. In [188], the occupancy rate of vehicles in Germany was investigated. This investigation is used to estimate the distribution of the vehicle mass with 550 kg tare weight and an additional weight corresponding to the occupation of the vehicle with an assumed occupant weight of 70 kg. The resulting distribution can be estimated with a Birnbaum-Saunders distribution with the parameters outlined in Table 6.1. The auxiliary power demand is not known in the actual development phase of the vehicle. But as the energy efficiency is the most important development goal of the project and the vehicle will not have many auxiliary consumers, the auxiliary power is assumed to be uniformly distributed in the interval $[250\,\mathrm{W}, 750\,\mathrm{W}]$, which is lower as, e.g., in [10]. The remaining parameters of the vehicle are affected by environmental conditions, which are mostly the influence of the weather that will cause variations in the ambient temperature ϑ_a and the air pressure p_{air}. Furthermore, it affects the rolling resistance c_r whether the road surface is dry or wet. The environmental parameters ϑ_a and p_{air} are modeled using data from the German Weather Service for one year, from 30/6/2020 to 30/6/2021 and from 6 am to 8 pm per day at the weather station Trier Petrisberg. For the temperature evaluation, data set [189] is used. It consists of temperatures measured 2 m above ground in a 10 min interval. The air pressure is evaluated using data set [190], which contains the air pressure on station height sampled in a 1 h interval. Figure 6.1 outlines the histograms for the ambient temperature and air pressure data and their Gaussian distribution fits, which are used for the sensitivity analysis. The rolling resistance distribution is defined according to [191] where it is stated that the rolling resistance increases up to 60 % when the condition changes from a dry to a wet surface. However, the exact change in the rolling resistance depends also on the tire type. To the author's best knowledge, no exact values are known for the used tires of the proTRon Evolution. Thus, a maximum increase of 50 % of the nominal rolling resistance coefficient $c_r = 0.01$ of a dry surface to $c_r = 0.015$ for a wet surface is assumed.

(a) Distribution of the ambient temperature ϑ_a *(b)* Distribution of the ambient air pressure p_{air}
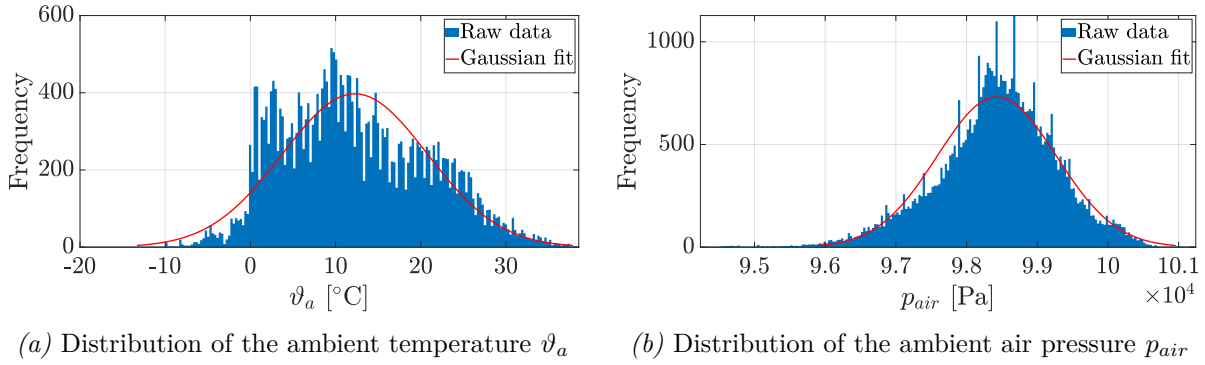
Figure 6.1: Histograms and their fit to a Gaussian distribution of the environmental parameters based on the data of the German Weather Service [189, 190].

6.2 Morris Screening

The first step in the open-loop analysis is to perform a Morris screening to distinguish important from unimportant parameters. This is necessary to reduce the number of parameters used in the variance-based sensitivity analysis to achieve reasonable computation times. The Morris screening is performed for the four drive cycles presented in Section 5.2. Since the study aims to analyze the energy consumption of the vehicle, the battery energy required in a drive cycle E_b and the power losses of the powertrain P_l are considered in the further analysis.

The parameter input space is discretized with $p = 4$ and a step size of $\Delta = 2/3$ is chosen. As recommended in [95–97], $r = 10$ trajectories are simulated. This setup leads to a total number of simulations for the Morris screening and the investigated parameters of Table 6.1 of $N_m = r(k+1) = 10(39+1) = 400$.

The results of the Morris screening for the four drive cycles regarding the consumed battery energy E_b are outlined in Figure 6.2. Similarly, the power losses of the powertrain P_l are depicted in Figure 6.3. Since the Morris screening is only a qualitative method, the absolute values of μ^* and σ are not essential. To obtain valuable information about the relation of parameters and their interactions, the relative relation between μ^* and σ is more interesting. For the consumed battery energy E_b in Figure 6.2, statement $\sigma \ll \mu^*$ holds for all parameters. It indicates a mostly linear dependency between the analyzed parameters. Thus, it can be said that the parameters with high values of μ^* affect the consumed battery energy most but probably do not interact with other parameters. In contrast, Figure 6.3 outlines that interactions between parameters of the output P_l can be assumed since $\mu^* \approx \sigma$ holds for most of the parameters.

Furthermore, Figures 6.2 and 6.3 outline that only a few of the investigated parameters have high values of μ^* and σ in relation to the other studied parameters. Consequently, only these parameters need to be considered for the open-loop variance-based sensitivity analysis and thus, an extensive parameter reduction can be performed. It needs to be mentioned that the Morris screening serves only as a qualitative rating of the parameter importance. Because of the small number of trajectories with $r = 10$ used for the screening, the ranking of the importance of parameters that are close to each other (see e.g. ϑ_a and ϑ_b in Figure 6.2c) could be differ to the quantitative variance-based sensitivity analysis. Nevertheless, many parameters can be identified as non-influential and excluded from the variance-based sensitivity analysis. The remaining parameters are outlined in Table 6.2.

(a) Drive cycle 1

(b) Drive cycle 2

(c) Drive cycle 3

(d) Drive cycle 4
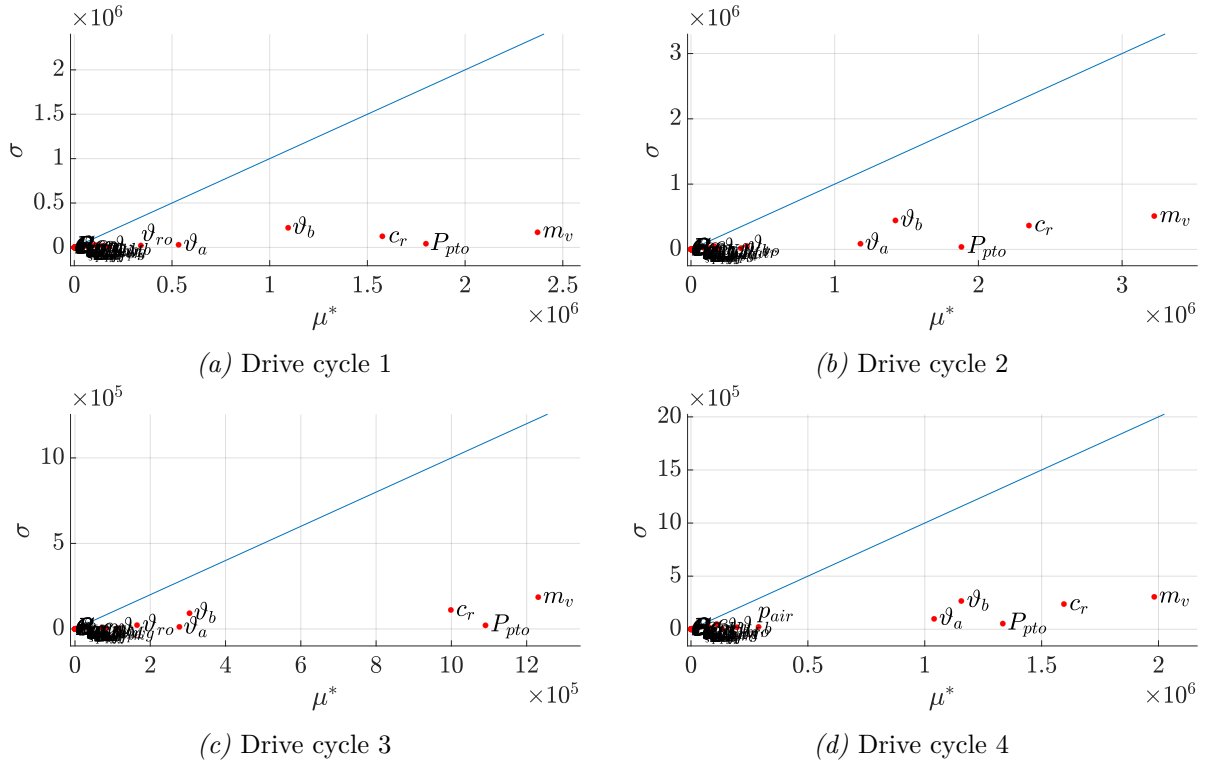
Figure 6.2: Open-loop Morris screening for the consumed battery energy E_b

Table 6.2: Reduced parameter set for the open-loop variance-based sensitivity analysis.

	Name	Description	Type of error	Distribution	Parameter	Values	Units
Battery	$e_{u_{ocv}}$	Deviation of open circuit voltage	relative	Normal	μ, σ	0, 0.05/3	−
	ϑ_b	Variation of start temperature	absolute	Uniform	a, b	20, 40	°C
Drive	ϑ_{ro}	Variation of rotor temperature ϑ_{ro}	absolute	Uniform	a, b	40, 80	°C
Vehicle	m_v	Variation of the vehicle mass	absolute	Birnbaum–Saunders	β, γ	652.11, 0.074	kg
	P_{pto}	Variation of auxiliary consumers	absolute	Uniform	a, b	250, 750	W
	ϑ_a	Variation of ambient temperature	absolute	Normal	μ, σ	12.26, 8.53	°C
	p_{air}	Variation of ambient pressure	absolute	Normal	μ, σ	98427.7, 843.09	Pa
	c_r	Variation of rolling resistance	absolute	Uniform	a, b	0.01, 0.015	−

Assuming a sample size for a variance-based sensitivity analysis of $N = 5000$, which will be proofed to be sufficient in Section 6.3.1 for the open-loop analysis, the initial Morris screening significantly reduces the computational effort. Calculating the sensitivity measures for all parameters from Table 6.1 would require $N_s = N(k+2) = 5000(39+2) = 205000$ simulation runs, whereas the reduced set of parameters from Table 6.2 would require only $N_s = N(k+2) = 5000(8+2) = 50000$ simulation runs. Therefore, the reduced parameter set requires only a quarter of the resources without losing significance.

(a) Drive cycle 1

(b) Drive cycle 2

(c) Drive cycle 3

(d) Drive cycle 4

Figure 6.3: Open-loop Morris screening for the total drive power losses P_l

6.3 Variance-Based Sensitivity Analysis

The variance-based sensitivity analysis for the open-loop setup is done for the reduced parameter set in Table 6.2. As already outlined in Section 3.2.5, the calculated sensitivity measures using the estimators of Jansen, Sobol and Saltelli need to be verified regarding their convergence and accuracy. Thus, besides of presenting the results of the open-loop sensitivity analysis, the approximation accuracy of the estimators will be presented and discussed in the following.

6.3.1 Evaluation of the Approximation Accuracy

The approximation error is evaluated using the methods presented in Section 3.2.5. Since the convergence behavior depends not only on the sampling strategy and the used estimators but is also influenced by the investigated system and the corresponding outputs, each of them need to be analyzed separately. Furthermore, according to (3.26), the investigated model changes when another drive cycle is analyzed. Consequently, the approximation accuracy of the estimated generalized first order effects $\hat{S}_i^G$ and total effects $\hat{S}_{T_i}^G$ need to be evaluated for different sample sizes $N \in [100, 5000]$ for each of the drive cycles, estimators and outputs of interest. Figures 6.4 and 6.5 outline the results of the estimators of the generalized first order and total order indices for the consumed battery energy E_b for different sample sizes.

(a) Drive cycle 1

(b) Drive cycle 2

(c) Drive cycle 3

(d) Drive cycle 4

Figure 6.4: Generalized first order indices for different estimators and different sample sizes for the open-loop variance-based sensitivity analysis of the consumed battery energy E_b.

In general, it can be seen that all estimators show convergence behavior according to the law of big numbers if N tends to have higher sample sizes. The same statement also holds for the convergence behavior of the estimates of the powertrain losses P_l, as outlined in Figures 6.6 and 6.7. However, it can be seen that the estimators from Jansen, Saltelli and Sobol for the generalized first order indices show clearly distinct convergence. The estimator from Sobol seems to have a bad convergence as the values are not stabilizing even for larger sample sizes. The estimator of Saltelli behaves better than the Sobol estimator but also shows unstable estimates. It can be clearly seen that the Jansen estimator shows the fastest convergence for the first order effects. Also, for smaller sample sizes, the estimates from the Jansen estimator do not vary much compared to the other estimators.

(a) Drive cycle 1

(b) Drive cycle 2

(c) Drive cycle 3

(d) Drive cycle 4
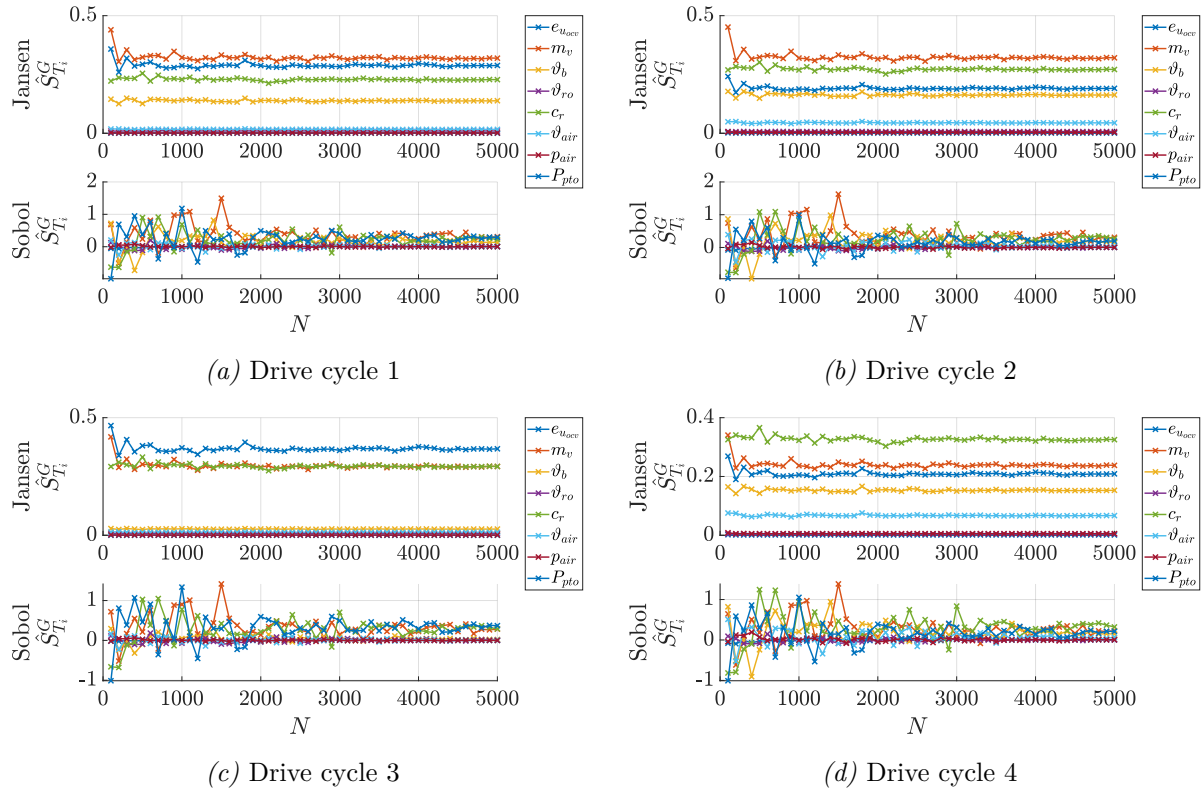
Figure 6.5: Generalized total indices for different estimators and different sample sizes for the open-loop variance-based sensitivity analysis of the consumed battery energy E_b.

Likewise, for the generalized total indices estimates, as shown in Figures 6.5 and 6.7, it can be clearly seen that the Jansen estimator provides more stable estimates than the Saltelli estimator. Also, it is worth mentioning that the driven drive cycle does not significantly impact the convergence.

However, plotting the sensitivity indices for different sample sizes provides only a qualitative assessment of the convergence behavior but is not suitable for quantifying the convergence of the different estimators and drive cycles. To overcome this issue, the scalar error measures, as outlined in (3.62) and (3.63), are calculated and shown in Figure 6.8 for the consumed battery energy E_b and in Figure 6.9 for the powertrain losses P_l. Furthermore, the maximum permissible error $\varepsilon_{max} = 0.01$, according to (3.65), is depicted as a quantitative convergence evaluation for different sample sizes N.

In general, the convergence errors $\varepsilon_{\hat{S}_j^G}$ and $\varepsilon_{\hat{S}_{T_j}^G}$ of the consumed battery energy E_b and the powertrain losses P_l show that the convergence error tends towards zero for higher sample sizes. However, the first order estimates converge more slowly than the total order estimates. In addition, the different drive cycles do not affect the convergence significantly. Thus, the choice of the correct estimator is more crucial than the influence of the chosen drive cycle. Comparing the first order estimation errors of E_b and P_l shows that the estimators for the power losses behave more equal than for the consumed battery energy. It can be observed that the first order estimators of Sobol and Saltelli do not achieve the required convergence error of $\varepsilon_{max} = 0.01$ within the maximum sample size $N = 5000$.

(a) Drive cycle 1

(b) Drive cycle 2

(c) Drive cycle 3

(d) Drive cycle 4
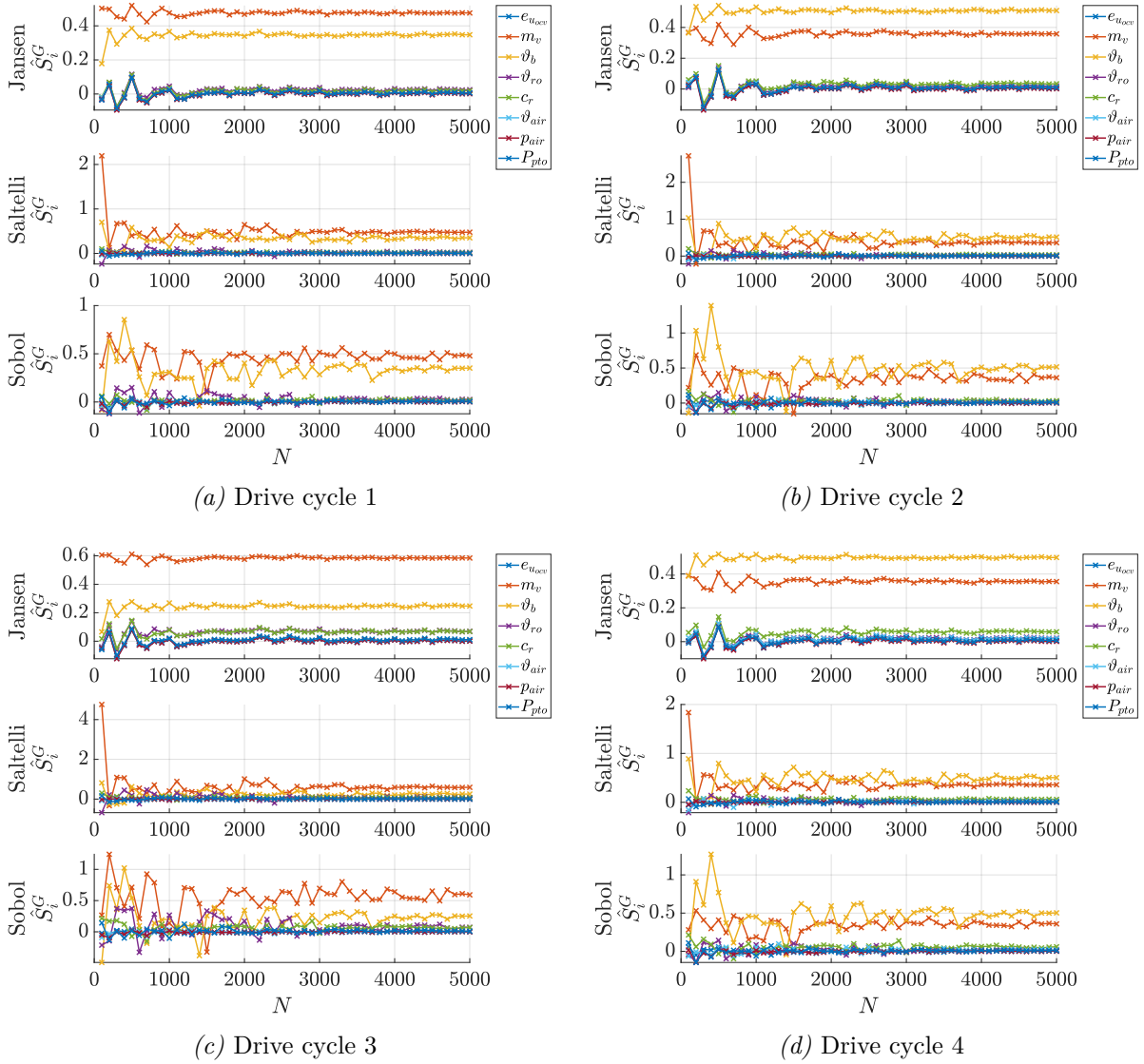
Figure 6.6: Generalized first order indices for different estimators and different sample sizes for the open-loop variance-based sensitivity analysis of the powertrain losses P_l.

The Jansen estimator clearly outperforms the other estimators and reaches the predefined convergence error goal. For the total order estimators, it is evident that the Jansen estimator is also far superior compared to the Saltelli estimator for both outputs. The Jansen estimator also provides reasonable estimates of the generalized total order indices for small sample sizes. This analysis clearly shows that the Jansen estimators for the first order and total indices are superior compared to the other investigated estimators for the open-loop analysis.

The above-discussed convergence errors provide a good quantitative scalar measure to compare the estimators against each other. However, to quantify the accuracy of each estimated parameter also the confidence intervals for each parameter of the first order and total effects are calculated using bootstrap resampling (see Section 3.2.5). For the open-loop analysis, the bootstrap samples of size $N_b = 5000$ are drawn randomly $B = 50$ times. Using these bootstrap resamples, the 95 % confidence intervals are calculated for the estimators and outlined as red error bars in the sensitivity analysis results in Figures 6.10

and 6.12.

(a) Drive cycle 1

(b) Drive cycle 2

(c) Drive cycle 3

(d) Drive cycle 4
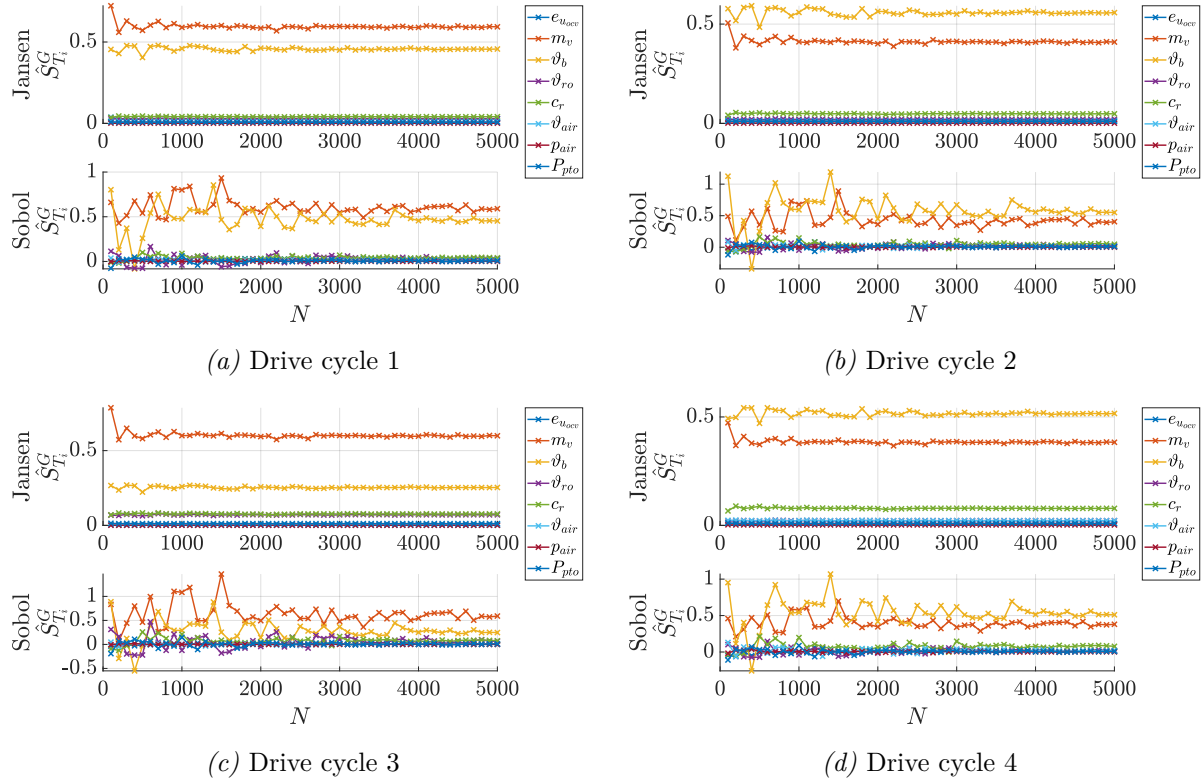
Figure 6.7: Generalized total indices for different estimators and different sample sizes for the open-loop variance-based sensitivity analysis of the powertrain losses P_l.

(a) First order effects $\varepsilon_{\hat{S}_j^G}$

(b) Total effects $\varepsilon_{\hat{S}_{T_j}^G}$
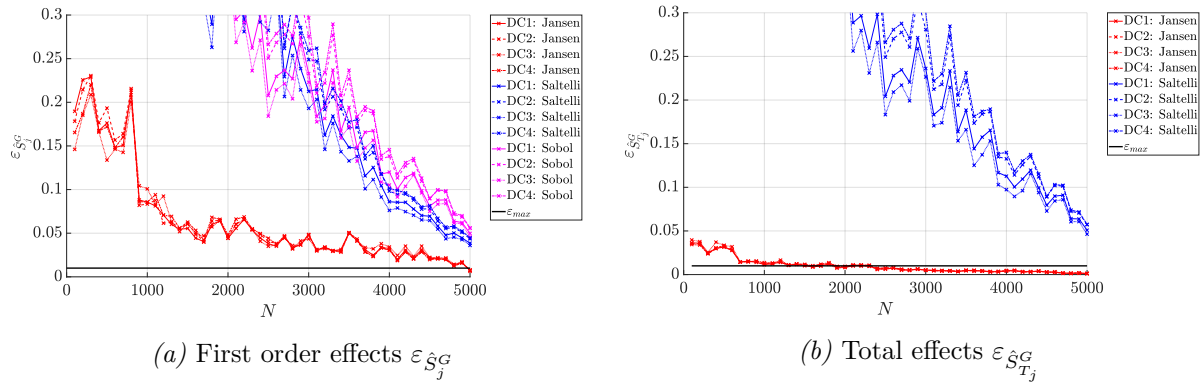
Figure 6.8: Convergence error of the first order and total generalized Sobol indices for the consumed battery energy E_b.

With the information provided by the scalar error measurements $\varepsilon_{\hat{S}_j^G}$ and $\varepsilon_{\hat{S}_{T_j}^G}$ and the bootstrap resampling, the performance of the estimators and their estimation accuracy are quantified. It has been proven that the Jansen estimators provide sufficient sensitivity estimates for the open-loop sensitivity analysis. Thus, only the results of the Jansen estimators are presented in the following.

(a) First order effects $\varepsilon_{\hat{S}_j^G}$

(b) Total effects $\varepsilon_{\hat{S}_{T_j}^G}$
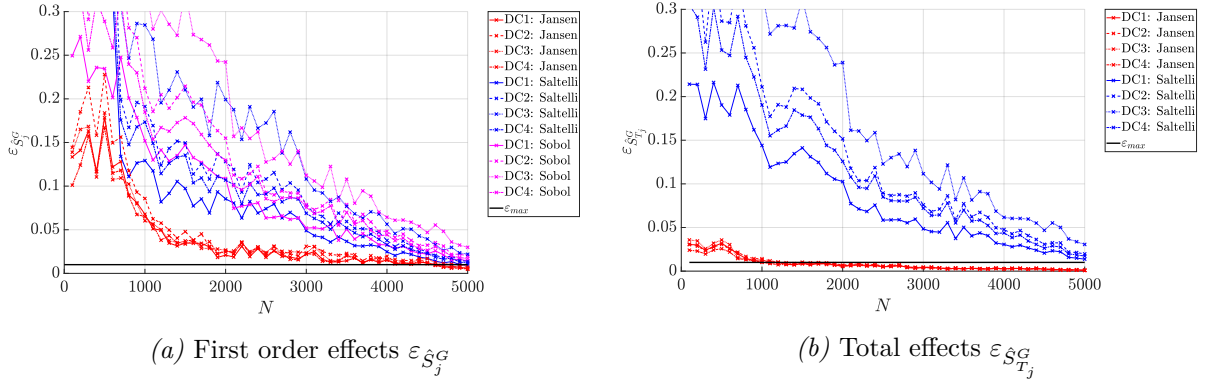
Figure 6.9: Convergence error of the first order and total generalized Sobol indices for the total powertrain losses P_l.

6.3.2 Sensitivity Analysis Results

The variance-based sensitivity analysis results using the reduced parameter set of Table 6.2 for the consumed battery energy E_b are outlined in Figure 6.10. To better understand and compare the four different drive cycles, Figure 6.11 additionally depicts the trajectories in the powertrain efficiency map and the distributions of the vehicle speed v_{ego} and the applied torque M_{em} of the manually driven drive cycles for nominal parameter values. From Figure 6.10a, it can be seen that the average energy consumption is different for the four investigated drive cycles. This is expected since the four drive cycles have different lengths and route profiles. Drive cycle 3 has the lowest average energy consumption as it is the shortest drive cycle with a primarily flat route profile and low average velocities, as Figure 6.11c shows. Drive cycle 2 has the highest average energy consumption, which is reasonable because it consists of the longest driven route with a distinct slope profile. Furthermore, according to Figure 6.11b, it was driven with the highest average velocity compared to the other drive cycles. Drive cycle 1 and drive cycle 4 have approximately the same average energy consumption. Since drive cycle 1 is longer and has a hillier slope profile, it could be expected that the average energy consumption should be higher than for drive cycle 4. However, drive cycle 4 consists in contrast to the other drive cycles of a highway section and thus has a higher average speed than drive cycle 1. This leads to higher energy consumption despite a shorter distance. Furthermore, it is evident that the examined parameters cause significant variance in the required battery energy.

As shown in Figure 6.10d, $\sum \hat{S}_i^G \approx \sum \hat{S}_{T_i}^G$ holds for all four drive cycles, which indicates a linear parameter dependency of the investigated parameters on the output E_b. This coincides with the results of the qualitative Morris screening shown in Figure 6.2. It proves the assumption that in the case of $\sigma \ll \mu^*$, no interaction effects between parameters exist for the consumed battery energy.

Comparing the generalized first order and total order effects of Figures 6.10b and 6.10c, it can be outlined that $\hat{S}_i^G \approx \hat{S}_{T_i}^G$ holds, which indicates that the first order and total effects are nearly equal. Furthermore, the 95 % confidence intervals are outlined in these figures as red error bars. The confidence of the approximation is much better for the total effects rather than the first order effects, which coincides with the convergence errors outlined in Figure 6.8. Since the first order and total order effects are equal for the output E_b, it is sufficient to analyze only the more confident total effects.

The generalized total order effects $\hat{S}_{T_i}^G$ outline that only a few parameters are responsible for the variance of the drive cycles shown in Figure 6.10a. The variation of the vehicle mass m_v, the rolling resistance c_r, the auxiliary consumers P_{pto} and the battery temperature ϑ_b are the four dominant parameters in this open-loop setup. The share of the vehicle mass deviation on the consumed battery energy is higher for drive cycles 1 and 2 than for drive cycles 3 and 4. The difference can be explained by the longitudinal

(a) Histograms

(b) First-order effects with 95 % confidence interval

(c) Total effects with 95 % confidence interval

(d) Sum of effects
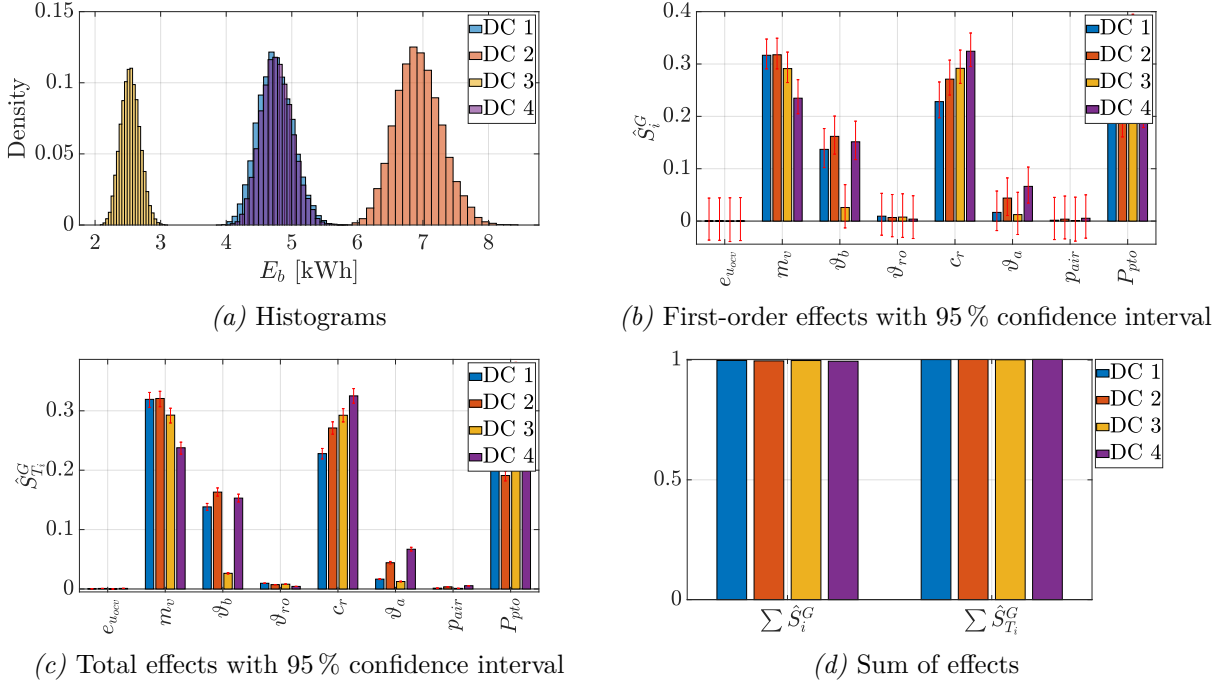
Figure 6.10: Generalized Sobol indices and histograms for the consumed battery energy E_b.

motion forces acting on the vehicle. Since the acceleration resistance force F_a acting on the vehicle behaves equally in all four drive cycles, the rolling resistance force F_r and the slope resistance force F_s are influenced by the slopes of the drive cycles. This results in different powertrain working points according to the mass distribution and the slope profile of the drive cycles. Consequently, since drive cycles 1 and 2 consist of the most volatile slope profile, the change in mass has the highest effect compared to the less hilly drive cycle 3 whereas the impact caused by the mass change is the smallest in drive cycle 4 as it is nearly flat.

The ranking of the remaining parameters can be explained by considering the required battery power during driving

$$P_b = \underbrace{P_a + P_r + P_s + P_{air}}_{\text{driving resistances}} + \underbrace{P_{pto}}_{\text{auxilliary power}} + \underbrace{P_l}_{\text{powertrain losses}}$$

$$= v_{ego}[m_{eq} \cdot a_{ego} + c_r \cdot m_v \cdot g \cdot \cos(\alpha) + m_v \cdot g \cdot \sin(\alpha) + \frac{1}{2}c_w \cdot A_v \cdot \rho_{air} \cdot v_{ego}^2]$$

$$+ P_{pto} + P_l \tag{6.3}$$

consisting of the driving resistances, as described in (5.1), the auxiliary power losses P_{pto} and the powertrain losses P_l. The driving resistance losses vary during driving according to the driven velocity and the slope profile of the drive cycle. Also, the powertrain losses differ according to the demanded power of the actual vehicle speed and slope and the efficiency of the powertrain. Only the auxiliary power is assumed to be constant during driving. Consequently, the dependence of the auxiliary power on the variance of E_b is influenced by the driving time relative to the energy consumption caused by the driving resistances and the powertrain losses. Thus, it is evident that the auxiliary power demand in drive cycle 3 has the most significant influence on the required battery energy compared to the other drive cycles since the total consumption in this driving cycle is the lowest. The more significant impact of drive cycle 1 than drive cycle 4, even though their energy consumption is almost identical, can be explained by the different driving times, as shown in Table 6.3. Since the driving time of drive cycle 1 is significantly

(a) Drive cycle 1

(b) Drive cycle 2

(c) Drive cycle 3
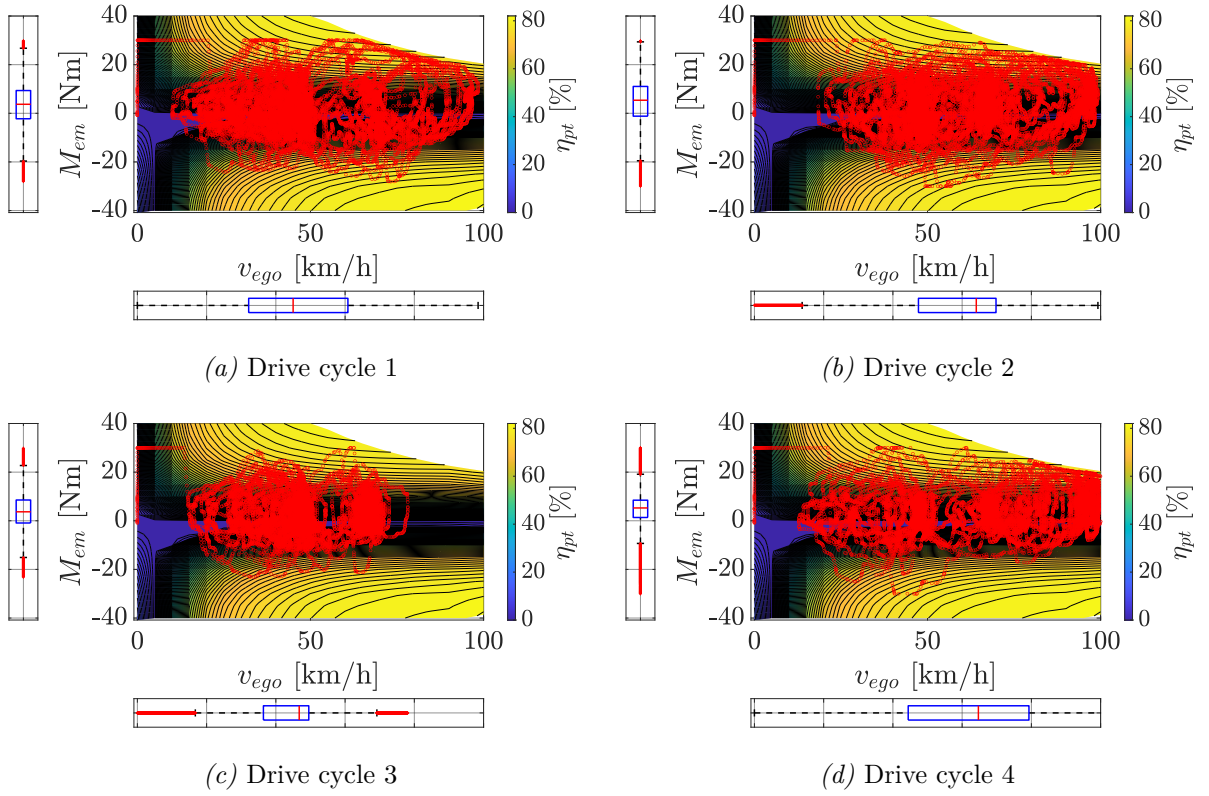
(d) Drive cycle 4

Figure 6.11: Trajectories of the manually driven drive cycles for nominal parameter values in the powertrain efficiency map η_{pt}. The boxplots on the axes outline the distribution of the vehicle speed v_{ego} and the output shaft torque M_{em} of one drive.

higher compared to drive cycle 4, the energy demand of the auxiliary consumers is higher than in drive cycle 4. Therefore, a variation of the required power of the auxiliary consumers impacts the variance of the required battery energy even more. Since the energy consumption and the driving time of drive cycle 2 are the largest, it is obvious that the auxiliary consumer power consumption variation has the lowest influence compared to the other drive cycles.

The total order effects for ϑ_b behave nearly similar except for drive cycle 3. Since the battery temperature impacts the internal resistances of the equivalent circuit model (see (5.14) and (5.15)), the powertrain losses of (6.3) will vary when the battery temperature changes. However, as drive cycle 3 consists of low average velocities and an almost flat route profile, the average power losses are small compared to the other drive cycles (see Figure 6.12a). Therefore, the battery current is also correspondingly lower. The battery losses are proportional to i_b^2 and therefore disproportionately lower than in the other driving cycles, which is reflected in a lower influence of the battery temperature.

From the total order effects, it can also be seen that the ambient temperature ϑ_{air} influences the needed battery energy, which is caused by influencing P_{air} of (6.3). Nevertheless, it can be seen that the impact of the ambient temperature is relatively small compared to the other parameters discussed above.

The results of the second output of interest, the overall powertrain losses P_l, are shown in Figure 6.12. Figure 6.12a outlines that the investigated parameters and their distributions cause significant variance in the power losses for each drive cycle. Furthermore, it can be seen that the distributions are not normally distributed but are skewed to the right. Figure 6.12d depicts that $\sum \hat{S}_i^G \neq \sum \hat{S}_{T_i}^G$ holds for all drive cycles, indicating the presence of nonlinear or interaction effects between parameters. This underpins

Table 6.3: Driving times and energy consumption for the four drive cycles with nominal parameter values as outlined in Appendix B.

Drive cycle	Energy consumption	Driving time
1	4.29 kWh	53.53 min
2	6.33 kWh	56.28 min
3	2.14 kWh	33.99 min
4	4.36 kWh	39.07 min

the assumption of the open-loop Morris screening, as outlined in Figure 6.3, of the presence of nonlinear effects since $\mu^* \approx \sigma$ holds for most of the investigated parameters in the Morris screening. It can be observed that the non-linearity is more distinct for drive cycles 1 and 2 than for drive cycles 3 or 4. However, as the calculation of driving losses, as described in Section 5.1, is not trivial and is subject

(a) Histograms

(b) First order effects with 95 % confidence interval

(c) Total effects with 95 % confidence interval

(d) Sum of effects
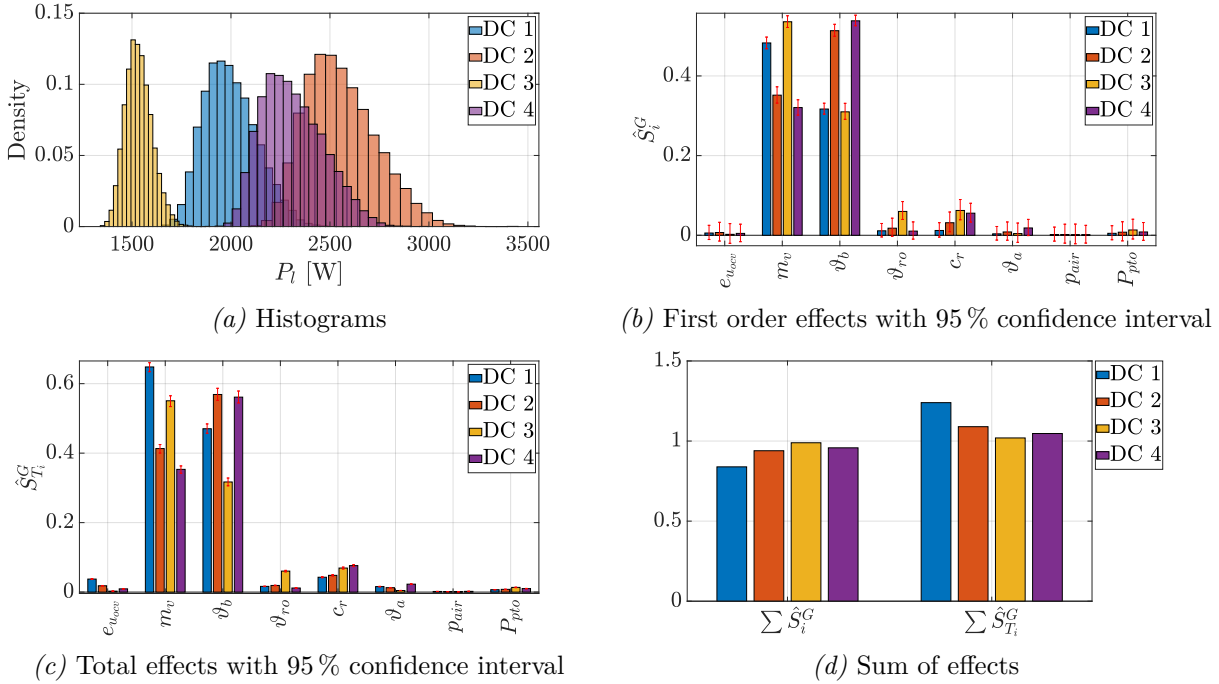
Figure 6.12: Generalized Sobol indices and histograms for the total drive power losses P_l.

to many different influencing factors, it is impossible to make a general statement on the cause of the differences in the driving cycles. It can be assumed that the hilly road gradient profile of drive cycles 1 and 2 and the associated shift in the operating points of the powertrain emphasize nonlinear effects more than in drive cycles 3 and 4.

In contrast to the consumed battery energy, only the parameters m_v and ϑ_b are dominant, which can be seen from the generalized first order effects as well as the total order effects. Both parameters are also affected by nonlinear effects, which can be seen since $\hat{S}_i^G \neq \hat{S}_{T_i}^G$ holds for both parameters for drive cycles 1 and 2. Nevertheless, from Figure 6.12d, it can be inferred that approximately 80 % of the variance is caused by first order and the remaining variance by nonlinear effects. Thus, considering m_v and ϑ_b

independently can still strongly influence the power losses P_l.

6.3.3 Influence of Changes in the PDFs

The outcome of a sensitivity analysis is influenced by the stimulating PDFs in the MC simulations. Thus, the effect of changing the distribution of the most influential parameters is investigated in this section. To analyze how sensitive the open-loop analysis reacts to changes in the corresponding PDFs, the open-loop sensitivity analysis is repeated with the new setting as outlined in Table 6.4. The changed parameters

Table 6.4: Changed PDF setting for analyzing the influence of different distributions on the results of the open-loop variance-based sensitivity analysis. The changed parameters of Table 6.2 are marked in red.

	Name	Description	Type of error	Distribution	Parameter	Values	Units
Battery	$e_{u_{ocv}}$	Deviation of open circuit voltage	relative	Normal	μ, σ	0, 0.05/3	−
	ϑ_b	Variation of start temperature	absolute	Normal	μ, σ	30, 10/3	°C
Drive	ϑ_{ro}	Variation of rotor temperature ϑ_{ro}	absolute	Uniform	a, b	40, 80	°C
Vehicle	m_v	Variation of the vehicle mass	absolute	Birnbaum–Saunders	β, γ	652.11, 0.074	kg
	P_{pto}	Variation of auxiliary consumers	absolute	Normal	μ, σ	500, 250/3	W
	ϑ_a	Variation of ambient temperature	absolute	Normal	μ, σ	12.26, 8.53	°C
	p_{air}	Variation of ambient pressure	absolute	Normal	μ, σ	98427.7, 843.09	Pa
	c_r	Variation of rolling resistance	absolute	Normal	μ, σ	0.0125, 0.0025/3	−

correspond to the parameters with the most significant influences. However, only the parameters for which no data are available for an exact determination of the distribution densities were selected. Therefore, the mass of the vehicle m_v is not considered at this point. The distributions of the investigated parameters are changed from uniform to normal distributions while retaining the same mean values as in the uniform distributions. Furthermore, the lower and upper bounds of the uniform distributions are set to the 3σ bounds in the normal distributions.

The results of the open-loop sensitivity analysis with the changed distributions are outlined in Figure 6.13 for the consumed battery energy E_b and in Figure 6.14 for the powertrain losses P_l. Comparing the histograms of Figures 6.10a and 6.13a, there could be only a slight change in the variance observed. Consequently, the change of the PDFs does not have a significant impact on the variance of E_b. However, it can be seen from Figures 6.10b and 6.13b that the ranking of the Sobol indices has changed as the influences of ϑ_b, c_r and P_{pto} are smaller compared to the original setup. This is reasonable because the distributions of ϑ_b, c_r and P_{pto} have been changed from uniform to normal distributions. This leads to a smaller number of outliers and extreme values near the limit of the distribution density function. Despite this significant change in the exciting distribution densities and the associated changes in the Sobol indices, it is still possible to separate the most influential parameters from the others. Only their order has changed slightly and none of the less important parameters have become dominant. Therefore, the sensitivity analysis can provide meaningful results for the output E_b even if the distribution densities are not precisely defined due to missing data.

The variance of P_l is more influenced than for E_b. Especially the skewing of the distribution is not so distinctive in Figure 6.14a as in Figure 6.12a. Furthermore, it can be outlined that the variance with the changed parameter set is a bit smaller than for the original parameter set.

(a) Histograms

(b) First order effects with 95 % confidence interval

(c) Total effects with 95 % confidence interval

(d) Sum of effects
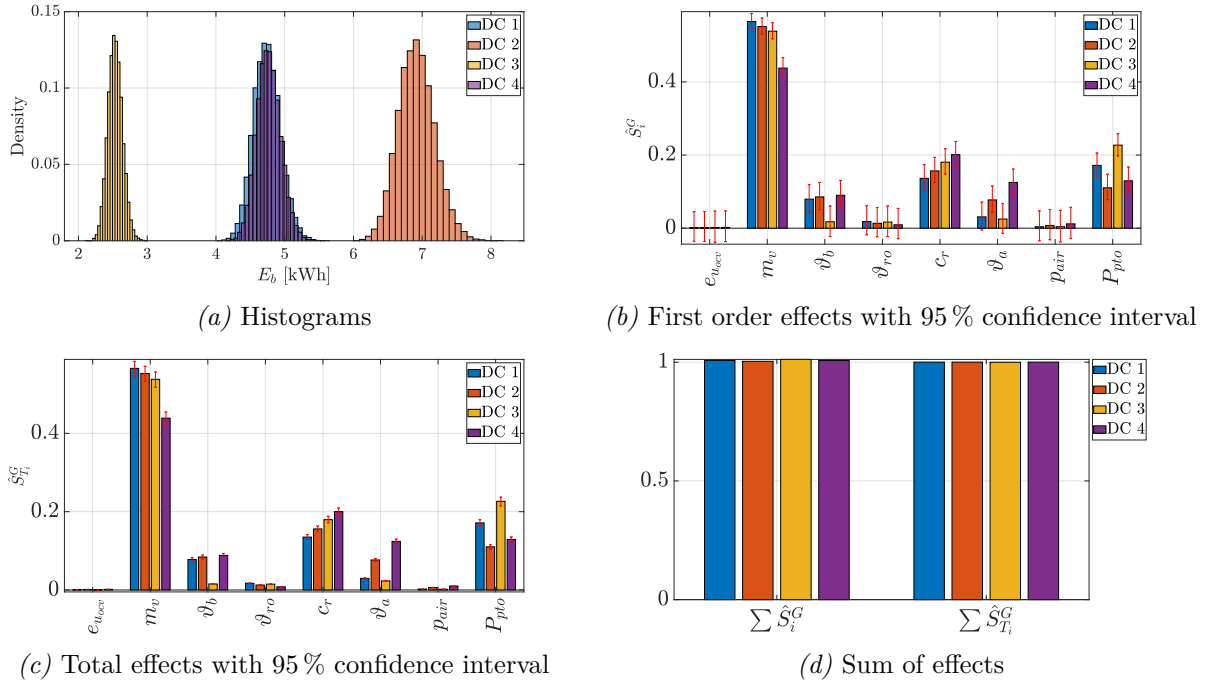
Figure 6.13: Generalized Sobol indices and histograms for the consumed battery energy E_b for the changed distributions according to Table 6.4.

(a) Histograms

(b) First order effects with 95 % confidence interval

(c) Total effects with 95 % confidence interval

(d) Sum of effects
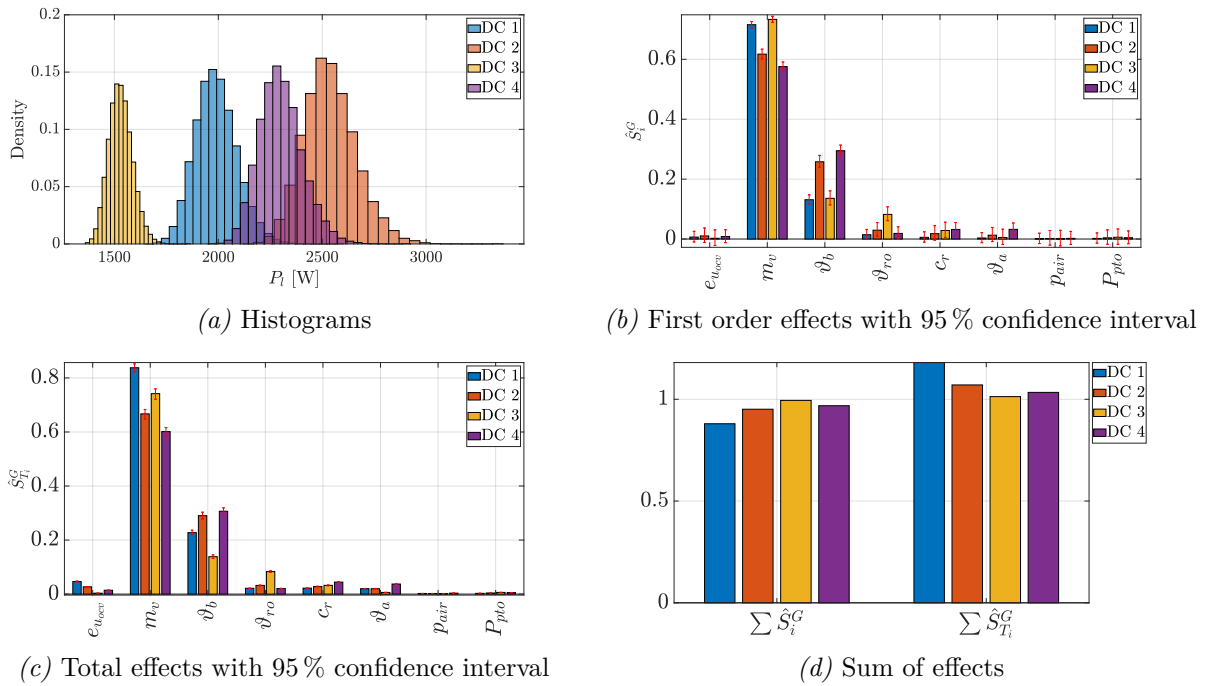
Figure 6.14: Generalized Sobol indices and histograms for the total drive power losses P_l for the changed distributions according to Table 6.4.

It can be assumed that the change to normal distributions reduces the average losses because the marginal

areas of the examined parameters are weighted less. Thus, unfavorable operating conditions are avoided more. Furthermore, it can be seen that the change in distribution densities has no significant effect on the model properties when comparing Figures 6.12d and 6.14d. Comparing the first order effects in Figures 6.12b and 6.14b, it can be seen that only the weighting of m_v and ϑ_b changed and the dominant parameters remain also clearly distinguishable for the output P_l.

6.4 Conclusions

In this chapter, the complex simulation model of the BEV on predefined drive cycles has been analyzed using the proposed sensitivity analysis methods Morris screening and generalized Sobol indices. In the first step, the PDFs of the 39 investigated parameters were defined. Next, a Morris screening was performed to reduce the computational cost of a variance-based sensitivity analysis. The influential from the non-influential parameters were separated, which resulted in a reduced parameter set for the variance-based sensitivity analysis. Consequently, the calculation time for the variance-based sensitivity analysis has been reduced by a factor of four.

The variance-based sensitivity analysis has been performed for the consumed battery energy E_b and the powertrain losses P_l using generalized Sobol indices as they consider the temporal dependency of technical processes. However, since the Sobol indices are determined using MC simulations, they need to be estimated. The convergence of the estimators depends on the sample size used in the MC simulation. Thus, the convergence has been proven using the two proposed methods of Chapter 3 based on the law of big numbers for computing the scalar convergence measures and using bootstrap resampling for calculating the confidence intervals. Accordingly, the chosen sample size of $N = 5000$ was suitable for providing reliable sensitivity analysis calculations.

Based on these analyses, it has been outlined that the investigated parameters cause significant variances in the examined outputs E_b and P_l. However, it has been shown that only a small subset of the 39 investigated parameters, consisting of the vehicle mass m_v, the battery temperature ϑ_b, the rolling resistance coefficient c_r and the auxiliary consumer power P_{pto}, are responsible for the variance of the outputs.

Since the type and shape of the PDFs influence the output of the sensitivity analysis and for the determination of several PDFs has been no data available, the influence of such blurred distribution has also been investigated in this chapter. It has been shown that the change in the PDFs of the most influential parameters has a significant effect and would cause the ranking of the parameters to change. However, it is still possible to separate the most influential from the non-influential parameters.

The investigations in this chapter serve as valuable insights into model dependencies and are used in the next chapter to design a controller which is capable of recognizing the most important parameters and is robust against parameter changes.

7 Model Predictive Energy-Efficient Longitudinal Control

The controller design of an MPC is subject to many degrees of freedom but also some constraints depending on the chosen implementation. However, the main advantage of predicting a model and considering constraints in the optimization problem is common to all designs. They all include the definition of a prediction model, a cost function with the corresponding weight factors, the consideration of constraints as well as the proper choice of a prediction horizon. However, the choice of the type of optimization problem, whether it is a convex or non-convex optimization, highly affects the complexity and the effort to solve the problem. This leads to a design conflict between the accuracy of the prediction model and the real-time capability of the controller. Consequently, the MPC should be designed carefully to achieve an acceptable compromise between these contrary design goals.

To prevent the controller design from being based on intuition, the results from Chapter 6 are used in the following to consider the most important influences of parameter variations in the controller design. Furthermore, as outlined in Chapter 5, the complex models serve as a basis for the well-founded derivation of an appropriate prediction model. The resulting concept of an ENMPC presented in the following is moreover investigated regarding its performance in the second part of this chapter. Furthermore, the real-time capability and the influence of different prediction horizon lengths are examined to ensure practical applicability. In the literature often quadratic or convex optimization problems are outlined to achieve real-time capability but with loss of accuracy in the prediction model. Therefore, the proposed controller, which is generally a more complex approach, is compared to the quadratic optimization problem approach from [48].

7.1 Economic NMPC Controller Design

In the following, the development of the ENMPC, including the prediction model, the cost function, constraints and reference trajectory generation, is presented and discussed.

7.1.1 Prediction Model

To realize an energy-efficient longitudinal control of the BEV, the prediction model of the ENMPC should contain all relevant loss information of the vehicle and the powertrain. However, including all details of the models presented in Chapter 5 in the prediction model of the ENMPC will lead to a highly nonlinear prediction model with a large number of states. Consequently, such a controller would not be real-time capable and therefore unsuitable for practical application. Thus, a simplified prediction model is presented in the following, which requires only a few states and still considers all driving resistances and powertrain losses.

MPCs use the prediction model to predict the future evolution of the state trajectory. Since the distance traveled by the vehicle depends on the driven velocity, the maximum distance covered by the prediction horizon varies with speed for a time-dependent prediction model. To obtain a prediction horizon of equal

length and independent of speed, the prediction model presented here is not modeled time-dependent but distance-dependent. Another important advantage of this domain change is that the route data, which is usually provided as a function of the vehicle position by the map data provider, can be directly used in the controller. The domain change is performed using the relation [24, 27]

$$\frac{\mathrm{d}}{\mathrm{d}t} = \frac{\mathrm{d}}{\mathrm{d}s}\frac{\mathrm{d}s}{\mathrm{d}t} = \frac{\mathrm{d}}{\mathrm{d}s}v. \tag{7.1}$$

Considering the results of the open-loop sensitivity analysis of Chapter 6, it could be outlined that the energy consumption and the power losses of the vehicle are sensitive to changes in the vehicle mass m_v and the rolling resistance coefficient c_r. Furthermore, the energy consumption is also significantly influenced by variations in the battery temperature ϑ_b and the auxiliary power demand P_{pto}. Consequently, the dependencies of m_v, c_r, ϑ_b and P_{pto} must be considered to be measurable or estimable inputs in the prediction model. However, in addition to the results of the open-loop sensitivity analysis, which only shows the sensitivity to parameter changes, the absolute shares of losses are also an important indicator for establishing a meaningful prediction model. Figure 7.1 outlines the individual shares of the energy consumption and power dissipation for static vehicle speeds and without slope influences for the nominal simulation parameters, as outlined in Appendix B. To underpin the dependence on parameter changes

(a) Energy consumption   *(b)* Power losses
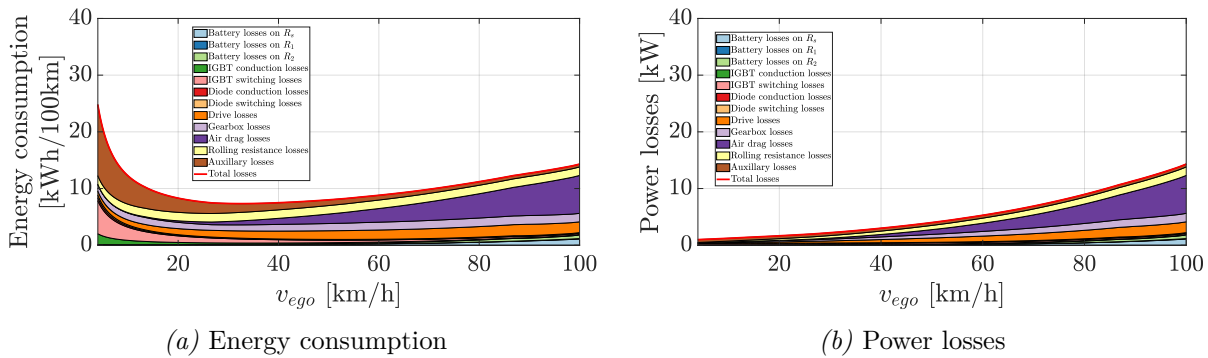
Figure 7.1: Static energy consumption and power losses for the nominal simulation parameters as outlined in Appendix B with $\alpha = 0°$.

of the most influenceable parameters, the shares of the energy consumption and power dissipation with a more worse vehicle setup ($\vartheta_b = 10\,°C$, $m_v = 850\,kg$, $c_r = 0.015$ and $P_{pto} = 750\,W$) are outlined in Figure 7.2. It can be clearly seen that the change of these parameters influences the energy consumption significantly and causes an increase in the energy consumption, especially for higher velocities, up to 69 %.

It can also be determined that besides the vehicle's driving resistances, the auxiliary power consumption, the battery temperature and the different powertrain components contribute non-negligible to the energy demand of the vehicle. Depending on the vehicle speed, the gearbox, drive and inverter losses cause up to 47 %. Since these components are not significantly influenced by changes in the parameters investigated in the open-loop sensitivity analysis, they can be simply modeled using a lookup table approximation to keep the prediction model simple. Furthermore, the time constants of these components are rather small compared to the time constant of the driving resistances and thus such a quasi-static approximation is valid.

In contrast, the battery dynamics are slow and have large time constants. From the investigated battery parameters, as already outlined in Figure 5.13, the time constant $\tau_1 = R_1 C_1$ lies between $0.7\,s$ and $1.2\,s$ and the time constant $\tau_2 = R_2 C_2$ lies between $50\,s$ and $92\,s$, depending on the actual working point of the battery. Due to this slow state evolution of the battery, the dynamics need to be considered in the model. However, as seen in Figure 7.1 and Figure 7.2, the losses on R_1 contribute only rarely to the energy consumption. Thus, they will be neglected in the prediction model to achieve real-time capability

(a) Energy consumption
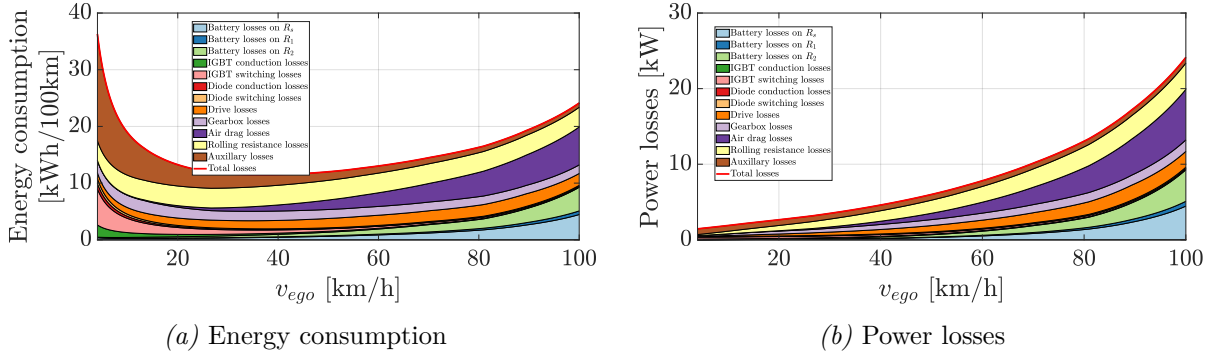
(b) Power losses

Figure 7.2: Static energy consumption and power losses for nominal simulation parameters $\alpha = 0°$ but changed the most influenceable open-loop parameters to $\vartheta_b = 10\,°\text{C}$, $m_v = 850\,\text{kg}$, $c_r = 0.015$ and $P_{pto} = 750\,\text{W}$.

of the proposed ENMPC and only the dominant time constant τ_2 is considered.

Nevertheless, investigating static operating points, as discussed above, does not fully cover the behavior of the vehicle dynamics. In particular, the slow battery dynamics cannot be fully considered therein. Furthermore, the operating points required for a change in vehicle speed caused by the acceleration resistance force are not considered and the influence of the road gradient is neglected. Consequently, it is of great interest to also analyze the loss shares in the four driving cycles. Since the total energy required in the driving cycles is different, Figure 7.3 outlines the normalized loss energies for the four drive cycles with the nominal simulation parameters. Furthermore, Figure 7.4 shows the normalized loss energies with nominal simulation parameters but changed the most influenceable open-loop sensitivity analysis parameters to $\vartheta_b = 10\,°\text{C}$, $m_v = 850\,\text{kg}$, $c_r = 0.015$ and $P_{pto} = 750\,\text{W}$. From these two Figures, it can be outlined that the shares of the power losses are not entirely different compared to the static working points. Furthermore, it shows the rise of battery losses and rolling resistance losses compared to the other losses for the worse parameter setup in Figure 7.4. Another important finding is that the loss distributions behave not that differently for the four different drive cycles. Only for drive cycle 3 a smaller amount of the battery and air drag losses could be observed. This is reasonable since the average velocity of this drive cycle is low and it has no distinct slope profile. Thus, the resulting low power demand on this drive cycle causes lower battery currents and therefore, lower battery losses. Also, the lower velocity results in fewer air drag losses.

The above-outlined investigations can now be used to formulate a suitable controller prediction model which will cover all relevant loss mechanisms, parameter influences and system dynamics. At first, the driving resistances have to be considered in the prediction model. Accordingly, the longitudinal motion model, as described in Section 5.1.1, and the transformation (7.1) lead to

$$\frac{\mathrm{d}}{\mathrm{d}s}v_{ego} = \frac{M_c\frac{i_g}{r_w} - c_r m_v g\cos(\alpha) - m_v g\sin(\alpha) - \frac{1}{2}\rho_{air}c_w A v_{ego}^2}{m_{eq}v_{ego}}, \tag{7.2}$$

representing the distance-dependent velocity as the first state of the controller design.

To predict the energy consumption of the vehicle and to be able to penalize it in the cost function, the consumed battery energy E_b is used as the second state. The state evolution is given by

$$\frac{\mathrm{d}}{\mathrm{d}s}E_b = \frac{u_{ocv}i_b n_{cell}}{v_{ego}}, \tag{7.3}$$
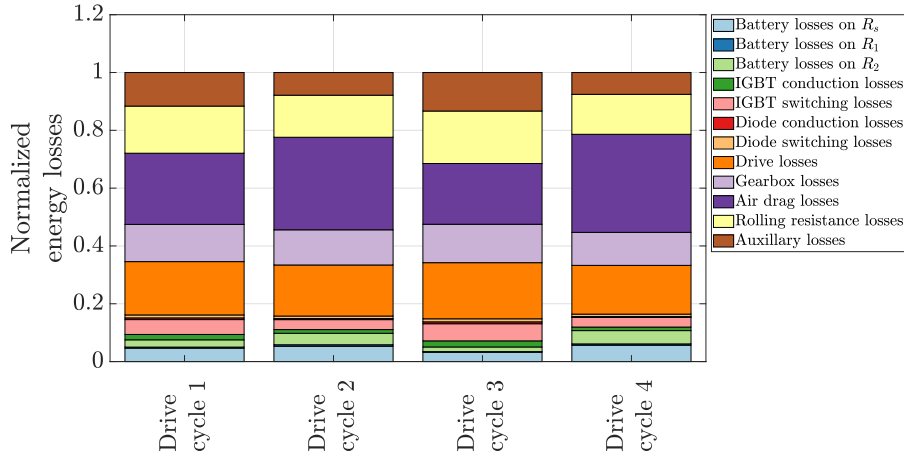
Figure 7.3: Normalized energy losses of the four drive cycles for the nominal simulation parameters.

where the open-circuit voltage u_{ocv} is assumed to be constant over the prediction horizon. The battery current can be determined with

$$P_{DC}(M_c, v_{ego}) + P_{pto} = i_b n_{cell}(u_{ocv} - u_{RC} - i_b R_s), \qquad (7.4)$$

using a battery equivalent circuit model with only one RC element, as explained above. Furthermore, $P_{DC}(M_c, v_{ego})$ denotes the DC-power requested by the inverters and P_{pto} outlines the power demand of the auxiliary consumers. Solving the quadratic equation leads to

$$
\begin{aligned}
i_b =& \frac{n_{cell}(u_{ocv} - u_{RC})}{2R_s n_{cell}} \\
& - \frac{\sqrt{-n_{cell}(n_{cell}(u_{RC}u_{ocv} - u_{RC}^2 - u_{ocv}^2) + 4R_s(P_{pto} + P_{DC}(M_c, v_{ego})))}}{2R_s n_{cell}}
\end{aligned}
\qquad (7.5)
$$

for the battery current.

To ensure real-time capability and thus, practical applicability of the controller, the complex and nonlinear behavior of the drive and inverter is not transferred directly into the prediction model as this would result in an overly complex controller design. Since the open-loop sensitivity analysis outlines that the battery parameters are the only significantly affected powertrain parameters, the inverter and drive, as well as the gearbox losses, can be modeled without considering parameter changes. Thus, the required DC-power is modeled as a lookup table as outlined in Figure 7.5. To use the DC-power map efficiently, it is approximated using a second-order polynomial of the form

$$P_{DC}(M_c, v_{ego}) \approx 227.2 - 1.12M_c + 60.04v_{ego} + 0.37M_c^2 + 20.67v_{ego}M_c + 1.21v_{ego}^2, \qquad (7.6)$$

which will be used in the controller design.

The voltage drop u_{RC} is calculated by

$$\frac{\mathrm{d}}{\mathrm{d}s}u_{RC} = \frac{\frac{i_b}{C_{1,c}} - \frac{u_{R_{1,c}}}{C_{1,c}R_{1,c}}}{v_{ego}}, \qquad (7.7)$$

and serves as the third system state for the controller design. To keep the controller simple, the parameters are assumed to be constant over the prediction horizon and only the dominant RC element consisting
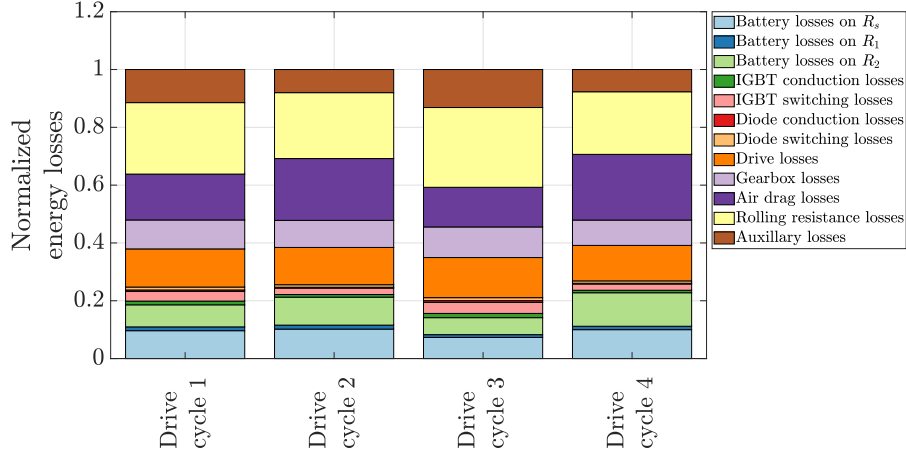
Figure 7.4: Normalized energy losses of the four drive cycles for the nominal simulation parameters but changed the most influencable open-loop parameters to $\vartheta_b = 10\,°C$, $m_v = 850\,\text{kg}$, $c_r = 0.015$ and $P_{pto} = 750\,\text{W}$.

of R_2 and C_2 of the battery model is considered with $R_{1,c} = R2$ and $C_{1,c} = C2$.

According to (7.2)-(7.7), the nonlinear state-space model can be fully described by

$$\frac{\mathrm{d}}{\mathrm{d}s}\begin{bmatrix} v_{ego} \\ E_b \\ u_{RC} \end{bmatrix} = \begin{bmatrix} \frac{M_c\frac{i_g}{r_w} - c_r m_v g \cos(\alpha) - m_v g \sin(\alpha) - \frac{1}{2}\rho_{air} c_w A v_{ego}^2}{m_{eq} v_{ego}} \\ \frac{u_{ocv} i_b n_{cell}}{v_{ego}} \\ \frac{\frac{i_b}{C_{1,c}} - \frac{u_{R_{1,c}}}{C_{1,c} R_{1,c}}}{v_{ego}} \end{bmatrix}, \tag{7.8}$$

with

$$\mathbf{u} = M_c = 2M_{em} \tag{7.9}$$

as the control input.

7.1.2 Additional Constraints on the Optimization Problem

To stay within the limitations of the powertrain, further inequality constraints need to be included in the optimization problem. The gearbox of each drive system at the rear wheels is designed for a maximum engine torque of $M_{em} = 30\,\text{Nm}$ for driving as well as recuperation. Since the torque is equally distributed to both rear-wheel drive systems, this leads to the inequality constraint

$$M_{min} \leq M_c(s) \leq M_{max} \quad \text{with} \quad s \in [0, S_p) \tag{7.10}$$

with $M_{min} = -60\,\text{Nm}$ and $M_{max} = 60\,\text{Nm}$.

In addition, the maximum applicable torque is limited according to the maximum battery current boundaries, especially for high speeds. As outlined in Section 5.1.2, the used batteries are capable of a maximum of 120 A continuous battery current for charging and discharging. This maximum battery current leads to a cut-off in the DC-power map P_{DC}, which is shown in Figure 7.6. The limitation of the maximum
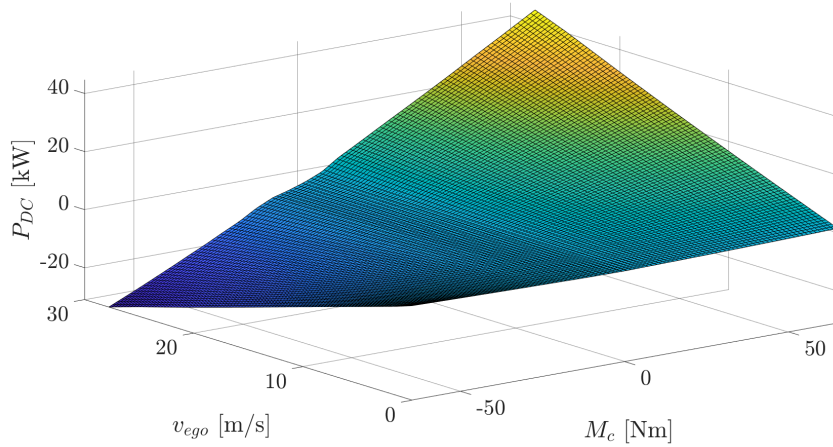
Figure 7.5: DC-power map
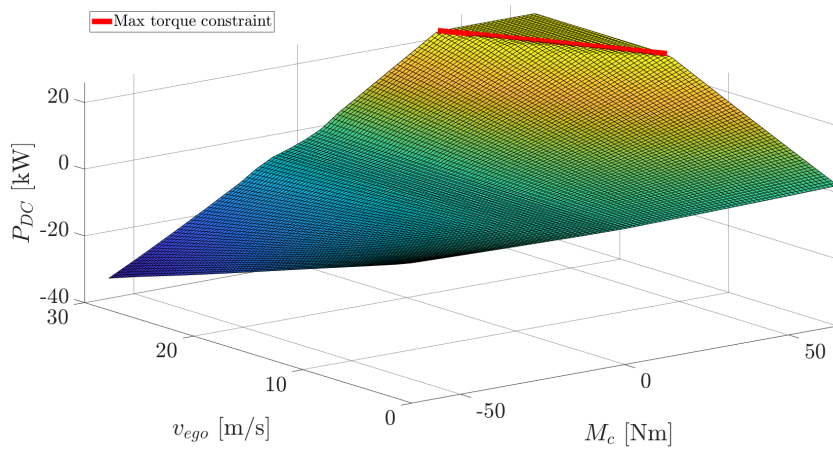
Figure 7.6: DC-power map with battery current limitation

DC-power is achieved by an additional constraint on the control input M_c. It can be described as a linear inequality constraint with

$$M_c(s) \leq 97.01 - 2.173 v_{ego}(s) \quad \text{with} \quad s \in [0, S_p), \tag{7.11}$$

which indirectly considers the battery current limitation.

Furthermore, another constraint is introduced, which considers the maximum allowed speed depending on the position and prevents exceeding it. Accordingly, it is introduced as a linear inequality constraint by

$$v_{ego}(s) \leq v_{max,mpc}(s) \quad \text{with} \quad s \in [0, S_p], \tag{7.12}$$

with $v_{max,mpc}$ as the maximum allowed speed. The determination of $v_{max,mpc}$ will be presented in Section 7.1.5.

In (7.8), the states consist of a singularity for $v_{ego} = 0\,\text{m/s}$. To avoid this singularity, the vehicle speed is also constrained on its lower bound. Furthermore, the optimization problem should be bounded

to ensure solvability and stability [192], which leads to the constraints

$$
\begin{bmatrix} 5 \\ -300000 \\ -50 \end{bmatrix} \leq \mathbf{x}(s) \leq \begin{bmatrix} v_{max,mpc}(s) \\ 300000 \\ 50 \end{bmatrix} \quad \text{with} \quad s \in [0, S_p], \tag{7.13}
$$

including $v_{max,mpc}(s)$ as an upper bound for the first system state of the prediction model.

7.1.3 Cost Function

In general, the cost function of an optimal control problem consists of two different terms. The term at the end of the prediction horizon belongs only to the states of the prediction model $\mathbf{x}(S_p)$ and is called the Mayer term. Furthermore, the states $\mathbf{x}$ and inputs $\mathbf{u}$ are considered continuously throughout the prediction horizon in the Lagrange term [193]. The general cost function can then be described by

$$
J(\mathbf{x}, \mathbf{u}) = \int_0^{S_p} \underbrace{f_{int}(\mathbf{x}(s), \mathbf{u}(s), s)}_{\text{Lagrange term}} \mathrm{d}s + \underbrace{f_{S_p}(\mathbf{x}(S_p), S_p)}_{\text{Mayer term}} \tag{7.14}
$$

for a distance-dependent prediction horizon, which will be minimized in the optimization problem where f_{end} and f_{int} consists of the considered penalizations.

The control objective for the use case of energy-efficient driving includes contrary goals. The controller should drive the vehicle in the most achievable energy-efficient way that is possible. However, penalizing only the amount of needed energy in the cost function would lead to a controller driving very slowly to avoid, e.g., a lot of air drag resistance. Consequently, the driving time would increase significantly, which would not be accepted by the drivers. Therefore, also the deviation from the maximum allowed vehicle speed $v_{max,mpc}$ needs to be considered, which leads to the target cost function

$$
\begin{aligned}
J(\mathbf{x}, \mathbf{u}) = \int_0^{S_p} & [a_c \cdot (v_{ego}(s) - v_{max,mpc}(s))^2 + b_c \cdot (M_c(s) - M_{ref}(s))^2] \mathrm{d}s \\
& + c_c \cdot E_b(S_p) + d_c \cdot (v_{ego}(S_p) - v_{max,mpc}(S_p))^2.
\end{aligned} \tag{7.15}
$$

In this economic cost function, the energy consumption during driving is considered using the penalization factor c_c of the consumed battery energy E_b at the end of the prediction horizon length S_p. The tracking of the vehicle speed close to $v_{max,mpc}$ is considered in the Lagrange as well as in the Mayer term and is penalized by a_c and d_c.

A longitudinal motion controller of a vehicle requires to be comfortable, which means it should output only smooth setpoint changes causing no high acceleration or jerk of the vehicle. Since an ENMPC design incorporates not directly a smooth behavior of the control variable, the deviation of the control variable M_c from the reference torque M_{ref} in the Lagrange term is penalized, which leads to a smoother and more comfortable controller behavior. The required reference torque is considered by calculating the amount of torque that is needed to drive the vehicle at a constant speed and zero acceleration using the longitudinal motion model of (7.2) which results into

$$
M_{ref} = \frac{r_w}{i_g} (c_r m_v g \cos(\alpha) + m_v g \sin(\alpha) + \frac{1}{2} \rho_{air} c_w A v_{ego}^2). \tag{7.16}
$$

7.1.4 Summarized Optimization Problem

The complete optimization problem, considering the prediction model, the additional constraints and the cost function, as described in the previous sections, is summarized in the following. The problem formulation for the ENMPC, which is implemented in the simulation, is described by

$$\min_{M_c} \int_0^{S_p} [a_c \cdot (v_{ego}(s) - v_{max,mpc}(s))^2 + b_c \cdot (M_c(s) - M_{ref}(s))^2] \mathrm{d}s$$
$$+ c_c \cdot E_b(S_p) + d_c \cdot (v_{ego}(S_p) - v_{max,mpc}(S_p))^2 \tag{7.17a}$$

$$\text{s.t.} \quad \frac{\mathrm{d}}{\mathrm{d}s} \begin{bmatrix} v_{ego} \\ E_b \\ u_{RC} \end{bmatrix} = \begin{bmatrix} \frac{M_c \frac{i_g}{r_w} - c_r m_v g \cos(\alpha) - m_v g \sin(\alpha) - \frac{1}{2} \rho_{air} c_w A v_{ego}^2}{m_{eq} v_{ego}} \\ \frac{u_{ocv} i_b n_{cell}}{v_{ego}} \\ \frac{\frac{i_b}{C_{1,c}} - \frac{u_{R_{1,c}}}{C_{1,c} R_{1,c}}}{v_{ego}} \end{bmatrix} \tag{7.17b}$$

$$\mathbf{x}(0) = \mathbf{x}_0 \tag{7.17c}$$

$$M_{min} \leq M_c(s) \leq M_{max} \qquad\qquad s \in [0, S_p) \tag{7.17d}$$

$$M_c(s) \leq 97.01 - 2.173 v_{ego}(s) \qquad\qquad s \in [0, S_p) \tag{7.17e}$$

$$\begin{bmatrix} 5 \\ -300000 \\ -50 \end{bmatrix} \leq \mathbf{x}(s) \leq \begin{bmatrix} v_{max,mpc}(s) \\ 300000 \\ 50 \end{bmatrix} \qquad\qquad s \in [0, S_p], \tag{7.17f}$$

which contains the cost function to be minimized and considers the nonlinear model and the inequality constraints. Furthermore, the initial guess $\mathbf{x}(0) = \mathbf{x}_0$ for the prediction and the constraints to bound the optimization problem are included.

To implement this continuous formulated optimization problem, it is discretized using a fourth-order Runge-Kutta algorithm with a prediction step size of $10\,\mathrm{m}$. The ENMPC is implemented in the simulation using the open-source frameworks CasADi [194] and acados [195, 196], containing the fast HPIPM [197] solver for nonlinear optimization problems to achieve real-time capability. Since the length of the prediction horizon highly affects the complexity and thus the computation time of the optimization problem, the influence of different prediction horizon lengths for the proposed solution will be further investigated and discussed in Section 7.2.3.

7.1.5 Speed Reference Generation

Besides the energy-efficient driving requirements, the constraint regarding the vehicle speed, as already outlined in (7.12), must be considered by the controller. In the following, the determination of the maximum allowed vehicle speed $v_{max,mpc}$ is presented.

Since the traffic in front of the vehicle is not considered in this thesis, two causes have left that influence the maximum vehicle speed on a given route. First, the controller must obtain the legal speed limit v_{max} to drive the vehicle inside the regulatory boundaries. The information on the maximum allowed vehicle speed for a given route is provided by the map data provider as already outlined in Section 5.2.

The second boundary which needs to be considered is the maximum speed when driving a curve to

avoid too high lateral accelerations and ensure safe driving. The average driving speed for a given curve radius r_c was investigated using field experiments with drivers of passenger cars in [198]. The resulting relation between the curve radius and the average driven curve speed, considered as the maximum allowed curve speed $v_{l,max}$, is outlined in Figure 7.7. To ensure that both required speed limits are considered
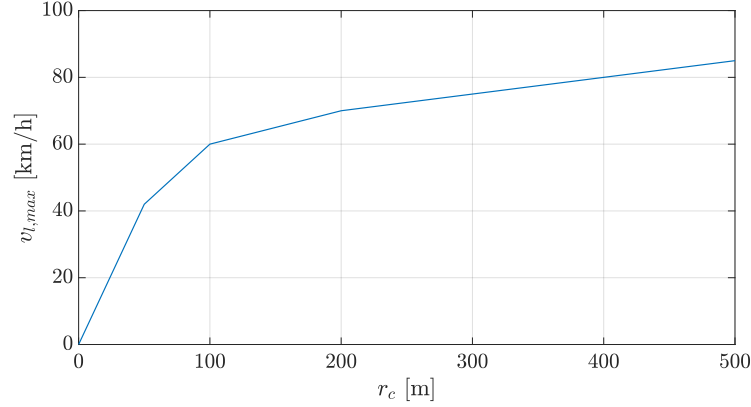
Figure 7.7: Average driving speed in curves for a given curve radius r_c based on field experiments with drivers of passenger cars. According to [198]

in the constraint of the ENMPC, the easiest way would be to process them using a minimum operator. However, this would lead to discontinuities in the reference trajectory and would make the optimization problem harder to solve or, in some special cases, infeasible. For this reason, the reference trajectory is smoothed using the discrete optimization problem [48]

$$\min_{v_{max,mpc}} \quad \sum_{i=1}^{N_p} (v_{max,ref}(k+i|k) - v_{max,mpc}(k+i|k))^2 \tag{7.18a}$$

$$\text{s.t.} \quad v_{max,mpc}(k+i+1|k) - v_{max,mpc}(k+i|k) \leq r_{max} \quad \forall i \in \{1, 2, \ldots, N_p\} \tag{7.18b}$$

$$v_{max,mpc}(k+i|k) \leq v_{max,ref}(k+i|k) \quad \forall i \in \{1, 2, \ldots, N_p\}. \tag{7.18c}$$

The cost function (7.18a) of the optimization problem ensures that the maximum allowed velocity is tracked closely. Furthermore, the constraint (7.18b) allows only a change in the optimization variable in one prediction step of r_{max} and the constraint (7.18c) ensures that the optimization variable is always smaller or equal to the maximum allowed vehicle speed. This optimization ensures a smooth evolution even when the reference trajectories for the legal speed limit or the maximum allowed curve speed contain discontinuities.

7.2 Simulations on the Closed-Loop Energy-Efficient Longitudinal Control

It is essential to investigate the developed ENMPC regarding its performance and capability. To evaluate the performance of the presented ENMPC, different scenarios and the reaction of the controller to them are discussed in the following. First, the response of the controller to changes in the speed setpoint as well as changes in the road gradient will be evaluated. Furthermore, the influence of the prediction horizon is investigated. Finally, the performance of the controller in the four drive cycles is examined and compared to the manually driven drive cycles.

7.2.1 Reaction to Speed Setpoint Changes

The reference velocity, composed of the maximum allowed legal speed and the maximum allowed curvature speed, plays a crucial role for a safe and legal longitudinal operation of the vehicle. Thus, the reaction to speed setpoint changes plays an important role in the controller design. It needs to be ensured that the controller will not overshoot the hard constraint of the maximum allowed speed and should also transits smoothly from one velocity setpoint to the next.

In Figure 7.8, an artificial speed setpoint profile is given, which includes different speed setpoints $v_{max,ref}$, as well as rising and falling gradients of different heights.

Figure 7.8: Controller reaction to changes in the reference speed $v_{max,ref}$ for different values of the economic cost function tuning factor c_c.

This profile is used to ensure the correct behavior of the presented controller. The reaction to the speed setpoint changes is evaluated with a prediction horizon of $S_p = 400\,\text{m}$ and a discretization of $10\,\text{m}$. Furthermore, the controller is assessed for four different values of the economic cost function parameter c_c. In general, it can be seen that the hard constraint is kept for rising as well as for falling gradients of the speed setpoint. Especially for higher velocities, the influence of the economic cost function parameter c_c gets more visible. Higher values of c_c result in a lower final speed of the vehicle to save energy. Consequently, c_c would also influence the driving time by additionally lowering the energy consumption as the consumed battery energy E_b shows.

Figure 7.9 shows an enlarged view of the velocity change to a higher velocity and the acceleration process in the distance interval $s_{ego} \in [2700\,\mathrm{m}, 3700\,\mathrm{m}]$.
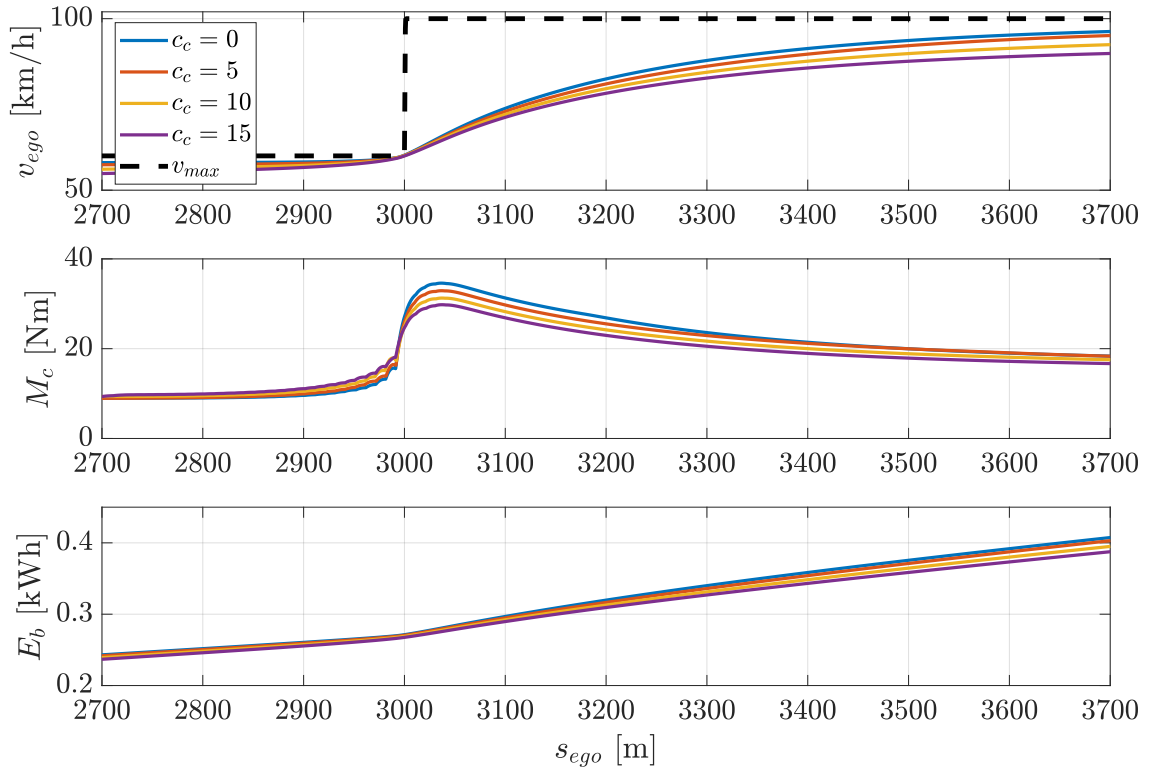
Figure 7.9: Controller reaction to a positive change in the reference speed $v_{max,ref}$ in the time distance interval $s_{ego} \in [2700\,\mathrm{m}, 3700\,\mathrm{m}]$ of Figure 7.8 for different values of the economic cost function tuning factor c_c.

Each of the four controller settings behaves very similarly regarding the applied torque profile M_c and varies only in the height of the applied torque. This results in a lower final velocity of the controller for higher values of c_c. The lower final velocities are evident since the controller reduces the amount of needed energy by driving slower and thus reducing the aerodynamic resistance of the vehicle. In general, the controller generates a smooth torque setpoint profile which will lead to a comfortable driving behavior without a lot of jerk and high accelerations. However, shortly before the reference speed change, a slight chattering of the torque profile could be observed.

The enlarged view of the deceleration process for distance interval $s_{ego} \in [5400\,\mathrm{m}, 6100\,\mathrm{m}]$ is shown in Figure 7.10. It is well illustrated that the reaction of the controller starts immediately as the speed setpoint change gets visible at the end of the prediction horizon, independent of the cost function parameterization. The evolution of the controller output M_c is nearly identical for the different parameterizations. However, it is interesting to observe that the setting with $a_c = 15$ needs the lowest braking torque since the vehicle is already slower than in the other configurations at $s_{ego} = 5600\,\mathrm{m}$ when the speed setpoint change gets visible. In general, as well as for a rising speed setpoint, the controller output behaves primarily smooth for the falling speed setpoint. However, in the controller output, chattering is also present. Furthermore, it can be seen from the consumed battery energy E_b that the controller with $a_c = 15$ has consumed about 4 % less energy than the controller with $a_c = 0$ at the end of this artificial drive cycle.
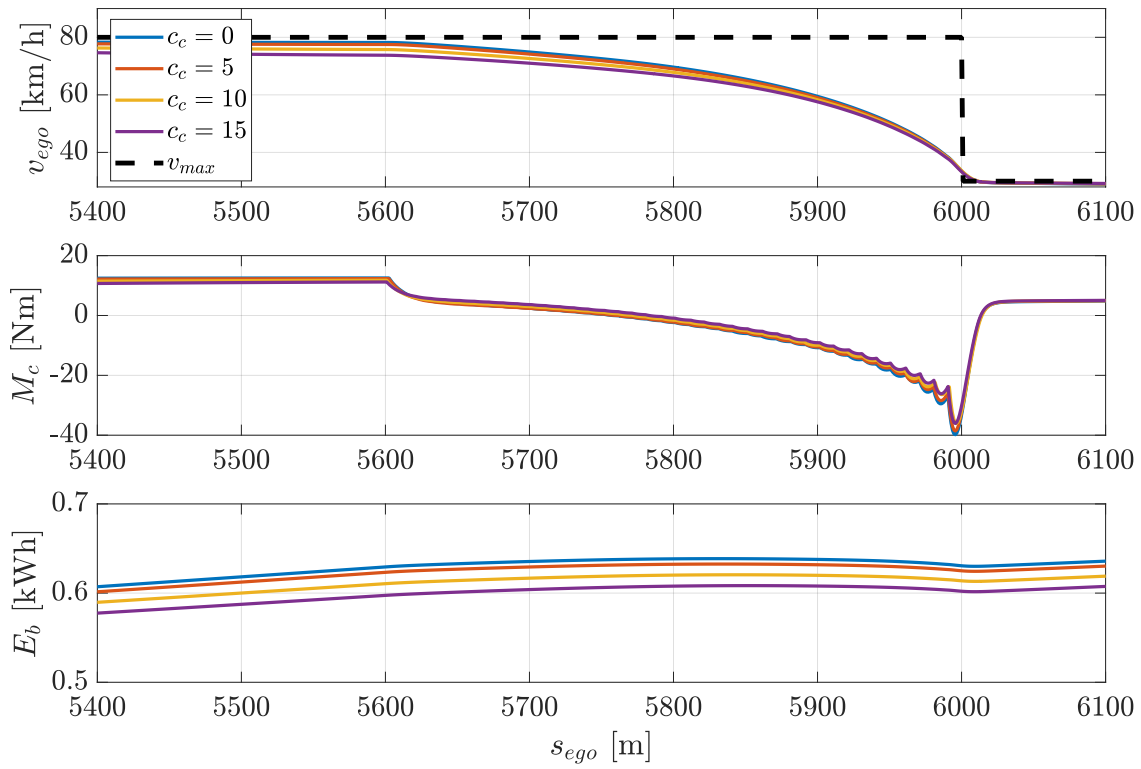
Figure 7.10: Controller reaction to a negative change in the reference speed $v_{max,ref}$ in the time distance interval $s_{ego} \in [5400\,\text{m}, 6100\,\text{m}]$ of Figure 7.8 for different values of the economic cost function tuning factor c_c.

7.2.2 Reaction to Slope Changes

Slope changes in the driven route are disturbances that act on the controller during operation. Thus, the controller should react appropriately to these disturbances in a comfortable manner for the passengers of the vehicle and are investigated in the following using an artificial slope change profile. In the presented controller design, the course of the slope is provided by the HERE map data and is known throughout the prediction horizon.

Figure 7.11 outlines the controller behavior for the artificial slope change profile for four different settings of the economic cost function tuning factor c_c.

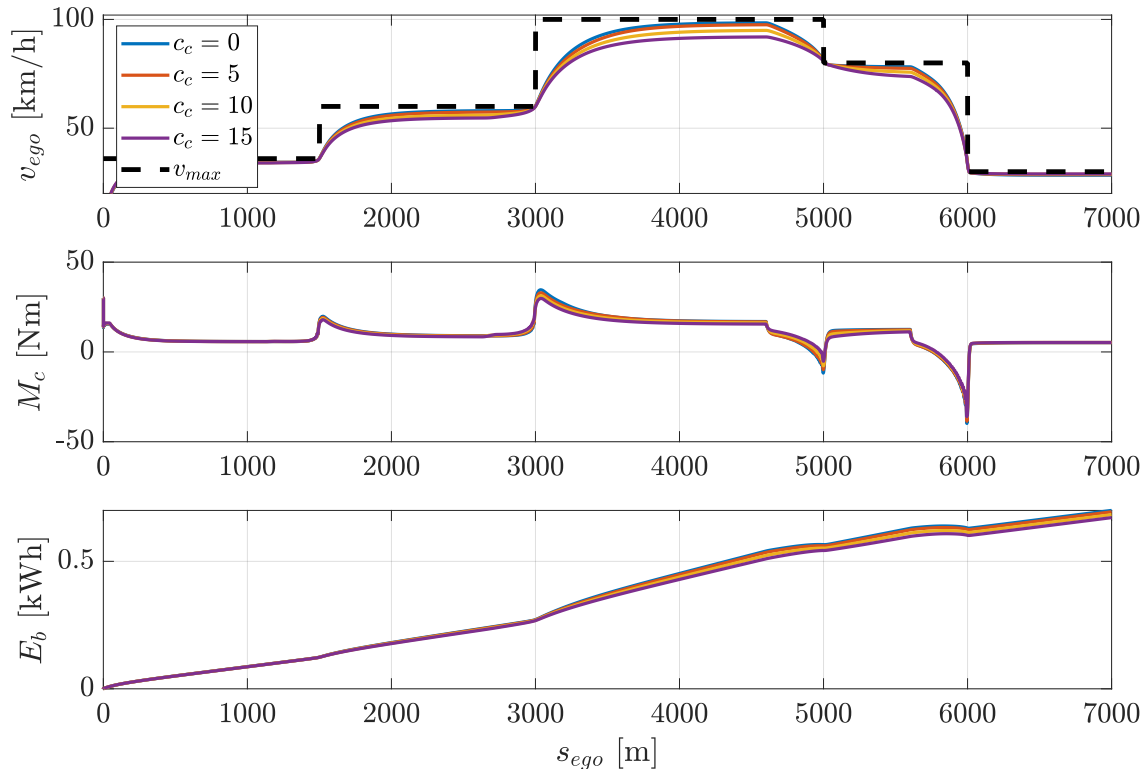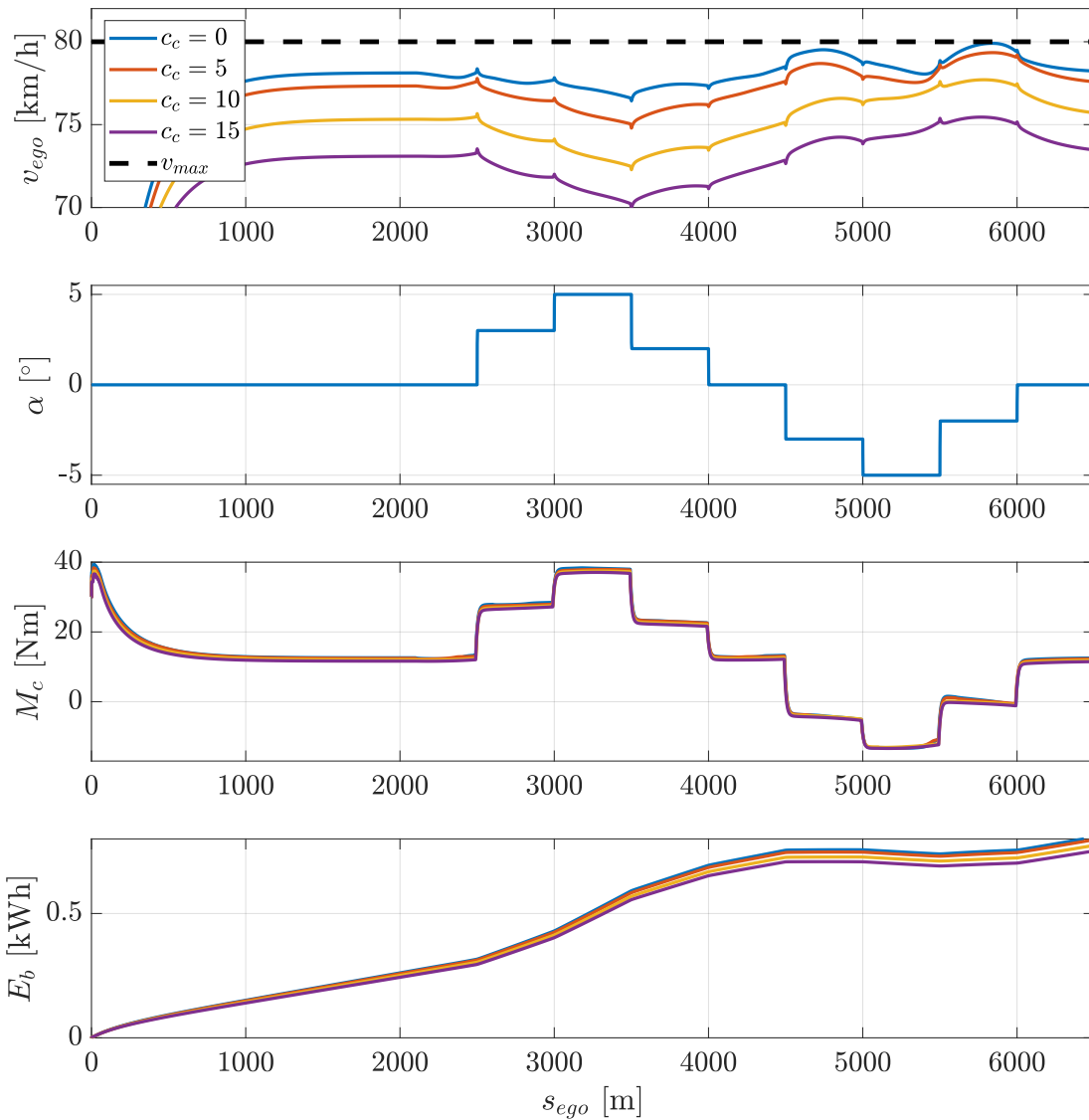*Figure 7.11:* Controller reaction to changes in the road slope α for different values of the economic cost function tuning factor c_c.

The reaction to slope changes is evaluated with a prediction horizon of $S_p = 400\,\text{m}$ with a discretization of $10\,\text{m}$ and the reference speed $v_{max,ref}$ remains constant at $80\,\text{km/h}$. For $a_c = 0$, the velocity is kept with a

slight deviation from the reference velocity. The deviation grows when c_c increases. This is obvious since, as already discussed in the previous section, increasing economic penalization results in a slower driven velocity to reduce the driving resistances. The rise in c_c also leads to a less energy consumption E_b of up to 6.7% for the investigated values of c_c. However, the lower velocity also causes a higher driving time.

Figure 7.12 outlines an enlarged view of the uphill slope in the distance interval $s_{ego} \in [2000\,\text{m}, 4100\,\text{m}]$ of the profile shown in Figure 7.11.
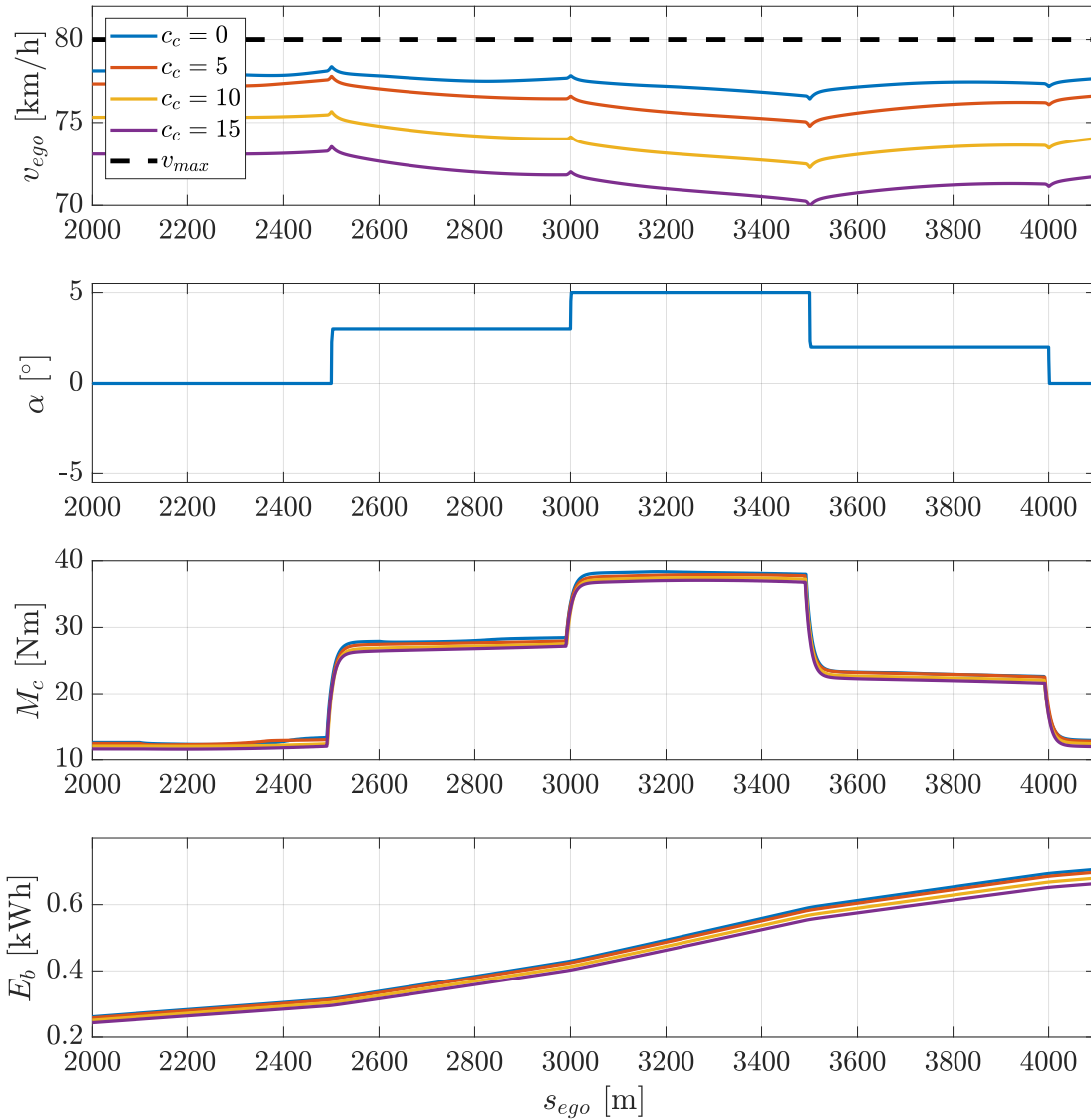
Figure 7.12: Controller reaction to an uphill slope of α in the distance interval $s_{ego} \in [2000\,\text{m}, 4100\,\text{m}]$ of Figure 7.11 for different values of the economic cost function tuning factor c_c.

The four controller settings behave nearly similar for this uphill slope but with the aforementioned difference in velocity. However, only a slight change in velocity could be observed when the slope change occurs since the controller smoothly adapts its applied torque to the new disturbance without significantly affecting the velocity.

The enlarged view of the downhill slope of the distance interval $s_{ego} \in [4000\,\text{m}, 6200\,\text{m}]$ is outlined in Figure 7.13.
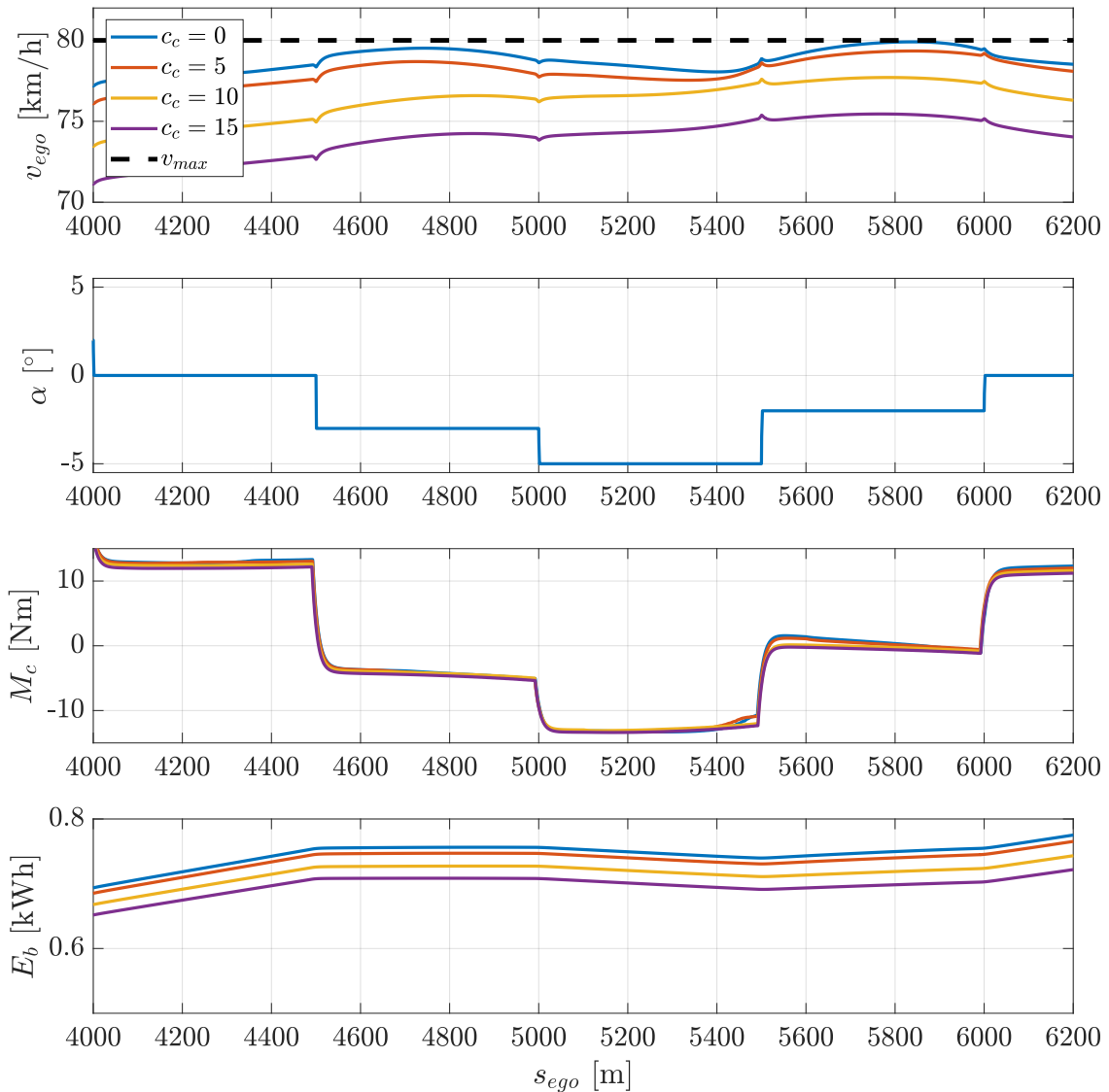
Figure 7.13: Controller reaction to a downhill slope of α in the distance interval $s_{ego} \in [4000\,\text{m}, 6200\,\text{m}]$ of Figure 7.11 for different values of the economic cost function tuning factor c_c.

For the downhill slope, the same disturbance suppression as for the uphill slope could be observed. As the potential energy of the vehicle is converted to kinetic energy when driving downhill, the vehicle would possibly accelerate beyond the legal speed limit. As this is modeled as a hard constraint in the controller design, the controller reliably ensures that this constraint is kept. Furthermore, the controller shows a smooth behavior in applying the torque to the powertrain of the vehicle.

7.2.3 Reaction to Prediction Horizon Changes

The prediction horizon of an MPC is an important parameter and should be wisely chosen. If it is chosen too small, the advantage of MPCs in adequately predicting the system behavior and generating a globally optimal solution is severely limited. Consequently, in the proposed controller setup, the controller could recognize slope and reference velocity changes too late and thus, no appropriate or optimal solution could be provided. However, a larger prediction horizon leads to a more complex optimization problem and therefore, to longer computation times which could jeopardize the real-time capability of the controller. Thus, the influence of different prediction horizon lengths is presented and discussed in the following.

Figure 7.14 outlines the reaction of the controller to changes in the reference speed $v_{max,ref}$ for different length of the prediction horizon between $S_p = 100\,\text{m}$ and $S_p = 1500\,\text{m}$ with a discretization of $10\,\text{m}$.
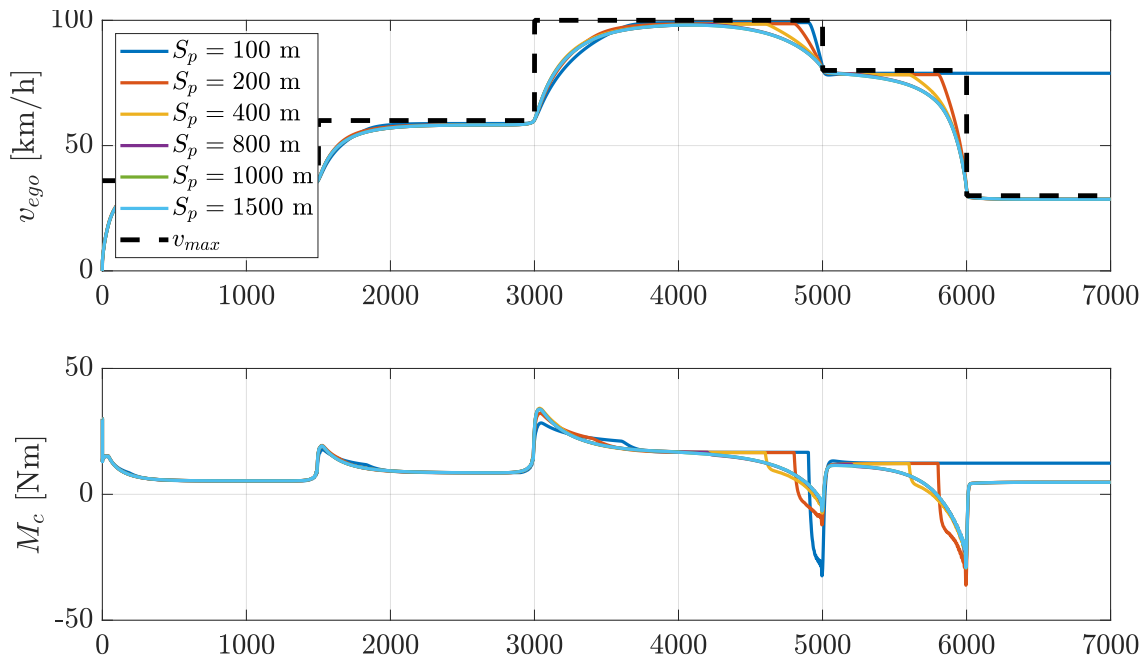
Figure 7.14: Controller reaction to changes in the reference speed $v_{max,ref}$ for different prediction horizon lengths S_p with a discretization of $10\,\text{m}$.

It can be clearly seen that higher prediction horizon lengths cause the controller to react earlier to the speed reference changes. This is obvious as the controller recognizes the reference velocity changes earlier if the prediction horizon is longer. However, Figure 7.14 also depicts that the trajectories for $S_p \geq 400\,\text{m}$ behave similarly so that a further increase of the prediction horizon shows no effect. In contrast, if the prediction horizon is too small, which can be seen for $S_p = 100\,\text{m}$ and $s_{ego} \geq 6000\,\text{m}$, the controller is not able to find a solution for the constrained optimization problem. This leads to undesired and unpredictable behavior of the controller and should be avoided.

Also, the influence of the prediction horizon on slope changes is further investigated and outlined in Figure 7.15.
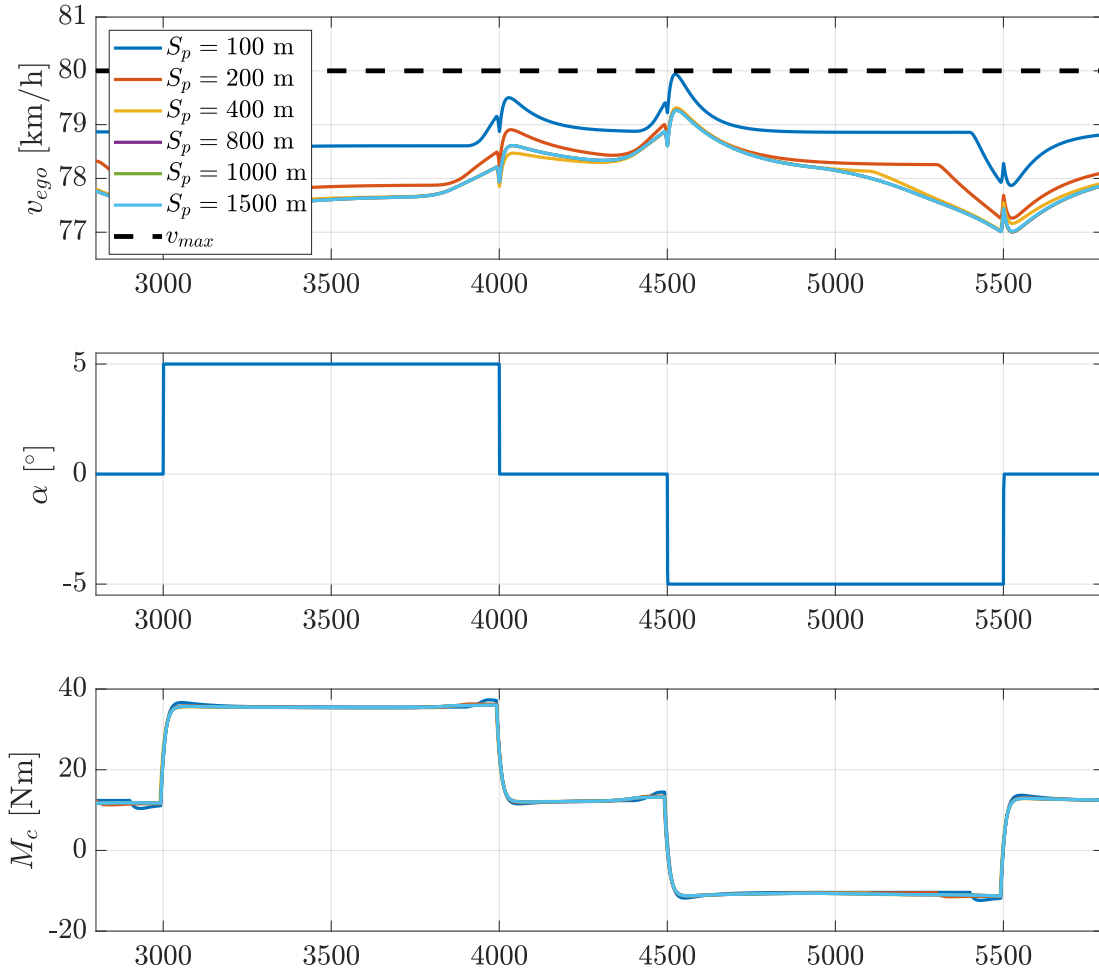
Figure 7.15: Controller reaction to changes in the road slope α for different prediction horizon lengths S_p with a discretization of $10\,\text{m}$.

It is shown that the impact of different prediction horizons behaves similarly to speed setpoint changes. It can be observed that the vehicle trajectories for $S_p \geq 400\,\text{m}$ are nearly equal. Since only the speed reference is modeled as a hard constraint in the controller design, short prediction horizons do not cause infeasibility of the optimization problem during slope changes.

The artificial driving cycles analyzed above give a good idea of how the controller behaves in clearly defined scenarios. However, also the impact of the prediction horizon on the controller performance regarding energy efficiency in the four drive cycles (see Section 5.2) needs to be analyzed. Furthermore, an assessment of the real-time capability of the controller is still pending. To answer these questions, the four drive cycles were simulated with the ENMPC using different prediction horizon lengths and their impact on the energy consumption, the driving time and the computation time of the optimization problem was investigated. The results are averaged over the four driving cycles and outlined in Figure 7.16, where the ENMPC was solved using acados [196] within Matlab R2020a on an Intel Core i7-8550U processor with a maximum frequency of $3.8\,\text{GHz}$.

(a) Mean energy consumption

(b) Mean computation time
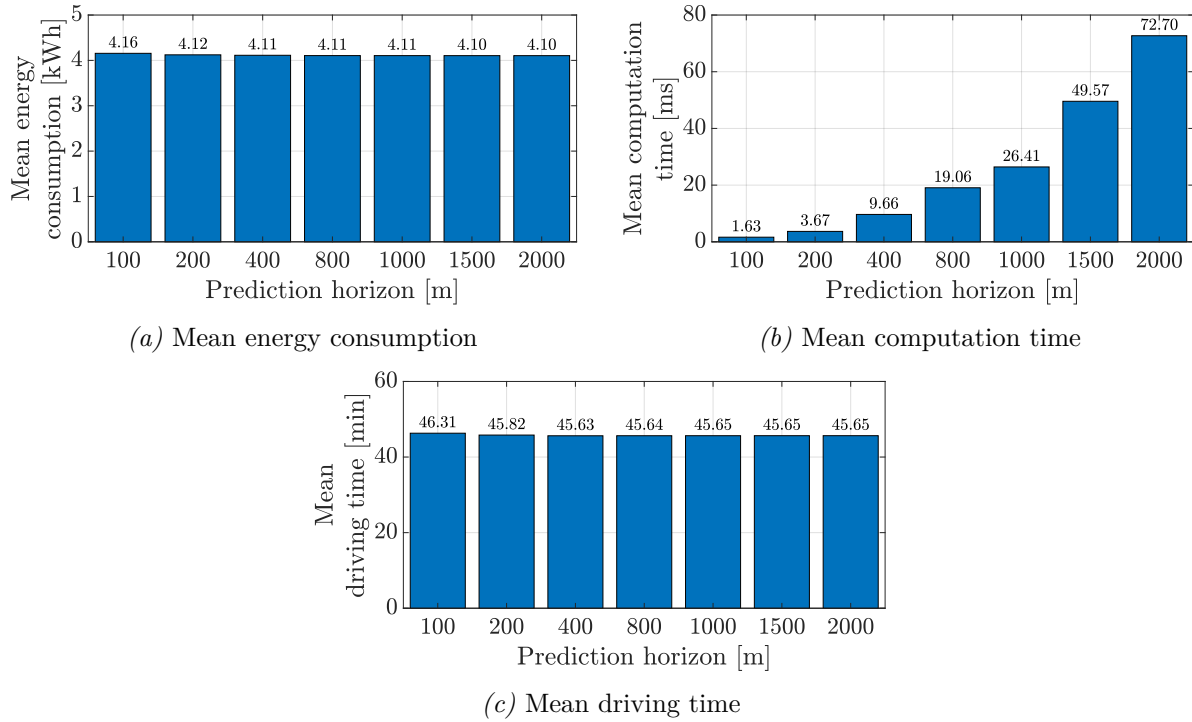
(c) Mean driving time

Figure 7.16: Investigation of different prediction horizon lengths S_p on the controller performance averaged over the four different drive cycles.

It is shown that the mean energy consumption and driving time converge to nearly constant values for prediction horizons greater than 400 m. Furthermore, it can be seen that the mean computation time increases not linearly with the prediction horizon length. Therefore, the prediction horizon should be kept as small as possible to achieve real-time capability of the controller. Consequently, a prediction horizon of 400 m is used throughout this thesis.

7.2.4 Controller Performance at the Drive Cycles

In the previous sections, the ENMPC has been presented and the performance has been evaluated using artificial test profiles for slope and speed changes. At these cycles, it could be demonstrated that the controller shows a suitable behavior for the use as an energy-efficient longitudinal controller for a BEV. However, these profiles do not represent realistic use cases for the vehicle. Therefore, in this section the controller performance driving the four drive cycles is evaluated using the nominal vehicle parameters (see Appendix B) and the cost function parameters $a_c = 6$, $b_c = 100$, $c_c = 100$ and $d_c = 15$.

The resulting trajectories in the powertrain efficiency map, which were simulated closed-loop for each drive cycle, are outlined in Figure 7.17. They also contain boxplots, which highlight the distributions of the output shaft torque of one drive M_{em} and the velocity of the vehicle v_{ego}. In comparison with the open-loop trajectories, as outlined in Figure 6.11, it can be generally seen that the amount of applied torque by the ENMPC is lower than for the manually driven drive cycles. Furthermore, the closed-loop trajectories are mostly do not reach the power envelope of the powertrain whereas the open-loop trajectories, in particular for drive cycle 1, 2 and 4 are often close to the power envelope. Moreover, the open-loop trajectories seem to be more randomly distributed as they are chosen manually by the driver whereas for the closed-loop trajectories the ENMPC uses similarly paths if transitioning from one speed setpoint to another. In particular, in the closed-loop trajectories of drive cycle 4 with an indistinct slope

(a) Drive cycle 1

(b) Drive cycle 2

(c) Drive cycle 3
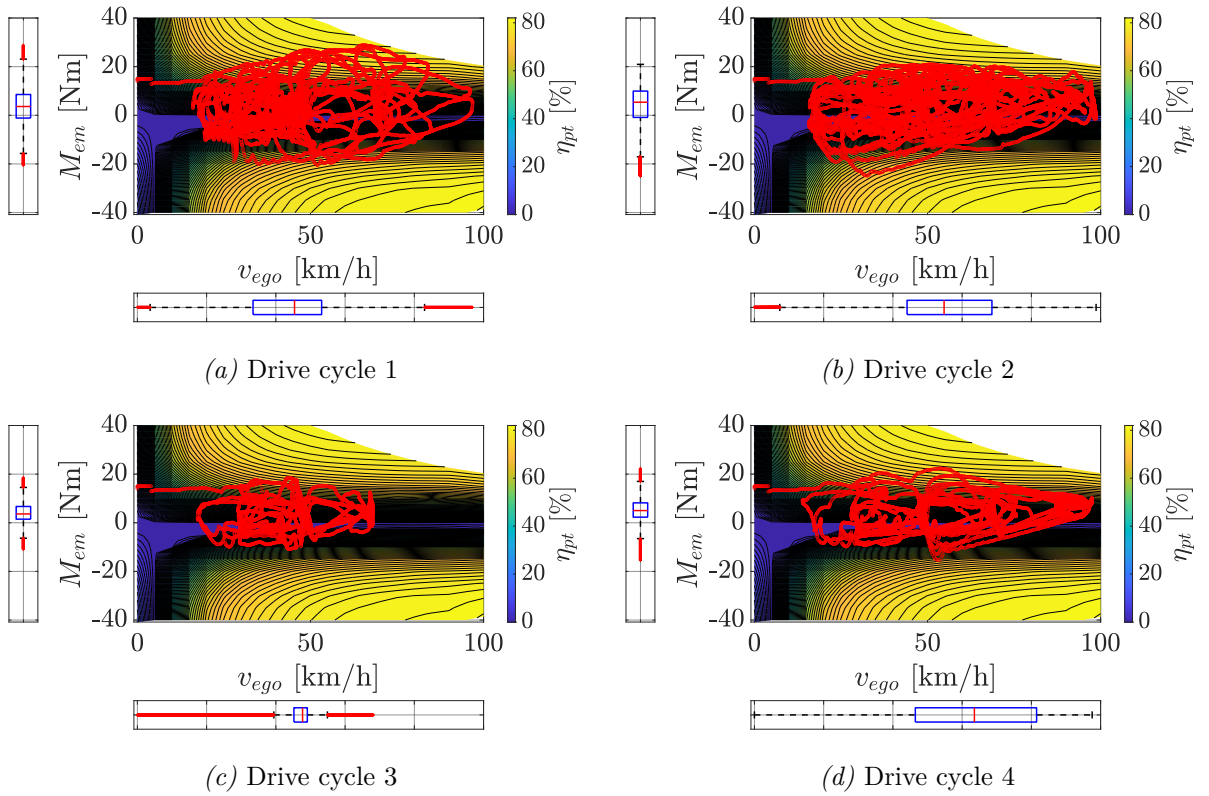
(d) Drive cycle 4

Figure 7.17: Closed-loop trajectories of the drive cycles for nominal parameter values in the powertrain efficiency map η_{pt}. The boxplots on the axes outline the distribution of the vehicle speed v_{ego} and the output shaft torque M_{em} of one drive.

profile, the similar transition paths gets visible.

Nevertheless, the trajectory profiles alone do not fully describe the controller behavior. Consequently, a comparison of the manually driven and the ENMPC driven drive cycles is given in Table 7.1.It can be seen that the proposed controller is capable of saving 5.1 % of energy on average by only increasing the average driving time by 1.1 %. However, the amount of energy that can be saved and the variation in driving time depends on the driven route and cannot be generalized. It can be seen that on hilly roads (drive cycles 1 and 2), the highest energy saving potential exists but with an increase of the driving time up to 8 %. In contrast, on the investigated routes with a less distinct slope profile (drive cycles 3 and 4), the energy-saving potential is more minor. Nevertheless, in drive cycle 4, the ENMPC is capable of saving 3.7 % of energy by simultaneously reducing the driving time by 1.5 %. Only in drive cycle 3 the ENMPC worsens the energy consumption by 1.4 % but reduces the driving time by 6.8 %.

The smooth behavior of the controller, which could already be observed in the artificial test profiles in the previous sections, could also be validated for the investigated drive cycles. It can be clearly seen that the maximum acceleration of the vehicle is significantly reduced to an average of $0.86 \, \mathrm{m/s^2}$, which is 57.7 % less compared to the manually driven routes. The same behavior could be observed for the maximum deceleration of the vehicle, which is reduced to an average of $-1.25 \, \mathrm{m/s^2}$ and is 46.5 % lower compared to manually driven routes.

As already seen in Figure 7.17, Table 7.1 also outlines a significant reduction of the maximum and minimum applied torque of -21% and -33.3%, which underpins, together with the lower minimum and maximum acceleration values, the smooth behavior of the proposed ENMPC.

Table 7.1: Comparison of the manual driven (open-loop) and ENMPC (closed-loop) controller regarding energy consumption, driving time, velocity, acceleration and applied torque.

| | Drive cycle | | | | |
	1	**2**	**3**	**4**	**Average**
Energy consumption					
Manual	4.29 kWh	6.33 kWh	2.14 kWh	4.36 kWh	4.28 kWh
ENMPC	3.98 kWh	5.99 kWh	2.17 kWh	4.20 kWh	4.06 kWh
Change	−7.2 %	−5.3 %	+1.4 %	−3.7 %	−5.1 %
Driving time					
Manual	53.5 min	56.3 min	34.0 min	39.1 min	45.7 min
ENMPC	54.1 min	60.8 min	31.6 min	38.5 min	46.3 min
Change	+1.1 %	+8.0 %	−6.8 %	−1.5 %	+1.1 %
Average velocity					
Manual	46.79 km/h	61.80 km/h	45.42 km/h	61.02 km/h	53.76 km/h
ENMPC	46.29 km/h	57.20 km/h	48.83 km/h	61.89 km/h	53.55 km/h
Change	−1.1 %	−7.4 %	+7.5 %	+1.4 %	+0.1 %
Maximum acceleration					
Manual	2.25 m/s²	1.89 m/s²	1.91 m/s²	1.96 m/s²	2.00 m/s²
ENMPC	0.83 m/s²	0.93 m/s²	0.76 m/s²	0.93 m/s²	0.86 m/s²
Change	−63.1 %	−50.8 %	−60.0 %	−57.0 %	−57.7 %
Minimum acceleration					
Manual	−2.43 m/s²	−2.34 m/s²	−1.95 m/s²	−2.48 m/s²	−2.30 m/s²
ENMPC	−1.19 m/s²	−1.36 m/s²	−1.03 m/s²	−1.43 m/s²	−1.25 m/s²
Change	−51.0 %	−41.9 %	−47.2 %	−45.7 %	−46.5 %
Maximum torque M_{em}					
Manual	30.00 Nm	30.00 Nm	30.00 Nm	30.00 Nm	30.00 Nm
ENMPC	28.82 Nm	20.94 Nm	18.53 Nm	22.35 Nm	22.66 Nm
Change	−3.9 %	−30.2 %	−25.5 %	−24.5 %	−21.0 %
Minimum torque M_{em}					
Manual	−28.07 Nm	−30.00 Nm	−23.18 Nm	−30.00 Nm	−27.81 Nm
ENMPC	−20.48 Nm	−24.83 Nm	−10.85 Nm	−15.40 Nm	−17.89 Nm
Change	−27.0 %	−17.2 %	−53.2 %	−35.7 %	−33.3 %

7.2.5 Comparison of the Economic NMPC Approach With a Convex Optimization Approach

Considering the battery dynamics in the presented controller concept has led to an ENMPC approach. To reduce the complexity and achieve real-time capability, MPCs are often formulated using convex optimization, which leads to an LMPC design. For this reason, the ENMPC is compared with the LMPC approach from Schwickart [48] which is summarized in the following and is adapted to the proTRon Evolution test vehicle. For details beyond this summary, the reader is referred to [48].

For comparability with the presented ENMPC approach in (7.17), the optimization problem outlined in [48] is reformulated in a continuous representation. Furthermore, the controller output is changed from the longitudinal traction force acting on the body of the vehicle to the engine output shaft torque, which results in an additional scaling in the prediction model. The optimization problem is described by

$$
\min_{M_c(s), u_{cons}(s)} \int_0^{S_p} [q_{s,s} \cdot (\hat{e}_{kin}(s) - \hat{e}_{kin,ref}(s))^2 + r_{s,s} \cdot (M_c(s) - M_{ref}(s))^2] \mathrm{d}s
$$
$$
+ l_{e,s} \cdot \hat{E}_{bat}(S_p) + \bar{q}_{e,s} \cdot (\hat{e}_{kin}(S_p) - \hat{e}_{kin,ref}(S_p))^2 \tag{7.19a}
$$

s.t.

$$
\frac{\mathrm{d}}{\mathrm{d}s} \begin{bmatrix} \hat{e}_{kin} \\ \hat{E}_{bat} \end{bmatrix} = \begin{bmatrix} M_c \frac{i_g}{r_w} - c_r m_v g \cos(\alpha) - m_v g \sin(\alpha) - \frac{\rho_{air} c_w A \hat{e}_{kin}}{m_{eq}} \\ u_{cons} \end{bmatrix} \tag{7.19b}
$$

$$
\mathbf{x}(0) = \mathbf{x}_0 \tag{7.19c}
$$
$$
0 \leq \hat{e}_{kin}(s) \qquad\qquad s \in [0, S_p) \tag{7.19d}
$$
$$
M_{min} \leq M_c(s) \leq M_{max} \qquad\qquad s \in [0, S_p) \tag{7.19e}
$$
$$
M_c(s) \leq g_3 \hat{e}_{kin}(s) + g_4 \qquad\qquad s \in [0, S_p) \tag{7.19f}
$$
$$
u_{cons}(s) \geq a_j \hat{e}_{kin}(s) + b_j M_c(s) + c_j \qquad \forall j \in \{0, 1, \dots, 4\} \qquad s \in [0, S_p). \tag{7.19g}
$$

Cost function (7.19a) is similar to the ENMPC cost function, which includes a penalty on the speed reference, the consumed battery energy over the prediction horizon as well as a deviation from the reference torque trajectory. However, the optimization considers an additional optimization variable u_{cons} which is used together with the second state of (7.19b) and the inequality constraint (7.19g) to include a static power consumption map inside the optimization problem using the technique of separable programming [199] to achieve a convex optimization problem formulation. In addition, the optimization variable M_c is constraint using (7.19e) and (7.19f). The torque constraints are outlined in Figure 7.18. They are adapted to the powertrain capabilities of the proTRon evolution. In Figure 7.18, the maximum available torque for acceleration and deceleration is enclosed by the maximum power envelopes for acceleration and deceleration and marked in blue and red. However, the two gearboxes of the vehicle are only capable of transferring a maximum engine torque of 60 Nm in both directions, which is denoted by (7.19e). Additionally, the power envelope for positive torques is approximated by (7.19f). The generation of the kinetic energy reference $\hat{e}_{kin,ref}$ is done in the same way as for the ENMPC described in Section 7.1.5, where the reference speed is converted into a kinetic energy equivalent by

$$
\hat{e}_{kin,ref} = \frac{1}{2} m_{eq} v_{max,mpc}^2. \tag{7.20}
$$

To compare the nominal controller behaviors of the ENMPC and the LMPC, the reactions of both controllers on slope changes and reference speed changes are outlined in Figures 7.19 and 7.20, where the cost function of the LMPC is parameterized
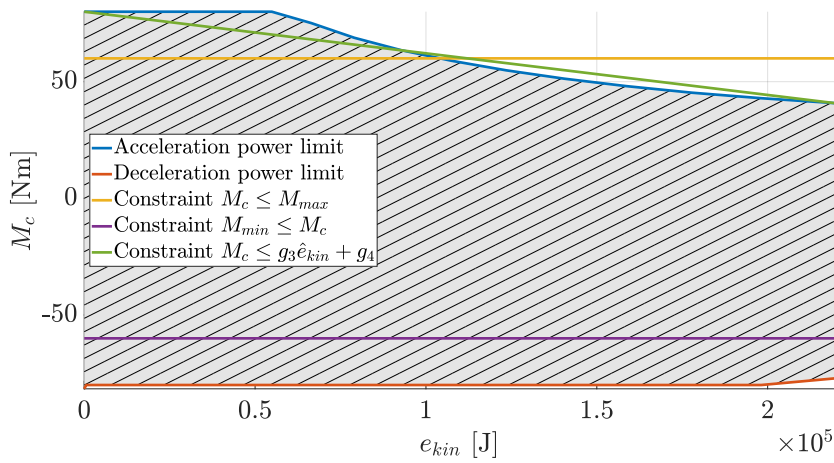
Figure 7.18: Constraints of the optimization problem regarding to power limitations.
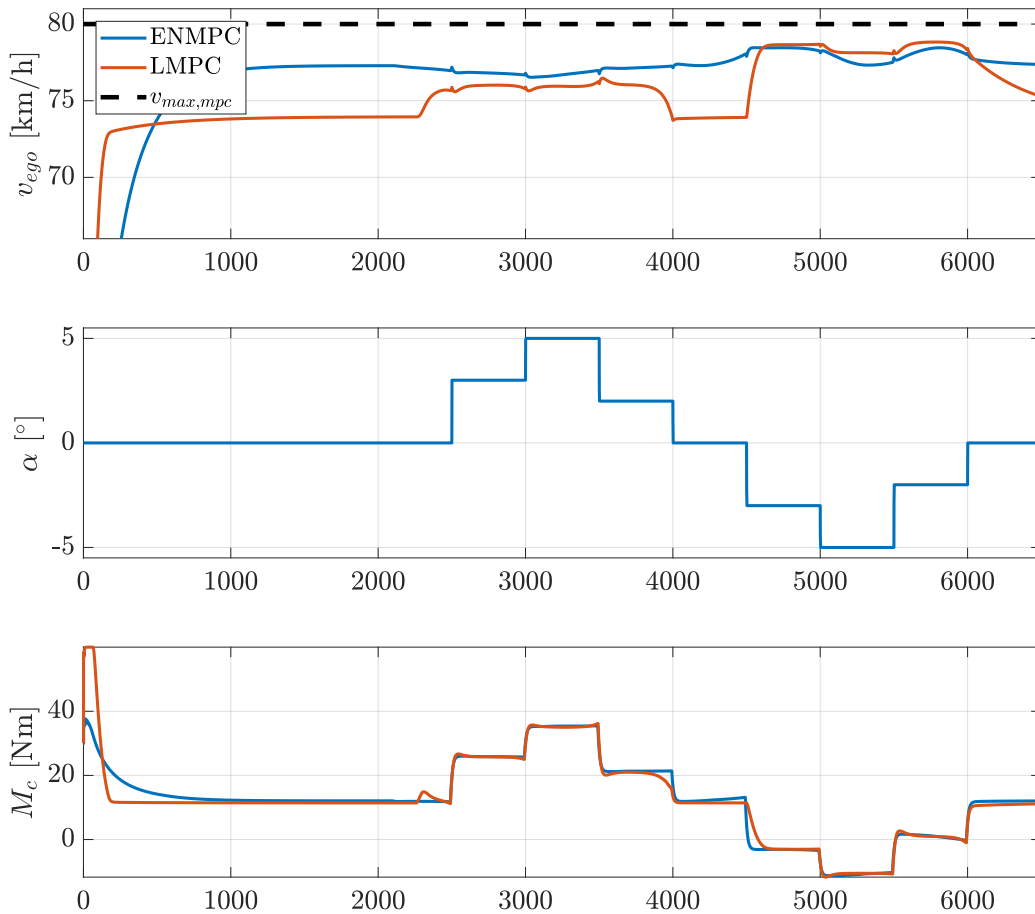
Figure 7.19: Controller reaction to changes in the road slope α for different prediction horizon lengths S_p with a discretization of $10\,\mathrm{m}$.

with $q_{s,s} = 2$, $r_{s,s} = 200 \times 10^4$, $l_{e,s} = 20 \times 10^6$ and $\bar{q}_{e,s} = 25.25$. Generally, it can be denoted that the LMPC reacts more harshly in both situations than the ENMPC. Especially for slope changes, it can be observed that the tracking error of the LMPC of the reference velocity is more prominent than for the ENMPC. Furthermore, slope changes are not suppressed in the linear approach as good as with the nonlinear ENMPC approach.

In Figure 7.20, a more direct reaction of the LMPC to speed reference changes compared to the ENMPC can be observed. It can be seen that the controller reacts later to the reference velocity change and thus, the applied torque needs to be larger. Consequently, it also results in a higher energy consumption than in the ENMPC approach and the controller behaves less smooth. Another drawback is the absence of
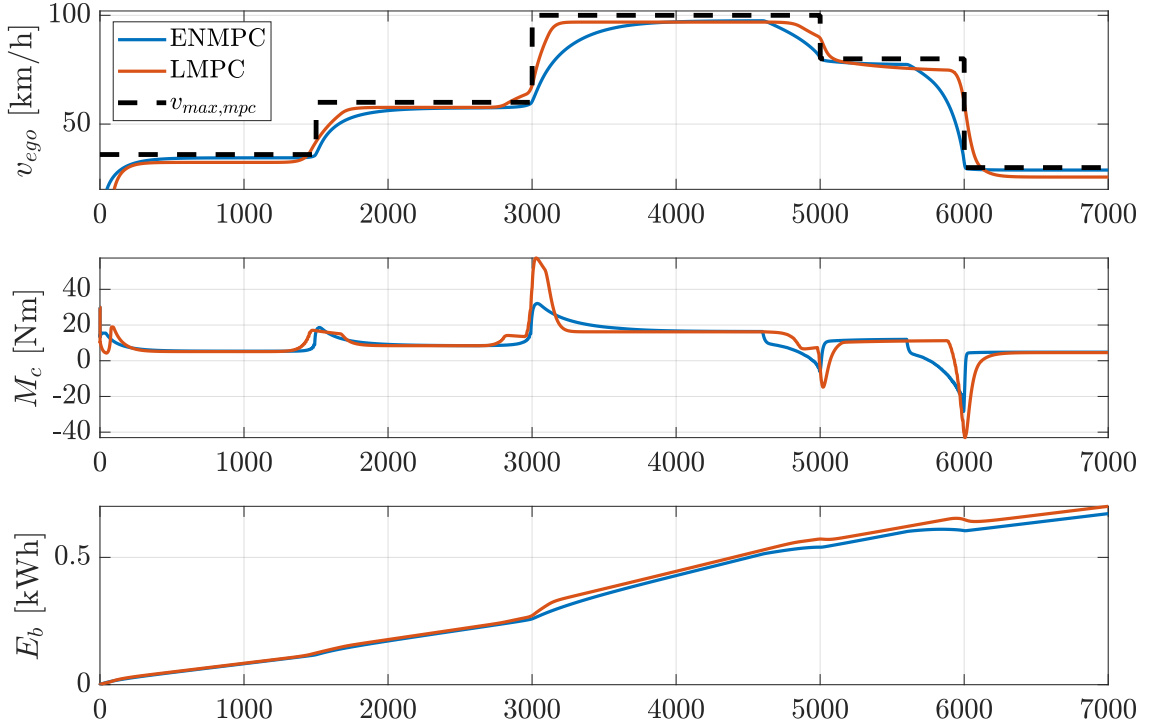
Figure 7.20: Controller reaction to changes in the reference speed $v_{max,mpc}$ for different prediction horizon lengths S_p with a discretization of $10\,\mathrm{m}$.

a constraint in the proposed LMPC of [48], which considers the maximum allowed speed as an upper boundary. Consequently, the legal speed limit is exceeded, especially for deceleration maneuvers, which is avoided in the ENMPC design.

To compare the performance on the four drive cycles also the LMPC has been simulated on these drive cycles. The results, compared to the ENMPC, are outlined in Table 7.2. It can be seen that the linear approach consumes 5.8 % more energy on average but also reduces the driving time by 6.6 % on average. This is reasonable because the LMPC reacts more harshly to environmental changes and has no constraint on the maximum allowed velocity. The lack of this constraint causes the LMPC to drive with a higher average speed, especially when the reference speed is reduced only for a small distance. This behavior could be observed, particularly when driving curves which leads to a too high curvature speed and is avoided by the ENMPC approach. The harsh controller reaction of the LMPC could also be seen from the maximum and minimum acceleration values outlined in Table 7.2, which are significantly higher than for the ENMPC. It needs to be noticed that the proTRon Evolution, due to its low tare weight of $550\,\mathrm{kg}$, is a special use case for a longitudinal controller where the compared LMPC of [48] was not initially designed for. Nevertheless, both controllers are suitable as longitudinal controllers of the BEV.

Table 7.2: Comparison of the LMPC and ENMPC controller regarding energy consumption, driving time, velocity, acceleration and applied torque.

	Drive cycle				
	1	**2**	**3**	**4**	**Average**
Energy consumption					
ENMPC	3.98 kWh	5.99 kWh	2.17 kWh	4.20 kWh	4.06 kWh
LMPC [48]	4.28 kWh	6.45 kWh	2.19 kWh	4.49 kWh	4.35 kWh
Change	$+7.5\%$	$+7.7\%$	$+0.9\%$	$+6.9\%$	$+5.8\%$
Driving time					
ENMPC	54.1 min	60.8 min	31.6 min	38.5 min	46.3 min
LMPC [48]	50.2 min	54.5 min	30.8 min	36.1 min	42.9 min
Change	-7.2%	-10.4%	-2.5%	-6.2%	-6.6%
Average velocity					
ENMPC	46.29 km/h	57.20 km/h	48.83 km/h	61.89 km/h	53.55 km/h
LMPC [48]	49.89 km/h	63.83 km/h	50.11 km/h	66.09 km/h	57.48 km/h
Change	$+7.8\%$	$+11.6\%$	$+2.6\%$	$+6.8\%$	$+7.2\%$
Maximum acceleration					
ENMPC	$0.83\,\mathrm{m/s^2}$	$0.93\,\mathrm{m/s^2}$	$0.76\,\mathrm{m/s^2}$	$0.93\,\mathrm{m/s^2}$	$0.86\,\mathrm{m/s^2}$
LMPC [48]	$1.76\,\mathrm{m/s^2}$	$2.01\,\mathrm{m/s^2}$	$1.08\,\mathrm{m/s^2}$	$1.71\,\mathrm{m/s^2}$	$1.64\,\mathrm{m/s^2}$
Change	$+112.0\%$	$+116.1\%$	$+42.1\%$	$+83.9\%$	$+88.5\%$
Minimum acceleration					
ENMPC	$-1.19\,\mathrm{m/s^2}$	$-1.36\,\mathrm{m/s^2}$	$-1.03\,\mathrm{m/s^2}$	$-1.43\,\mathrm{m/s^2}$	$-1.25\,\mathrm{m/s^2}$
LMPC [48]	$-1.99\,\mathrm{m/s^2}$	$-2.14\,\mathrm{m/s^2}$	$-1.06\,\mathrm{m/s^2}$	$-2.37\,\mathrm{m/s^2}$	$-2.30\,\mathrm{m/s^2}$
Change	$+67.2\%$	$+57.4\%$	$+2.9\%$	$+65.8\%$	$+48.3\%$
Maximum torque M_{em}					
ENMPC	28.82 Nm	20.94 Nm	18.53 Nm	22.35 Nm	22.66 Nm
LMPC [48]	29.99 Nm	29.71 Nm	22.53 Nm	29.92 Nm	28.04 Nm
Change	$+4.1\%$	$+41.9\%$	$+21.6\%$	$+33.9\%$	$+25.4\%$
Minimum torque M_{em}					
ENMPC	-20.48 Nm	-24.83 Nm	-10.85 Nm	-15.40 Nm	-17.89 Nm
LMPC [48]	-29.99 Nm	-29.99 Nm	-13.16 Nm	-26.61 Nm	-24.94 Nm
Change	$+46.4\%$	$+20.8\%$	$+21.3\%$	$+72.8\%$	$+40.3\%$

7.3 Conclusions

This chapter has outlined the development of an ENMPC approach for the energy-efficient longitudinal motion control of a BEV. To achieve real-time capability also for a nonlinear approach, the optimization problem has been kept as simple as possible. To include all important parameter dependencies into the prediction model of the controller without unnecessarily increasing the problem size, the open-loop sensitivity analysis results of Chapter 6 and nominal simulations on the four drive cycles have been used. It has been led to a prediction model using a lookup table approximation for the electrical drive and inverter power demands and is combined with a battery dynamics model. Furthermore, the longitudinal motion model has been integrated to predict the vehicle behavior and an economic cost function has been presented to achieve energy-efficient driving behavior of the controller.

The proposed controller has been simulatively tested on artificial test scenarios as well as on the four drive cycles to evaluate the performance of the controller. It has been shown that the ENMPC is capable of saving 5.1 % of energy on average by only increasing the driving time by 1.1 % on average compared to the manually driven routes.

Since the complexity of an ENMPC approach is high and it is difficult to solve, the controller has also been compared to a less complex quadratic optimization problem. It has been shown that the proposed ENMPC behaves, in general, more smoothly and is capable of saving up to 5.8 % energy on average.

It can be summarized that the proposed ENMPC outperforms the LMPC by considering all parameters which are identified as relevant by the open-loop sensitivity analysis. Furthermore, it has been shown that the chosen complexity of the controller using the acados [196] and HPIPM [197] implementation is real-time capable and thus, applicable on real vehicle hardware.

8 Sensitivity Analysis of the Closed-Loop Energy-Efficient Longitudinal Control

Applying the ENMPC presented in the previous chapter results in a complex closed-loop controlled system consisting of many parameter dependencies which could influence the energy consumption of the vehicle. In the following investigation, a sensitivity analysis of the vehicle model is performed closed-loop together with the ENMPC on each of the four drive cycles from Section 5.2. In contrast to the open-loop analysis, the vehicle operation gains the degree of freedom of free driving speed selection. However, the system complexity also increases significantly, which becomes noticeable by an increase to 54 parameters to be examined. Besides the vehicle parameters, the controller contains several tuning parameters and measured quantities. Setting these tuning parameters and the accuracy of the measured or estimated quantities could significantly influence the energy consumption of the vehicle. Consequently, these dependencies need to be considered in the closed-loop investigation. Due to the free choice of the vehicle speed by the ENMPC, the driving time could also be influenced and thus it is also investigated throughout this chapter.

For the closed-loop sensitivity analysis at first, the PDFs for the investigated parameters need to be defined. Afterward, a Morris screening is performed to separate influential from non-influential parameters and to determine the parameter set for the subsequent variance-based sensitivity analysis. The generalized Sobol indices are estimated and the convergence is proven and outlined using the law of big numbers and bootstrap resampling. Correspondingly, the results of the closed-loop analysis are presented and the most influential parameters are discussed.

Accordingly, based on the findings of the closed-loop sensitivity analysis, an optimal parameter setup for an energy-optimal driving of the BEV is proposed and conclusions for a proper vehicle setup are drawn.

8.1 Definition of the Input Parameter Distributions

For the closed-loop simulations, the PDFs of the open-loop analysis from Section 6.1 were adopted and additionally expanded to the controller related parameters that also will be investigated. The resulting parameter set for the closed-loop sensitivity analysis is outlined in Table 8.1. In the last section of the table, the 15 additional controller parameters are outlined. The only tunable controller parameter investigated is the energy penalization parameter c_c in the cost function. It could be used by the driver or the application engineer to adapt the controller even to a better reference speed tracking or to improve the energy savings.

All other parameters outlined in the table relate to measured or estimated quantities that need to be known in the controller. The parameters which cannot directly be measured in the vehicle and need to be estimated from other information sources, e.g., the SoC of the battery, are outlined as estimation errors.

Table 8.1: Distributions of parameters for the closed-loop sensitivity analysis.

	Name	Description	Type of error	Distribution	Parameter	Values	Units
Battery	$e_{R_s,b}$	Deviation of series resistance R_s	relative	Normal	μ, σ	0, 0.05/3	–
	e_{C_1}	Deviation of capacitance C_1	relative	Normal	μ, σ	0, 0.05/3	–
	e_{R_1}	Deviation of resistance R_1	relative	Normal	μ, σ	0, 0.05/3	–
	e_{C_2}	Deviation of capacitance C_2	relative	Normal	μ, σ	0, 0.05/3	–
	e_{R_2}	Deviation of resistance R_2	relative	Normal	μ, σ	0, 0.05/3	–
	$e_{u_{ocv}}$	Deviation of open circuit voltage	relative	Normal	μ, σ	0, 0.05/3	–
	ϑ_b	Variation of start temperature	absolute	Uniform	a, b	20, 40	°C
	$R_{th_{ca}}$	Variation of thermal resistance $R_{th_{ca}}$	absolute	Normal	μ, σ	2.6, 0.13/3	Ω
	$R_{th_{ct}}$	Variation of thermal resistance $R_{th_{ct}}$	absolute	Normal	μ, σ	0.37, 0.02/3	Ω
	$R_{th_{ta}}$	Variation of thermal resistance $R_{th_{ta}}$	absolute	Normal	μ, σ	1.05, 0.05/3	Ω
	C_c	Variation of thermal capacitance C_c	absolute	Normal	μ, σ	2544.2, 127.21/3	F
	C_t	Variation of thermal capacitance C_t	absolute	Normal	μ, σ	8.072, 3.4/3	F
Inverter	e_{a_t}	Deviation of forward characteristics IGBT	relative	Normal	μ, σ	0, 0.05/3	–
	e_{b_t}		relative	Normal	μ, σ	0, 0.05/3	–
	e_{a_d}	Deviation of forward characteristics diode	relative	Normal	μ, σ	0, 0.05/3	–
	e_{b_d}		relative	Normal	μ, σ	0, 0.05/3	–
	$e_{a_{Err}}$	Deviation of reverse recovery characteristics diode	relative	Normal	μ, σ	0, 0.05/3	–
	$e_{b_{Err}}$		relative	Normal	μ, σ	0, 0.05/3	–
	$e_{c_{Err}}$		relative	Normal	μ, σ	0, 0.05/3	–
	$e_{a_{Eon}}$	Deviation of turn on losses IGBT	relative	Normal	μ, σ	0, 0.05/3	–
	$e_{b_{Eon}}$		relative	Normal	μ, σ	0, 0.05/3	–
	$e_{c_{Eon}}$		relative	Normal	μ, σ	0, 0.05/3	–
	$e_{a_{Eoff}}$	Deviation of turn off losses IGBT	relative	Normal	μ, σ	0, 0.05/3	–
	$e_{b_{Eoff}}$		relative	Normal	μ, σ	0, 0.05/3	–
	$e_{c_{Eoff}}$		relative	Normal	μ, σ	0, 0.05/3	–
	$\vartheta_{w,in}$	Variation of water inlet temperature	absolute	Uniform	a, b	0, 60	°C
Drive	$e_{R_s,EM}$	Deviation of winding resistance R_s	relative	Normal	μ, σ	0, 0.03/3	–
	e_{L_d}	Deviation of direct inductance L_d	relative	Normal	μ, σ	0, 0.0133/3	–
	e_{L_q}	Deviation of quadrature inductance L_q	relative	Normal	μ, σ	0, 0.015/3	–
	$e_{\Psi_{pm}}$	Deviation of magnetic flux Ψ_{pm}	relative	Normal	μ, σ	0, 0.025/3	–
	e_{ξ_q}	Deviation of quadrature iron losses ξ_q	relative	Normal	μ, σ	0, 0.05/3	–
	e_{ξ_d}	Deviation of direct iron losses ξ_d	relative	Normal	μ, σ	0, 0.05/3	–
	ϑ_{ro}	Variation of rotor temperature ϑ_{ro}	absolute	Uniform	a, b	40, 80	°C
	ϑ_{st}	Variation of stator temperature ϑ_{st}	absolute	Uniform	a, b	40, 80	°C
Vehicle	m_v	Variation of the vehicle mass	absolute	Birnbaum–Saunders	β, γ	652.11, 0.074	kg
	P_{pto}	Variation of auxiliary consumers	absolute	Uniform	a, b	250, 750	W
	ϑ_a	Variation of ambient temperature	absolute	Normal	μ, σ	12.26, 8.53	°C
	p_{air}	Variation of ambient pressure	absolute	Normal	μ, σ	98427.7, 843.09	Pa
	c_r	Variation of rolling resistance	absolute	Uniform	a, b	0.01, 0.015	–
Controller	c_c	Energy related cost function parameter	absolute	Uniform	a, b	0, 6	-
	$e_{\vartheta_a,mpc}$	Error of ambient temperature measurement	relative	Normal	μ, σ	0, 0.05/3	–
	$p_{air,mpc}$	Error of air pressure estimation	absolute	Normal	μ, σ	98427.7, 843.09	Pa
	$c_{r,mpc}$	Error of rolling resistance estimation	absolute	Uniform	a, b	0.01, 0.015	–
	$m_{v,mpc}$	Error of vehicle mass estimation	relative	Normal	μ, σ	0, 0.1/3	–
	$e_{u_{ocv},mpc}$	Error of open circuit voltage estimation	relative	Normal	μ, σ	0, 0.1/3	–
	$e_{R_s,mpc}$	Error of battery series resistance estimation	relative	Normal	μ, σ	0, 0.1/3	–
	$e_{R_1,mpc}$	Error of battery RC-resistance estimation	relative	Normal	μ, σ	0, 0.1/3	–
	$e_{C_1,mpc}$	Error of battery RC-capacitance estimation	relative	Normal	μ, σ	0, 0.1/3	–
	$e_{\alpha,mpc}$	Error of slope measurement	relative	Normal	μ, σ	0, 0.05/3	–
	$e_{P_{pto},mpc}$	Error of auxiliary power estimation	Relative	Normal	μ, σ	0, 0.05/3	W
	$e_{curv,mpc}$	Error of curvature measurement	relative	Normal	μ, σ	0, 0.05/3	–
	$e_{SoC,mpc}$	Error of SoC estimation	relative	Normal	μ, σ	0, 0.10/3	–
	$e_{\vartheta_b,mpc}$	Error of battery temperature estimation	relative	Normal	μ, σ	0, 0.1/3	–
	$e_{I_b,mpc}$	Error of battery current measurement	relative	Normal	μ, σ	0, 0.05/3	–

Parameters that can directly be measured, e.g., the battery current I_b, are outlined as measurement errors. The distributions of these errors are assumed based on how difficult the specific quantity can be measured or estimated. For example, the battery-related parameter fluctuations are considered to be $3\sigma = 0.1/3$ since only current, voltage and temperature can be measured externally and all internal parameters must be determined from these. This leads to a more difficult identification than, for example, the measurement of the battery current, whose acquisition is not a major technical challenge.

8.2 Morris Screening

The first step in the closed-loop analysis is to perform a Morris screening to distinguish important from unimportant parameters, similar to the Morris screening in the open-loop analysis outlined in Section 6.2. In the closed-loop setup the consumed battery energy E_b and the powertrain losses P_l are considered to analyze the energy consumption and the power losses of the vehicle during operation.

The parameter input space is discretized with $p = 4$ and a step size of $\Delta = 2/3$ is chosen. As recommended in [95–97], $r = 10$ trajectories are simulated. This setup leads to a total number of simulations for the Morris screening and the investigated parameters of Table 6.1 of $N_m = r(k+1) = 10(54+1) = 550$.

The results of the Morris screening for the four drive cycles regarding the consumed battery energy E_b are outlined in Figure 8.1. Similarly, the power losses of the powertrain P_l are depicted in Figure 8.2.

For the consumed battery energy E_b, as outlined in Figure 8.1, it can be observed that the statement $\sigma \ll \mu^*$ holds. It indicates a mostly linear dependency between the analyzed parameters. Thus, it can be said that the parameters with high values of μ^* affect the consumed battery energy most but probably do not interact with other parameters. In contrast, Figure 8.2 outlines that interactions between parameters of the output P_l can be assumed since $\mu^* \approx \sigma$ holds for most of the parameters. In comparison to the open-loop Morris screening of Section 6.2, the parameter influences changed slightly. The error of the open-circuit voltage $e_{u_{ocv}}$ and the variation of p_{air} are less influential, whereas the rotor temperature ϑ_{ro} should be considered.

Figures 8.1 and 8.2 outline that only a subset of the investigated parameters still has high values of μ^* and σ in relation to the other studied parameters. Also, a subset of the added controller parameters is identified as important. Consequently, only these parameters need to be considered in the closed-loop variance-based sensitivity analysis and thus, an extensive parameter reduction can be performed. The remaining parameters are outlined in Table 8.2.

Assuming a sample size for a variance-based sensitivity analysis of $N = 5000$, which will be outlined as sufficient in Section 8.3.1 for the closed-loop analysis, the initial Morris screening significantly reduces the computational effort. Calculating the sensitivity measures for all parameters from Table 8.1 would require $N_s = N(k+2) = 5000(54+2) = 280000$ simulation runs, whereas the reduced set of parameters from Table 8.2 would require only $N_s = N(k+2) = 5000(13+2) = 75000$ simulation runs. Therefore, the reduced parameter set requires only a quarter of the resources without losing significance.

(a) Drive cycle 1

(b) Drive cycle 2

(c) Drive cycle 3

(d) Drive cycle 4
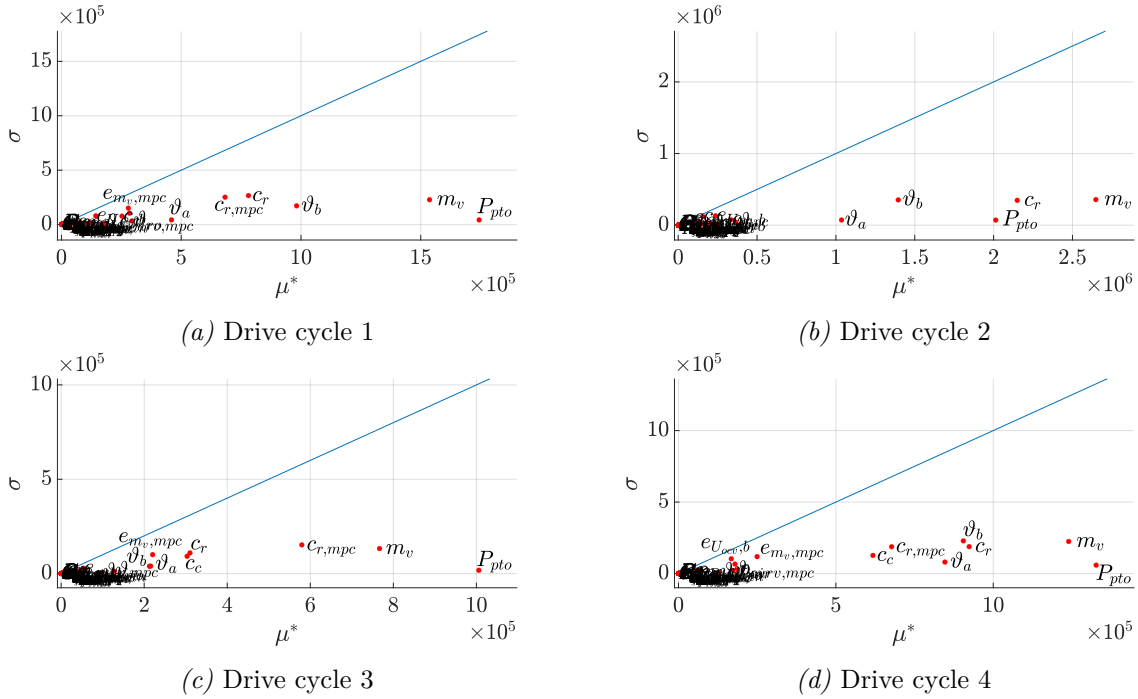
Figure 8.1: Closed-loop Morris screening for the consumed battery energy E_b

(a) Drive cycle 1

(b) Drive cycle 2

(c) Drive cycle 3

(d) Drive cycle 4
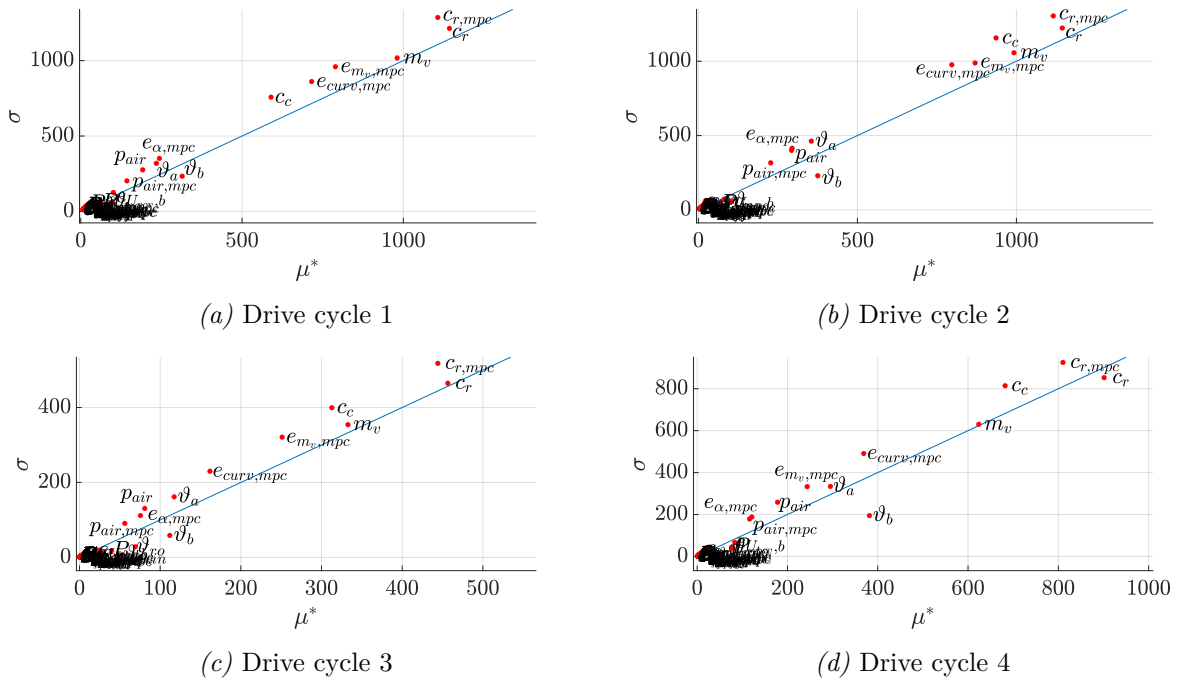
Figure 8.2: Closed-loop Morris screening for the total drive power losses P_l

Table 8.2: Reduced parameter set for the closed-loop variance-based sensitivity analysis.

	Name	Description	Type of error	Distribution	Parameter	Values	Units
Battery	ϑ_b	Variation of start temperature	absolute	Uniform	a, b	20, 40	$^\circ$C
Inverter	$\vartheta_{w,in}$	Variation of water inlet temperature	absolute	Uniform	a, b	0, 50	$^\circ$C
Drive	ϑ_{ro}	Variation of rotor temperature ϑ_{ro}	absolute	Uniform	a, b	40, 80	$^\circ$C
Vehicle	m_v	Variation of the vehicle mass	absolute	Birnbaum–Saunders	β, γ	652.11, 0.074	kg
	P_{pto}	Variation of auxiliary consumers	absolute	Uniform	a, b	250, 750	W
	ϑ_a	Variation of ambient temperature	absolute	Normal	μ, σ	12.26, 8.53	$^\circ$C
	c_r	Variation of rolling resistance	absolute	Uniform	a, b	0.01, 0.015	–
Controller	c_c	Energy related cost function parameter	absolute	Uniform	a, b	0, 6	-
	$c_{r,mpc}$	Error of rolling resistance estimation	absolute	Uniform	a, b	0.01, 0.015	–
	$m_{v,mpc}$	Error of vehicle mass estimation	relative	Normal	μ, σ	0, 0.1/3	–
	$e_{P_{pto},mpc}$	Error of auxiliary power estimation	Relative	Normal	μ, σ	0, 0.05/3	W
	$e_{curv,mpc}$	Error of curvature measurement	relative	Normal	μ, σ	0, 0.05/3	–

8.3 Variance-Based Sensitivity Indices

The variance-based sensitivity analysis for the closed-loop setup is done for the reduced parameter set in Table 8.2. As already outlined in Section 3.2.5, the calculated sensitivity measures using the estimators of Jansen, Sobol and Saltelli need to be verified regarding their convergence and accuracy. However, since the scalar measures provide a very good measure of convergence, in the following, the evaluation of the individual sensitivity measures for different sample sizes as in the open-loop analysis is omitted.

In contrast to the open-loop investigation, the ENMPC offers another degree of freedom by adapting the velocity during the drive cycle instead of keeping it fixed to predefined values. Thus, besides the consumed battery energy E_b and the powertrain losses P_l, the influence on the driving time t_d is also investigated.

The closed-loop analysis results, as well as the results for ensuring convergence, are presented and discussed in the following.

8.3.1 Evaluation of the Approximation Accuracy

The approximation error is evaluated using the methods presented in Section 3.2.5. Since the convergence behavior depends not only on the sampling strategy and the used estimators but is also influenced by the investigated system and the corresponding outputs, each of them needs to be analyzed separately. Furthermore, according to (3.26), the investigated model changes when another drive cycle is analyzed. Consequently, the approximation accuracy of the estimated generalized first order effects $\hat{S}_i^G$ and generalized total effects $\hat{S}_{T_i}^G$ need to be evaluated for different sample sizes $N \in [100, 5000]$ for each of the drive cycles, estimators and outputs of interest.

As already mentioned above, only the results of the scalar error measures $\varepsilon^G_{\hat{S}_j}$ and $\varepsilon^G_{\hat{S}_{T_j}}$ are presented. These are outlined in Figures 8.3, 8.4 and 8.5 for the consumed battery energy E_b, the powertrain losses P_l and the driving time t_d. Generally, it can be seen that the convergence errors $\varepsilon^G_{\hat{S}_j}$ and $\varepsilon^G_{\hat{S}_{T_j}}$ of each

(a) First order effects $\varepsilon_{\hat{S}^G_j}$ *(b) Total effects $\varepsilon_{\hat{S}^G_{T_j}}$*
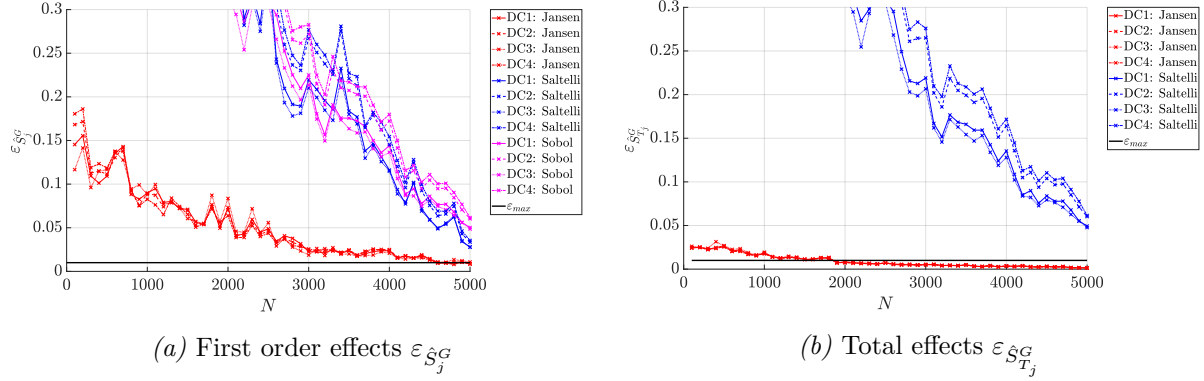
Figure 8.3: Convergence error of the first order and total generalized Sobol indices for the consumed battery energy E_b.

(a) First order effects $\varepsilon_{\hat{S}^G_j}$ *(b) Total effects $\varepsilon_{\hat{S}^G_{T_j}}$*
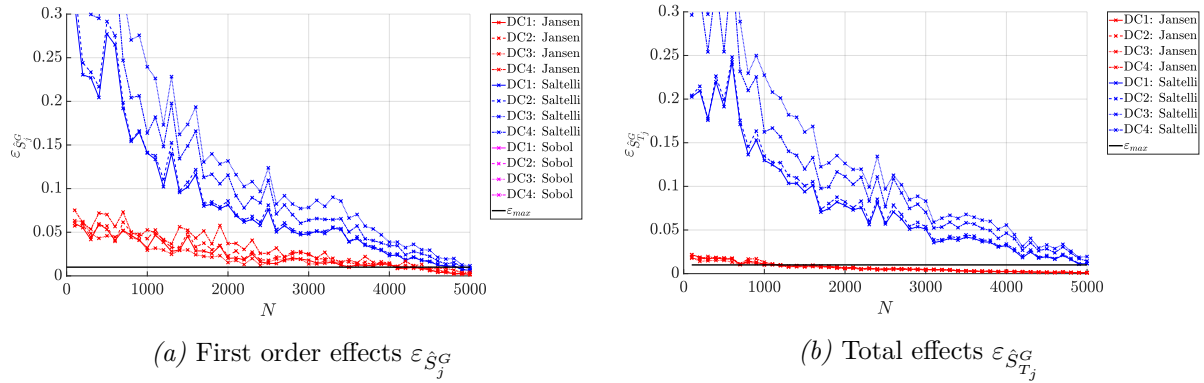
Figure 8.4: Convergence error of the first order and total generalized Sobol indices for the total powertrain losses P_l.

of the three model outputs tend towards zero for higher sample sizes. However, the first order estimates converge more slowly than the total order estimates. It can also be outlined that the driven drive cycle is not significantly influencing the convergence behavior of the estimators. Instead, the choice of the estimator is crucial to achieving valuable convergence rates with adequate sample rates. It can be clearly seen that the Jansen estimators for the first and for the total order indices outperform the other estimators. Furthermore, they reach the predefined convergence error goal $\varepsilon_{max} \leq 0.01$ for each analyzed model output. This analysis clearly shows that the Jansen estimators for the first order and total indices are superior to the other investigated estimators for the closed-loop analysis. Thus, only the results of the Jansen estimators are presented in the following.

The above-discussed convergence errors provide a good quantitative scalar measure to compare the estimated parameters against each other. However, to quantify the accuracy of each estimated parameter, the confidence intervals for each parameter of the first order and total effects are calculated using bootstrap resampling (see Section 3.2.5). For the closed-loop analysis, the bootstrap samples of size $N_b = 5000$ are drawn randomly $B = 50$ times. Using these bootstrap resamples, the 95 % confidence intervals are calculated for the estimators and outlined as red error bars in the sensitivity analysis results in Figures 8.6,

(a) First order effects $\varepsilon_{\hat{S}_j^G}$

(b) Total effects $\varepsilon_{\hat{S}_{T_j}^G}$
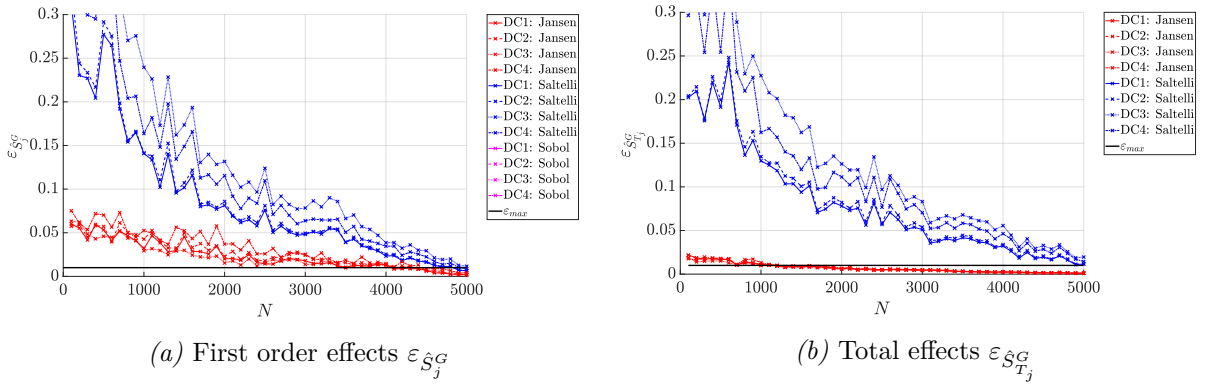
Figure 8.5: Convergence error of the first order and total generalized Sobol indices for the driving time t_d.

8.7 and 8.8.

8.3.2 Sensitivity Analysis Results

The variance-based sensitivity analysis results using the reduced parameter set of Table 8.2 for the consumed battery energy E_b are outlined in Figure 8.6. From Figure 8.6a, it can be seen that, compared to

(a) Histograms

(b) First-order effects with 95 % confidence interval

(c) Total effects with 95 % confidence interval

(d) Sum of effects

Figure 8.6: Generalized Sobol Indices and histograms for consumed battery energy E_b.

the open-loop investigations of Figure 6.10a, the histograms for the closed-loop setup are shifted to the left, which underpins the performance evaluation of Section 7.2.4 that the proposed ENMPC is capable

of saving energy on the four drive cycles. Furthermore, for the closed-loop analysis, the parameter dependencies of the consumed battery energy E_b behave linearly since Figure 8.6d outlines that $\sum \hat{S}_i^G \approx \sum \hat{S}_{T_i}^G$ holds. Thus, it is obvious that $\hat{S}_i^G \approx \hat{S}_{T_i}^G$ holds and therefore, only the total order indices because of their smaller confidence intervals will be discussed in the following. The generalized total order indices $\hat{S}_{T_i}^G$, as shown in Figure 8.6c, of the vehicle parameters are nearly the same as for the open-loop analysis in Figure 6.10c. They are a bit smaller since the sensitivity indices a normalized to one and the controller parameters also show a minor influence on the variance of the battery energy. It can be noted that the controller parameters, including measurement and estimation errors, only influence the variance of E_b by a maximum of $2\,\%$ in drive cycle 4. For the other drive cycles, the influence is even less compared to the parameters belonging to the vehicle itself or the parameters which can be influenced during operation. It can be concluded that only the different setting of the cost function parameter c_c has a significant impact on the energy efficiency of the ENMPC and can change the variance of the energy consumption by a maximum of $2\,\%$. However, as it will be seen throughout this chapter, the change of the cost function parameter c_c also significantly influences the driving time, which could possibly not be accepted by the users of the car.

The results of the closed-loop analysis for the powertrain losses P_l are shown in Figure 8.7. Figure 8.7a

(a) Histograms

(b) First-order effects with $95\,\%$ confidence interval

(c) Total effects with $95\,\%$ confidence interval

(d) Sum of effects
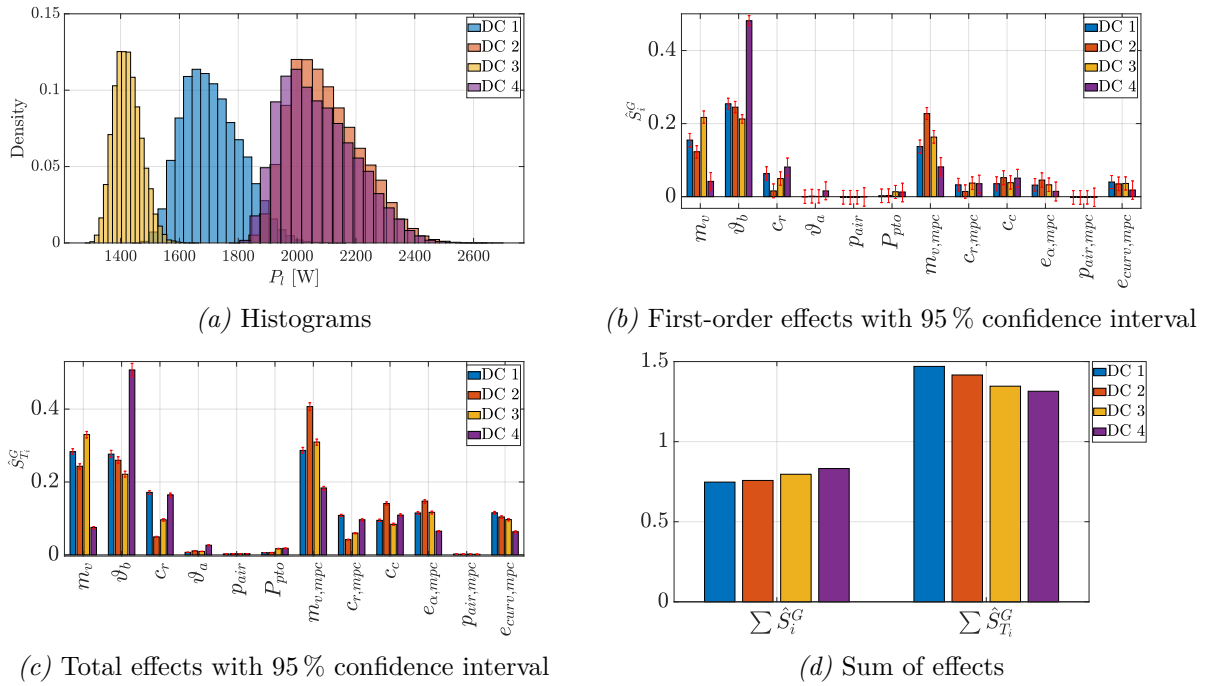
Figure 8.7: Generalized Sobol Indices and histograms for the total drive power losses P_l.

outlines the distributions of the power losses for each drive cycle. Compared to the open-loop results in Figure 6.12a, it can be outlined that the histograms are also shifted to the left as for the consumed battery energy. This coincides with the results of Section 7.2.4 that the proposed ENMPC achieves an energy-efficient driving 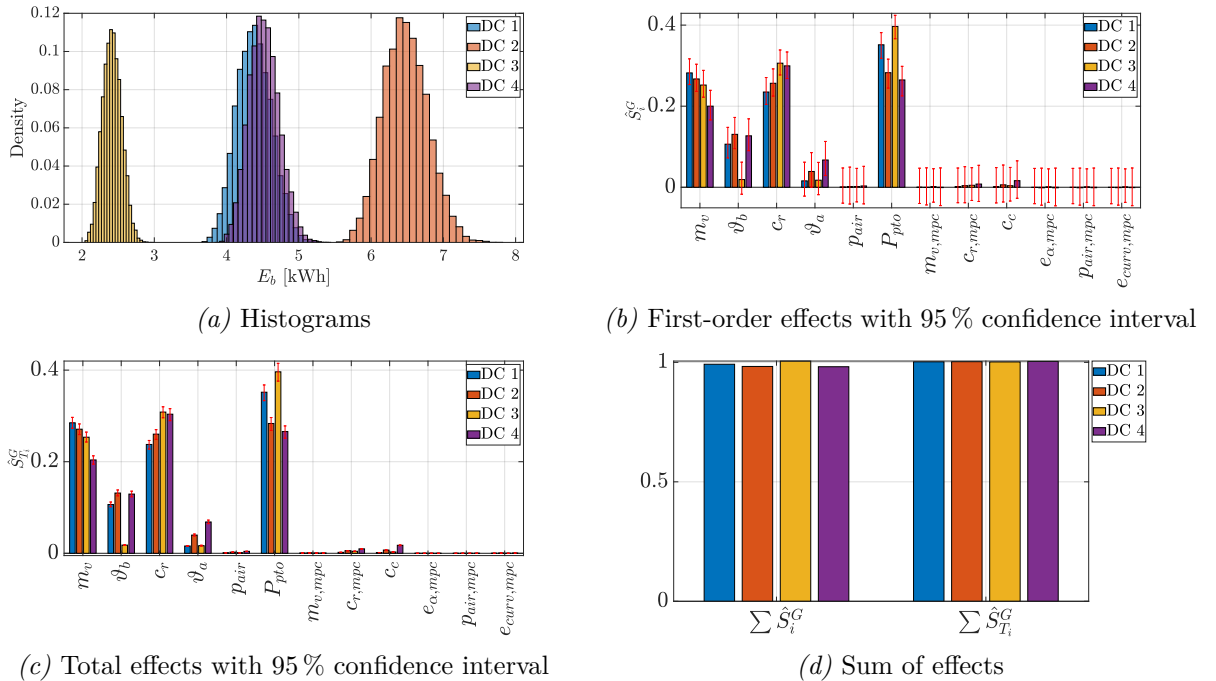and thus reducing also the losses in the powertrain during operation. Figure 8.7d depicts a more nonlinear behavior of the closed-loop analysis than for the open-loop analysis since $\sum \hat{S}_{T_i}^G$ is more significant for the closed-loop compared to the open-loop analysis. Because $\sum \hat{S}_i^G \neq \hat{S}_{T_i}^G$, the generalized first order and total order effects need to be analyzed separately. Starting with the total order indices, they outline that the influence of the change in the vehicle mass m_v in relation to the battery start temperature ϑ_b has decreased compared to the open-loop analysis. Thus, it seems that the ENMPC is capable of reducing the influence of a changing vehicle mass due to different occupancy rates. A reduction in the influence of a changing battery temperature could also be observed but only for drive

cycles 1 to 3. The total order effect of the battery temperature ϑ_b remains high for drive cycle 4. This is reasonable, as drive cycle 4 is not consisting of a driving profile with a distinct slope and curvature profile. Furthermore, the average velocity of this drive cycle is even higher as it contains highway sections and thus, as already outlined in Figure 8.7a, it consists of high average losses. Consequently, the losses at the internal battery resistances, due to high battery currents, are more influenced in this drive cycle. In addition, the lack of a distinct road profile reduces the amount of freedom for the ENMPC to improve the velocity trajectory of the vehicle as it sticks to the reference speed requirement in (7.15).

Moreover, the investigated controller parameters significantly influence the variance of the powertrain losses. From the generalized total order effects, it can be outlined that the mass estimation error of the controller is the most influential parameter. Furthermore, all other estimation errors in the controller, except the air pressure estimation, have a non-negligible influence. The controller's tuning parameter c_c also has a non-negligible effect, but, as will be shown later, it also impacts the driving time, which partially amortizes the reduction in losses.

Comparing the generalized first order indices of Figure 8.7b with the generalized total order indices of Figure 8.6c, it can be seen that all controller parameters show interactions with other parameters since $\sum \hat{S}_i^G \neq \hat{S}_{T_i}^G$ holds for these parameters. Furthermore, the mass of the vehicle m_v and the rolling resistance coefficient c_r are also interacting with other parameters. Only the battery start temperature is not significantly interacting with other parameters since $\sum \hat{S}_i^G \approx \hat{S}_{T_i}^G$ holds for this parameter. However, the amount of nonlinearity regarding the powertrain losses is only a maximum of $1 - \sum \hat{S}_i^G = 25.3\,\%$ for drive cycle 1, as Figure 8.7d outlines. Consequently, the first order effects of the power losses are responsible for $74.7\,\%$ of the variance. Thus, focusing only on the first order effects is more suitable since the source for the amount of variance is clearly attributable to one parameter.

Since the required driving time strongly affects the acceptance of driver assistance systems, the influence of the parameter variations on the driving time t_d is also examined in the following. The closed-loop sensitivity analysis results for the driving time are outlined in Figure 8.8. Figure 8.8a outlines the distri-
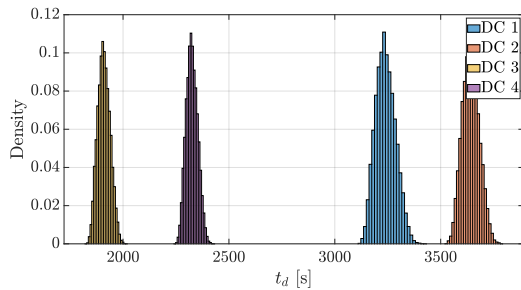
(a) Histograms
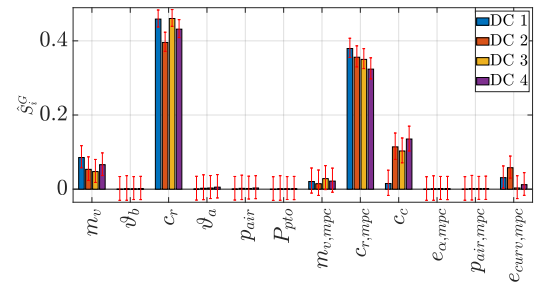
(b) First-order effects with 95 % confidence interval
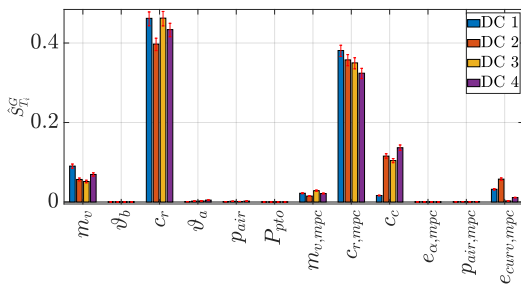
(c) Total effects with 95 % confidence interval
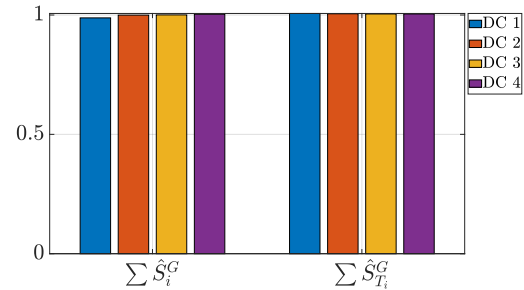
(d) Sum of effects

Figure 8.8: Generalized Sobol Indices and histograms for the total driving time t_d.

butions of the driving times for each drive cycle. It is obvious that the average driving time for each drive

cycle is different since they have different lengths. However, it can also be seen that the variations of the investigated parameters significantly influence the driving time. As Figure 8.8d outlines, $\sum \hat{S}_i^G \approx \sum \hat{S}_{T_i}^G$ holds for the driving time and thus, $\hat{S}_i^G \approx \hat{S}_{T_i}^G$ holds also. Consequently, only the generalized total order indices for the driving time will be discussed in the following because of their smaller convergence intervals. From Figure 8.8, it can be seen that the influence of the individual drive cycles on the distribution of the sensitivity indices is marginal for the driving time. Furthermore, it outlines that most of the variance is caused by the rolling resistance of the vehicle (up to 46.3 %) and the estimation of the rolling resistance by the controller (up to 38.1 %). Another significant influence is caused by the tuning factor c_c of the ENMPC by up to 13.7 %. Additionally, the vehicle mass variation influences the variance of the driving time by up to 9 % and their estimate by up to 2.9 %. The curvature measurement also affects the variance of the driving time up to 5.8 %.

From the above-outlined results of the closed-loop sensitivity analysis, it can be concluded that only a small part of the parameters causes most of the variance of the three investigated outputs. The variation in the mass of the vehicle, the rolling resistance, the battery start temperature as well as in the auxiliary consumers are responsible for the majority of the variance of the consumed battery energy E_b. Furthermore, it is shown that the setting of the controller tuning parameter c_c has only a small influence on the consumed battery energy E_b but influences the driving time significantly. Consequently, the tuning parameter of the cost function seems not to be a good choice for improving the energy efficiency of the controller without worsening the driving time significantly. Based on these results, it should be focused on the optimization of the vehicle mass and the rolling resistance of the vehicle. In addition, the auxiliary power demand should be reduced and the battery start temperature should be adapted, which will also lead to a reduced variance of the battery energy. Furthermore, it should be focused on the estimation of the mass of the vehicle, the rolling resistance coefficient and the curvature within the ENMPC to reduce the variance in driving time.

The sensitivity analysis outlines how the variation of each parameter affects the variance and how the variance decreases if this parameter is fixed to a particular value within its PDF. Furthermore, the most influential parameters have been identified and quantified using this variance-based sensitivity analysis. However, this method is not able to make a statement which parameter value of each investigated parameter is the optimal one to optimize the energy consumption but also the driving time. Consequently, this is discussed in the next section.

8.4 Controller Improvements

In this chapter, the results of the closed-loop sensitivity analysis presented above are converted into an ideal parameter setup for the four driving cycles. Since some parameters, such as the battery start temperature, cannot be influenced by the controller but only by the driver, recommendations for action are presented. Furthermore, the validity of the sensitivity analysis is confirmed for each of the most influential parameters.

The condition $\sum \hat{S}_i^G \approx \sum \hat{S}_{T_i}^G$ holds for E_b and t_d. Consequently, the percentage share of the variance of an output for one parameter σ_{x_i} can be specified as

$$\sigma_{x_i} = \sqrt{S_i}\sqrt{V(y)} \tag{8.1}$$

according to (3.20). Consequently, the sensitivity analysis results and their effects must always be considered in relation to the determined standard deviation of the model outputs. Therefore, in addition to considering absolute changes in the required battery energy or driving time, their relative change, in relation to the standard deviation, is also considered in the following sections.

8.4.1 Nominal Parameter Influences

Influence of the Vehicle Mass

The mass of an electric vehicle does not change during a trip, unlike an internal combustion engine, which becomes lighter due to burning fuel. However, the total mass of a BEV can also vary depending on the number of people transported and the load condition. Therefore, two different cases are compared in the following. The minimum case for the proTRon Evolution comprises a kerb weight of 550 kg and a driver with 70 kg, resulting in a total weight of 620 kg. The case with four occupants leads to a maximum vehicle weight of 830 kg.

The first two rows of Table 8.3 outline the nominal values y_{nom} of the consumed battery energy E_b and the driving time t_d for $m_v = 620$ kg. In rows three and four, the nominal values for $m_v = 830$ kg are depicted. The rest of the parameters retain the nominal values as shown in Appendix B. Lines five and six show the change in energy consumption and travel time for the two different parameters. It can be clearly seen that the change in vehicle mass causes a significant increase in energy consumption of up to 12.8 % in all driving cycles. On the other hand, the driving time only increases in absolute terms by a maximum of 2.23 % in driving cycle 1. Comparing the values with the Sobol indices of the sensitivity analysis from Figures 8.6 and 8.8, it can be seen that the sensitivity index for the vehicle mass differs on average by a factor of three between energy consumption and driving time. As explained above, however, the absolute difference is more extensive. This can be explained because, as shown in (8.1), the sensitivity indices always refer to the standard deviation of the study. Here, the energy consumption has a larger standard deviation in relation to y_{nom} than the travel time. This is shown in Table 8.3 with $\frac{\sqrt{V(Y)}}{y_{nom}}$. Therefore, the absolute deviation is correspondingly larger. If the change is related to the standard deviation of the two variables, as shown in Table 8.3 in the last two rows, it is evident that the difference is not that large and gets closer to the ratio of the sensitivity indices. Nevertheless, a direct conversion of the sensitivity indices referring to the variance into absolute changes is not possible, as this observation shows. Nonetheless, the significant influence on energy consumption and a minor influence on travel time are in accordance with the sensitivity analysis results.

Table 8.3: Influence of a change in the vehicle mass m_v on the four drive cycles.

	Drive cycle 1		Drive cycle 2		Drive cycle 3		Drive cycle 4	
	y_{nom}	$\frac{\sqrt{V(Y)}}{y_{nom}}$	y_{nom}	$\frac{\sqrt{V(Y)}}{y_{nom}}$	y_{nom}	$\frac{\sqrt{V(Y)}}{y_{nom}}$	y_{nom}	$\frac{\sqrt{V(Y)}}{y_{nom}}$
$m_{v,1} = 620$ kg	4.19 kWh	5.72 %	6.26 kWh	4.88 %	2.27 kWh	5.77 %	4.37 kWh	4.79 %
	54.21 min	1.43 %	60.61 min	1.11 %	31.45 min	1.56 %	38.40 min	1.19 %
$m_{v,2} = 830$ kg	4.72 kWh	5.07 %	6.93 kWh	4.41 %	2.52 kWh	5.19 %	4.73 kWh	4.42 %
	55.42 min	1.40 %	61.44 min	1.10 %	31.99 min	1.54 %	38.91 min	1.18 %
$\sqrt{V(E_b)}$	0.24 kWh		0.31 kWh		0.13 kWh		0.21 kWh	
$\sqrt{V(t_d)}$	0.77 min		0.67 min		0.49 min		0.46 min	
$\frac{E_b(m_{v,2})}{E_b(m_{v,1})}$	+12.80 %		+10.67 %		+11.06 %		+8.37 %	
$\frac{t_d(m_{v,2})}{t_d(m_{v,1})}$	+2.23 %		+1.37 %		+1.73 %		+1.34 %	
$\frac{E_b(m_{v,2})-E_b(m_{v,1})}{\sqrt{V(E_b)}}$	+223.92 %		+218.69 %		+191.72 %		+174.99 %	
$\frac{t_d(m_{v,2})-t_d(m_{v,1})}{\sqrt{V(t_d)}}$	+156.03 %		+123.20 %		+110.59 %		+112.25 %	

Influence of the Rolling Resistance

The rolling resistance can change during a change in the road surface profile or can vary due to dry and wet surfaces. Since the sensitivity analysis outlines the rolling resistance coefficient c_r as one of the most relevant parameters, it is investigated here for $c_r = 0.01$ and $c_r = 0.015$. The results are outlined in Table 8.4. Line seven of Table 8.4 shows that the change in the rolling resistance leads to a significant increase in energy consumption. However, the travel time is also not insignificantly affected. Nevertheless, it can be seen that the absolute change of the travel time is smaller than the change of the energy consumption, although the sensitivity index of the travel time is larger than that of the energy consumption. If the change is related to the standard deviation, as shown in the last two rows of Table 8.4, it can be clearly seen that the relative change of the travel time is larger than that of the energy consumption. Altogether, despite the smaller standard deviation of the travel time, this leads to the fact that both examined variables are significantly influenced.

Table 8.4: Influence of a change in the rolling resistance c_r on the four drive cycles.

	Drive cycle 1		Drive cycle 2		Drive cycle 3		Drive cycle 4	
	y_{nom}	$\frac{\sqrt{V(Y)}}{y_{nom}}$	y_{nom}	$\frac{\sqrt{V(Y)}}{y_{nom}}$	y_{nom}	$\frac{\sqrt{V(Y)}}{y_{nom}}$	y_{nom}	$\frac{\sqrt{V(Y)}}{y_{nom}}$
$c_{r,1} = 0.01$	4.19 kWh	5.72 %	6.26 kWh	4.88 %	2.27 kWh	5.77 %	4.37 kWh	4.79 %
	54.21 min	1.43 %	60.61 min	1.11 %	31.45 min	1.56 %	38.40 min	1.19 %
$c_{r,2} = 0.015$	4.58 kWh	5.22 %	6.79 kWh	4.50 %	2.50 kWh	5.22 %	4.78 kWh	4.38 %
	56.39 min	1.38 %	62.27 min	1.08 %	32.76 min	1.50 %	39.55 min	1.16 %
$\sqrt{V(E_b)}$	0.24 kWh		0.31 kWh		0.13 kWh		0.21 kWh	
$\sqrt{V(t_d)}$	0.77 min		0.67 min		0.49 min		0.46 min	
$\frac{E_b(c_{r,2})}{E_b(c_{r,1})}$	+9.45 %		+8.47 %		+10.46 %		+9.35 %	
$\frac{t_d(c_{r,2})}{t_d(c_{r,1})}$	+4.03 %		+2.74 %		+4.16 %		+3.02 %	
$\frac{E_b(c_{r,2}) - E_b(c_{r,1})}{\sqrt{V(E_b)}}$	+165.36 %		+173.56 %		+181.36 %		+195.47 %	
$\frac{t_d(c_{r,2}) - t_d(c_{r,1})}{\sqrt{V(t_d)}}$	+281.40 %		+246.65 %		+266.34 %		+252.82 %	

Influence of the Auxiliary Consumers

The auxiliary power demand P_{pto} varies with the power demand of the auxiliary consumers, e.g., using the lights or heating the vehicle. The change in P_{pto} is investigated here for $P_{pto} = 250\,\text{W}$ and $P_{pto} = 750\,\text{W}$ and the results are outlined in Table 8.5. An interesting observation is that the controller does not change the velocity to avoid additional auxiliary power demand due to higher driving times. Consequently, the consumed battery energy is increased by up to 12.9 % when the auxiliary power demand increases, but the driving time remains nearly the same, which is outlined in lines seven and eight of Table 8.5. Figures 8.6 and 8.8 underpin this observation since the Sobol indices are significant regarding the consumed battery energy E_b but approximately zero regarding the driving time t_d for P_{pto}.

Table 8.5: Influence of a change in the auxiliary consumers power demand P_{pto} on the four drive cycles.

	Drive cycle 1		Drive cycle 2		Drive cycle 3		Drive cycle 4	
	y_{nom}	$\frac{\sqrt{V(Y)}}{y_{nom}}$	y_{nom}	$\frac{\sqrt{V(Y)}}{y_{nom}}$	y_{nom}	$\frac{\sqrt{V(Y)}}{y_{nom}}$	y_{nom}	$\frac{\sqrt{V(Y)}}{y_{nom}}$
$P_{pto,1} = 250\,\text{W}$	3.93 kWh	6.09 %	5.97 kWh	5.12 %	2.12 kWh	6.16 %	4.17 kWh	5.09 %
	54.21 min	1.43 %	60.61 min	1.11 %	31.45 min	1.56 %	38.40 min	1.19 %
$P_{pto,2} = 750\,\text{W}$	4.44 kWh	5.39 %	6.56 kWh	4.66 %	2.41 kWh	5.43 %	4.57 kWh	4.58 %
	54.22 min	1.43 %	60.62 min	1.11 %	31.45 min	1.56 %	38.40 min	1.19 %
$\sqrt{V(E_b)}$	0.24 kWh		0.31 kWh		0.13 kWh		0.21 kWh	
$\sqrt{V(t_d)}$	0.77 min		0.67 min		0.49 min		0.46 min	
$\frac{E_b(P_{pto,2})}{E_b(P_{pto,1})}$	+12.90 %		+9.91 %		+13.46 %		+9.38 %	
$\frac{t_d(P_{pto,2})}{t_d(P_{pto,1})}$	+0.02 %		+0.01 %		+0.00 %		+0.00 %	
$\frac{E_b(P_{pto,2}) - E_b(P_{pto,1})}{\sqrt{V(E_b)}}$	+211.95 %		+193.50 %		+218.66 %		+187.38 %	
$\frac{t_d(P_{pto,2}) - t_d(P_{pto,1})}{\sqrt{V(t_d)}}$	+1.39 %		+0.47 %		+0.00 %		+0.00 %	

Influence of the Battery Start Temperature

The battery start temperature can be influenced in various ways. The greatest influence is a change caused directly by the ambient temperature. However, exposure of the vehicle to direct sunlight can also affect the battery temperature. Furthermore, the battery can heat up during a charging process because of the charging losses. As the following investigation shows, it is not an increase in temperature that is critical for the energy consumption, but a reduction. It should be mentioned that the battery temperature cannot be increased arbitrarily since aging processes in the battery increase significantly above a temperature of 45 °C [200]. From Table 8.6, it can be seen that a change in the battery start temperature substantially influences the energy consumption of the vehicle in all drive cycles. It can be clearly outlined that a lower battery temperature results in increasing losses and thus, in an increased energy demand. However, the driving time is not affected by a change in the battery temperature, which is underpinned by the sensitivity analysis results of Figures 8.6 and 8.8.

Table 8.6: Influence of a change in the battery start temperature ϑ_b on the four drive cycles.

	Drive cycle 1		Drive cycle 2		Drive cycle 3		Drive cycle 4	
	y_{nom}	$\frac{\sqrt{V(Y)}}{y_{nom}}$	y_{nom}	$\frac{\sqrt{V(Y)}}{y_{nom}}$	y_{nom}	$\frac{\sqrt{V(Y)}}{y_{nom}}$	y_{nom}	$\frac{\sqrt{V(Y)}}{y_{nom}}$
$\vartheta_{b,1} = 10\,°C$	4.66 kWh	5.14 %	7.00 kWh	4.36 %	2.42 kWh	5.40 %	4.83 kWh	4.33 %
	54.32 min	1.43 %	60.62 min	1.11 %	31.45 min	1.56 %	38.40 min	1.19 %
$\vartheta_{b,2} = 40\,°C$	3.96 kWh	6.05 %	5.93 kWh	5.16 %	2.21 kWh	5.90 %	4.15 kWh	5.04 %
	54.20 min	1.43 %	60.61 min	1.11 %	31.45 min	1.56 %	38.40 min	1.19 %
$\sqrt{V(E_b)}$	0.24 kWh		0.31 kWh		0.13 kWh		0.21 kWh	
$\sqrt{V(t_d)}$	0.77 min		0.67 min		0.49 min		0.46 min	
$\frac{E_b(\vartheta_{b,2})}{E_b(\vartheta_{b,1})}$	−15.07 %		−15.38 %		−8.59 %		−14.22 %	
$\frac{t_d(\vartheta_{b,2})}{t_d(\vartheta_{b,1})}$	−0.22 %		−0.01 %		+0.00 %		+0.00 %	
$\frac{E_b(\vartheta_{b,2})-E_b(\vartheta_{b,1})}{\sqrt{V(E_b)}}$	−293.30 %		−352.45 %		−159.09 %		−328.65 %	
$\frac{t_d(\vartheta_{b,2})-t_d(\vartheta_{b,1})}{\sqrt{V(t_d)}}$	−15.48 %		−0.99 %		+0.02 %		+0.00 %	

Influence of the Controller Tuning Parameter

The controller tuning parameter c_c is intended to allow the driver or the application engineer to tune the controller behavior, whether it should save more energy or stick to the maximum allowed vehicle speed. The sensitivity analysis has shown that the influence of this tuning factor is small compared to the vehicle parameters themselves. However, there is still an influence that should not be neglected. Table 8.7 outlines that for $c_c = 6$, the energy consumption can be reduced by up to $1.18\,\%$ by only worsening the driving time by $1.11\,\%$. Consequently, besides using an ENMPC to reduce the energy consumption, in the investigated controller parameterization, c_c is the only parameter that significantly influences the energy consumption.

Table 8.7: Influence of a change in the controller tuning parameter a_c on the four drive cycles.

	Drive cycle 1		Drive cycle 2		Drive cycle 3		Drive cycle 4	
	y_{nom}	$\frac{\sqrt{V(Y)}}{y_{nom}}$	y_{nom}	$\frac{\sqrt{V(Y)}}{y_{nom}}$	y_{nom}	$\frac{\sqrt{V(Y)}}{y_{nom}}$	y_{nom}	$\frac{\sqrt{V(Y)}}{y_{nom}}$
$c_{c,1} = 0$	4.19 kWh	5.71 %	6.26 kWh	4.88 %	2.27 kWh	5.77 %	4.37 kWh	4.79 %
	54.21 min	1.43 %	60.61 min	1.11 %	31.45 min	1.56 %	38.40 min	1.19 %
$c_{c,2} = 6$	4.16 kWh	5.75 %	6.20 kWh	4.93 %	2.25 kWh	5.81 %	4.32 kWh	4.84 %
	54.42 min	1.43 %	61.09 min	1.10 %	31.80 min	1.54 %	38.71 min	1.18 %
$\sqrt{V(E_b)}$	0.24 kWh		0.31 kWh		0.13 kWh		0.21 kWh	
$\sqrt{V(t_d)}$	0.77 min		0.67 min		0.49 min		0.46 min	
$\frac{E_b(c_{c,2})}{E_b(c_{c,1})}$	−0.62 %		−0.95 %		−0.68 %		−1.18 %	
$\frac{t_d(c_{c,2})}{t_d(c_{c,1})}$	+0.38 %		+0.78 %		+1.11 %		+0.82 %	
$\frac{E_b(c_{c,2})-E_b(c_{c,1})}{\sqrt{V(E_b)}}$	−10.96 %		−19.56 %		−11.85 %		−24.62 %	
$\frac{t_d(c_{c,2})-t_d(c_{c,1})}{\sqrt{V(t_d)}}$	+25.58 %		+70.50 %		+70.92 %		+68.69 %	

Influence of the Estimated Controller Parameters

In addition to the state feedback, further inputs are required by the controller for the prediction, which must either be directly measured or estimated. As the sensitivity analysis has shown, the accuracy of these parameters affects the control result or energy consumption and driving time. Exemplary, the influence of the inaccuracy of the estimated rolling resistance $c_{r,mpc}$ is investigated. For this purpose, the estimated rolling resistance is simulated with $c_{r,mpc} = 0.01$ and with $c_{r,mpc} = 0.015$. However, the real rolling resistance of the vehicle remains constant with $c_r = 0.01$. Table 8.8 shows that the incorrect assumption of the rolling resistance increases the absolute energy consumption by up to $1.74\,\%$. At the same time, the controller reduces the driving time by up to $3\,\%$. Since in this work the optimization of the energy consumption is the focus, this example clearly shows that the controller parameters of the sensitivity analysis, which are evaluated as significant, should be measured or estimated as accurately as possible to avoid a suboptimal controller behavior.

Table 8.8: Influence of a change in the estimated value of $c_{r,mpc}$ on the four drive cycles.

	Drive cycle 1		Drive cycle 2		Drive cycle 3		Drive cycle 4	
	y_{nom}	$\frac{\sqrt{V(Y)}}{y_{nom}}$	y_{nom}	$\frac{\sqrt{V(Y)}}{y_{nom}}$	y_{nom}	$\frac{\sqrt{V(Y)}}{y_{nom}}$	y_{nom}	$\frac{\sqrt{V(Y)}}{y_{nom}}$
$c_{r,mpc} = 0.01$	4.19 kWh	5.72 %	6.27 kWh	4.88 %	2.27 kWh	5.77 %	4.37 kWh	4.79 %
	54.21 min	1.43 %	60.61 min	1.11 %	31.45 min	1.56 %	38.40 min	1.19 %
$c_{r,mpc} = 0.015$	4.23 kWh	5.66 %	6.35 kWh	4.81 %	2.30 kWh	5.68 %	4.44 kWh	4.70 %
	54.61 min	1.47 %	59.31 min	1.14 %	30.51 min	1.61 %	37.56 min	1.22 %
$\sqrt{V(E_b)}$	0.24 kWh		0.31 kWh		0.13 kWh		0.21 kWh	
$\sqrt{V(t_d)}$	0.77 min		0.67 min		0.49 min		0.46 min	
$\frac{E_b(c_{r,mpc}=0.015)}{E_b(c_{r,mpc}=0.01)}$	+1.08 %		+1.36 %		+1.54 %		+1.74 %	
$\frac{t_d(c_{r,mpc}=0.015)}{t_d(c_{r,mpc}=0.01)}$	−2.96 %		−2.15 %		−3.00 %		−2.18 %	
$\frac{E_b(c_{r,mpc}=0.015)-E_b(c_{r,mpc}=0.01)}{\sqrt{V(E_b)}}$	+18.82 %		+27.84 %		+26.72 %		+36.37 %	
$\frac{t_d(c_{r,mpc}=0.015)-t_d(c_{r,mpc}=0.01)}{\sqrt{V(t_d)}}$	−206.74 %		−193.69 %		−192.06 %		−182.93 %	

8.4.2 Optimal Vehicle Setup

In the previous section, the influence of the most significant parameters of the closed-loop sensitivity analysis is outlined. It has been shown that each of these parameters significantly influences the energy efficiency of the BEV. An optimal parameter set can now be derived from these findings. To have the most significant effect on energy consumption, the following were defined as optimal parameters: $m_v = 620$ kg, $c_r = 0.01$, $P_{pto} = 250$ W, $\vartheta_b = 40\,°$C, $a_c = 6$ and $c_{r,mpc} = c_r$. The resulting change with this optimized parameter set compared to the nominal parameter set (see Appendix B) is shown in Table 8.9.

Table 8.9: Comparison of the nominal parameter set with the optimal parameter set of the closed-loop ENMPC.

	Drive cycle				
	1	**2**	**3**	**4**	**Average**
Energy consumption					
Nominal parameter	4.19 kWh	6.27 kWh	2.27 kWh	4.37 kWh	4.28 kWh
Optimal parameter	3.70 kWh	5.61 kWh	2.06 kWh	3.93 kWh	3.83 kWh
Change	−11.7 %	−10.5 %	−9.3 %	−10.1 %	−10.5 %
Driving time					
Nominal parameter	54.21 min	60.61 min	31.45 min	38.40 min	46.17 min
Optimal parameter	54.38 min	61.07 min	31.78 min	38.70 min	46.48 min
Change	+0.3 %	+0.8 %	+1.0 %	0.8 %	+0.7 %

It can be clearly seen that the optimized parameters result in a significant overall energy-saving potential of 10.5 % on average for all four drive cycles. Despite these significant savings, the driving time increases

by only 0.7 % on average.

To achieve this energy-saving potential in practice, the vehicle mass should be reduced as much as possible by not carrying unnecessary loads during a trip. Furthermore, tires and road surfaces with low rolling resistance coefficients should be chosen. The road surfaces are, in general, not influenceable. However, setting the correct tire pressure could significantly influence the rolling resistance coefficient of the tires, as Figure 5.4 underpins. Reducing the power demand of the auxiliary consumer by, e.g., switching off the air conditioning, would also be beneficial for the energy consumption of the vehicle. Another significant influence is denoted by the battery start temperature. This parameter can directly be influenced by the driver, e.g., parking the vehicle in a garage to avoid icy starting conditions of the battery. The controller-related parameters a_c and $c_{r,mpc}$ also affect the energy demand and driving time. As the previous investigations have shown, parameter a_c can be used to improve the energy efficiency of the ENMPC by only slightly increasing the driving time. Also, the estimated rolling resistance $c_{r,mpc}$ should be determined as precisely as possible to avoid drawbacks in the optimality of the controller.

8.5 Conclusions

In this chapter, the complex simulation model of the BEV on predefined drive cycles has been analyzed closed-loop together with the ENMPC using the proposed sensitivity analysis methods Morris screening and generalized Sobol indices. In the first step, the PDFs of the 54 parameters to be investigated were defined. Next, a Morris screening was performed to reduce the computational cost of a variance-based sensitivity analysis. It has separated the influential from the non-influential parameters, which resulted in a reduced parameter set for the variance-based sensitivity analysis. Consequently, the calculation time for the variance-based sensitivity analysis has been reduced by a factor of four.

The variance-based sensitivity analysis has been performed for the consumed battery energy E_b, the powertrain losses P_l and the driving time t_d using generalized Sobol indices as they consider the temporal dependency of technical processes. However, since the Sobol indices are determined using MC simulations, they need to be estimated. The convergence of these estimators depends on the sample size used in the MC simulation. Thus, the convergence has been proven using the two proposed methods of Chapter 3 based on the law of big numbers for computing the scalar convergence measures and using bootstrap resampling for calculating the confidence intervals. Accordingly, the chosen sample size of $N = 5000$ was suitable for providing reliable sensitivity analysis calculations.

Based on these analyses, it has been shown that only a small subset of the 54 investigated parameters are responsible for the variance of the outputs. Furthermore, an investigation of these influential variables on the energy consumption and the driving time has been done in this chapter which underpins the findings of the sensitivity analysis. It has been outlined that an optimized parameter setup of the vehicle and controller parameters leads to an energy saving potential of 10.5 % on average at the four drive cycles by only increasing the driving time by 0.7 % on average.

9 Conclusion and Outlook

This thesis presents the use of variance-based sensitivity analysis and screening methods to analyze and improve the energy-efficient longitudinal vehicle control of a BEV. For this purpose, the work was divided into four main parts.

At first, a computation time optimized complete vehicle model of an electric vehicle was developed. In order to obtain meaningful sensitivity analysis results, the presented model includes detailed models of the powertrain in addition to the modeling of the longitudinal vehicle dynamics. The powertrain models consist of a battery, an inverter, a motor and a transmission model whose modeling accuracy with regard to energy consumption was evaluated on component test benches. Thus, a complex vehicle model was developed in this thesis which meets the requirements for the sensitivity analysis.

The second part consists of performing a sensitivity analysis to the developed vehicle model on four different drive cycles which represents typical commuter routes. The velocity of the vehicle for this sensitivity analysis was prerecorded on the four presented drive cycles using a human driver for the open-loop investigation. To execute the sensitivity analysis, firstly, the PDFs of the examined input parameters were defined. Afterwards, a Morris screening was done to identify non-influential parameters to reduce the computational effort for the subsequent MC-based analysis. Based on this reduced parameter set a quantitative variance-based sensitivity analyses was performed to identify the most influential parameters using generalized Sobol indices.

In the third part, the information of the open-loop sensitivity analysis were used to decide which parts need to be included in the controller design. Based on these information a novel ENMPC approach was presented for the longitudinal control of the BEV. It has been shown, that the ENMPC controller is capable of saving energy in artificial driving situations as well as on the four realistic drive cycles up to 7.2 % in comparison to the manual driven vehicle. Furthermore, the proposed controller is real-time capable for future implementations on real automotive vehicle hardware.

The last part outlined the investigation of the closed-loop sensitivity analysis on the ENMPC controlled BEV. Here, in the same way as for the open-loop analysis, first a Morris screening was performed for parameter reduction and then the generalized Sobol indices were calculated. In contrast to the open-loop analysis, the vehicle speed was determined by the ENMPC and the controller-related parameters were included in the sensitivity analysis. It has been shown that only a small subset of the 54 investigated system parameters are significantly influencing the energy consumption of the vehicle. It was outlined that there exists a significant variance on the energy consumption where optimizing all dominant parameter can save 10.5 % energy on average at the four drive cycles.

It can be concluded that the sensitivity analysis of such complex systems generates valuable insights into model characteristics and is able to identify the most important parameters. Based on these information the researcher or engineer can focus on the most relevant parameters during controller design and optimization of the system. This enables shorter development times and well-founded decisions in the controller design and optimization phase. Furthermore, the proposed sensitivity analysis outlined how measurement or estimation errors of input quantities of the controller would affect the energy efficiency.

For future research a more precise determination of the PDFs for the input parameters of the model could be considered which would increase the accuracy of the provided results. However, as it has already been shown, deviations in the most relevant parameter distributions did not affect the results of

the sensitivity analysis significantly. To reduce the computation time another future research topic is the development of surrogate models. Furthermore, the development of methods for the treatment of statistically dependent input parameters should be carried out.

Beside of improvements of the sensitivity analysis, the presented eco-CC algorithm could be extended to an eco-ACC system considering the preceding vehicle. Furthermore, the possibility of Car2X communication with e.g. traffic-lights could be a promising extension of the proposed algorithm to enhance the possible use cases.

The implementation of the proposed ENMPC algorithm on a real-time capable automotive hardware on the proTRon Evolution can be aimed to take the step towards industrial implementation.

A Testbenches

A.1 Battery Testbench

The battery test bench was built up and used in [201] and [149] to parameterize the used battery cell. However, a short overview of the test bench will be given here. Figure A.1 outlines the schematic structure of the test bench. Furthermore, Figure A.2 provides an overview of the components. It consists of a DC-current source capable of supplying currents up to 60A. An IGBT is attached in parallel to the current source to control the battery current i_b. If the cell is charged, condition $i_q < I_s$ is valid. For discharging the battery, condition $i_q > I_s$ holds. The resulting battery current is then $i_b = I_s - i_q$ with $i_q \in [0\,\mathrm{A}, 120\,\mathrm{A}]$. The UniControl [202] controls the IGBT and measures the actual battery current and
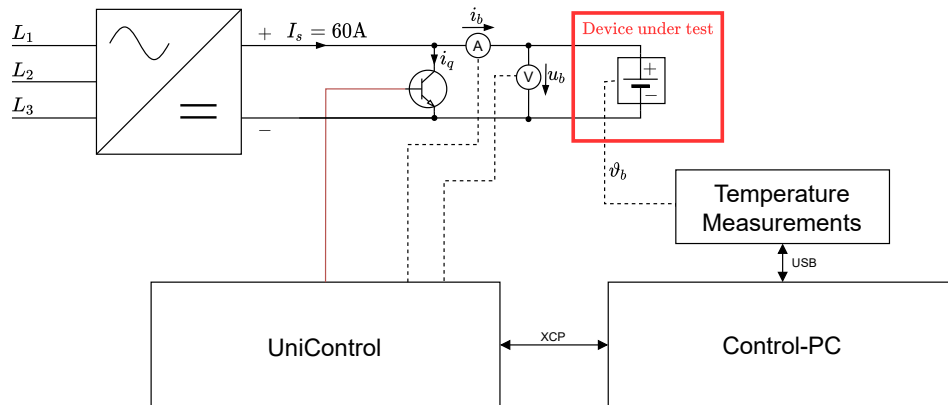
Figure A.1: Battery test bench configuration

terminal voltage and transfers it using Universal Measurement and Calibration Protocol (XCP) to the Control-PC. The battery is encapsulated in a climate chamber to vary the temperature working point precisely. The temperature ϑ_b is recorded using thermocouples on the battery housing and directly at the terminals. Further information about the battery testbench can be found in [149, 201].

(a) Climate chamber

(b) Battery cell with attached thermo-couples

(c) Measurement setup

Figure A.2: Battery test bench overview [149]

A.2 Drive and Inverter Test Benches

The drive and inverter test benches are used to parameterize and evaluate the developed models in Section 5.1.4 and Section 5.1.3. During this work, two different configurations of drive and inverter test benches were built and presented in the following two sections. The first test bench consists of a direct coupling between the load machine and the device under test, whereas the second test bench consists of a complete drive system of the proTRon Evolution. The direct coupling is suitable for parameter identification and model verification due to the stiff connection between the load and the device under test. However, the second test bench is used to test and evaluate the complete drive system of the vehicle.

A.2.1 DTB1: Direct Coupling

The DTB1 is a typical testbench configuration to measure and test electrical drives and inverters. The schematic structure is depicted in Figure A.3. The device under test, marked by the red frame, consists of the inverter (hofer PE250) and the PMSM M_1 (EMRAX 188). The inverter is supplied by a bidirectional DC-Source capable of feeding energy back into the mains. The PMSM M_1 is directly coupled to the load machine M_2 using a torque measuring shaft. Also, the inverter of the load machine is able to feed energy
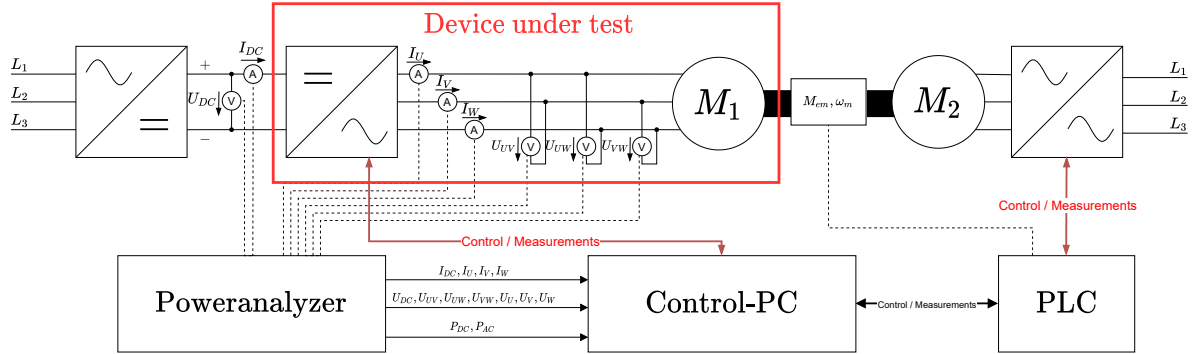

Figure A.3: Drive and inverter test bench configuration

back into the mains. This makes it possible to approach all quadrants of the electric drive system during the operation. In addition, the configuration of the test bench allows not only to measure steady-state working points but also dynamic working points with varying speeds, e.g., drive cycles. The test bench
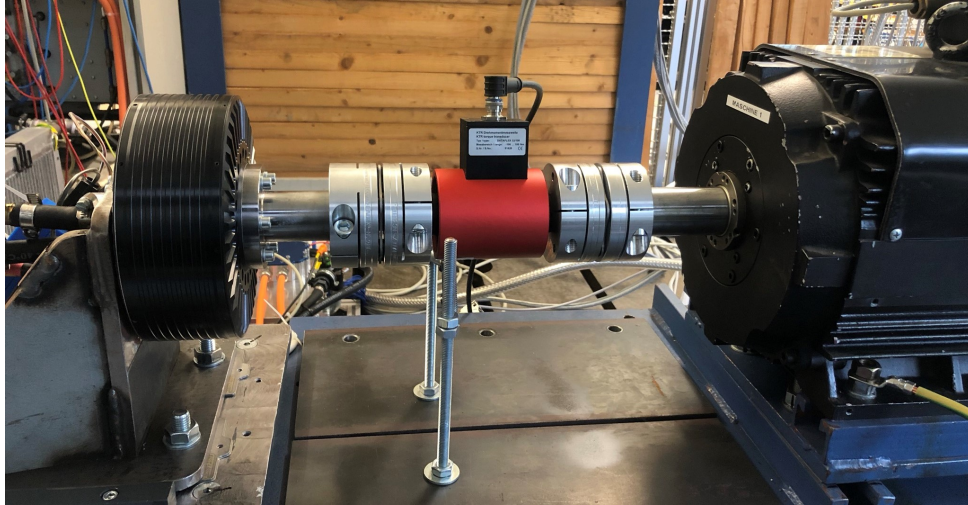
Figure A.4: Direct coupling of drive and inverter setup

is equipped with several measurement equipment. To measure the electrical quantities very accurately, a power analyzer is used. In this setup, the DC voltage U_{DC}, the current I_{DC} and also the AC voltages U_{UV}, U_{UW}, U_{VW} and currents I_U, I_V, I_W are measured. Therefore, it is possible to precisely determine the AC and DC power. Furthermore, the inverter's internal software variables can be measured directly using XCP. The mechanical torque T_m and velocity ω_m are measured using the torque measuring shaft from which the mechanical power can be calculated. With this measurement configuration, the test bench system is capable of measuring all quantities needed for the accurate measurement of component efficiencies. Figure A.4 shows the real structure of the assembled system. On the left, the engine of the device under test M_1 can be seen. This device is coupled via the torque measurement shaft with the load machine M_2 on the right.

A.2.2 DTB2: Complete Drive System

The DTB2 consists mainly of the same parts as the DTB1. The difference is mainly that the drive M_1 is not directly coupled with the load device M_2. Instead, the gearbox of the proTRon Evolution is assembled between them. Also, a second torque measuring shaft at the output of the gearbox is assembled. With the two torque measuring shafts, the mechanical power at the input shaft and the output shaft of the gearbox can be measured. The schematic structure of the DTB2 is depicted in Figure A.5 and the real

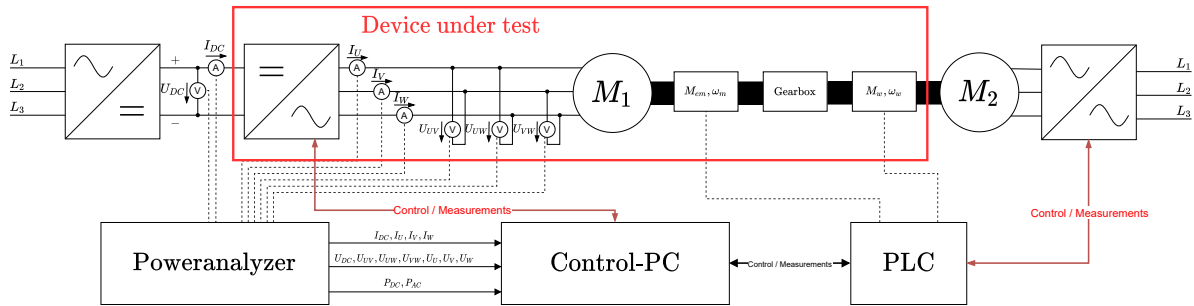*Figure A.5:* Drive and inverter test bench configuration with gearbox

system is shown in Figure A.6.

Figure A.6: Drive and inverter test bench with gearbox

A.2.3 Measurement Errors

To determine the accuracy of the evaluation of the models presented in Sections 5.1.1, 5.1.4 and 5.1.3, the measurement errors of the test benches have to be estimated. The quantities of interest are the

efficiencies of each component

$$\eta_{inv} = \frac{P_{AC}}{P_{DC}} \tag{A.1}$$

$$\eta_{em} = \frac{P_{em}}{P_{AC}} \tag{A.2}$$

$$\eta_{ds} = \frac{P_{em}}{P_{DC}} \tag{A.3}$$

$$\eta_{gb} = \frac{P_w}{P_{em}} \tag{A.4}$$

$$\eta_{sys} = \frac{P_w}{P_{DC}} \tag{A.5}$$

where η_{inv} describes the efficiency of the inverter and η_{em} the efficiency of the PMSM. η_{ds} denotes the system efficiency, including the PMSM and the inverter. The efficiency of the gearbox is expressed with η_{gb} and the overall system efficiency with η_{sys}. The effective powers of the DC side P_{DC} and the AC side P_{AC} of the inverter and the mechanical power P_{em} must be calculated using the measured quantities. The effective DC power is described by

$$P_{DC} = U_{DC}I_{DC}, \tag{A.6}$$

where U_{DC} depicts the True Root Mean Squared (TRMS) voltage and I_{DC} the TRMS current of the DC side. The effective AC power for a symmetric three-phase system is calculated using

$$P_{AC} = 3U_{AC}I_{AC}\cos(\varphi) \tag{A.7}$$

with U_{AC} describing the TRMS voltage and I_{AC} the TRMS current of the AC side. $\cos(\varphi)$ outlines the electrical phase angle between U_{AC} and I_{AC}. Using the measurement of the shaft torque of the PMSM P_{em} and the angular velocity ω_m, the mechanical power P_{em} is expressed by

$$P_{em} = M_{em}\omega_m. \tag{A.8}$$

The torque at the gearbox output can be calculated similarly using

$$P_w = M_w\omega_w, \tag{A.9}$$

where M_w is the measured output torque of the gearbox and ω_w is the measured angular velocity of the gearbox output shaft.

Measurement Error Estimation

The efficiencies outlined in (A.1) to (A.5) are subject to measurement errors. To estimate the maximum measurement errors, linear error propagation, as described in [203], is used. In general, the linear error propagation for two independent measured variables can be expressed by

$$\Delta z = \left|\frac{\partial f(x,y)}{\partial x}\Delta x\right| + \left|\frac{\partial f(x,y)}{\partial y}\Delta y\right|, \tag{A.10}$$

where $\frac{\partial f(x,y)}{\partial x}$ denotes the partial derivative of the function $f(x,y)$ with respect to x and $\frac{\partial f(x,y)}{\partial y}$ the partial derivative with respect to y. Δz is the absolute maximum error of the function value. Transferring the concept of linear error propagation to the efficiency measurements, the maximum error of the inverter

efficiency $\Delta\eta_{inv}$ can be calculated by

$$
\begin{aligned}
\Delta\eta_{inv} &= \pm\left(\left|\frac{\partial\eta_{inv}}{\partial U_{AC}}\Delta U_{AC}\right| + \left|\frac{\partial\eta_{inv}}{\partial I_{AC}}\Delta I_{AC}\right| + \left|\frac{\partial\eta_{inv}}{\partial\varphi}\Delta\varphi\right| + \left|\frac{\partial\eta_{inv}}{\partial U_{DC}}\Delta U_{DC}\right| + \left|\frac{\partial\eta_{inv}}{\partial I_{DC}}\Delta I_{DC}\right|\right) \\
&= \pm 3\left(\left|\frac{I_{AC}\cos(\varphi)}{U_{DC}I_{DC}}\Delta U_{AC}\right| + \left|\frac{U_{AC}\cos(\varphi)}{U_{DC}I_{DC}}\Delta I_{AC}\right| + \left|-\frac{U_{AC}I_{AC}\sin(\varphi)}{U_{DC}I_{DC}}\Delta\varphi\right| \right. \\
&\qquad \left. + \left|\frac{U_{AC}I_{AC}\cos(\varphi)}{U_{DC}^2 I_{DC}}\Delta U_{DC}\right| + \left|\frac{U_{AC}I_{AC}\cos(\varphi)}{U_{DC}I_{DC}^2}\Delta I_{DC}\right|\right).
\end{aligned}
\tag{A.11}
$$

Similarly, the efficiency errors for the PMSM

$$
\begin{aligned}
\Delta\eta_{em} &= \pm\left(\left|\frac{\partial\eta_{em}}{\partial M_{em}}\Delta M_{em}\right| + \left|\frac{\partial\eta_{em}}{\partial\omega_m}\Delta\omega_m\right| + \left|\frac{\partial\eta_{em}}{\partial U_{AC}}\Delta U_{AC}\right| + \left|\frac{\partial\eta_{em}}{\partial I_{AC}}\Delta I_{AC}\right| + \left|\frac{\partial\eta_{em}}{\partial\varphi}\Delta\varphi\right|\right) \\
&= \pm\frac{1}{3}\left(\left|\frac{\omega_m}{U_{AC}I_{AC}\cos(\varphi)}\Delta M_{em}\right| + \left|\frac{M_{em}}{U_{AC}I_{AC}\cos(\varphi)}\Delta\omega_m\right| \right. \\
&\qquad \left. + \left|\frac{M_{em}\omega_m}{U_{AC}^2 I_{AC}\cos(\varphi)}\Delta U_{AC}\right| + \left|\frac{M_{em}\omega_m}{U_{AC}I_{AC}^2\cos(\varphi)}\Delta I_{AC}\right| + \left|\frac{2M_{em}\omega_m\sin(\varphi)}{U_{AC}I_{AC}(\cos(2\varphi)+1)}\Delta\varphi\right|\right)
\end{aligned}
\tag{A.12}
$$

and the drive system efficiency

$$
\begin{aligned}
\Delta\eta_{ds} &= \pm\left(\left|\frac{\partial\eta_{ds}}{\partial M_{em}}\Delta M_{em}\right| + \left|\frac{\partial\eta_{ds}}{\partial\omega_m}\Delta\omega_m\right| + \left|\frac{\partial\eta_{ds}}{\partial U_{DC}}\Delta U_{DC}\right| + \left|\frac{\partial\eta_{ds}}{\partial I_{DC}}\Delta I_{DC}\right|\right) \\
&= \pm\left(\left|\frac{\omega_m}{U_{DC}I_{DC}}\Delta M_{em}\right| + \left|\frac{M_{em}}{U_{DC}I_{DC}}\Delta\omega_m\right| + \left|\frac{M_{em}\omega_m}{U_{DC}^2 I_{DC}}\Delta U_{DC}\right| + \left|\frac{M_{em}\omega_m}{U_{DC}I_{DC}^2}\Delta I_{DC}\right|\right)
\end{aligned}
\tag{A.13}
$$

are calculated. The efficiency measurements for the gearbox can be calculated by

$$
\begin{aligned}
\Delta\eta_{gb} &= \pm\left(\left|\frac{\partial\eta_{gb}}{\partial M_{em}}\Delta M_{em}\right| + \left|\frac{\partial\eta_{gb}}{\partial\omega_m}\Delta\omega_m\right| + \left|\frac{\partial\eta_{gb}}{\partial M_w}\Delta M_w\right| + \left|\frac{\partial\eta_{gb}}{\partial\omega_w}\Delta\omega_w\right|\right) \\
&= \pm\left(\left|\frac{M_w\omega_w}{M_{em}^2\omega_m}\Delta M_{em}\right| + \left|\frac{M_w\omega_w}{M_{em}\omega_m^2}\Delta\omega_m\right| + \left|\frac{\omega_w}{M_{em}\omega_m}\Delta M_w\right| + \left|\frac{M_w}{M_{em}\omega_m}\Delta\omega_w\right|\right)
\end{aligned}
\tag{A.14}
$$

using only mechanical quantities. The overall system efficiency $\Delta\eta_{sys}$ is similar to the drive system efficiency $\Delta\eta_{ds}$ and is calculated with

$$
\begin{aligned}
\Delta\eta_{sys} &= \pm\left(\left|\frac{\partial\eta_{sys}}{\partial M_w}\Delta M_w\right| + \left|\frac{\partial\eta_{sys}}{\partial\omega_w}\Delta\omega_w\right| + \left|\frac{\partial\eta_{sys}}{\partial U_{DC}}\Delta U_{DC}\right| + \left|\frac{\partial\eta_{sys}}{\partial I_{DC}}\Delta I_{DC}\right|\right) \\
&= \pm\left(\left|\frac{\omega_w}{U_{DC}I_{DC}}\Delta M_w\right| + \left|\frac{M_w}{U_{DC}I_{DC}}\Delta\omega_w\right| + \left|\frac{M_w\omega_w}{U_{DC}^2 I_{DC}}\Delta U_{DC}\right| + \left|\frac{M_w\omega_w}{U_{DC}I_{DC}^2}\Delta I_{DC}\right|\right).
\end{aligned}
\tag{A.15}
$$

The errors of the measured quantities depend on the used measurement equipment and their corresponding measurement errors. This will be outlined below in more detail for each measured physical value. For a better overview, all measurement errors are summarized in Table A.1.

Current measurement errors

Current measurements occur in the test benches for measuring the quantities I_{DC}, I_U, I_V and I_W. However, the measurement process is equal for all quantities. The currents are measured using current transducers. Thus, the current measurement process contains two stages. First, the current will be transformed by the current transducer and then sampled by the power analyzer. Therefore, the measurement errors need to be considered separately. The maximum error of the current transducer ΔI_{CT} can be

Variable	Description	$0\,\mathrm{Hz}\ldots10\,\mathrm{Hz}$	$10\,\mathrm{Hz}\ldots2\,\mathrm{kHz}$	$2\,\mathrm{kHz}\ldots10\,\mathrm{kHz}$	$10\,\mathrm{kHz}\ldots100\,\mathrm{kHz}$	Unit
$\varepsilon_{CT,f}$	Measurement error of the current transducer	0.0015	0.01	0.2	2.5	%
$\varepsilon_{I,PA,mv}$	Measurement value dependent current measurement error of the power analyzer	0.02	0.015	0.03	0.2	%
$\varepsilon_{I,PA,mr}$	Measurement range dependent current measurement error of the power analyzer	0.06	0.03	0.06	0.4	%
$\varepsilon_{U,PA,mv}$	Measurement value dependent voltage measurement error of the power analyzer	0.02	0.02	0.03	0.1	%
$\varepsilon_{U,PA,mr}$	Measurement range dependent voltage measurement error of the power analyzer	0.06	0.03	0.06	0.2	%

Variable	Description	Value	Unit
$\varepsilon_{CT,c}$	Constant measurement error of the current transducer	0.01	%
I_o	Current offset of the current transducer	0.03	A
$\varepsilon_{TMS,n}$	Velocity measurement error of the torque measuring shaft	0.2	%
$\varepsilon_{TMS,M}$	Torque measurement error of the torque measuring shaft	0.1	%
ε_{PLC}	Error of the analog input of the Programmable Logic Controller (PLC)	0.05	%

Table A.1: Measurement errors

expressed with

$$\Delta I_{CT} = \varepsilon_{CT,f} I_{mr} + \varepsilon_{CT,c} I_{mv} + I_o, \tag{A.16}$$

where $\varepsilon_{CT,f}$ denotes the measurement range dependent error and is also dependent on the frequency of the measured signal. $\varepsilon_{CT,c}$ represents a constant measurement error over all frequencies. The measurement errors $\varepsilon_{CT,f}$ and $\varepsilon_{CT,c}$ are given in [204] and are also outlined in Table A.1. Due to the physical measurement principle of the current transducers, they are also afflicted with an offset I_o. I_{mr} represents the selected measurement range of the current measurement and I_{mv} outlines the actual measurement value.

The current measurement error in the power analyzer ΔI_{PA} can be expressed similarly with

$$\Delta I_{PA} = \varepsilon_{I,PA,mv} I_{mv} + \varepsilon_{I,PA,mr} I_{mr}. \tag{A.17}$$

Here, no constant term needs to be considered and the two error indicators $\varepsilon_{I,PA,mv}$ and $\varepsilon_{I,PA,mr}$ are frequency-dependent as described in [205]. The proposed errors for both measurement stages then sum up to the total error of the current measurements

$$\Delta I = \Delta I_{CT} + \Delta I_{PA}. \tag{A.18}$$

The resulting AC and DC current measurement errors differ only in the chosen measurement range and can be outlined as

$$\Delta I_{DC} = \varepsilon_{CT,f} I_{mr,DC} + \varepsilon_{CT,c} I_{mv} + I_o + \varepsilon_{I,PA,mv} I_{mv} + \varepsilon_{I,PA,mr} I_{mr,DC} \tag{A.19}$$

$$\Delta I_{AC} = \varepsilon_{CT,f} I_{mr,AC} + \varepsilon_{CT,c} I_{mv} + I_o + \varepsilon_{I,PA,mv} I_{mv} + \varepsilon_{I,PA,mr} I_{mr,AC}, \tag{A.20}$$

where $I_{mr,DC}$ and $I_{mr,AC}$ denote the measurement ranges for the DC and AC measurements. For the proposed application, $I_{mr,DC} = 66.5\,\text{A}$ and $I_{mr,AC} = 200\,\text{A}$ are chosen.

Voltage measurement errors

The voltage measurement is used to measure the quantities U_{DC}, U_{UV}, U_{UW} and U_{VW} and is only affected by the errors of the power analyzer. The corresponding measurement error can be expressed by

$$\Delta U = \varepsilon_{U,PA,mv} U_{mv} + \varepsilon_{U,PA,mr} U_{mr} \tag{A.21}$$

with $\varepsilon_{U,PA,mv}$ and $\varepsilon_{U,PA,mr}$ as frequency-dependent measurement errors related to the actual measurement value and the corresponding measurement range. The values are given in [205].

As for the current measurement, the resulting AC and DC voltage measurement errors also differ only in the chosen measurement range and can be outlined as

$$\Delta U_{DC} = \varepsilon_{U,PA,mv} U_{mv} + \varepsilon_{U,PA,mr} U_{mr,DC} \tag{A.22}$$

$$\Delta U_{AC} = \varepsilon_{U,PA,mv} U_{mv} + \varepsilon_{U,PA,mr} U_{mr,AC}, \tag{A.23}$$

where $U_{mr,DC}$ and $U_{mr,AC}$ denote the measurement ranges for the DC and AC measurements. For the proposed application, $I_{mr,DC} = 400\,\text{V}$ and $I_{mr,AC} = 400\,\text{V}$ are chosen.

Torque measurement errors

The torque measurement is also a two-stage process. The torque itself is measured in the torque measurement shaft and converted into an analog signal. In the second stage, the analog signal is processed by the PLC. The error produced by the torque measurement shaft depends only on the torque measurement range M_{mr} and is calculated with

$$\Delta M_{TMS} = \varepsilon_{TMS,M} M_{mr}, \tag{A.24}$$

where $\varepsilon_{TMS,M}$ denotes the relative error given in [206].

Similarly, the error of the analog input of the PLC depends only on its measurement range Umr, PLC. Thus, it can be expressed by

$$\Delta M_{PLC} = \varepsilon_{PLC} U_{mr,PLC} \alpha_{TMS,T}, \tag{A.25}$$

where ε_{PLC} denotes the relative error and $\alpha_{TMS,T}$ the scaling of the input as outlined in [207]. Accordingly, the total error of the torque measurement

$$\Delta M = \Delta M_{TMS} + \Delta M_{PLC} \tag{A.26}$$

is the sum of all related errors. The torque measurement errors differ in their measurement ranges $M_{mr,m}$ and $M_{mr,w}$ and their corresponding scalings $\alpha_{TMS,T,m}$ and $\alpha_{TMS,T,w}$. This is expressed by

$$\Delta M_{em} = \varepsilon_{TMS,M} M_{mr,m} + \varepsilon_{PLC} U_{mr,PLC} \alpha_{TMS,T,m} \tag{A.27}$$
$$\Delta M_w = \varepsilon_{TMS,M} M_{mr,w} + \varepsilon_{PLC} U_{mr,PLC} \alpha_{TMS,T,w} \tag{A.28}$$

for the PMSM and the wheel torque measurement. For the proposed application, $M_{mr,m} = 100\,\mathrm{Nm}$, $M_{mr,w} = 500\,\mathrm{Nm}$, $\alpha_{TMS,T,m} = 10\,\mathrm{Nm/V}$ and $\alpha_{TMS,T,w} = 50\,\mathrm{Nm/V}$ are chosen.

Velocity measurement errors

The velocity measurement is equal to the torque measurement and also a two-stage process. Thus, the measurement error of the velocity depends only on the measurement range w_{mr} of the torque measuring shaft and can be calculated by

$$\Delta \omega_{TMS} = \varepsilon_{TMS,\omega} \omega_{mr}, \tag{A.29}$$

where $\varepsilon_{TMS,\omega}$ denotes the relative error of the velocity measurement given in [206]. The PLC error can be calculated similarly as for the torque measurement with

$$\Delta \omega_{PLC} = \varepsilon_{PLC} U_{mr,PLC} \alpha_{TMS,\omega}, \tag{A.30}$$

where only $\alpha_{TMS,\omega}$ needs to be considered with the corresponding scaling. Likewise, the individual errors sum up to the total error Total error of the velocity measurement

$$\Delta \omega = \Delta \omega_{TMS} + \Delta \omega_{PLC} \tag{A.31}$$

of the velocity measurement. Also, the velocity measurements differ only in their measurement ranges $\omega_{mr,m}$ and $\omega_{mr,w}$ and the corresponding scalings $\alpha_{TMS,\omega,m}$ $\alpha_{TMS,\omega,w}$. The resulting errors can be calculated with

$$\Delta \omega_m = \varepsilon_{TMS,\omega} \omega_{mr,m} + \varepsilon_{PLC} U_{mr,PLC} \alpha_{TMS,\omega,m} \tag{A.32}$$
$$\Delta \omega_w = \varepsilon_{TMS,\omega} \omega_{mr,w} + \varepsilon_{PLC} U_{mr,PLC} \alpha_{TMS,\omega,w} \tag{A.33}$$

for the PMSM and the wheel velocity measurement. For the proposed application, $\omega_{mr,m} = 628\,\text{rad/s}$, $\omega_{mr,w} = 209.34\,\text{rad/s}$, $\alpha_{TMS,\omega,m} = 62.8\,\frac{\text{rad}}{\text{Vs}}$ and $\alpha_{TMS,\omega,w} = 20.934\,\frac{\text{rad}}{\text{Vs}}$ are chosen.

Efficiency errors

The maximum possible efficiency measurement errors for the different measurement configurations, as outlined in (A.11) to (A.15), are depicted in Figures A.7 to A.11. If electrical quantities are involved, it
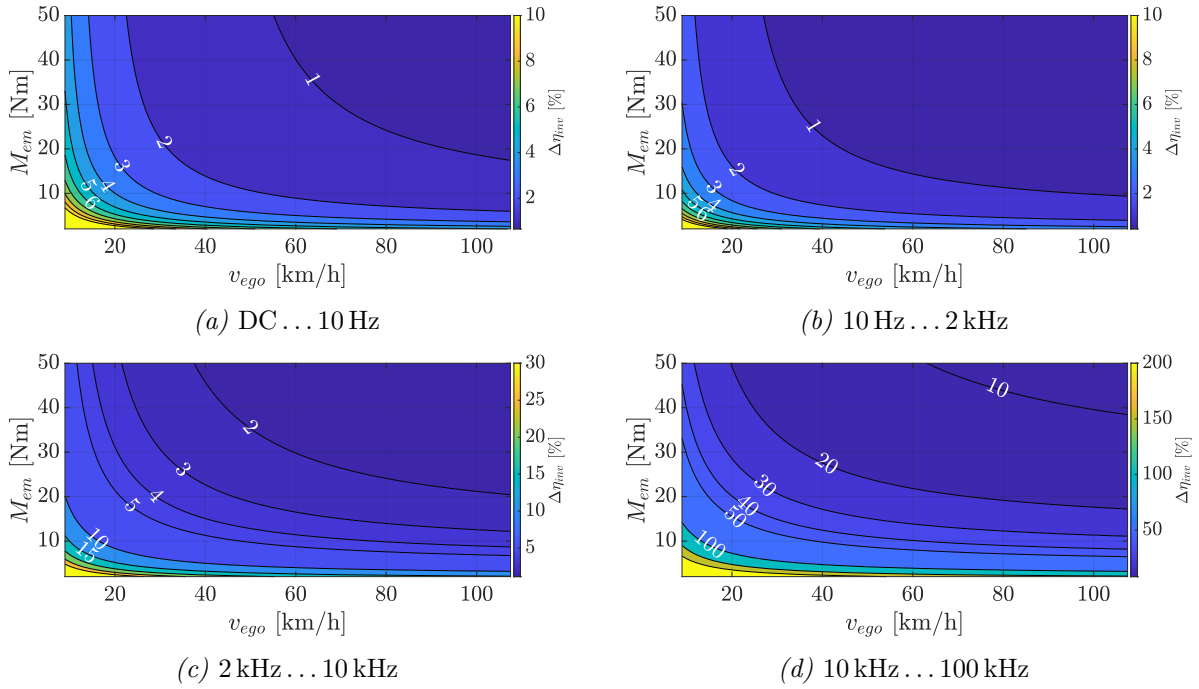

(a) $\text{DC} \dots 10\,\text{Hz}$

(b) $10\,\text{Hz} \dots 2\,\text{kHz}$

(c) $2\,\text{kHz} \dots 10\,\text{kHz}$

(d) $10\,\text{kHz} \dots 100\,\text{kHz}$

Figure A.7: Inverter efficiency measurement errors for different measurement frequencies

must be distinguished between different measurement frequencies of these quantities because the measurement errors of the power analyzer are giving according to frequency ranges of the measured signal. This is outlined in the corresponding subfigures for each measurement configuration. For the sake of completeness, the complete measurement range of the current transducers up to $100\,\text{kHz}$ is displayed. However, the frequency dependency is only important for the AC side and the frequencies higher than $2\,\text{kHz}$ are less important since the most amount of energy is included in the fundamental wave of the PMSM. From this error analysis, it can be seen that the maximum possible errors are in the areas of low power measurements, which are, in general, low torque or low-speed working points. In the other working points, the measurement errors are significantly decreasing. Considering that the worst-case errors are shown and that these will be considerably smaller in practice, the measurement accuracies in the test bench design are sufficient.

Figure A.8: Drive efficiency measurement errors for different measurement frequencies
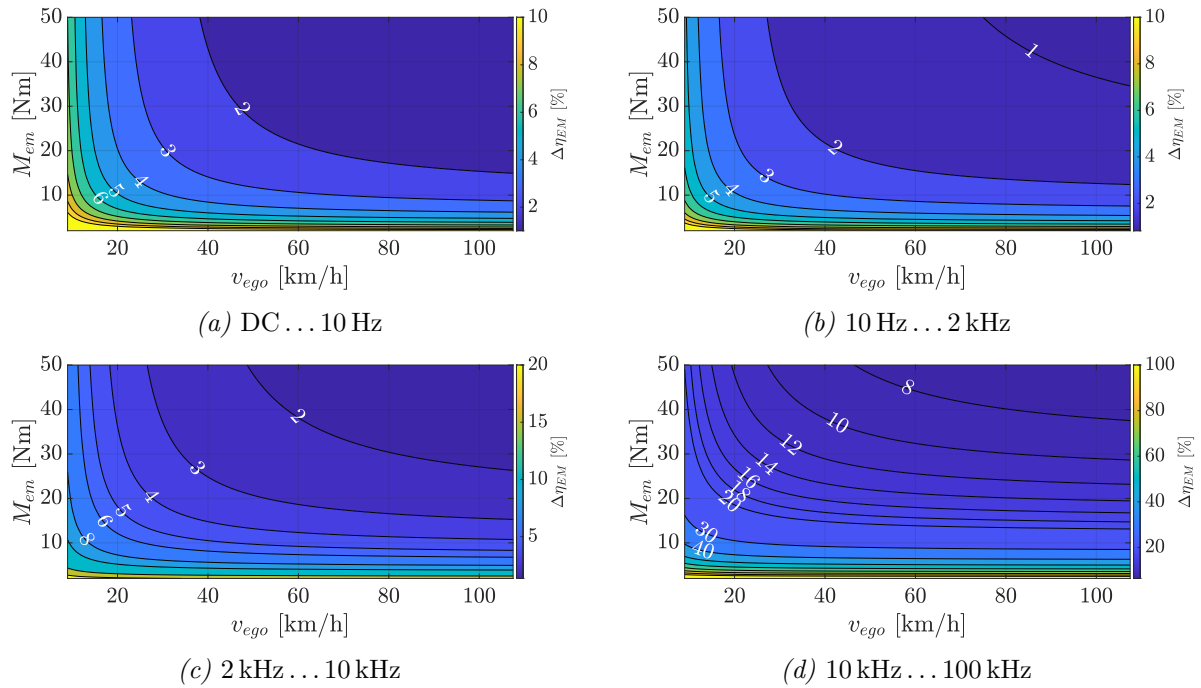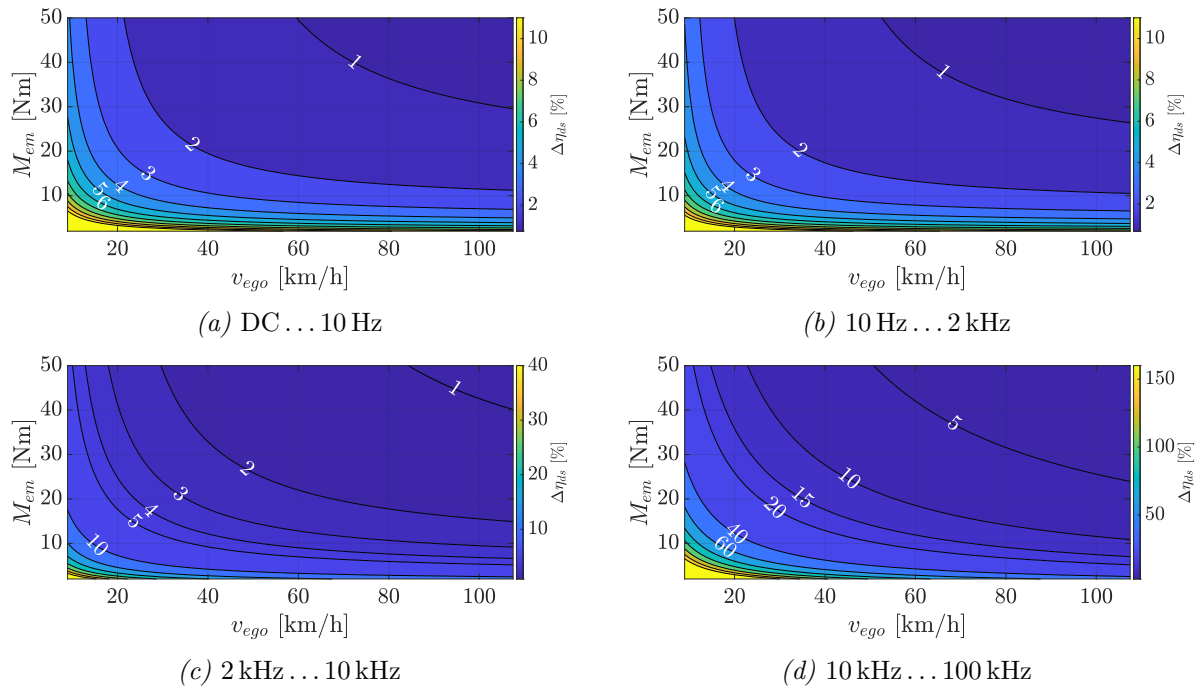

Figure A.9: Drive System efficiency measurement errors for different measurement frequencies
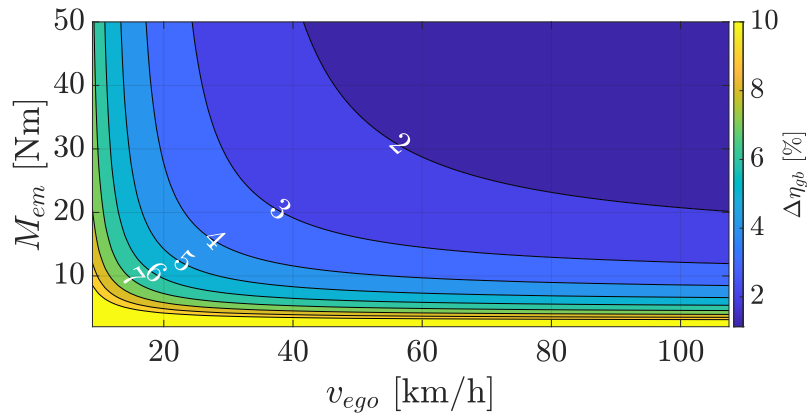
Figure A.10: Gearbox efficiency measurement errors for different measurement frequencies

(a) DC . . . 10 Hz

(b) 10 Hz . . . 2 kHz

(c) 2 kHz . . . 10 kHz

(d) 10 kHz . . . 100 kHz
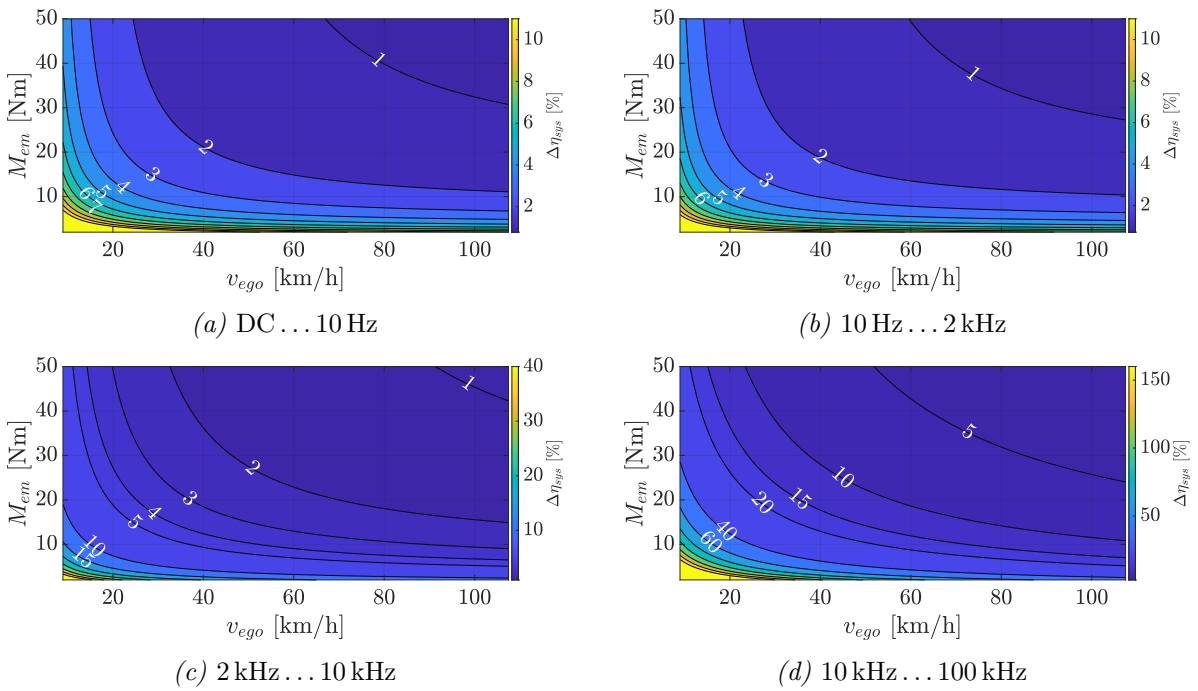
Figure A.11: System efficiency measurement errors for different measurement frequencies

B Nominal Vehicle Parameters

Table B.1: Nominal vehicle parameters

Name	Description	Type	Values	Unit
m_v	Vehicle mass including one passenger	Scalar	620	kg
m_{eq}	Vehicle equivalent mass	Scalar	639	kg
c_r	Rolling resistance coefficient	Scalar	0.01	–
c_w	Aerodynamic drag coefficient	Scalar	0.262	–
A_v	Frontal area	Scalar	2.036	m^2
ρ_{air}	Ambient air pressure	Scalar	984.23	hPa
ϑ_{air}	Ambient temperature	Scalar	20	°C
r_w	Wheel diameter	Scalar	0.283	m
i_g	Gear ratio	Scalar	5.85	–
ϑ_g	Measured gearbox efficiency	Matrix	See Figure 5.6	%
P_{pto}	Auxiliary power consumption	Scalar	500	W

Table B.2: Nominal battery system parameters

Name	Description	Type	Values	Unit
R_s	Working point dependent series resistance	Matrix	See Figure 5.13a	Ω
R_1	Working point dependent parallel resistance	Matrix	See Figure 5.13b	Ω
R_2	Working point dependent parallel resistance	Matrix	See Figure 5.13c	Ω
C_1	Working point dependent parallel capacitance	Matrix	See Figure 5.13d	F
C_2	Working point dependent parallel capacitance	Matrix	See Figure 5.13e	F
n_{cell}	Number of battery cells	Scalar	76	–
u_{ocv}	Open circuit voltage	Vector	See Figure 5.14a	V
Q_b	Battery capacity	Vector	See Figure 5.14b	Ah
$R_{th_{ca}}$	Thermal resistance between case and ambient	Scalar	0.37	K/W
$R_{th_{ct}}$	Thermal resistance between case and terminal	Scalar	2.6	K/W
$R_{th_{ta}}$	Thermal resistance between terminal and ambient	Scalar	1.05	K/W
C_c	Thermal capacitance of the core	Scalar	2544.24	Ws/K
C_t	Thermal capacitance of the terminals	Scalar	68.07	Ws/K
ϑ_{air}	Ambient temperature	Scalar	20	°C

Table B.3: Nominal inverter parameters

Name	Description	Type	Values	Unit
f_s	Inverter switching frequency	Scalar	16	kHz
$a_{c,T}$	Transistor conduction losses linear coefficient	Vector	See Figure B.1a	V
$b_{c,T}$	Transistor conduction losses quadratic coefficient	Vector	See Figure B.1a	Ω
$a_{c,D}$	Diode conduction losses linear coefficient	Vector	See Figure B.1b	V
$b_{c,D}$	Diode conduction losses quadratic coefficient	Vector	See Figure B.1b	Ω
$u_{ref,T}$	Transistor reference blocking voltage working point	Scalar	400	V
α_T	Transistor switching losses temperature coefficient	Scalar	0.0018	$-$
$\vartheta_{ref,T}$	Transistor switching losses reference temperature	Scalar	150	$^\circ$C
a_{Eon}	Transistor switch on losses linear coefficient	Scalar	3.17×10^{-5}	Vs
b_{Eon}	Transistor switch on losses quadratic coefficient	Scalar	7.24×10^{-9}	Vs/A
c_{Eon}	Transistor switch on losses constant coefficient	Scalar	0.0014	Ws
a_{Eoff}	Transistor switch off losses linear coefficient	Scalar	4.9×10^{-5}	Vs
b_{Eoff}	Transistor switch off losses quadratic coefficient	Scalar	1.7×10^{-8}	Vs/A
c_{Eoff}	Transistor switch off losses constant coefficient	Scalar	0.0029	Ws
κ_T	Transistor nonlinear blocking voltage dependency exponent	Scalar	1.3	$-$
$u_{ref,D}$	Diode reference blocking voltage working point	Scalar	400	V
α_D	Diode switching losses temperature coefficient	Scalar	0.004	$-$
$\vartheta_{ref,D}$	Diode switching losses reference temperature	Scalar	150	$^\circ$C
a_{Err}	Reverse recovery losses linear coefficient	Scalar	4.13×10^{-5}	Vs
b_{Err}	Reverse recovery losses quadratic coefficient	Scalar	-3.85×10^{-8}	Vs/A
c_{Err}	Reverse recovery losses constant coefficient	Scalar	0.0015	Ws
κ_D	Diode nonlinear blocking voltage dependency exponent	Scalar	0.6	$-$
$R_{th_{jw},T}$	Thermal resistance between transistor junction and coolant	Scalar	0.145	K/W
$R_{th_{jw},D}$	Thermal resistance between diode junction and coolant	Scalar	0.206	K/W
$\vartheta_{wg,in}$	Coolant inlet temperature	Scalar	30	$^\circ$C
$\dot{V}_{wg}$	Coolant flow rate	Scalar	6.5	l/min

Table B.4: Nominal drive parameters

Name	Description	Type	Values	Unit
p	Number of pole pairs	Scalar	10	$-$
R_{s,ϑ_0}	Series resistance at reference temperature	Scalar	16	Ω
L_d	Working point dependent direct inductance	Matrix	See Figure 5.27a	µH
L_q	Working point dependent quadrature inductance	Matrix	See Figure 5.27b	µH
Ψ_{pm,ϑ_0}	Magnetic flux of the permanent magnet	Vector	See Figure 5.27c	mV s
ξ_d	Working point dependent direct axis iron loss parameter	Matrix	See Figure 5.29a	$\mathrm{rad}^2/\mathrm{As}^3$
ξ_q	Working point dependent quadrature axis iron loss parameter	Matrix	See Figure 5.29b	$\mathrm{rad}^2/\mathrm{As}^3$
α_{cu}	Copper temperature coefficient	Scalar	0.0039	$-$
$\vartheta_{0,cu}$	Reference temperature stator winding	Scalar	20	$^\circ$C
α_{pm}	Magnet temperature coefficient	Scalar	-0.0021	$-$
$\vartheta_{0,pm}$	Magnet reference temperature	Scalar	20	$^\circ$C
ϑ_{st}	Stator temperature	Scalar	25	$^\circ$C
ϑ_{ro}	Rotor temperature	Scalar	25	$^\circ$C
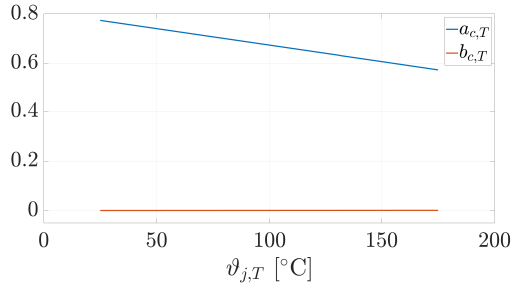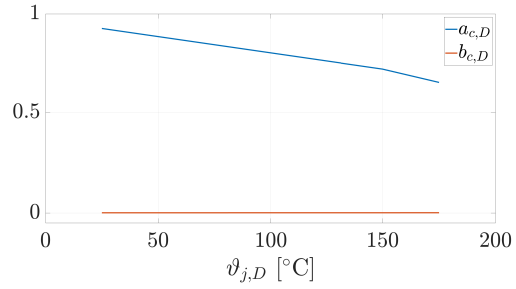
(a) IGBT   *(b)* Diode

Figure B.1: Temperature dependent conduction loss coefficients for IGBT and diode

Bibliography

[1] United Nations. Paris Agreement, 12.12.2015.

[2] Federal Ministry for the Environment, Nature Conservation, Building and Nuclear Safety. Climate Action Plan 2050: Principles and goals of the German government's climate policy.

[3] Crippa M, Guizzardi D, Solazzo E, Muntean M, Schaaf E, Monforti-Ferrario F, Banja M, Olivier J, Grassi G, Rossi S, and Vignati E. GHG emissions of all world countries: Scientific analysis or review. *1831-9424*, (EUR 30831 EN). `doi:10.2760/173513`.

[4] Petra Icha, Thomas Lauf, and Gunter Kuhs. Entwicklung der spezifischen Treibhausgas-Emissionen des deutschen Strommix in den Jahren 1990-2021.

[5] Atiyeh Vaezipour, Andry Rakotonirainy, and Narelle Haworth. Reviewing In-vehicle Systems to Improve Fuel Efficiency and Road Safety. *Procedia Manufacturing*, 3:3192–3199, 2015. `doi:10.1016/j.promfg.2015.07.869`.

[6] Jack N. Barkenbus. Eco-driving: An overlooked climate change initiative. *Energy Policy*, 38(2):762–769, 2010. `doi:10.1016/j.enpol.2009.10.021`.

[7] Max D. Morris. Factorial Sampling Plans for Preliminary Computational Experiments. *Technometrics*, 33(2):161–174, 1991. `doi:10.1080/00401706.1991.10484804`.

[8] Ilja M. Sobol. Sensitivity Analysis for Nonlinear Mathematical Models. *Mathematical Modeling and Computational Experiments*, 1(4):407–414, 1993.

[9] Jari Vepsäläinen, Kevin Otto, Antti Lajunen, and Kari Tammi. Computationally efficient model for energy demand prediction of electric city bus in varying operating conditions. *Energy*, 169:433–443, 2019. `doi:10.1016/j.energy.2018.12.064`.

[10] Johannes Asamer, Anita Graser, Bernhard Heilmann, and Mario Ruthmair. Sensitivity analysis for energy demand estimation of electric vehicles. *Transportation Research Part D: Transport and Environment*, 46:182–199, 2016. `doi:10.1016/j.trd.2016.03.017`.

[11] Shi Zhao and David A. Howey. Global Sensitivity Analysis of Battery Equivalent Circuit Model Parameters. In *2016 IEEE Vehicle Power and Propulsion Conference (VPPC)*, pages 1–4. IEEE, 2016. `doi:10.1109/VPPC.2016.7791696`.

[12] Thomas R. B. Grandjean, Liuying Li, Maria Ximena Odio, and Widanalage D. Widanage. Global Sensitivity Analysis of the Single Particle Lithium-Ion Battery Model with Electrolyte. In *2019 IEEE Vehicle Power and Propulsion Conference (VPPC)*, pages 1–7. IEEE, 2019. `doi:10.1109/VPPC46532.2019.8952455`.

[13] Matthias Braband, Michael Adams, Andreas Wilhelmi, and Matthias Scherer. Global Sensitivity Analysis on the Torque Accuracy of the Powertrain in Electric Vehicles. *IFAC-PapersOnLine*, 53(2):14067–14072, 2020. `doi:10.1016/j.ifacol.2020.12.939`.

[14] Elmer G. Gilbert. Vehicle cruise: Improved fuel economy by periodic control. *Automatica*, 12(2):159–166, 1976. `doi:10.1016/0005-1098(76)90079-0`.

[15] A. B. Schwarzkopf and R. B. Leipnik. Control of highway vehicles for minimum fuel consumption over varying terrain. *Transportation Research*, 11(4):279–286, 1977. `doi:10.1016/0041-1647(77)90093-4`.

[16] Y. Seki, J. Ohya, and M. Miyoshi. Collision avoidance system for vehicles applying model predictive control theory. In *Proceedings 199 IEEE/IEEJ/JSAI International Conference on Intelligent Transportation Systems*, pages 453–458. IEEE, 1999. `doi:10.1109/ITSC.1999.821100`.

[17] Frank Lattemann, Konstantin Neiss, Stephan Terwen, and Thomas Connolly. The Predictive Cruise Control – A System to Reduce Fuel Consumption of Heavy Duty Trucks. In *SAE Commercial Vehicle Engineering Congress & Exhibition*, SAE Technical Paper Series, 2004. `doi:10.4271/2004-01-2616`.

[18] Daniele Corona and Bart de Schutter. Comparison of a linear and a hybrid adaptive cruise controller for a SMART. In *2007 46th IEEE Conference on Decision and Control*, pages 4779–4784. IEEE, 2007. `doi:10.1109/CDC.2007.4434054`.

[19] Shengbo Li, Keqiang Li, Jianqiang Wang, Lei Zhang, Xiaomin Lian, Hiroshi Ukawa, and Dongsheng Bai. MPC based vehicular following control considering both fuel economy and tracking capability. In *2008 IEEE Vehicle Power and Propulsion Conference*, pages 1–6. IEEE, 2008. `doi:10.1109/VPPC.2008.4677689`.

[20] Gerrit Naus, Jeroen Ploeg, Rene van de Molengraft, and Maarten Steinbuch. Explicit MPC design and performance-based tuning of an Adaptive Cruise Control Stop-&-Go. In *2008 IEEE Intelligent Vehicles Symposium*, pages 434–439. IEEE, 2008. `doi:10.1109/IVS.2008.4621248`.

[21] G.J.L. Naus, J. Ploeg, M.J.G. van de Molengraft, W.P.M.H. Heemels, and M. Steinbuch. Design and implementation of parameterized adaptive cruise control: An explicit model predictive control approach. *Control Engineering Practice*, 18(8):882–892, 2010. `doi:10.1016/j.conengprac.2010.03.012`.

[22] Shengbo Li, Keqiang Li, Rajesh Rajamani, and Jianqiang Wang. Model Predictive Multi-Objective Vehicular Adaptive Cruise Control. *IEEE Transactions on Control Systems Technology*, 19(3):556–566, 2011. `doi:10.1109/TCST.2010.2049203`.

[23] Michael Henzler, Michael Buchholz, and Klaus Dietmayer. Online velocity trajectory planning for manual energy efficient driving of heavy duty vehicles using model predictive control. In *17th International IEEE Conference on Intelligent Transportation Systems (ITSC)*, pages 1814–1819. IEEE, 2014. `doi:10.1109/ITSC.2014.6957956`.

[24] T. Schwickart, H. Voos, J.-R. Hadji-Minaglou, M. Darouach, and A. Rosich. Design and simulation of a real-time implementable energy-efficient model-predictive cruise controller for electric vehicles. *Journal of the Franklin Institute*, 352(2):603–625, 2015. `doi:10.1016/j.jfranklin.2014.07.001`.

[25] Tim Schwickart, Holger Voos, Jean-Régis Hadji-Minaglou, and Mohamed Darouach. A Fast Model-Predictive Speed Controller for Minimised Charge Consumption of Electric Vehicles. *Asian Journal of Control*, 18(1):133–149, 2016. `doi:10.1002/asjc.1251`.

[26] Yanzhao Jia, Rabee Jibrin, Yutaro Itoh, and Daniel Görges. Energy-Optimal Adaptive Cruise Control for Electric Vehicles in Both Time and Space Domain based on Model Predictive Control. *IFAC-PapersOnLine*, 52(5):13–20, 2019. `doi:10.1016/j.ifacol.2019.09.003`.

[27] Nicholas J. Kohut, Professor J. Karl Hedrick, and Professor Francesco Borrelli. Integrating Traffic Data and Model Predictive Control to Improve Fuel Economy. *IFAC Proceedings Volumes*, 42(15):155–160, 2009. `doi:10.3182/20090902-3-US-2007.0032`.

[28] M. A. S. Kamal, Masakazu Mukai, Junichi Murata, and Taketoshi Kawabe. Ecological Vehicle Control on Roads With Up-Down Slopes. *IEEE Transactions on Intelligent Transportation Systems*, 12(3):783–794, 2011. `doi:10.1109/TITS.2011.2112648`.

[29] M.A.S. Kamal, M. Mukai, J. Murata, and T. Kawabe. Ecological Driving Based on Preceding Vehicle Prediction Using MPC. *IFAC Proceedings Volumes*, 44(1):3843–3848, 2011. doi:10.3182/20110828-6-IT-1002.02748.

[30] Md. Abdus Samad Kamal, Masakazu Mukai, Junichi Murata, and Taketoshi Kawabe. Model Predictive Control of Vehicles on Urban Roads for Improved Fuel Economy. *IEEE Transactions on Control Systems Technology*, 21(3):831–841, 2013. doi:10.1109/TCST.2012.2198478.

[31] Payman Shakouri, Andrzej Ordys, and Mohamad R. Askari. Adaptive cruise control with stop&go function using the state-dependent nonlinear model predictive control approach. *ISA transactions*, 51(5):622–631, 2012. doi:10.1016/j.isatra.2012.05.001.

[32] Payman Shakouri and Andrzej Ordys. Nonlinear Model Predictive Control approach in design of Adaptive Cruise Control with automated switching to cruise control. *Control Engineering Practice*, 26:160–177, 2014. doi:10.1016/j.conengprac.2014.01.016.

[33] M. Wang, W. Daamen, S. P. Hoogendoorn, and B. van Arem. Driver assistance systems modeling by model predictive control. In *2012 15th International IEEE Conference on Intelligent Transportation Systems*, pages 1543–1548. IEEE, 2012. doi:10.1109/ITSC.2012.6338824.

[34] Yan Chen, Xiaodong Li, Christopher Wiet, and Junmin Wang. Energy Management and Driving Strategy for In-Wheel Motor Electric Ground Vehicles With Terrain Profile Preview. *IEEE Transactions on Industrial Informatics*, 10(3):1938–1947, 2014. doi:10.1109/TII.2013.2290067.

[35] Kaijiang Yu, Junqi Yang, and Daisuke YAMAGUCHI. Model predictive control for hybrid vehicle ecological driving using traffic signal and road slope information. *Control Theory and Technology*, 13(1):17–28, 2015. doi:10.1007/s11768-015-4058-x.

[36] Roman Schmied, Harald Waschl, Rien Quirynen, Moritz Diehl, and Luigi del Re. Nonlinear MPC for Emission Efficient Cooperative Adaptive Cruise Control. *IFAC-PapersOnLine*, 48(23):160–165, 2015. doi:10.1016/j.ifacol.2015.11.277.

[37] Andreas Weißmann, Daniel Görges, and Xiaohai Lin. Energy-Optimal Adaptive Cruise Control based on Model Predictive Control. *IFAC-PapersOnLine*, 50(1):12563–12568, 2017. doi:10.1016/j.ifacol.2017.08.2196.

[38] Seyed Amin Sajadi-Alamdari, Holger Voos, and Mohamed Darouach. Nonlinear model predictive extended eco-cruise control for battery electric vehicles. In *2016 24th Mediterranean Conference on Control and Automation (MED)*, pages 467–472. IEEE, 2016. doi:10.1109/MED.2016.7535929.

[39] Mahyar Vajedi and Nasser L. Azad. Ecological Adaptive Cruise Controller for Plug-In Hybrid Electric Vehicles Using Nonlinear Model Predictive Control. *IEEE Transactions on Intelligent Transportation Systems*, 17(1):113–122, 2016. doi:10.1109/TITS.2015.2462843.

[40] Sadegh Tajeddin and Nasser L. Azad. Ecological Cruise Control of a Plug-in Hybrid Electric Vehicle: A comparison of different GMRES-based Nonlinear Model Predictive Controls. In *2017 American Control Conference (ACC)*, pages 3607–3612. IEEE, 2017. doi:10.23919/ACC.2017.7963505.

[41] Kenny A. Q. Caldas and Valdir Grassi. Eco-cruise NMPC Control for Autonomous Vehicles. In *2019 19th International Conference on Advanced Robotics (ICAR)*, pages 356–361. IEEE, 2019. doi:10.1109/ICAR46387.2019.8981639.

[42] Giorgio Frezza and Simos A. Evangelou. Ecological Adaptive Cruise Controller for a Parallel Hybrid Electric Vehicle. In *2020 European Control Conference (ECC)*, pages 491–498. IEEE, 2020. doi:10.23919/ECC51009.2020.9143700.

[43] M. Bichi, G. Ripaccioli, S. Di Cairano, D. Bernardini, A. Bemporad, and I. V. Kolmanovsky. Stochastic model predictive control with driver behavior learning for improved powertrain control. In *49th IEEE Conference on Decision and Control (CDC)*, pages 6077–6082. IEEE, 2010. doi:10.1109/CDC.2010.5717791.

[44] Dominik Moser, Harald Waschl, Harald Kirchsteiger, Roman Schmied, and Luigi del Re. Co-operative adaptive cruise control applying stochastic linear model predictive control strategies. In *2015 European Control Conference (ECC)*, pages 3383–3388. IEEE, 2015. `doi:10.1109/ECC.2015.7331057`.

[45] Seyed Amin Sajadi-Alamdari, Holger Voos, and Mohamed Darouach. Risk-averse Stochastic Nonlinear Model Predictive Control for Real-time Safety-critical Systems. *IFAC-PapersOnLine*, 50(1):5991–5997, 2017. `doi:10.1016/j.ifacol.2017.08.1431`.

[46] Seyed Amin Sajadi-Alamdari, Holger Voos, and Mohamed Darouach. Fast stochastic non-linear model predictive control for electric vehicle advanced driver assistance systems. In *2017 IEEE International Conference on Vehicular Electronics and Safety (ICVES)*, pages 91–96. IEEE, 2017. `doi:10.1109/ICVES.2017.7991907`.

[47] Richard Bellman. *Dynamic Programming*. Dover Books on Computer Science. Dover Publications, Newburyport, 2003.

[48] Tim Klemens Schwickart. *Energy-Efficient Driver Assistance System for Electric Vehicles Using Model-Predictive Control*. PhD thesis, University of Luxembourg, Luxemburg, 2015.

[49] Genyuan Li, Carey Rosenthal, and Herschel Rabitz. High Dimensional Model Representations. *The Journal of Physical Chemistry A*, 105(33):7765–7777, 2001. `doi:10.1021/jp010450t`.

[50] Seyed Amin Sajadi-Alamdari, Holger Voos, and Mohamed Darouach. Nonlinear Model Predictive Control for Ecological Driver Assistance Systems in Electric Vehicles. *Robotics and Autonomous Systems*, 112:291–303, 2019. `doi:10.1016/j.robot.2018.12.001`.

[51] Dan G. Cacuci. Sensitivity theory for nonlinear systems. I. Nonlinear functional analysis approach. *Journal of Mathematical Physics*, 22(12):2794–2802, 1981. `doi:10.1063/1.525186`.

[52] Dan G. Cacuci. Sensitivity theory for nonlinear systems. II. Extensions to additional classes of responses. *Journal of Mathematical Physics*, 22(12):2803–2812, 1981. `doi:10.1063/1.524870`.

[53] Tams Turányi. Sensitivity analysis of complex kinetic systems. Tools and applications. *Journal of Mathematical Chemistry*, 5(3):203–248, 1990. `doi:10.1007/BF01166355`.

[54] Andrea Saltelli, Ksenia Aleksankina, William Becker, Pamela Fennell, Federico Ferretti, Niels Holst, Sushan Li, and Qiongli Wu. Why so many published sensitivity analyses are false: A systematic review of sensitivity analysis practices. *Environmental Modelling & Software*, 114:29–39, 2019. `doi:10.1016/j.envsoft.2019.01.012`.

[55] Jon C. Helton. Uncertainty and sensitivity analysis techniques for use in performance assessment for radioactive waste disposal. *Reliability Engineering & System Safety*, 42(2-3):327–367, 1993. `doi:10.1016/0951-8320(93)90097-I`.

[56] R.I Cukier, H.B Levine, and K.E Shuler. Nonlinear sensitivity analysis of multiparameter model systems. *Journal of Computational Physics*, 26(1):1–42, 1978. `doi:10.1016/0021-9991(78)90097-9`.

[57] A. Saltelli, S. Tarantola, and K. P.-S. Chan. A Quantitative Model-Independent Method for Global Sensitivity Analysis of Model Output. *Technometrics*, 41(1):39–56, 1999. `doi:10.1080/00401706.1999.10485594`.

[58] S. Tarantola, D. Gatelli, and T. A. Mara. Random balance designs for the estimation of first order global sensitivity indices. *Reliability Engineering & System Safety*, 91(6):717–727, 2006. `doi:10.1016/j.ress.2005.06.003`.

[59] Thierry Alex Mara. Extension of the RBD-FAST method to the computation of global sensitivity indices. *Reliability Engineering & System Safety*, 94(8):1274–1281, 2009. `doi:10.1016/j.ress.2009.01.012`.

[60] Andrea Saltelli, Paola Annoni, Ivano Azzini, Francesca Campolongo, Marco Ratto, and Stefano Tarantola. Variance based sensitivity analysis of model output. Design and estimator for the total sensitivity index. *Computer Physics Communications*, 181(2):259–270, 2010. `doi:10.1016/j.cpc.2009.09.018`.

[61] Henri Faure. Discrépance de suites associées à un système de numération (en dimension s). *Acta Arithmetica*, 41(4):337–351, 1982.

[62] Harald Niederreiter. Point sets and sequences with small discrepancy. *Monatshefte für Mathematik*, 104(4):273–337, 1987. `doi:10.1007/BF01294651`.

[63] J. H. Halton. On the efficiency of certain quasi-random sequences of points in evaluating multi-dimensional integrals. *Numerische Mathematik*, 2(1):84–90, 1960. `doi:10.1007/BF01386213`.

[64] Ilja M. Sobol. On the distribution of points in a cube and the approximate evaluation of integrals. *USSR Computational Mathematics and Mathematical Physics*, 7(4):784–802, 1967. `doi:10.1016/0041-5553(67)90144-9`.

[65] I. M. Sobol. Uniformly distributed sequences with an additional uniform property. *USSR Computational Mathematics and Mathematical Physics*, 16(5):236–242, 1976. `doi:10.1016/0041-5553(76)90154-3`.

[66] Katherine Campbell, Michael D. McKay, and Brian J. Williams. Sensitivity analysis when model outputs are functions. *Reliability Engineering & System Safety*, 91(10-11):1468–1472, 2006. `doi:10.1016/j.ress.2005.11.049`.

[67] Matieyendou Lamboni, Hervé Monod, and David Makowski. Multivariate sensitivity analysis to measure global contribution of input factors in dynamic models. *Reliability Engineering & System Safety*, 96(4):450–459, 2011. `doi:10.1016/j.ress.2010.12.002`.

[68] Amandine Marrel, Bertrand Iooss, Michel Jullien, Béatrice Laurent, and Elena Volkova. Global sensitivity analysis for models with spatially dependent outputs. *Environmetrics*, 22(3):383–397, 2011. `doi:10.1002/env.1071`.

[69] Alen Alexanderian, Pierre A. Gremaud, and Ralph C. Smith. Variance-based sensitivity analysis for time-dependent processes. *Reliability Engineering & System Safety*, 196:106722, 2020. `doi:10.1016/j.ress.2019.106722`.

[70] Volker Schwieger. Sensitivity analysis as a general tool for model optimisation – examples for trajectory estimation. *Journal of Applied Geodesy*, 1(1):27–34, 2007. `doi:10.1515/jag.2007.004`.

[71] I. Zentner, E. de Rocquigny, and C. Stoisser. A Methodology for Treating Epistemic Uncertainties in Dynamic Response Analysis of Turboset. In *Proceedings of the 2nd International Conference on Uncertainty in Structural Dynamics, S*, pages 165–174, 2009.

[72] Ying Li, Thomas Pfeiffer, Jürgen Nuffer, Joachim Bös, and Holger Hanselka. Experimental sensitivity analysis for robustness studies of a controlled system. *Smart Materials and Structures*, 21(6):064002, 2012. `doi:10.1088/0964-1726/21/6/064002`.

[73] J. D. Herman, J. B. Kollat, P. M. Reed, and T. Wagener. Technical Note: Method of Morris effectively reduces the computational demands of global sensitivity analysis for distributed watershed models. *Hydrology and Earth System Sciences*, 17(7):2893–2903, 2013. `doi:10.5194/hess-17-2893-2013`.

[74] Alida Cosenza, Giorgio Mannina, Peter A. Vanrolleghem, and Marc B. Neumann. Global sensitivity analysis in wastewater applications: A comprehensive comparison of different methods. *Environmental Modelling & Software*, 49:40–52, 2013. `doi:10.1016/j.envsoft.2013.07.009`.

[75] Samir Touzani and Daniel Busby. Screening method using the derivative-based global sensitivity indices with application to reservoir simulator.

[76] Kathrin Menberg, Yeonsook Heo, and Ruchi Choudhary. Sensitivity analysis methods for building energy models: Comparing computational costs and extractable information. *Energy and Buildings*, 133:433–445, 2016. `doi:10.1016/j.enbuild.2016.10.005`.

[77] F. Baudoin, S. Le Roy, G. Teyssedre, C. Laurent, I. Alhossen, F. Bugarin, S. Segonds, and N. Binaud. Parameters sensitivity analysis in charge transport model using Sobol indexes for optimization purpose. In *2016 IEEE International Conference on Dielectrics (ICD)*, pages 832–835. IEEE, 2016. `doi:10.1109/ICD.2016.7547745`.

[78] Leszek J. Opalski. Efficient global sensitivity analysis method for models of systems with functional outputs. In *2015 European Conference on Circuit Theory and Design (ECCTD)*, pages 1–4. IEEE, 2015. `doi:10.1109/ECCTD.2015.7300048`.

[79] Junfeng Zhao, Wan Li, Junmin Wang, and Xuegang Ban. Dynamic Traffic Signal Timing Optimization Strategy Incorporating Various Vehicle Fuel Consumption Characteristics. *IEEE Transactions on Vehicular Technology*, 65(6):3874–3887, 2016. `doi:10.1109/TVT.2015.2506629`.

[80] B. Assaad, K. El kadri Benkara, G. Friedrich, S. Vivier, and A. Michon. Reducing the complexity of thermal models for electric machines via sensitivity analyses. In *2017 IEEE Energy Conversion Congress and Exposition (ECCE)*, pages 4658–4665. IEEE, 2017. `doi:10.1109/ECCE.2017.8096795`.

[81] Matthias Braband, Andreas Wilhelmi, and Matthias Scherer. Quantifizierung von Einflussfaktoren auf die Drehmomentgenauigkeit in elektrischen Antrieben mittels Sensitivitätsanalyse. In Heinz Schäfer, editor, *Elektrische Antriebstechnologie für Hybrid- und Elektrofahrzeuge*, pages 199–217. expert Verlag, 2019.

[82] Zonggen Yi and Peter H. Bauer. Sensitivity Analysis of Environmental Factors for Electric Vehicles Energy Consumption. In *2015 IEEE Vehicle Power and Propulsion Conference (VPPC)*, pages 1–6. IEEE, 2015. `doi:10.1109/VPPC.2015.7353012`.

[83] Zonggen Yi and Peter H. Bauer. Effects of environmental factors on electric vehicle energy consumption: a sensitivity analysis. *IET Electrical Systems in Transportation*, 7(1):3–13, 2017. `doi:10.1049/iet-est.2016.0011`.

[84] Toheed Ghandriz, Leo Laine, Jonas Hellgren, and Bengt Jacobson. Sensitivity analysis of optimal energy management in plug-in hybrid heavy vehicles. In *2017 2nd IEEE International Conference on Intelligent Transportation Engineering (ICITE)*, pages 320–327. IEEE, 2017. `doi:10.1109/ICITE.2017.8056932`.

[85] Nived Abhay, Jianning Dong, Pavol Bauer, and Simon Nouws. Efficiency Map based Modelling of Electric Drive for Heavy Duty Electric Vehicles and Sensitivity Analysis. In *2021 IEEE Transportation Electrification Conference & Expo (ITEC)*, pages 875–880. IEEE, 2021. `doi:10.1109/ITEC51675.2021.9490191`.

[86] Jari Vepsäläinen, Antti Ritari, Antti Lajunen, Klaus Kivekäs, and Kari Tammi. Energy Uncertainty Analysis of Electric Buses. *Energies*, 11(12):3267, 2018. `doi:10.3390/en11123267`.

[87] Bertrand Iooss and Paul Lemaître. A Review on Global Sensitivity Analysis Methods. In Gabriella Dellino and Carlo Meloni, editors, *Uncertainty Management in Simulation-Optimization of Complex Systems*, volume 59 of *Operations Research/Computer Science Interfaces Series*, pages 101–122. Springer US, Boston, MA, 2015. `doi:10.1007/978-1-4899-7547-8{\textunderscore}5`.

[88] Dennis K. J. Lin. A new class of supersaturated designs. *Technometrics*, 35(1):28–31, 1993. `doi:10.2307/1269286`.

[89] Bert Bettonvil and Jack P.C. Kleijnen. Searching for important factors in simulation models with many factors: Sequential bifurcation. *European Journal of Operational Research*, 96(1):180–194, 1997. `doi:10.1016/S0377-2217(96)00156-7`.

[90] Douglas C. Montgomery. *Design and analysis of experiments*. Wiley, Hoboken, NJ, tenth edition, 2020.

[91] T. W. Simpson, J. D. Poplinski, P. N. Koch, and J. K. Allen. Metamodels for Computer-based Engineering Design: Survey and recommendations. *Engineering with Computers*, 17(2):129–150, 2001. `doi:10.1007/PL00007198`.

[92] Kai-Tai Fang, Runze Li, and Agus Sudjianto. *Design and Modeling for Computer Experiments*. Chapman and Hall/CRC, 2005. `doi:10.1201/9781420034899`.

[93] Curtis B. Storlie and Jon C. Helton. Multiple predictor smoothing methods for sensitivity analysis: Description of techniques. *Reliability Engineering & System Safety*, 93(1):28–54, 2008. `doi:10.1016/j.ress.2006.10.012`.

[94] Andrea Saltelli. *Global sensitivity analysis: The primer*. Wiley, Chichester, 2008.

[95] Francesca Campolongo and Andrea Saltelli. Sensitivity analysis of an environmental model: an application of different analysis methods. *Reliability Engineering & System Safety*, 57(1):49–69, 1997. `doi:10.1016/S0951-8320(97)00021-5`.

[96] F. Campolongo, S. Tarantola, and A. Saltelli. Tackling quantitatively large dimensionality problems. *Computer Physics Communications*, 117(1-2):75–85, 1999. `doi:10.1016/S0010-4655(98)00165-9`.

[97] Andrea Saltelli, K. Chan, and E. M. Scott. *Sensitivity analysis*. Wiley, Chichester and Weinheim, 2008.

[98] Francesca Campolongo, Jessica Cariboni, and Andrea Saltelli. An effective screening design for sensitivity analysis of large models. *Environmental Modelling & Software*, 22(10):1509–1518, 2007. `doi:10.1016/j.envsoft.2006.10.004`.

[99] Toshimitsu Homma and Andrea Saltelli. Importance measures in global sensitivity analysis of nonlinear models. *Reliability Engineering & System Safety*, 52(1):1–17, 1996. `doi:10.1016/0951-8320(96)00002-6`.

[100] Fabrice Gamboa, Alexandre Janon, Thierry Klein, and Agnès Lagnoux. Sensitivity analysis for multidimensional and functional outputs. *Electronic Journal of Statistics*, 8(1):575–603, 2014. `doi:10.1214/14-EJS895`.

[101] Michiel J.W. Jansen. Analysis of variance designs for model output. *Computer Physics Communications*, 117(1-2):35–43, 1999. `doi:10.1016/S0010-4655(98)00154-4`.

[102] Ilja M. Sobol. Global sensitivity indices for the investigation of nonlinear mathematical models. *Matematicheskoe Modelirovanie*, 19(11):23–24, 2007.

[103] Makoto Matsumoto and Takuji Nishimura. Mersenne twister. *ACM Transactions on Modeling and Computer Simulation*, 8(1):3–30, 1998. `doi:10.1145/272991.272995`.

[104] John K. Salmon, Mark A. Moraes, Ron O. Dror, and David E. Shaw. Parallel random numbers. In Scott Lathrop, Jim Costa, and William Kramer, editors, *Proceedings of 2011 International Conference for High Performance Computing, Networking, Storage and Analysis on - SC '11*, page 1, New York, New York, USA, 2011. ACM Press. `doi:10.1145/2063384.2063405`.

[105] Guy L. Steele, Doug Lea, and Christine H. Flood. Fast splittable pseudorandom number generators. *ACM SIGPLAN Notices*, 49(10):453–472, 2014. `doi:10.1145/2714064.2660195`.

[106] Josef Dick and Friedrich Pillichshammer. *Digital Nets and Sequences*. Cambridge University Press, Cambridge, 2010. `doi:10.1017/CBO9780511761188`.

[107] William H. Press, Brian P. Flannery, Saul A. Teukolsky, and Wiliam T. Vetterling. *Numerical recipes in FORTRAN: The art of scientific computing.* Cambridge Univ. Press, Cambridge, 2. ed., reprinted. edition, 1992.

[108] Paul Bratley and Bennett L. Fox. Algorithm 659: Implementing Sobol's Quasirandom Sequence Generator. *ACM Transactions on Mathematical Software*, 14(1):88–100, 1988. `doi:10.1145/42288.214372`.

[109] I. M. Sobol and S. S. Kucherenko. On global sensitivity analysis of quasi-Monte Carlo algorithms. *Monte Carlo Methods and Applications*, 11(1):83–92, 2005. `doi:10.1515/1569396054027274`.

[110] B. Efron. Bootstrap Methods: Another Look at the Jackknife. *The Annals of Statistics*, 7(1):1–26, 1979. `doi:10.1214/aos/1176344552`.

[111] S. Dubreuil, M. Berveiller, F. Petitjean, and M. Salaün. Construction of bootstrap confidence intervals on sensitivity indices computed by polynomial chaos expansion. *Reliability Engineering & System Safety*, 121:263–275, 2014. `doi:10.1016/j.ress.2013.09.011`.

[112] Thomas J. DiCiccio and Bradley Efron. Bootstrap Confidence Intervals. *Statistical Science*, 11(3):189–212, 1996. `doi:10.1214/ss/1032280214`.

[113] G. E. B. Archer, A. Saltelli, and I. M. Sobol. Sensitivity measures, anova-like techniques and the use of bootstrap. *Journal of Statistical Computation and Simulation*, 58(2):99–120, 1997. `doi:10.1080/00949659708811825`.

[114] Lev Semenovich Pontryagin. *Mathematical theory of optimal processes.* CRC press, 1987.

[115] Jorge Nocedal and Stephen J. Wright. *Numerical optimization.* Springer series in operation research and financial engineering. Springer, New York, NY, second edition edition, 2006.

[116] Leonhard Euler. *Institutiones calculi integralis*, volume 1. impensis Academiae imperialis scientiarum, 1792.

[117] Karl Heun. Neue Methoden zur approximativen Integration der Differentialgleichungen einer unabhängigen Veränderlichen. *Z. Math. Phys*, 45:23–38, 1900.

[118] Wilhelm Kutta. Beitrag zur näherungsweisen Integration totaler Differentialgleichungen. *Z. Math. Phys.*, 46:435–453, 1901.

[119] H. G. Bock and K. J. Plitt. A Multiple Shooting Algorithm for Direct Solution of Optimal Control Problems *. *IFAC Proceedings Volumes*, 17(2):1603–1608, 1984. `doi:10.1016/S1474-6670(17)61205-9`.

[120] Thomas Binder, Luise Blank, H. Georg Bock, Roland Bulirsch, Wolfgang Dahmen, Moritz Diehl, Thomas Kronseder, Wolfgang Marquardt, Johannes P. Schlöder, and Oskar von Stryk. Introduction to Model Based Optimization of Chemical Processes on Moving Horizons. In Martin Grötschel, Sven O. Krumke, and Jörg Rambau, editors, *Online Optimization of Large Scale Systems*, pages 295–339. Springer Berlin Heidelberg, Berlin, Heidelberg, 2001. `doi:10.1007/978-3-662-04331-8{\textunderscore}18`.

[121] Lars Grüne and Jürgen Pannek. *Nonlinear Model Predictive Control: Theory and Algorithms.* Springer International Publishing, Cham, 2011. `doi:10.1007/978-0-85729-501-9`.

[122] Lars Grüne and Marleen Stieler. Asymptotic stability and transient optimality of economic MPC without terminal conditions. *Journal of Process Control*, 24(8):1187–1196, 2014. `doi:10.1016/j.jprocont.2014.05.003`.

[123] Matthew Ellis and Panagiotis D. Christofides. Real-time economic model predictive control of nonlinear process systems. *AIChE Journal*, 61(2):555–571, 2015. `doi:10.1002/aic.14673`.

[124] Matthew Ellis, Helen Durand, and Panagiotis D. Christofides. A tutorial review of economic model predictive control methods. *Journal of Process Control*, 24(8):1156–1178, 2014. `doi:10.1016/j.jprocont.2014.03.010`.

[125] Lino Guzzella and Antonio Sciarretta. *Vehicle Propulsion Systems*. Springer Berlin Heidelberg, Berlin, Heidelberg, 2013. `doi:10.1007/978-3-642-35913-2`.

[126] Lydia Dorrmann, Kerstin Sann-Ferro, Patrick Heininger, and Jochen Mähliß. Compendium: Li-ion batteries: Principles, characteristics, laws and standards.

[127] Peter. Kurzweil and Otto K. Dietlmeier. *Elektrochemische Speicher: Superkondensatoren, Batterien, Elektrolyse-Wasserstoff, Rechtliche Rahmenbedingungen*. Springer Vieweg, Wiesbaden, 2 edition, 2018. `doi:10.1007/978-3-658-21829-4`.

[128] Reiner Korthauer. *Handbuch Lithium-Ionen-Batterien*. Springer Berlin Heidelberg, Berlin, Heidelberg, 2013. `doi:10.1007/978-3-642-30653-2`.

[129] Heiko Witzenhausen. *Electrical battery models : modelling, parameter identification and model reduction*. RWTH Aachen University, 2017. `doi:10.18154/RWTH-2017-03437`.

[130] Marc Doyle, Thomas F. Fuller, and John Newman. Modeling of Galvanostatic Charge and Discharge of the Lithium/Polymer/Insertion Cell. *Journal of The Electrochemical Society*, 140(6):1526–1533, 1993. `doi:10.1149/1.2221597`.

[131] Thomas F. Fuller, Marc Doyle, and John Newman. Simulation and Optimization of the Dual Lithium Ion Insertion Cell. *Journal of The Electrochemical Society*, 141(1):1–10, 1994. `doi:10.1149/1.2054684`.

[132] Ulrike Krewer, Fridolin Röder, Eranda Harinath, Richard D. Braatz, Benjamin Bedürftig, and Rolf Findeisen. Review—Dynamic Models of Li-Ion Batteries for Diagnosis and Operation: A Review and Perspective. *Journal of The Electrochemical Society*, 165(16):A3656–A3673, 2018. `doi:10.1149/2.1061814jes`.

[133] Ruxiu Zhao, Phillip J. Kollmeyer, Robert D. Lorenz, and Thomas M. Jahns. A Compact Methodology Via a Recurrent Neural Network for Accurate Equivalent Circuit Type Modeling of Lithium-Ion Batteries. *IEEE Transactions on Industry Applications*, 55(2):1922–1931, 2019. `doi:10.1109/TIA.2018.2874588`.

[134] C.-F. Chiasserini and R. R. Rao. Energy efficient battery management. *IEEE Journal on Selected Areas in Communications*, 19(7):1235–1245, 2001. `doi:10.1109/49.932692`.

[135] Steven C. Hageman. Simple PSpice models let you simulate common battery types. *Electronic Design News*, 38(22):117–129, 1993.

[136] Ari Hentunen, Teemu Lehmuspelto, and Jussi Suomela. Time-Domain Parameter Extraction Method for Thévenin-Equivalent Circuit Battery Models. *IEEE Transactions on Energy Conversion*, 29(3):558–566, 2014. `doi:10.1109/TEC.2014.2318205`.

[137] S. Buller, M. Thele, R.W.A.A. DeDoncker, and E. Karden. Impedance-Based Simulation Models of Supercapacitors and Li-Ion Batteries for Power Electronic Applications. *IEEE Transactions on Industry Applications*, 41(3):742–747, 2005. `doi:10.1109/TIA.2005.847280`.

[138] S. M. Mousavi G. and M. Nikdel. Various battery models for various simulation studies and applications. *Renewable and Sustainable Energy Reviews*, 32:477–485, 2014. `doi:10.1016/j.rser.2014.01.048`.

[139] Jakama - Green Energy. Picture of Winston WB-LYP40AHA cell, 2022. Accessed on 22.04.2022. URL: `https://www.jakama-ge.sk/Winston-WB-LYP40AHA-LiFeYPO4-3-3V-40Ah-d431.htm`.

[140] gwl power. FAQ: What is inside the prismatic cell?, 2016. Accessed on 22.04.2022. URL: https://gwl-power.tumblr.com/post/137968557771/faq-what-is-inside-the-prismatic-cell-gwlpower.

[141] Stephan Buller. *Impedance based simulation models for energy storage devices in advanced automotive power systems.* PhD thesis, Aachen, 2003.

[142] Evgenij Barsoukov and J. Ross Macdonald. *Impedance Spectroscopy.* John Wiley & Sons, Inc, Hoboken, NJ, USA, 2018. doi:10.1002/9781119381860.

[143] Suleiman Abu-Sharkh and Dennis Doerffel. Rapid test and non-linear model characterisation of solid-state lithium-ion batteries. *Journal of Power Sources*, 130(1-2):266–274, 2004. doi:10.1016/j.jpowsour.2003.12.001.

[144] Taesic Kim and Wei Qiao. A Hybrid Battery Model Capable of Capturing Dynamic Circuit Characteristics and Nonlinear Capacity Effects. *IEEE Transactions on Energy Conversion*, 26(4):1172–1180, 2011. doi:10.1109/TEC.2011.2167014.

[145] Min Chen and G. A. Rincon-Mora. Accurate electrical battery model capable of predicting runtime and I-V performance. *IEEE Transactions on Energy Conversion*, 21(2):504–511, 2006. doi:10.1109/TEC.2006.874229.

[146] Hanlei Zhang and Mo-Yuen Chow. Comprehensive dynamic battery modeling for PHEV applications. In *IEEE PES General Meeting*, pages 1–6. IEEE, 2010. doi:10.1109/PES.2010.5590108.

[147] B. Schweighofer, K. M. Raab, and G. Brasseur. Modeling of high power automotive batteries by the use of an automated test system. *IEEE Transactions on Instrumentation and Measurement*, 52(4):1087–1091, 2003. doi:10.1109/TIM.2003.814827.

[148] Rolf Isermann. *Identifikation dynamischer Systeme 1.* Springer Berlin Heidelberg, Berlin, Heidelberg, 1992. doi:10.1007/978-3-642-84679-3.

[149] Peter Hamm. *Thermische Charakterisierung und Evaluierung einer LiFePO4-Batteriezelle.* Master project report, University of Applied Sciences Trier, 2021.

[150] Marcel Lehnertz. *Entwicklung eines Schätzverfahrens zur Bestimmung der inneren Zelltemperatur von LiFePO4 Batteriezellen.* Master project report, University of Applied Sciences Trier, Trier, 2021.

[151] J. W. Kolar, H. Ertl, and F. C. Zach. Influence of the modulation method on the conduction and switching losses of a PWM converter system. *IEEE Transactions on Industry Applications*, 27(6):502–512, 1991. doi:10.1109/28.108456.

[152] Dierk Schröder. *Elektrische Antriebe - Regelung von Antriebssystemen.* Springer-Verlag, Berlin, Heidelberg, 4 edition, 2015. doi:10.1007/978-3-642-30096-7.

[153] Infineon Technologies AG. HybridPACK Drive Module FS820R08A6P2: Final Data Sheet, V3.3.

[154] Uwe Drofenik and Johann W. Kolar. A general scheme for calculating switching-and conduction-losses of power semiconductors in numerical circuit simulations of power electronic systems. In *Proc. IPEC*, volume 5, pages 4–8, 2005.

[155] M. H. Bierhoff and F. W. Fuchs. Semiconductor losses in voltage source and current source IGBT converters based on analytical derivation. In *2004 IEEE 35th Annual Power Electronics Specialists Conference*, pages 2836–2842. IEEE, 2004. doi:10.1109/PESC.2004.1355283.

[156] Thomas Windisch. *Energieeffiziente Antriebsregelung für hochausgenutzte Drehstrommotoren in elektrisch angetriebenen Fahrzeugen.* Dissertation, Technische Universität Dresden and Shaker Verlag GmbH, 2018.

[157] Thomas Windisch and Wilfried Hofmann. Energieeffiziente Regelung von Fahrzeugantrieben mit permanenterregten Synchron- und Asynchronmotoren unter Berücksichtigung von Umrichter, Eisenverlusten und Sättigung. In Heinz Schäfer, editor, *Elektrische Antriebstechnologie für Hybrid- und Elektrofahrzeuge*, pages 218–237. expert Verlag, 2019.

[158] Arendt Wintrich, Ulrich Nicolai, Werner Tursky, and Tobias Reimann. *Applikationshandbuch Leistungshalbleiter*. ISLE Verlag, Ilmenau, second edition, 2015.

[159] Sven Konrad. *Ein Beitrag zur Auslegung und Integration spannungsgespeister IGBT-Wechselrichter*. PhD thesis, Unversity of Ilmenau, Ilmenau, 1997.

[160] Hans Dieter Baehr and Karl Stephan. *Wärme- und Stoffübertragung*. Springer-Lehrbuch. Springer Vieweg, Berlin, 8 edition, 2013. `doi:10.1007/978-3-642-36558-4`.

[161] Dierk Schröder. *Elektrische Antriebe - Grundlagen*. Springer-Lehrbuch. Springer, Berlin, Heidelberg, 5 edition, 2013. `doi:10.1007/978-3-642-30471-2`.

[162] Andreas Binder. *Elektrische Maschinen und Antriebe: Grundlagen Betriebsverhalten*. VDI-Buch. Springer Berlin Heidelberg, Berlin, Heidelberg, 2012. `doi:10.1007/978-3-540-71850-5`.

[163] Sven Ludwig Kellner. *Parameteridentifikation bei permanenterregten Synchronmaschinen*. PhD thesis, University of Erlangen-Nuremberg, Erlangen, 2012.

[164] Ji-Young Lee, Sang-Ho Lee, Geun-Ho Lee, Jung-Pyo Hong, and Jin Hur. Determination of parameters considering magnetic nonlinearity in an interior permanent magnet synchronous motor. *IEEE Transactions on Magnetics*, 42(4):1303–1306, 2006. `doi:10.1109/TMAG.2006.871951`.

[165] T. J. Woolmer and M. D. McCulloch. Analysis of the Yokeless And Segmented Armature Machine. In *2007 IEEE International Electric Machines & Drives Conference*, pages 704–708. IEEE, 2007. `doi:10.1109/IEMDC.2007.382753`.

[166] Otfried Georg. *Elektromagnetische Felder und Netzwerke*. Springer Berlin Heidelberg, Berlin, Heidelberg, 1999. `doi:10.1007/978-3-642-58420-6`.

[167] Nguyen Phung Quang and Jörg-Andreas Dittrich. *Vector Control of Three-Phase AC Machines*. Springer Berlin Heidelberg, Berlin, Heidelberg, 2015. `doi:10.1007/978-3-662-46915-6`.

[168] Uwe Vollmer. *Entwurf, Auslegung und Realisierung eines verlustoptimierten elektrischen Antriebs für Hybridfahrzeuge*. PhD thesis, 2012. `doi:10.14279/depositonce-3417`.

[169] R. H. Park. Two-reaction theory of synchronous machines generalized method of analysis-part I. *Transactions of the American Institute of Electrical Engineers*, 48(3):716–727, 1929. `doi:10.1109/T-AIEE.1929.5055275`.

[170] G. Bertotti. General properties of power losses in soft ferromagnetic materials. *IEEE Transactions on Magnetics*, 24(1):621–630, 1988. `doi:10.1109/20.43994`.

[171] G. E. Fish. Soft magnetic materials. *Proceedings of the IEEE*, 78(6):947–972, 1990. `doi:10.1109/5.56909`.

[172] R. Weninger. Einfluß der Maschinenparameter auf Zusatzverluste, Momentoberschwingungen und Kommutierung bei der Umrichterspeisung von Asynchronmaschinen. *Archiv für Elektrotechnik*, 63(1):19–28, 1981. `doi:10.1007/BF01574583`.

[173] Chas. Proteus Steinmetz. On the Law of Hysteresis. *Transactions of the American Institute of Electrical Engineers*, IX(1):1–64, 1892. `doi:10.1109/T-AIEE.1892.5570437`.

[174] J. Reinert, A. Brockmeyer, and R.W.A.A. de Doncker. Calculation of losses in ferro- and ferrimagnetic materials based on the modified Steinmetz equation. *IEEE Transactions on Industry Applications*, 37(4):1055–1061, 2001. `doi:10.1109/28.936396`.

[175] Jieli Li, T. Abdallah, and C. R. Sullivan. Improved calculation of core loss with nonsinusoidal waveforms. In *Conference Record of the 2001 IEEE Industry Applications Conference. 36th IAS Annual Meeting (Cat. No.01CH37248)*, pages 2203–2210. IEEE, 2001. doi:10.1109/IAS.2001.955931.

[176] K. Venkatachalam, C. R. Sullivan, T. Abdallah, and H. Tacca. Accurate prediction of ferrite core loss with nonsinusoidal waveforms using only Steinmetz parameters. In *2002 IEEE Workshop on Computers in Power Electronics, 2002. Proceedings*, pages 36–41. IEEE, 2002. doi:10.1109/CIPE.2002.1196712.

[177] F. Fernandez-Bernal, A. Garcia-Cerrada, and R. Faure. Determination of parameters in interior permanent-magnet synchronous motors with iron losses without torque measurement. *IEEE Transactions on Industry Applications*, 37(5):1265–1272, 2001. doi:10.1109/28.952501.

[178] N. Urasaki, T. Senjyu, and K. Uezato. A novel calculation method for iron loss resistance suitable in modeling permanent-magnet synchronous motors. *IEEE Transactions on Energy Conversion*, 18(1):41–47, 2003. doi:10.1109/TEC.2002.808329.

[179] S. Morimoto, Y. Tong, Y. Takeda, and T. Hirasa. Loss minimization control of permanent magnet synchronous motor drives. *IEEE Transactions on Industrial Electronics*, 41(5):511–517, 1994. doi:10.1109/41.315269.

[180] United Nations. Addendum 100: Regulation No. 101, 2013.

[181] United Nations. Addendum 15: United Nations Global Technical Regulation No. 15: Worldwide harmonized Light vehicles Test Procedures (WLTP), 2021.

[182] Michel André. Real-world driving cycles for measuring cars pollutant emissions-Part A: The ARTEMIS European driving cycles.

[183] Michel André. The ARTEMIS European driving cycles for measuring car pollutant emissions. *The Science of the total environment*, 334-335:73–84, 2004. doi:10.1016/j.scitotenv.2004.04.070.

[184] M. André. Driving patterns analysis and driving cycles, within the project: European Development of Hybrid Technology approaching efficient Zero Emission Mobility (HYZEM). *INRETS report, n LEN*, 9709:47, 1997.

[185] HERE Technologies. HERE Plattform, 2022. Accessed on 22.03.2022. URL: https://www.here.com/platform.

[186] Fernando Puente León and Uwe Kiencke. *Messtechnik*. Springer Berlin Heidelberg, Berlin, Heidelberg, 2011. doi:10.1007/978-3-642-20239-1.

[187] Fernando Puente León. *Messtechnik: Systemtheorie für Ingenieure und Informatiker*. Lehrbuch. Springer Vieweg, Berlin and Heidelberg, 10. auflage edition, 2015. doi:10.1007/978-3-662-44821-2.

[188] DLR, infas 360 GmbH, infas Institut für angewandte Sozialwissenschaft, and IVT Research GmbH. Mobilität in Deutschland: Tabellarische Grundauswertung: Deutschland, 2018.

[189] DWD Climate Data Center. 10-minute values of station observations of air temperature 2 m above ground in °C for Germany, version v19.3, 2022. Accessed on 27.05.2022. URL: https://cdc.dwd.de/portal/.

[190] DWD Climate Data Center. Hourly station observations of air pressure at station level in hPa for Germany, version v21.3, 2022. Accessed on 27.05.2022. URL: https://cdc.dwd.de/portal/.

[191] Jerzy Ejsmont, Leif Sjögren, Beata Świeczko-Żurek, and Grzegorz Ronowski. Influence of Road Wetness on Tire-Pavement Rolling Resistance. *Journal of Civil Engineering and Architecture*, 9(11), 2015. doi:10.17265/1934-7359/2015.11.004.

[192] Timm Faulwasser, Lars Grüne, and Matthias A. Müller. Economic Nonlinear Model Predictive Control. *Foundations and Trends® in Systems and Control*, 5(1):1–98, 2018. `doi:10.1561/2600000014`.

[193] Jan Marian Maciejowski. *Predictive control: With constraints.* Prentice Hall, Harlow, 2002.

[194] Joel A E Andersson, Joris Gillis, Greg Horn, James B Rawlings, and Moritz Diehl. CasADi – A software framework for nonlinear optimization and optimal control. *Mathematical Programming Computation*, 11(1):1–36, 2019. `doi:10.1007/s12532-018-0139-4`.

[195] Robin Verschueren, Gianluca Frison, Dimitris Kouzoupis, Jonathan Frey, Niels van Duijkeren, Andrea Zanelli, Branimir Novoselnik, Thivaharan Albin, Rien Quirynen, and Moritz Diehl. acados: a modular open-source framework for fast embedded optimal control. URL: `http://arxiv.org/pdf/1910.13753v3`.

[196] Robin Verschueren, Gianluca Frison, Dimitris Kouzoupis, Jonathan Frey, Niels van Duijkeren, Andrea Zanelli, Branimir Novoselnik, Thivaharan Albin, Rien Quirynen, and Moritz Diehl. acados – a modular open-source framework for fast embedded optimal control. *Mathematical Programming Computation*, 2021. `doi:10.1007/s12532-021-00208-8`.

[197] Gianluca Frison and Moritz Diehl. HPIPM: a high-performance quadratic programming framework for model predictive control. *IFAC-PapersOnLine*, 53(2):6563–6569, 2020. `doi:10.1016/j.ifacol.2020.12.073`.

[198] Ulrich Brannolte and Siegfried Holz. Simulation des Verkehrsablaufs auf Landstraßen-Modellerweiterung-. *Forschung Straßenbau und Straßenverkehrstechnik*, (402), 1983.

[199] Stefan M. Stefanov. *Separable Programming*, volume 53. Springer US, Boston, MA, 2001. `doi:10.1007/978-1-4757-3417-1`.

[200] Helmut Tschöke. *Die Elektrifizierung des Antriebsstrangs: Basiswissen.* ATZ/MTZ-Fachbuch. Springer Fachmedien Wiesbaden, Wiesbaden, 2015. `doi:10.1007/978-3-658-04644-6`.

[201] Jonas Feldmann. *Parameteridentikation an Lithiumeisenphosphatzellen.* Bachelor project report, University of Applied Sciences Trier, 2020.

[202] Matthias Scherer. UniControl - eine universelle Steuer- und Regelelektronik, 2022. Accessed on 22.04.2022. URL: `https://www.hochschule-trier.de/hauptcampus/technik/ies/fahrzeugsystemtechnik-und-elektronik/projekte/unicontrol`.

[203] Lothar Papula. *Mathematik für Ingenieure und Naturwissenschaftler Band 3.* Springer Fachmedien Wiesbaden and Imprint Springer Vieweg, Wiesbaden, 7. aufl. 2016 edition, 2016. `doi:10.1007/978-3-658-11924-9`.

[204] ZES ZIMMER Electronic Systems GmbH. Sensors & Accessories for LMG Family User Manual.

[205] ZES ZIMMER Electronic Systems GmbH. LMG 500 User Manual.

[206] KTR Systems GmbH. DATAFLEX 32/... Drehmomentmesswelle: Betriebs-/Montageanleitung.

[207] Siemens AG. 6ES7134-6HB00-0CA1 Datasheet.